UNIVERSITY OF SOUTHAMPTON

FACULTY OF ENGINEERING AND THE ENVIRONMENT

Solar Energy Laboratory

Application of Fluorescent and Photonic Concentrators to Solar cells

by

Thomas Stephen Parel

Thesis for the degree of Doctor of Philosophy

February 2015

UNIVERSITY OF SOUTHAMPTON

ABSTRACT

FACULTY OF ENGINEERING AND THE ENVIRONMENT

Solar Energy

Thesis for the degree of Doctor of Philosophy

APPLICATION OF FLUORESCENT AND PHOTONIC CONCENTRATORS TO SOLAR CELLS

Thomas Stephen Parel

Fluorescent solar collectors are cheap plates made generally of glass or plastic that is doped with fluorescent molecules. Fluorescence can be used to trap incident solar radiation in order to concentrate light and also to shift the radiation to wavelengths converted at higher efficiencies. This project investigates both these aspects. Solar concentration using fluorescent solar collectors is examined for different combinations of solar cells and mirrors coupled to different surfaces of fluorescent solar collectors. The effects of the fabrication method i.e. spin coating or moulding is also studied. Modelling of the fluorescence re-absorption is the key to obtain the efficiency of such systems and these models will be shown to be useful in the optimisation of certain configurations of fluorescent collectors that behave like ideal models. On comparison with experimental results these models can also be used to quantify and identify losses in configurations that suffer additional losses. Devices tested in the lab are estimated to have the potential to achieve power conversion efficiencies close to 4% while results of optimisation results indicate possible further improvements. Angular resolved measurements of the fluorescence exiting the fluorescent solar collector edge is also used to study the photon transport of light within these devices. The combination of solar concentration and wavelength shifting (to wavelengths with superior solar cell performance) has been exploited for application to cadmium telluride solar cells for the first time. The theory of operation of these devices is used to model the current output measured experimentally. Novel photonic-based structures that incorporate fluorescent molecules within one-dimensional photonic crystals has also been fabricated and characterised. It will be shown that these devices have the potential to reduce fundamental loss mechanisms found in conventional fluorescent solar collectors by suppressing and reducing emission within loss cones and tuning emission reaching the solar cells to certain wavelengths. The theory of operation of these devices will used to describe the propagation of light within the structure and explain the experimentally measured emission characteristics. The maximum theoretical efficiencies of photonic-based fluorescent solar collectors have also been derived and adapted from previous work to show the potential of such devices.

Table of contents

List of tables

List of figures

Declaration of authorship

I, Thomas Stephen Parel declare that this thesis and the work presented in it are my own and has been generated by me as the result of my own original research.

Application of fluorescent and photonic concentrators to solar cells.

I confirm that:

1. This work was done wholly or mainly while in candidature for a research degree at this University;
2. Where any part of this thesis has previously been submitted for a degree or any other qualification at this University or any other institution, this has been clearly stated;
3. Where I have consulted the published work of others, this is always clearly attributed;
4. Where I have quoted from the work of others, the source is always given. With the exception of such quotations, this thesis is entirely my own work;
5. I have acknowledged all main sources of help;
6. Where the thesis is based on work done by myself jointly with others, I have made clear exactly what was done by others and what I have contributed myself;
7. Parts of this work have been published as:

Journal publications

Parel, T.S., Danos, L., Fang, L. and Markvart, T., 2014. *Modelling photon transport in fluorescent solar concentrators.* Progress in Photovoltaics. DOI: 10.1002/pip.2553.

Danos, L., Parel, T. and Markvart, T., 2012. *Increased efficiencies on CdTe solar cells via luminescence down-shifting with excitation energy transfer between dyes.* Solar Energy Materials and Solar Cells. 98, 486-490. DOI: 10.1016/j.solmat.2011.11.009.

Fang, L., Parel, T. Danos, L. and Markvart, T., 2012. *Photon reabsorption in fluorescent solar collectors*. Journal of Applied Physics. 111: 076104 1-3. DOI: 10.1063/1.3702815.

Markvart, T., Danos, L., Fang, L., Parel, T. and Soleimani, N., 2012. *Photon frequency management for trapping & concentration of sunlight*. RSC Advances. 2: 3173-3179. DOI: 10.1039/C2RA01160C.

Journal publications in preparation/under review

Parel, T.S., Pistolas, C., Danos, L. and Markvart, T., 2014. *Modelling and experimental analysis of the angular distribution of the emitted light from the edge of luminescent solar concentrators.* Optical Materials. Corrections submitted.

Parel, T. and Markvart, T., 2014. *Fabrication and characterisation of a 1D integrated photonic fluorescent concentrator*. In Preparation.

Parel, T., Danos, L. and Markvart, T., 2014. *Combining spectral matching and light concentration properties of fluorescent collectors to improve the performance of CdTe solar cells with poor short wavelength response.* In Preparation.

Conference proceedings

Alderman, N., Danos, L., Fang, L., Parel, T. and Markvart, T., 2014. *Enhancing light capture by silicon – with the help of molecules.* Proceedings of the 40th IEEE Photovoltaics Specialists Conference. June 8-13, Denver, Colorado. 17-21. DOI: 10.1109/PVSC.2014.6924987.

Parel, T.S., Danos, L. and Markvart, T., 2013. *Photon transport in fluorescent solar concentrators.* Proceedings of the 39th IEEE Photovoltaics Specialists Conference. June 16-21, Tampa, Florida, USA. 1761-1765. DOI: 10.1109/PVSC.2013.6744484.

Pistolas, C., Parel, T.S., Danos, L. and Markvart, T., 2013. *Experimental analysis of the angular distribution of emission from the edge of fluorescent collectors.* Proceedings of the 9th Photovoltaic Science, Applications and Technology Conference. April 10-12, Swansea, United Kingdom. 191-194. **[Winner of best poster/paper: solar cell characterisation]**

Markvart, T., Danos, L., Alderman, N., Fang, L. and Parel, T.S., 2012. *Harvesting sunshine: solar cells, photosynthesis and the thermodynamics of light.* Proceedings of the 27th European Photovoltaic Solar Energy Conference. September 24-28, Frankfurt, Germany. 1-6. **[Keynote address]**

Parel, T., Fang, L., Chu, X., Danos, L. and Markvart, T., 2011. *Comparison of fluorescent down-shifting layers for increasing the efficiency of CdS/CdTe solar cells*. Proceedings of the 7th Photovoltaic Science, Applications and Technology Conference. April 6-8, Edinburgh, United Kingdom. 87-90.

Fang, L., Parel, T., Danos, L. and Markvart, T., 2011. *Modelling the performance of fluorescent solar collectors*. Proceedings of 7th Photovoltaic Science, Applications and Technology Conference. April 6-8, Edinburgh, United Kingdom. 165-168.

Oral presentations

Photon transport in fluorescent solar concentrators. 39th IEEE Photovoltaics Specialists Conference. 19 June 2013, Tampa, Florida, USA.

Comparison of fluorescent down-Shifting layers for increasing the efficiency of CdS/CdTe solar cells. 7th Photovoltaic Science, Applications and Technology Conference. 8 April, 2011, Heriot-Watt University, Edinburgh, United Kingdom.

Signed: .....

Date:.....

Acknowledgements

I would like to thank Prof. Tomas Markvart for guidance and advice with the research conducted, Dr. Lefteris Danos for help with experimental measurements and exchange of ideas and Dr. Liping Fang, Dr. Robert Greef, Dr. Nicholas Alderman and Dr. Nazila Soleimani for useful discussions on the analysis of fluorescent solar collectors. Thank you also to the following Masters students: Ms. Xishu Chu for discussions on fluorescent down-shifting structures, Mr. Christos Pistolas for discussions on angular resolved fluorescence measurements and Mr. Natawatana Lerdsurawitaya for discussions on fabrication of fluorescent solar collectors. Many thanks to the University of Southampton Engineering and Design Manufacturing Centre and Mr. Mark Scully for the fabrication of the fluorescent edge concentrator jig and Mr. Gareth Savage for solar cell mounting/soldering. I would also like to thank Lambda Research Corporation for a gratis copy of TracePro, Dr. Thomas Meyer and Teknova for providing Lumogen F Red 305 based moulded fluorescent solar collectors, the National Renewable Energy Centre and the Centre for Solar Energy Research for solar cells supplied. This work has also benefitted from the Sustainable Power Generation and Supply, Photovoltaics for the 21st Century Initiative and the Engineering and Physical Sciences Research Council.

List of symbols

Greek

α Absorption coefficient

$\alpha_{\mathbf{eff}}$ Effective absorption coefficient at the emission wavelength

$\alpha_{\mathbf{em}}$ Absorption coefficient at the emission wavelength

$\alpha_{\mathbf{ex}}$ Absorption coefficient at the excitation wavelength

β Azimuthal angle of emission of incidence on the solar cell

γ Inclination angle of solar cell with respect to the fluorescent solar collector top surface

$\gamma_{\mathbf{L}}$ Ratio of the local density of states in a photonic crystal to the local density of states in a homogenous medium

$\gamma_{\mathbf{p}}$ Photon

δ_{mn} Kronecker delta function

Δ Difference between Δ_s and Δ_p

$\Delta_{\mathbf{p}}$ Phase angle of the *p* reflection coefficient

$\Delta_{\mathbf{s}}$ Phase angle of the *s* reflection coefficient

Γ Re-absorption probability for different azimuthal angles of emission

Γ' Average angular re-absorption probability for different azimuthal angles of emission

ε Dielectric constant

$\varepsilon_{1,2}$ Dielectric constants of alternating layers in 1D photonic crystal

$\varepsilon_{\mathbf{a}}$ Extinction coefficient

$\varepsilon_{\mathbf{n}}$ Dielectric constant of n^{th} layer

$\eta_{\mathbf{p}}$ Power conversion efficiency

$\boldsymbol{\eta_s}$ Optical quantum efficiency

$\boldsymbol{\eta_{SQ}}$ Shockley-Queisser limit

$\boldsymbol{\eta_u}$ Ultimate efficiency

$\boldsymbol{\theta}$ Zenith angle

$\boldsymbol{\theta_{1,2}}$ Range of zenith angle, for a given frequency of propagation that encloses forbidden modes

$\boldsymbol{\theta_c}$ Critical angle

$\boldsymbol{\kappa}$ Emission probability enhancement factor

$\boldsymbol{\lambda}$ Wavelength

$\boldsymbol{\lambda_{abs}}$ Critical wavelength of photonic band stop filter

$\boldsymbol{\lambda_g}$ Band gap wavelength of solar cell

$\boldsymbol{\Lambda}$ Operator

$\boldsymbol{\mu}$ Chemical potential

$\boldsymbol{\mu_\gamma}$ Chemical potential of photons

$\boldsymbol{\mu_{cell}}$ Chemical potential of solar cell

$\boldsymbol{\mu_e}$ Chemical potential of electrons in excited state

$\boldsymbol{\mu_f}$ Chemical potential of the fluorescent molecules

$\boldsymbol{\mu_h}$ Chemical potential of holes in ground state

$\boldsymbol{\mu_{mpp}}$ Chemical potential of the solar cell at the maximum power point

$\boldsymbol{\mu_n}$ Magnetic permeability of n^{th} layer

$\boldsymbol{\mu_{N_*}}$ Chemical potential of ground state fluorescent molecules

$\boldsymbol{\mu_{N^*}}$ Chemical potential of excited state fluorescent molecules

$\boldsymbol{\mu_{N_{*0}}}$ Lowest energy of the ground state of the fluorescent molecules

$\boldsymbol{\mu_{N_0^*}}$ Lowest energy of the excited state of the fluorescent molecules

$\boldsymbol{\nu_0}$ Frequency with energy equal to the transition energy from the ground to the excited state

$\boldsymbol{\nu_n}$ Angle subtended by the electromagnetic wave with the interface in the n^{th}

ξ Etendue of emission

$\boldsymbol{\xi_{cell}}$ Etendue of the emission from the solar cell

$\boldsymbol{\xi_t}$ Etendue of the trapped photon flux

$\boldsymbol{\xi_{inc}}$ Etendue of the incident photon flux

$\boldsymbol{\xi_{top}}$ Etendue of the escaping photon flux

$\boldsymbol{\rho}$ Average angular collection efficiency of a fluorescent solar collector

$\boldsymbol{\tau_{nr}}$ Non-radiative lifetime of fluorescent molecules

$\boldsymbol{\tau_p}$ Recombination lifetime of holes in the *n*-type

$\boldsymbol{\tau_{rad}}$ Radiative lifetime of fluorescent molecules

$\boldsymbol{\tau_{tot}}$ Total lifetime of fluorescent molecules

$\boldsymbol{\phi}$ Azimuthal angle

$\boldsymbol{\phi_{1,2}}$ Extent of azimuthal angle of emission towards a solar cell in 4Cell setup

$\boldsymbol{\phi_f}$ Quantum yield of fluorescent species

$\boldsymbol{\phi_h}$ Quantum yield of fluorescent species in homogenous medium

$\boldsymbol{\phi_{pc}}$ Quantum yield of fluorescent species in a photonic crystal

$\boldsymbol{\phi_n}$ Phase angle

$\boldsymbol{\chi_e}$ Ratio between the Fresnel *s* and *p* reflection coefficients

$\boldsymbol{\omega}$ Angular frequency

$\boldsymbol{\Omega}$ Relevant solid angle

$\boldsymbol{\Omega_{edge}}$ Solid angle of emission within the edge escape cone

$\boldsymbol{\Omega_{inc}}$ Solid angle of incident light

$\boldsymbol{\Omega_{t}}$ Solid angle of trapped emission

$\boldsymbol{\Omega_{t\&b}}$ Solid angle of emission within the top and bottom escape cones

Latin

$\boldsymbol{a}$ Length of unit cell in a 1D photonic crystal or a 1D integrated photonic fluorescent solar collector

$\bar{\boldsymbol{a}}$ is the reciprocal lattice constant

$\boldsymbol{a_0}$ Amplitude of the right travelling wave in air

$\boldsymbol{a_n}$ Electric field amplitude of right travelling wave in the n^{th} layer, right interface

$\boldsymbol{a'_n}$ Electric field amplitude of right travelling wave in the n^{th} layer, left interface

$\boldsymbol{a_s}$ Amplitude of the right travelling wave in the substrate

$\boldsymbol{A}$ Absorbance

$\boldsymbol{A}$, $\boldsymbol{B}$, $\boldsymbol{C}$ and $\boldsymbol{D}$ Amplitudes of electric field in layered device

$\mathbf{A}$, $\mathbf{B}$, $\mathbf{C}$, $\mathbf{D}$ Matrix elements of translational matrix

$\boldsymbol{A_{cell}}$ Top surface area of the solar cell

$\boldsymbol{A_{FSC}}$ Top surface area of the fluorescent solar collector

$\boldsymbol{A_{rad}}$ Einstein A coefficient

$\boldsymbol{b}$ Thickness of layer with dielectric constant ε_1

$\boldsymbol{b_0}$ Amplitude of the left travelling wave in air

$\boldsymbol{b_n}$ Electric field amplitude of left travelling wave in the n^{th} layer, right interface

$\boldsymbol{b'_n}$ Electric field amplitude of left travelling wave in the n^{th} layer, left interface

$\boldsymbol{b_s}$ Amplitude of the left travelling wave in the substrate

$\boldsymbol{c}$ speed on light

$\boldsymbol{c_a}$ Concentration of absorbing molecules

$\boldsymbol{c_n}$ Fourier coefficient

$\boldsymbol{C}$ Fitting constant

$\overline{\boldsymbol{C}}$ Eigenmode

$\boldsymbol{d}$ Thickness of emitting layer

$\boldsymbol{d_n}$ Thickness of n^{th} layer

$\boldsymbol{d_m}$ Fourier coefficient

$\boldsymbol{D}$ Fitting constant

$\boldsymbol{D_n}$ Diffusion constant of electron in the *p*-type

$\boldsymbol{D_p}$ Diffusion constant of holes in the *n*-type

$\boldsymbol{e}$ Electron

$\boldsymbol{E}$ Electric field

$\boldsymbol{E_0}$ Ground state energy level

$\boldsymbol{E_1}$ Excited state energy level

$\boldsymbol{E_{eh}}$ Energy

$\boldsymbol{E_x}$ Electric field in the *x* direction

$\boldsymbol{E_n}$ Electric field corresponding to a particular mode in the n^{th} band

$\boldsymbol{EQE}$ EQE of the solar cell

$\boldsymbol{EQE_f}$ EQE of the solar cell to the fluorescence incident on it

$\boldsymbol{EQE_{ref}}$ EQE of the reference solar cell

$\boldsymbol{f}$ Fluorescence normalised to represent probability density

f_0 Frequency of maximum normal reflectance

f_1 First generation fluorescence

FF Fill factor

g Shape function of emission

G Generation rates of electrons and holes

h Planck's constant

h_q Hole

I Current output of the solar cell

I_0 Reverse saturation current

I_d Current output of solar cell due to excitation light

I_f Current output of solar cell due to fluorescence

IQE Internal quantum efficiency of a solar cell

I_{sc} Short circuit current output of solar cell

J Current density output of solar cell

J_{cell} Short circuit current density output of solar cell

J_d Photo-current density in the depletion region

J_n Electron current density in the *p*-type

J_p Hole current density in the *n*-type

J_{ref} Short circuit current density output of reference solar cell

J_{tot} Total photocurrent

k Boltzmann's constant

k_{nz} Magnitude of the wave vector in the *z* direction at the n^{th} layer

k_r Wave number corresponding to position r'

$\boldsymbol{k_x}$ Wave number in the *x* direction

$\boldsymbol{k_y}$ Wave number in the *y* direction

$\boldsymbol{K_z}$ Bloch wave number

$\boldsymbol{k_{1,2y}}$ Range of wave numbers in the *y* direction, for a given frequency of propagation, that encloses forbidden modes

$\boldsymbol{k_{1,2z}}$ Wave vector in the *z* direction of alternate layers photonic crystal

$\boldsymbol{k_{1,2,3z}}$ Wave vector in the *z* direction within medium 1,2 and 3

$\boldsymbol{l}$ Path length

$\boldsymbol{L}$ Length of fluorescent solar collector

$\boldsymbol{L_n}$ Diffusion length of electrons in the *p*-type

$\boldsymbol{L_p}$ Diffusion length of holes in the *n*-type

$\mathbf{M}$ Matrix connecting the amplitude of the electromagnetic wave in two different layers

$\mathbf{M_{11}}$, $\mathbf{M_{12}}$, $\mathbf{M_{21}}$ and $\mathbf{M_{22}}$ Matrix elements of matrix M

$\boldsymbol{n}$ Refractive index

$\boldsymbol{\bar{n}}$ Average refractive index of materials in photonic crystals (weighted by thicknesses)

$\boldsymbol{n_{1,2}}$ Refractive index of the two materials used to form a photonic crystal

$\boldsymbol{N}$ Number of bi-layers in photonic crystal

$\boldsymbol{N_*}$ Population of ground state fluorescent molecules

$\boldsymbol{N^*}$ Population of excited state fluorescent molecules

$\boldsymbol{N_\gamma}$ Number of photons

$\boldsymbol{N_a}$ Photon flux absorbed

$\boldsymbol{N_{BB}}$ Black body radiation

$\boldsymbol{N_{BE}}$ Bose-Einstein distribution

$\boldsymbol{N_{bottom}}$ Photon flux from the bottom surface of a fluorescent solar collector

$\boldsymbol{N_{cell}}$ Photon flux emitted by the solar cell

$\boldsymbol{N_D}$ Density of states

$\boldsymbol{N_e}$ Number of electrons

$\boldsymbol{N_{es}}$ Escape cone photon flux

$\boldsymbol{N_{es}^{+}}$ Escape cone photon flux per unit area in the forward direction

$\boldsymbol{N_{es}^{-}}$ Escape cone photon flux per unit area in the backward direction

$\boldsymbol{N_{edge}}$ Photon flux emitted reaching the edge

$\boldsymbol{N_{ex}}$ Photon flux extracted by solar cell

$\boldsymbol{N_{GP}}$ Generalised Planck's law of emission

$\boldsymbol{N_h}$ Number of holes

$\boldsymbol{N_{inc}}$ Excitation photon flux incident on the device

$\boldsymbol{N_L}$ Local density of states

$\boldsymbol{N_{mpp}}$ Photon flux extracted by the solar cell at its maximum power point

$\boldsymbol{N_{nr}}$ Flux of non-radiative relaxation

$\boldsymbol{N_R}$ Photon flux reflected

$\boldsymbol{N_t}$ Trapped photon flux

$\boldsymbol{N_t^{+}}$ Trapped photon flux per unit area in the forward direction

$\boldsymbol{N_t^{-}}$ Trapped photon flux per unit area in the backward direction

$\boldsymbol{N_{top}}$ Photon flux from the top surface of the fluorescent solar collector

$\boldsymbol{N_T}$ Photon flux transmitted

$\boldsymbol{OQE}$ Optical quantum efficiency

$\boldsymbol{p}$ Hole concentration per unit volume

$\boldsymbol{p_0}$ Hole concentration per unit volume at thermal equilibrium in the *n*-type

$\boldsymbol{P}$ Fraction of photons emitted within the top and bottom escape cones

$\boldsymbol{p_a}$ $p_a dV$ is the probability that an absorbed photon is absorbed in a volume element dV

$\boldsymbol{P_{inc}}$ Power of the incident light

$\boldsymbol{P_{mpp}}$ Solar cell generated power at the maximum power point

$\boldsymbol{p_r}$ $p_r d\Omega$ is, assuming unity quantum yield, the probability that an absorbed excitation photon is re-emitted within a solid angle element $d\Omega$ and is not re-absorbed

$\boldsymbol{P_{rad,pc}}$ Probability of radiative relaxation in a photonic crystal

$\boldsymbol{q}$ charge of an electron

$\boldsymbol{Q_a}$ Absorption efficiency

$\boldsymbol{Q_c}$ Collection efficiency

$\boldsymbol{Q_{c1}}$ Collection efficiency of first generation fluorescence

$\boldsymbol{Q_{cn}}$ Fraction of absorbed excitation photons that results in a fluorescent photon reaching a solar cell after the n^{th} absorption event

$\boldsymbol{Q_{e1}}$ Escape efficiency of first generation fluorescence

$\boldsymbol{r}$ Trapped photon flux re-absorption probability

$\boldsymbol{r'}$ Position in the *xyz* coordinates

$\boldsymbol{r_{1Cell}}$ Trapped re-absorption probability in 1Cell setup

$\boldsymbol{r_{4Cell}}$ Trapped re-absorption probability in 4Cell setup

$\boldsymbol{r_\Omega}$ the re-absorption probability of photons emitted into a solid angle Ω

$\boldsymbol{r_b}$ Re-absorption probability of the bottom escape cone photon flux

$\boldsymbol{r_{edge}}$ Re-absorption probability of edge escape cone photon flux

$\boldsymbol{r_{mn}}$ Fresnel reflection coefficient between medium m and n

r_s Reflection coefficient of *s* polarisation

r_p Reflection coefficient of *p* polarisation

$r_{t\&b}$ Average top and bottom escape cone reabsorption probability

R Re-absorption probability of trapped photon flux

$R_{t\&b}$ Average re-absorption probability of the escape cone photon flux

R_{top} Reflectance from the top surface of device

S_n Surface recombination velocity of electron in the *p*-type

S_p Surface recombination velocity of holes in the *n*-type

t Thickness

t' Time

t_a Thickness of active fluorescent dye layer

t_{mn} Fresnel transmission coefficient between medium m and n

$\tan\psi$ Ratio of amplitudes of the *s* and *p* reflection coefficients

T Transmittance

T_g Temperature

T_{cell} Temperature of solar cell

T_{FSC} Temperature of fluorescent solar collector

T_{inc} Temperature of emitting source

u Periodic function from Bloch's theorem

U Recombination rate of electrons and holes

V Volume

V_{oc} Open circuit voltage of the solar cell

V_q Voltage

z_d Thickness of the depletion region

z_f Distance between emitting line and left interface of emitting layer

z_n Thickness of the p-type

z_p Depletion region edge of the n-type

List of abbreviations

1Cell setup A fluorescent edge concentrator with one edge mounted solar cell and 3 edge mounted mirrors

1.BZ 1st Brillouin zone

4Cell setup A fluorescent edge concentrator with four edge mounted solar cells

AM1.5 Air mass 1.5

AM1.5G Air mass 1.5 global

cSi Crystalline silicon

CdTe Cadmium telluride

CdS Cadmium selenide

CIGS Copper indium gallium di-selenide

C-FDS Fluorescent down-shifting concentrator

EQE External quantum efficiency of a solar cell

FDS Fluorescent down-shifting structure

FSC Fluorescent solar collector

GaAs Gallium arsenide

GaInP Gallium indium phosphide

IP-FSC Integrated photonic fluorescence collector

IQE Internal quantum efficiency of a solar cell

LB Langmuir Blodgett

LSC Fluorescent edge concentrator

Mold-fluorescent solar collector Fluorescent solar collector fabricated by moulding

***n*-type** Semiconductor with excess electrons

O Lumogen F series Orange240 dye

OQE Optical quantum efficiency

p Transverse magnetic electromagnetic wave

***p*-type** Semiconductor with excess holes due to doping

PLSC 1D integrated photonic fluorescent solar collector

PMMA Poly(methyl methacrylate)

Pt(TPBP) Tetraphenyltetrabenzoporphyrin platinum

R Lumogen F series Red305 dye

s Transverse electric electromagnetic wave

SiO_2 Silicon dioxide

Spin-fluorescent solar collector Fluorescent solar collector fabricated by spin coating

TiO_2 Titanium dioxide

TMM Transfer matrix method

UV Ultra-violet

V Lumogen F series Violet570 dye

Y Lumogen F series Yellow083 dye

1. Introduction

1.1. Motivation

Currently, close to 81% of the primary energy consumed globally is from fossil fuels (IEA, 2011). Since fossil fuels are naturally replenished much slower than current consumption rates they are a non-sustainable source of energy. The depletion of fossil fuels indicates that a shift towards other more sustainable sources of energy is inevitable in the long term. There are however a number of other reasons to limit the use of fossil fuels. Due to the uneven distribution of these resources across the world and geopolitical tensions, it would be in the interest of a number of nations to attain energy independence. Furthermore, the burning of fossil fuels result in the emission of pollutants harmful to health and gases deemed to be responsible for increasing temperatures and widespread climate change. The latter is especially believed to pose a major threat to human populations and ecosystems worldwide.

A number of negative consequences of increasing global temperature have been predicted including and not limited to mass extinction of wildlife, rising sea levels, increasing frequency of extreme weather, reduction in freshwater resources and mass migrations (IPCC, 2007).

Alternative energy sources include nuclear, hydropower, wind, solar, tidal, wave, geothermal and biomass. However, the technically extractable power on land or near shore of most of these energy sources is less than the power consumed by mankind (Tsao *et al.*, 2006). The exception is solar energy which is in fact the source of the energy contained in fossil fuels and, wholly or partly, of nearly all the other energy sources mentioned except geothermal, tidal and nuclear.

The amount of solar energy incident on the Earth in one and a half hours is close to the total primary energy consumed by humans in a year. This means that simply utilising 10% of the energy falling on 0.17% of the surface area of the Earth is enough to meet our energy requirements. Utilisation of solar energy also ensures energy independence and security of supply.

Solar energy can be used in the production of electricity, fuels or thermal energy. The main barrier to the wide spread utilisation of solar energy is the higher cost of energy extracted from solar energy as compared to conventional sources of energy such as coal.

A number of different strategies have been employed to reduce the cost of solar energy extraction including research into improving efficiencies, reducing the cost of systems and concentration of solar energy so that smaller energy conversion devices can be used (Goetzberger and Wittwer, 1981).

This project focuses on solar electricity generating devices (i.e. solar cells) attached to devices known as fluorescent solar collectors. These fluorescent solar collectors, which will also be referred to as photon management structures or simply collectors, are generally plates doped with molecules that absorb solar photons and re-emit light in a process known as fluorescence. These devices have the potential to reduce solar electricity costs through light concentration and can also increase energy conversion efficiencies by shifting light to wavelengths converted by the solar cells at a higher efficiency. A number of different types of fluorescent solar collectors have been investigated in this project. These include:

- Photon management structures that focus solely on light concentration (Figure 1 (a)). These frequently have solar cells optically coupled to their edges and will be referred to as fluorescent edge concentrators in this project.
- Fluorescent solar collectors used primarily for increasing solar cell efficiencies by wavelength shifting (Figure 1 (b-i)). These collectors are generally coupled to bottom mounted solar cells and will be referred to as fluorescent down-shifting structures.
- Photon management structures coupled to bottom mounted solar cells that exploits both the wavelength shifting and light concentration properties of fluorescent solar collectors (Figure 1 (b-ii)). These will be referred to as concentrating fluorescent down-shifting structures.
- Collectors consisting of fluorescent molecules embedded within 1D photonic crystals. These will be referred to as 1D integrated photonic fluorescent solar collectors (Figure 1 (c)).

Fluorescent edge concentrators are devices in which light is collected from a large area and concentrated using fluorescence. These devices operate by trapping light. Light is absorbed by the fluorescent material and is re-emitted isotropically (Garwin, 1960). Emitted photons incident on the top or bottom surface of the fluorescent edge

concentrator at an angle greater than a critical angle will be trapped through total internal reflection and concentrated onto the edge.

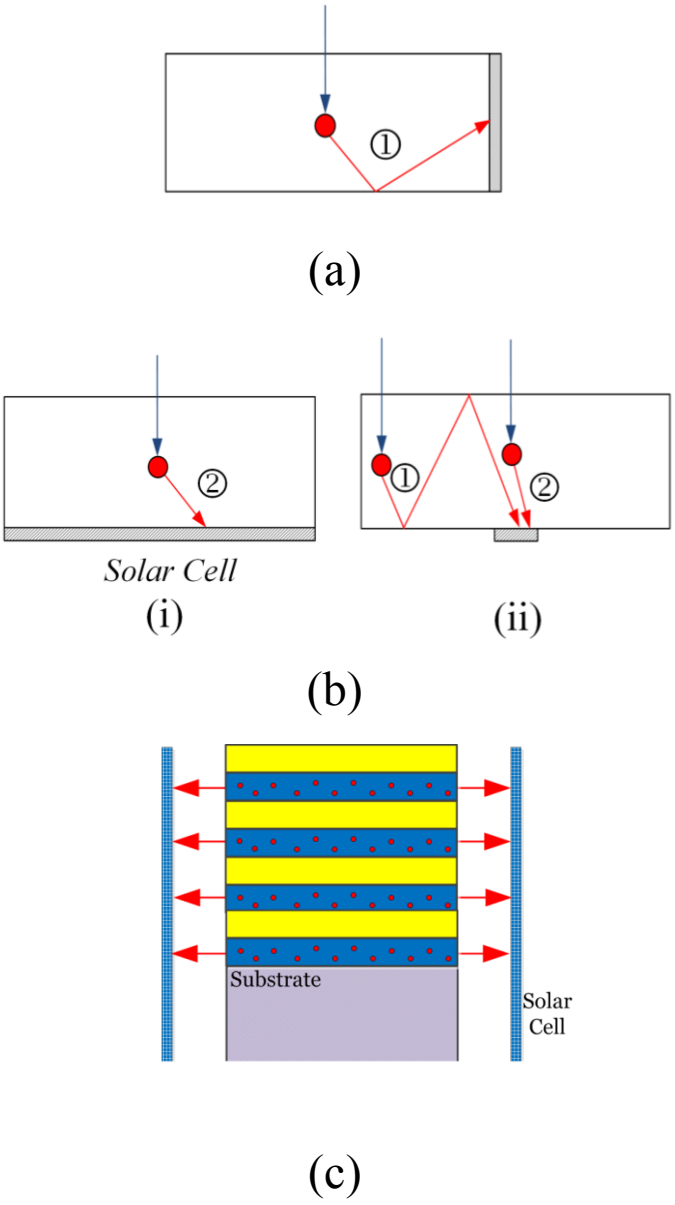

Figure 1 Comparisons of different collector geometries (red circles represent fluorescent molecules) (a) an edge mounted collector i.e. a fluorescent edge concentrator, (b) bottom mounted collectors and (c) a 1D integrated photonic fluorescent solar collector. Bottom mounted collectors are divided further into (i) a fluorescent down-shifting structure (no concentration, only wavelength shifting) and (ii) a concentrating fluorescent down-shifting structure. The different rays shown are 1) trapped fluorescence reaching the solar cell and 2) fluorescence directly reaching the solar cell.

The use of fluorescent edge concentrators for solar electricity generation has a number of advantages. These devices can be made using low cost plastic host material and reduce the quantity of solar cells required to generate a certain power output. They can concentrate both direct and diffuse light and therefore, there is no need to track the sun. Fluorescent edge concentrators also have good heat dissipation due to a large surface area. This helps keep the solar cell cooler, thereby enhancing their performance.

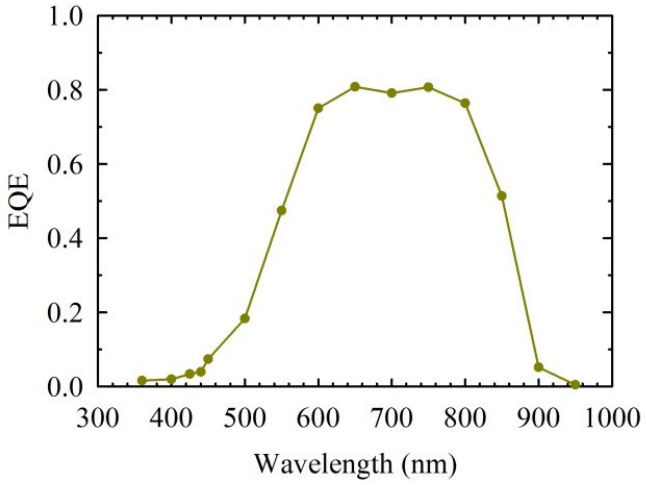

(a)

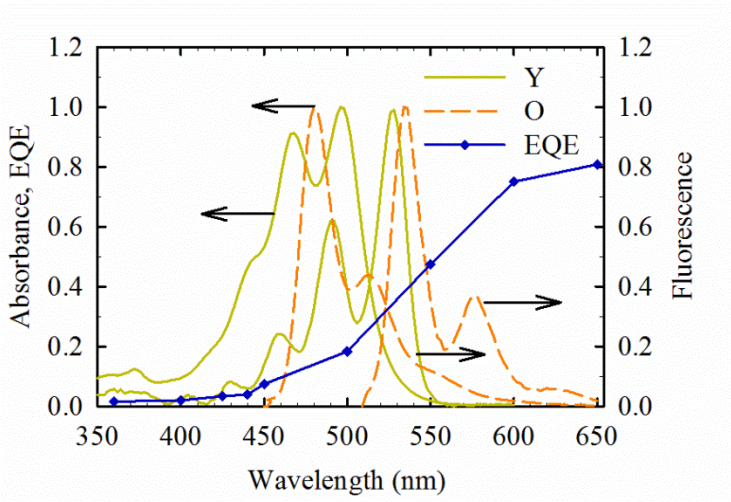

(b)

Figure 2 (a) External quantum efficiency of a CdTe solar cell with a poor short wavelength response and (b) fluorescent dyes that absorb at wavelengths with a poor solar cell response.

A number of solar cells display a poor spectral response to short wavelength light. One reason for a poor short wavelength performance is that a large fraction of short

wavelength light is absorbed in the top micron of the solar cell, an area that has generally high recombination (see Chapter 3 for details about recombination in solar cells) of electrons and holes (Klampaftis et al., 2009). In certain solar cells such as those based on cadmium telluride (CdTe), the buffer/window layer consists of cadmium sulphide that absorbs short wavelength light. This results in a poor response at these wavelengths as shown in **Figure 2** (a) (EQE refers to external quantum efficiency, i.e. the fraction of photons incident on the solar cell at a particular wavelength that results in the output of current from the solar cell).

One method of improving the short wavelength response of solar cells is through the use of a fluorescent down-shifting structure that shifts incident short wavelength light to longer wavelengths where the response of the solar cell is superior. **Figure 2** (b) shows the absorption and emission spectra of two dyes i.e. labelled as Yellow dye and Orange dye that absorb light at short wavelengths and emits at longer wavelengths converted by the solar cell with a higher efficiency. The overlap of the emission by the Yellow dye and the absorption by the Orange dye also indicates the possibility of energy transfer between these dyes in the case of a multi-dye collector. Energy transfer could serve to shift short wavelength photons absorbed by the Yellow dye to the even longer wavelengths associated with the emission of the Orange dye, thereby enhancing the effect of wavelengths shifting.

The concept of a fluorescent down-shifting structure and bottom mounted fluorescent edge concentrators can be taken one step further with concentrating fluorescent down-shifting structures that simultaneously improve the short wavelength response of solar cells and also concentrate light.

A concentrating fluorescent down-shifting structure has a number of key advantages. A concentrating fluorescent down-shifting structure can be used to collect light from regions where, for example, shading due to front contacts or gaps between modules prevents capture of solar energy. Additionally, the poor short wavelength response found in many solar cells is simultaneously improved. This offers the possibility of achieving higher efficiencies on existing solar cell devices.

The application of photonic structures to collectors have also been proposed to improve the efficiency of these devices (see for example, Richards *et al.*, 2004). Initial work however, only looked into the use of photonic band stop filters on top of conventional fluorescent solar collectors as a method to trap escaping light (Glaeser and

Rau, 2006)(Goldschmidt *et al.*, 2008). The integrated photonic fluorescent solar collector (Goldschmidt *et al.*, 2010) is a more advanced concept that is now also being considered as a method of improving the efficiency of collectors even further. These devices combine the concepts of photonic crystals and fluorescent solar collectors into an integrated device i.e. a photonic crystal doped with fluorescent molecules. The presence of the photonic crystal is expected to fundamentally modify the emission characteristics of fluorescent molecules in such a way as to allow the design of devices with higher efficiencies. 1D periodic stacks are widely referred to as 1D photonic crystals (Joannopoulos *et al.*, 2008) and this terminology will be used throughout this thesis.

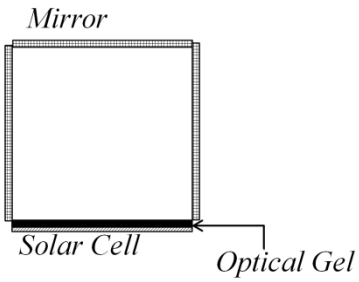

(a)

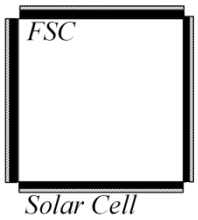

(b)

Figure 3 Top view of (a) 1Cell and (b) 4Cell setups.

In this thesis, theoretical models describing both conventional and photonic based photon management structures will be outlined and shown to be verified both experimentally and through the use of computer simulations. The theoretical modelling of fluorescent edge concentrators is obtained by looking at the re-absorption (self absorption) probability of the fluorescence emission, an early example of this is given in (Weber and Lambe, 1976). In this paper the re-absorption of a system equivalent to a fluorescent edge concentrator with edges mounted with 1 solar cell and 3 mirrors (1Cell setup) was considered (top view of the 1Cell setup is shown in Figure 3(a), FSC

indicates fluorescent solar collector). Optical gel is used to couple the solar cell to the FSC so that all the light reaching the FSC edge reaches the solar cell.

The highest efficiency systems reported in the literature, however, are all seen to consist of fluorescent edge concentrators coupled to four edge solar cells (i.e. 4Cell setup. Top view of the 4Cell setup is shown in Figure 3(b)) (Sloof *et al*., 2008)(Currie *et al.*, 2008)(Goldschmidt *et al.*, 2009). Therefore, it is important to adapt re-absorption models to such systems. This has been investigated in this project. Furthermore, in depth knowledge of losses found within fluorescent edge concentrators coupled to solar cells/mirrors need to be studied and quantified. For this, angular resolved measurements of emission emitted by fluorescent edge concentrators is analysed. Losses have also been quantified for not only different setups i.e. 1Cell and 4Cell setups but for also two different fabrication methods. Performance of edge concentrators fabricated by moulding plastic plates doped with fluorescent molecules and spin coating fluorescent thin films on glass substrates have been compared. These fabrication methods will be denoted by Mold and Spin-fluorescent solar collectors (see **Figure 4**).

Fluorescent edge concentrators tested in the laboratory are seen to have estimated power conversion efficiencies close to 4% and even higher potential efficiencies according to results of optimisation studies obtained from the models developed.

The use of fluorescent solar collectors as hybrid devices, i.e. concentrating fluorescent down-shifting structures, that simultaneously concentrates light and improves the efficiency of CdTe solar cells is proposed and was investigated through modelling and experimental work. It will also be shown that the theory of operation of these devices is useful in predicting the contribution of the collector on the current output of the attached solar cell. The use of down-shifting structures containing multiple dyes with energy transfer has also been investigated in order to enhance the effect of wavelength shifting.

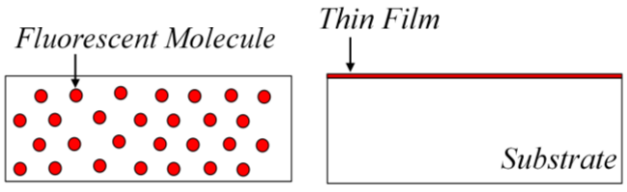

(a) (b)

Figure 4 Side view of (a) Mold and (b) Spin-fluorescent solar collectors.

The first 1D integrated photonic fluorescent solar collector has also been fabricated and characterised. The results of this investigation show how these devices have the potential to reduce fundamental loss mechanisms found in conventional photon management structures. The results of the experimental work will be explained using the theory of operation of these devices.

Thermodynamic treatments have also been used to derive the maximum theoretical efficiencies of solar cells and photonic fluorescent solar collectors. These treatments will be shown to lead to new insights into the operation of these devices such as the effect of light concentration on the current voltage relationship of a solar cell and the differences between the light emitted by a solar cell attached to a collector and the light incident on it.

1.2. Aims and objectives

This project aims to carry out an in-depth investigation into the operation of fluorescent solar collectors and its application to solar cells. Theoretical and experimental analyses of these devices as well as loss mechanisms will be presented. The specific objectives are as follows:

- Conventional fluorescent solar collectors:
  - Extend the Weber and Lambe re-absorption model to model the re-absorption probability of the different streams of fluorescence emitted within conventional (i.e. not photonic based) photon management structures. Verify these models experimentally where possible or through computer simulations.
  - Use these re-absorption models to predict the efficiencies of systems consisting of edge concentrators coupled to solar cells. Experimentally verify the accuracy of these methods and use these models as a tool to optimise the power conversion efficiency.
  - Identify the losses in these fluorescent edge concentrators by looking at the angle resolved emission exiting the collector edge. Also quantify losses in edge concentrator systems by comparing ideal models to experimental measurements.

- Conduct an in-depth theoretical and experimental study of photon management structures for increasing the power output of CdTe solar cells by exploiting both its light concentration and wavelength shifting properties. Investigate the use of multiple dyes with energy transfer to further enhance the effect of wavelength shifting. Estimate the contribution of the fluorescent solar collector on the current output of these systems based on the theory of its operation and also characterise the loss mechanisms present.

o 1D integrated photonic fluorescent solar collector:
  - Fabricate and characterise novel photonic based collectors and determine the potential of these devices for solar concentrating applications from experimental measurements and modelling of the light transport.
  - Obtain ideal efficiencies of photonic based photon management structures by extending existing treatments.

1.3. Outline

An outline of the core chapters that make up this thesis is given here. The report is split up into two main sections i.e.:

- Part I: Literature review.
- Part II: Results and discussions.

Part I: Literature review

- **Chapter 2 Fundamentals on the interaction of light with matter:** gives an overview of absorption and emission of light by matter. Emission from non-thermal sources known as fluorescence is discussed and it is shown that Planck's law of blackbody radiation can be refined to describe emissions from fluorescent materials. The basics of photonic crystals and light propagation within layered structures is described through the use of two different methods, i.e. the transfer matrix method and the plane wave expansion method.
- **Chapter 3 Basics of solar cell operation and modelling:** reviews the operation and classifications of solar cells. Particular emphasis is placed on crystalline

silicon solar cells based on the so called *p-n* junction, the modelling of these devices have been detailed using semiconductor statistics. The performance of a typical device has been calculated from these models. The maximum theoretical efficiency of single band gap solar cells i.e. the Shockley-Queisser limit is also derived and used to highlight fundamental loss mechanisms that limit solar cell performance.

- **Chapter 4 Review of fluorescent solar collectors:** details the basic operation, fabrication and efficiencies of collectors as reported in the literature. Photon management structures are divided into two categories i.e. conventional and photonic fluorescent solar collectors. For conventional collectors both wavelength shifting and light concentrating applications are discussed while for photonic fluorescent solar collectors integrated devices that embeds fluorescent molecules in photonic crystals is described. A brief outline of the history and progress of the research into these different photon management structures have been outlined in this chapter.
- **Chapter 5 Modelling fluorescent solar collectors:** outlines different techniques for modelling collectors as reported in the literature. It will be shown that there are two main methods of modelling conventional fluorescent solar collectors. The first involves modelling the emission within collectors as emission from non-thermal sources with the fluorescent molecules under thermal equilibrium. The second method involves calculating the re-absorption probability of emitted fluorescence and in effect tracking these absorption/emission cycles to calculate the amount of light reaching a coupled solar cell. For photonic based photon management structures, modelling based on the local density of states of photonic crystals and electromagnetic simulations is described.

Part II: Results and discussions

- **Chapter 6 Theory:** in this chapter, a general treatment to unify the modelling of different types of fluorescent solar collectors is proposed. Models specific to conventional collectors that calculate the re-absorption probabilities of different streams of fluorescence emitted are also derived. The approach used is related to

a re-absorption model proposed by Weber and Lambe. It is shown that these re-absorption probabilities along with other properties of the fluorescent solar collector and solar cells attached can be used to calculate the efficiencies of these systems. The derivation of the maximum theoretical efficiencies of photonic collectors is also shown and extended from previous work to calculate the limits of the different types of efficiencies used to characterise collectors. Expressions that can be used to calculate the electric field intensity outside 1D photonic crystals doped with fluorescent molecules is also derived.

- **Chapter 7 Experimental details:** describes the different equipment used to characterise fluorescent solar collectors. The fabrication and composition of the collectors studied as well as properties of the solar cells used are also detailed. Measurements of absorption and fluorescence using spectrometers and current output measurements from solar cells attached to fluorescent solar collectors in solar simulators have also been described. The methodology used in computer simulations using the ray tracing software TracePro by Lambda Research Corporation has also been outlined.
- **Chapter 8 Results and discussion:** shows the results of experimental and computer simulations and comparison of this with the theoretical models developed. Losses in edge concentrators are studied by looking at the angular dependence of the emission within these devices. In particular, two configurations for solar concentrating application, i.e. the 1Cell and 4Cell setups, are analysed and compared. Comparisons with ideal theoretical models are used to quantify non-ideal losses in such systems. Another application of the theoretical models developed is illustrated through the optimisation of the power conversion efficiency of edge concentrators. The effect of using conventional photon management structures as hybrid devices that simultaneously improves the efficiencies of CdTe solar cells and concentrates light are also shown and discussed. The theory of the operation of these devices is also used to estimate the contribution of fluorescent solar collectors to the current output of these systems. Measurements of the world's first photonic collector consisting of fluorescent molecules doped in a one-dimensional photonic crystal are also presented and analysed by comparisons with the theory of operation of these devices.

1.4. Key achievements

The key achievements of this thesis are listed below:

- Fluorescent edge concentrators:
  - Adaptation of the Weber and Lambe re-absorption models to different photon flux streams within fluorescent solar collectors and especially in the modelling of the most promising geometry in fluorescent edge concentrators, i.e. the 4Cell setup.
  - Application of the models developed in the quantification of losses in the 1Cell and 4Cell setups of fluorescent edge concentrators. Also quantification of losses due to fabrication method. This allows the design of improved efficiency systems.
  - Application of the models developed in the optimisation of power conversion efficiencies of fluorescent edge concentrators in the 4Cell setup.
  - In-depth analysis of the photon transport in fluorescent edge concentrators by angular resolved studies of the 1Cell and 4Cell setups.

- Concentrating fluorescent down-shifting structures:
  - Application of concentrating fluorescent down-shifting structures to CdTe solar cells to show the potential of such devices for increasing solar cell current output.
  - The use of multiple dyes with energy transfer to enhance the effect of wavelength shifting.
  - Development of a general expression describing different types of photon management structures and using this to model the current output of the CdTe solar cell coupled to concentrating fluorescent down-shifting structures.

- 1D integrated photonic fluorescent solar collector:
  - Fabrication and characterisation of the first 1D integrated photonic fluorescent solar collector.

- Analysis of the photon transport in these devices to explain the distinct emission measured from the fabricated 1D integrated photonic collector.

References

Currie, M.J., Mapel, J.K., Heidel, T.D., Goffri, S. and Baldo M.A., 2008. *High efficiency organic solar concentrators for photovoltaics*. Science. 321: 226-228. DOI: 10.1126/science.1158342.

Garwin, R.L., 1960. *The collection of light from scintillation counters*. Review of Scientific Instruments. 31: 1010-1011. DOI: 10.1063/1.1717105.

Glaeser, G.C. and Rau, U., 2006. *Collection properties of photovoltaic fluorescent systems - simulations and experiments*. IEEE 4th World Conference on Photovoltaic Energy Conversion. May 7-12, Waikoloa, Hawaii, USA. 1: 205-208. DOI: 10.1109/WCPEC.2006.279418.

Goetzberger, A. and Wittwer, V., 1981. *Fluorescent planar collector-concentrators: A review*. Solar Cells. 4: 3-23. DOI: 10.1016/0379-6787(81)90033-8.

Goldschmidt, J.C., Peters, M., Prönneke, L., Steidl, L., Zentel, R., Bläsi, B., Gombert, A., Glunz, S., Willeke, G. and Raa, U., 2008. *Theoretical and experimental analysis of photonic structures for fluorescent concentrators with increased efficiencies*. Physica Status Solidi A. 205: 2811-2821. DOI: 10.1002/pssa.200880456.

Goldschmidt, J. C., Peters, M., Bösch, A., Helmers, H., Dimroth, F., Glunz, S. W. and Willeke, G., 2009. *Increasing the efficiency of fluorescent concentrator systems*. Solar Energy Materials and Solar Cells. 93: 176–182. DOI: 10.1016/j.solmat.2008.09.048.

Goldschmidt, J.C., Peters, M., Gutmann, J., Steidl, L., Zentel, R., Bläsi, B. and Hermle, M., 2010. *Increasing fluorescent concentrator light collection efficiency by restricting the angular emission characteristic of the incorporated luminescent material: the*

'nano-fluko' concept. Proceedings of SPIE Photonics for Solar Energy Systems III. April 13-15, Brussels, Belgium. 7725: 0S 1-11. DOI: 10.1117/12.854278.

IEA, 2011. *World Energy Outlook. Organisation for Economic Co-orporation and Development*. International Energy Agency: Paris, France.

IPCC, 2007. *Climate Change: 2007 Synthesis Report*. Intergovernmental Panel on Climate Change: Geneva, Switzerland.

Joannopoulos, J.D., Johnson, S.G., Winn, J.N. and Meade, R.D., 2008. *Photonic crystals: molding the flow of light*. Princeton University Press.

Klampaftis, E., Ross, D., McIntosh, K.R. and Richards, B.S., 2009. *Enhancing the performance of solar cells via luminescent down-shifting of the incident spectrum: A review*. Solar Energy Materials and Solar Cells. 93: 1182-1194. DOI: 10.1016/j.solmat.2009.02.020.

Lewis, N.S. and Nocera, D.G., 2006. *Powering the planet: Chemical challenges in solar energy utilization*. Proceedings of the National Academy of Sciences of the United States of America. 103: 15729-15735. DOI: 10.1073/pnas.0603395103.

Richards, B.S., Shalav, A. and Corkish, R.P., 2004. *A low escape-cone-loss luminescent solar concentrator.* Proceedings of the 19th European Photovoltaics Solar Energy Conference. June 7 -11, Paris, France. 113-116.

Sloof, L.H., Bende, E.E., Burgers, A.R., Budel, T., Pravettoni, M., Kenny, R.P., Dunlop, E.D. and Büchtemann, A., 2008. *A luminescent solar concentrator with 7.1% efficiency*. Physica Status Solidi - Rapid Research Letters. 2: 257-259. DOI: 10.1002/pssr.200802186.

Tsao, J., Lewis, N.S., and Crabtree, G., 2006. *Solar FAQs*. Sandia National Laboratory Report.

Weber, W. H. and Lambe, J., 1976. *Luminescent greenhouse collector for solar radiation*. Applied Optics. 15: 2299-2300. DOI: 10.1364/AO.15.002299.

PART I: LITERATURE REVIEW

2. Fundamentals on the interaction of light with matter

2.1. Introduction

This chapter outlines some fundamental topics relating to absorption and emission of light by matter. Topics discussed include the Beer-Lambert law of absorption, fluorescence, the generalised Planck's law of emission and light propagation in photonic crystals. These topics will serve as a foundation for explaining modelling of solar cells and fluorescent solar collectors found in the literature i.e. Chapter 3 and Chapter 5 respectively as well as modelling developed in this project i.e. Chapter 6.

2.2. Beer-Lambert law

The Beer-Lambert law relates the transmission of light by a medium to its thickness, t, and a constant known as the absorption coefficient, α. An early description of this law was described by Bouguer in 1729 (Bouguer, 1729) (Perrin, 1948) who studied the diminution of light passing through stacks of transparent glass plates. It was initially expected that if the number of glass plates in the stack is doubled the number of rays absorbed would also be double. The experimental results indicated, however, that it is in fact the absorbed fraction of rays incident on each pate which remains constant and not the number of rays absorbed. Bouguer realised that there existed a logarithmic relationship between the fraction of incident rays transmitted by the medium and its thickness. It was however Lambert in 1760 (Lambert, 1760) (Perrin, 1948) who wrote this relationship explicitly in the form used today. The expression given by Lambert can be written as:

$$\frac{N_{\mathrm{inc}}}{N_{\mathrm{inc}} - N_{\mathrm{a}}} = \exp(-\alpha t) \tag{1}$$

where N_{inc} is the incident photon flux (i.e. number of photons incident per unit time) and N_{a} is the photon flux absorbed by the medium.

Beer extended on this work to show that increasing the concentration of absorbing molecules increases the absorption coefficient of the medium (Beer, 1852) (Perrin, 1948). This is known as Beer's law and is given by:

$$A = \varepsilon_{\mathrm{a}} c_{\mathrm{a}} t \tag{2}$$

where A is the absorbance of the medium, ε_{a} is the extinction coefficient and c_{a} is the concentration of the absorbing molecules. The absorbance is related to the absorption coefficient by:

$$A = \frac{\alpha t}{\ln 10} \tag{3}$$

2.3. Fluorescence

Fluorescence is a type of luminescence, i.e. emission from a non-thermal source. An early observation of fluorescence was that from an infusion of Mexican wood (later called lignum nephriticum) used for medicinal purposes and reported during the 16$^{\mathrm{th}}$ century by Nicolás Monardes (Acuña *et al*. 2009). Reports by Bernardino de Sahagún also indicated that the Aztecs were already familiar with the fluorescent properties of the infusion (Acuña *et al*. 2009).

Milestones in the understanding of fluorescence include experiments by Robert Boyle in the mid 17$^{\mathrm{th}}$ century that determined that the fluorescence in lignum nephriticum was due to "essential salts" in the wood (Boyle, 1725). In 1852 a paper by George Gabriel Stokes reports that the wavelength of fluorescence emission is generally different from that of incident excitation light (Stokes, 1852)(Lakowicz, 2010). The difference between the absorption and emission maximum of fluorescent materials is now known as the Stokes shift.

In the 20$^{\mathrm{th}}$ century, the use of energy level diagrams of molecules to describe absorption and emission was introduced (Perrin, 1920) (Berberan-Santos, 2001). The

Born-Oppenheimer approximation (Born and Oppenheimer, 1927)(Atkins and de Paula, 2010) is used to calculate the energy and wave function of a molecule from the solution of the Schrödinger equation. This approximation assumes that, due to the larger mass of the nuclei, the velocity of electrons is much larger and therefore the nucleus can be assumed to be stationary. The equation is solved by assuming the nuclei are in a particular configuration (i.e. fixed intermolecular distances and angles) (Atkins and de Paula, 2010).

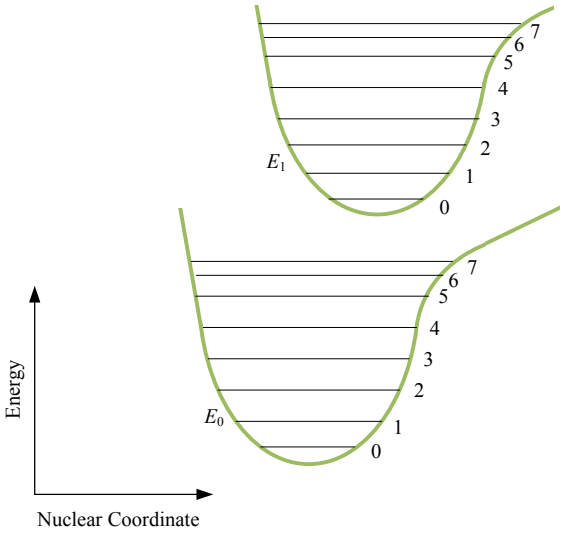

(a)

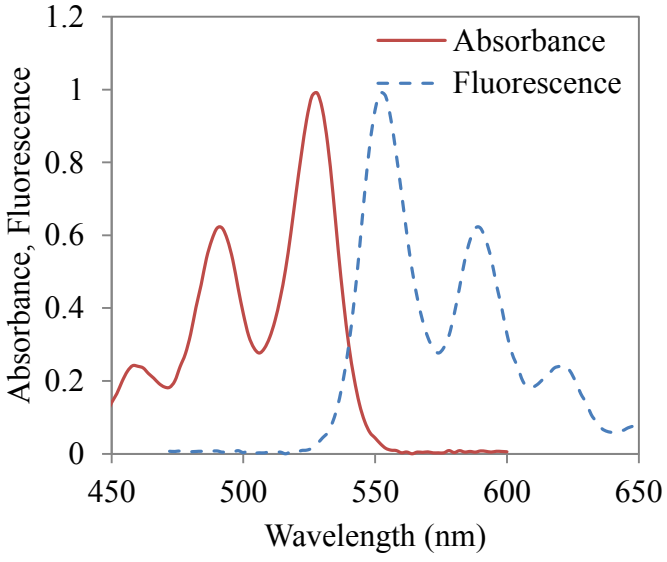

(b)

Figure 5 (a) Energy levels of a fluorescent molecule. (b) An example of the mirror image between the absorbance and fluorescence likely to be seen in fluorescent dyes.

Figure 5 (a) shows a typical schematic energy level diagram (as a function of a hypothetical nuclear coordinate) that can be obtained by solving the Schrödinger equation using the Born-Oppenheimer approximation. Here, E_0 and E_1 are the ground and excited states respectively and the numbers indicate the different vibrational energy levels within these states. It is clear from this figure that the lowest vibrational levels of the ground and excited states are not aligned in the nuclear coordinates. The nuclear coordinates represent a spatial distance. In the case of a diatomic molecule, for example, the nuclear coordinate axis refers to the inter-nuclear distance (Sauer *et al.*, 2011).

The probability of transition between the ground and excited states is related to the wave function overlap of the relevant vibrational levels. Polyatomic molecular entities emit mainly from the lowest energy of the same multiplicity. When the vibrational potential curves are parabolic, there will be a symmetry in the overlap between vibrational wave functions. This results in a mirror image between the absorbance and emission spectra of a fluorescent dye. An example of mirror image symmetry between the absorbance and fluorescence of a fluorescent dye is shown Figure 5 (b). The difference in the energy of peak absorbance and fluorescence is known as the Stokes shift energy.

From the energy level diagram, it appears that only specific energies can be absorbed and emitted corresponding to the difference in energy between the ground and excited state vibrational levels. This is true for the absorption and emission spectra of molecules in gaseous medium however the spectra of fluorescent molecules dissolved in solids or liquids are observed to be continuous rather than sharp peaks. Due to local interactions, different atoms absorb and emit at different energies as compared to an isolated single atom (Rubinov *et al*., 1983). When averaged, the result is a broadening of the absorption and emission spectrum.

2.4. Generalised Planck's law

The generalised Planck's law is an extension of Planck's law to emission from non-thermal sources. Planck's law describes the emission of a perfect absorber of light (black body) at a certain temperature (Planck, 1914).

In addition to temperature, the generalised Planck's law also makes the emission dependant on the chemical potential of the emitting medium. The chemical potential is

the energy required to add a particle to a system when the entropy and volume are kept constant (Baierlein, 2000). For blackbody radiation from the sun, the chemical potential is considered to be zero since the number of particles is not conserved and therefore there is no correlation between the number of particles and energy.

This is also clear when the Planck's distribution is compared to the Bose-Einstein distribution (Baierlein, 2000). Planck's distribution, N_{BB}, gives the number of photons expected to occupy states of a particular energy due to emission from a black body at temperature T_g. It can be written as:

$$N_{BB}(\lambda) = N_D(\lambda)\frac{1}{\exp\left(\frac{hc}{\lambda k T_g}\right) - 1} \tag{4}$$

where N_D is the density of states, h is Planck's constant, c is the speed of light, k is Boltzmann's constant and λ is the wavelength.

The Bose-Einstein distribution, N_{BE}, gives the same for a collection of bosons at a chemical potential μ:

$$N_{BE}(\lambda) = N_D(\lambda)\frac{1}{\exp\left(\frac{hc}{\lambda k T_g} - \mu\right) - 1} \tag{5}$$

Photons are bosons, therefore the Bose-Einstein distribution should be valid for black body radiation. From Planck's distribution it is clear that this occurs when the chemical potential is equal to zero.

However, it has been argued that a zero chemical potential for light is only applicable for photons emitted from incandescent sources (Herrmann and Würfel, 2005), i.e. objects that emit photons due to heating. It is observed that emission from non-thermal thermal sources (like emission from fluorescent molecules) cannot be explained by solely using the temperature of the emitting medium. In order to describe this thermodynamically, the use of an effective temperature, i.e. a temperature at which the intensity of black body radiation equals the intensity of this non-thermal emission, was promoted by some (see for example Landsberg and Evans, 1968).

The generalised Planck's law was proposed to describe non-thermal emission (Würfel, 1982). Kirchhoff's law of radiation tells us that a body, which can absorb light of a particular wavelength, can also emit at the same wavelength and vice versa (Kirchhoff, 1860) (Würfel, 2005). In non-thermal sources with strong absorption, emission can be re-absorbed and re-emitted until the emitting medium reaches thermal equilibrium with its surrounding. The final emission should therefore be described by the temperature of the emitting medium.

The generalised Planck's law calculates emission based on this temperature as well as a non-zero chemical potential. Würfel (1982) argued that the chemical potential of emission can be measured using the following argument.

The excitation of an electron in a molecule from a ground to an excited state due to the absorption of a photon results in an extra electron in the excited state and a vacancy in the ground state, that will be referred to as a hole. The excited electron can relax back to the ground state and fills this hole (i.e. recombination occurs). Assuming that processes that allow non-radiative relaxation are not present, the energy difference of the transition will result in the emission of a photon. This can be denoted by the following reversible reaction:

$$e + h_{\mathrm{q}} \leftrightarrow \gamma_{\mathrm{p}} \tag{6}$$

where e is an electron, h_{q} is a hole and γ is a photon. Assuming constant entropy and volume before and after the transition, conservation of energy tells us that:

$$dE_{\mathrm{eh}} = \mu_{\mathrm{e}} dN_{\mathrm{e}} + \mu_{\mathrm{h}} dN_{\mathrm{h}} + \mu_{\gamma} dN_{\gamma} = 0 \tag{7}$$

where dE_{eh} is the change in energy after the reaction, μ_{e} is the chemical potential of the electrons in the excited state, μ_{h} is the chemical potential of the holes in the ground state, μ_{γ} is chemical potential of the photons emitted and dN_{e}, dN_{h} and dN_{γ} are the change in the number of electrons, holes and photons after the reaction respectively.

Taking the following also into consideration:

$$dN_{\mathrm{e}} = dN_{\mathrm{h}} = -dN_{\gamma} \tag{8}$$

we obtain:

$$\mu_{\mathrm{e}} + \mu_{\mathrm{h}} = \mu_{\gamma} \tag{9}$$

i.e. the chemical potential of emission can be obtained from the chemical potential of electrons in the excited state and holes in the ground state.

The generalised Planck's emission, N_{GP}, can then be obtained from the generalised Planck's law:

$$N_{\mathrm{GP}}(\lambda) = \xi \frac{2c}{\lambda^4} \frac{1}{\exp\left(\frac{\left(\frac{hc}{\lambda} - \mu_{\gamma}\right)}{kT_{\mathrm{g}}}\right) - 1} \tag{10}$$

where ξ is the étendue of the emission and takes into account the effective area of emission as well as the solid angle of emission.

2.5. Photonic crystals

The presence of a periodic potential in semi-conductors is seen to lead to the formation of an electronic band gap. Photonic crystals are the optical equivalent of semi-conductors wherein the periodic potential is replaced by a periodic dielectric constant and give rise to optical band gaps. A simple photonic crystal known as a quarter-wave stacks was described by Lord Rayleigh as early as 1887 (Strutt, 1887). This device consisted of alternating layers of high and low refractive index materials that resulted in forbidden frequency ranges in certain directions for photon propagation i.e. high reflection of incident photons at certain wavelengths and directions. Such quarter-wave stacks are the basis of dielectric mirrors, dielectric Fabry Perrot filters and distributed feedback lasers. Florin Abelès showed in (Abelès, 1950) (Ben Abdelaziz *et al.,* 2005) a method using matrices for calculating the amplitude of the electric field reflected and transmitted from layered structures. This work was extended in (Yeh *et al.,* 1977) to look at the propagation of light in one-dimensional periodic stratified media for

both infinite and finite stacks. In this work the band structure of such devices was also calculated (the transfer matrix method section of this chapter will describe the methods developed in this work in greater detail). Publications by Vldaimir Bykov were, however, amongst the earliest to examine the effect of photonic crystals on spontaneous emission (Bykov, 1975). In this work, the effect of the photonic crystal on the emitting molecule was modelled as a perturbation of the Hamiltonian of the system.

For three-dimensional photonic crystals Ohtaka (1979) calculated the energy band of such structures using the Green's function. However, interest in these materials only grew substantially after the use of three-dimensional photonic crystals was proposed for suppressing spontaneous emission (Yablonovitch, 1987) and localisation of photons (John, 1987). The first three-dimensional photonic crystal was produced by Yablonovitch (Yablonovitch *et al*., 1991) and operated at microwave wavelengths. A common method used to calculate the band structure and field distribution in these devices, a method that will also be used in this work, is known as the plane wave expansion method (Ho *et al.*, 1990) wherein the property of discrete translational symmetry of these devices is used to write the amplitude of the field in terms of Fourier expansions (see the plane wave expansion method section in this chapter for more details). The effect of three-dimensional photonic crystals on spontaneous emission both experimentally as well as theoretically (using for example Fermi's golden rule) has also been investigated in a number of studies (Busch and John, 1998) (Barth *et al.*, 2005) and is a topic of on-going investigation (Gutmann *et al.*, 2013).

Though there are similarities between semi-conductors and photonic crystals, there are also differences. Photonic crystals are described by electromagnetism while quantum mechanics describes semi-conductors. In electromagnetism, unlike in quantum mechanics, there isn't any fundamental scale therefore the properties of photonic crystals scale with length.

In order to understand the propagation of photons in a photonic crystal, it is necessary to determine the electromagnetic waves that are allowed to propagate within a photonic crystal. The propagation of an electromagnetic wave in time is described by its frequency and in space by its wave vector. Therefore electromagnetic waves can be classified by their frequencies and wave vector. A dispersion relation is a plot that shows the allowed combinations of frequency and wave vectors of electromagnetic waves that can propagate within a photonic crystal. This plot gives insights into how

and where these electromagnetic waves propagate within the crystal and how emissions inside these devices are modified.

Two different methods of calculating the dispersion relation in 1D photonic crystals are discussed in this chapter, i.e. the plane wave expansion method and the transfer matrix method.

2.5.1. The plane wave expansion method

In this section the dispersion relation in 1D photonic crystals will be derived using the plane wave expansion method.

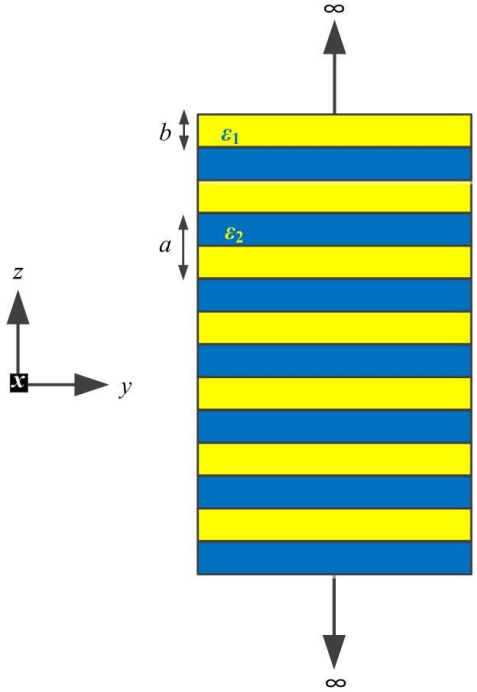

Figure 6 1D photonic crystal (infinite stack).

We consider an infinite 1D photonic crystal with a variation in its dielectric constant in the z direction as shown in Figure 6. The plane of incidence of the electromagnetic wave is assumed to be in the yz plane. This device has continuous translational symmetry in the x and y directions, i.e. the dielectric constant is invariant under translation by any distance in these directions.

In a 1D photonic crystal, it is clear that there is discrete translational symmetry along the z axis, i.e. if a point is translated by a distance ma in the z direction where m is an integer and a is equal to the length of the unit cell, it is equivalent to the starting point.

In such a structure due to the periodicity in the z direction, Bloch's theorem can be used to describe the electric field in photonic crystals, *E* (Joannopoulos *et al.*, 2008):

$$E(\mathrm{z}) \propto \mathrm{e}^{\mathrm{i}K_{\mathrm{z}}z}u(z) \tag{11}$$

where K_z is the Bloch wave number and *u* is a periodic function in the *z* direction.

Also taking into account the continuous translational symmetry in the *x* and *y* directions in a 1D photonic crystal gives a more complete description (Joannopoulos *et al.*, 2008):

$$\mathrm{E}(r') = \mathrm{e}^{\mathrm{i}k_{\mathrm{x}}x}\mathrm{e}^{\mathrm{i}k_{\mathrm{y}}y}\mathrm{e}^{\mathrm{i}K_{\mathrm{z}}z}u(z) \tag{12}$$

where r' indicates the position considered in the *xyz* coordinate system and k_{x} and k_{y} are the component of the wave vector of the electromagnetic wave in the *x* and *y* directions respectively.

Assuming that the electric field has a component only in the *x* direction (since the plane of incidence is assumed to be in the *yz* plane this corresponds to transverse electric polarisation or *s* polarisation), we obtain:

$$\mathrm{E}_x(\mathrm{y},\mathrm{z}) = \mathrm{e}^{\mathrm{i}k_{\mathrm{y}}y}\mathrm{e}^{\mathrm{i}K_{\mathrm{z}}z}u(z) \tag{13}$$

It can be shown that Maxwell's equations reduce to the so called wave equation in the case of propagation through photonic crystals (Joannopoulos *et al.*, 2008):

$$\nabla \times \nabla \times \mathrm{E}_x(\mathrm{y},\mathrm{z}) = \left(\frac{\omega}{c}\right)^2 \varepsilon(z)\mathrm{E}_x(\mathrm{y},\mathrm{z}) \tag{14}$$

$$-\frac{\partial^2 \mathrm{E}_x(\mathrm{y},\mathrm{z})}{\partial z^2} - k_{\mathrm{y}}^2\mathrm{E}_x(\mathrm{y},\mathrm{z}) = \left(\frac{\omega}{c}\right)^2 \varepsilon(r')\mathrm{E}_x(\mathrm{y},\mathrm{z}) \tag{15}$$

where ε is the dielectric constant, ω is the angular frequency and *c* is the speed of light.

The dielectric constant and the periodic function *u* (due to their periodicity) can be expanded using a Fourier series:

$$u(z) = \sum_{n=-\infty}^{\infty} c_{\mathrm{n}} e^{-in\bar{a}z} \tag{16}$$

$$\varepsilon(z) = \sum_{m=-\infty}^{\infty} d_{\mathrm{m}} e^{-im\bar{a}z} \tag{17}$$

where c_{n} and d_{m} are Fourier coefficients and $\bar{a}$ is the reciprocal lattice constant. Similar to the primitive lattice a where the structure repeats after a distance a, after an interval in K_{z} equal to the primitive reciprocal constant, i.e. $\bar{a}$, the dispersion relationship of the device also repeats.

Defining $z = 0$ to be at the centre of the layer with dielectric constant ε_1 and substituting Equation (13), Equation (16) and Equation (17) in Equation (15), on rearranging and simplification we obtain (Kolle, 2011):

$$\sum_{n=-\infty}^{\infty} \left[(\bar{a}n + K_{\mathrm{z}})^2 + k_{\mathrm{y}}^2\right] d_{\mathrm{m-n}} c_{\mathrm{n}} = \left(\frac{\omega}{c}\right)^2 c_{\mathrm{m}} \tag{18}$$

The Fourier coefficient $d_{\mathrm{m-n}}$ can be obtained through an inverse Fourier transform:

$$d_{\mathrm{m-n}} = \frac{1}{\varepsilon_2}\delta_{mn} + \left(\frac{1}{\varepsilon_1} - \frac{1}{\varepsilon_2}\right)\frac{b}{a}\mathrm{sinc}\left(\frac{(m-n)b}{a}\right) \tag{19}$$

where b is the thickness of the layers with dielectric constant ε_1, ε_2 is the dielectric constant of layer with thickness a - b and δ_{mn} is the Kronecker delta function.

After symmetric truncation of Equation (18), i.e. reducing the infinite summation in Equation (18) to a finite range, an eigenvalue equation can be obtained where c_{n} and c_{m} will be elements of a vector that form the eigenmodes of the equation. Naming this vector $\bar{C}$, Equation (18) can be re-written in the form:

$$\Lambda\bar{C} = \left(\frac{\omega}{c}\right)^2 \bar{C} \tag{20}$$

The operator, Λ, is a matrix that depends on k_{y} and K_{z}. The eigenvalues of this operator gives the frequency of propagation corresponding to these wavenumbers i.e.

the dispersion relation. For the case of the transverse magnetic or *p* polarisation case where the magnetic field is assumed to only have a component in the *x* direction, a similar eigenvalue equation can be obtained (refer to Shumpert, 2011 for further details).

The dispersion relation of a photonic crystal shows all allowed eigenvalues. Figure 7 shows the dispersion relation for a 1D photonic crystal (quarter-wave stack) with ε_1 equal to 2 and ε_2 equal to 13 calculated using the plane wave expansion method. The right hand side of this plot shows the dispersion relation for *s* polarisation (electric field in the *x* direction) and the left hand side shows the dispersion relation for *p* polarisation (magnetic field in the *x* direction). Different bands have been coloured with the lowest index band being by definition the band with the lowest frequency. This plot shows the allowed modes that can propagate within the photonic crystal, these modes are catalogued by their wave vector and frequency. The *x* axis is the normalised k_y and the *y* axis is the normalised frequency. A complete description of the wave vector requires both k_y and K_z. Each band contains all allowed modes for K_z between 0 and π/a.

The eigenmodes of the discrete translational operator are non-degenerate only for K_z between $-\pi/a$ and π/a. However, due to the symmetry of the unit cell a complete description can be obtained by only considering K_z between 0 and π/a.

The dashed line in Figure 7 shows the maximum value of k_y which satisfies the dispersion relation in air, i.e.:

$$k_y = \frac{\omega}{c} \tag{21}$$

If k_y is larger than this, then the *z* component of the wave number i.e. k_z will need to be imaginary so as to satisfy the dispersion relation in air:

$$|k_r| = \frac{\omega}{c} \tag{22}$$

where $|k_r|$ is the magnitude of the wave vector. An imaginary k_z indicates that no propagating waves exist in air. The line corresponding to Equation (21) is known as the light line since modes below this line is trapped in the photonic crystal. Within the light line is the light cone, i.e. the region of the dispersion relation containing modes that can couple out of the photonic crystal into air (i.e k_z is real).

Un-shaded regions in Figure 7 shows forbidden modes. It is clear that for the 1D photonic crystal modelled, there is a large continuous band gap for a range of frequencies between the first and second bands within the entire light cone for both polarisations. Photonic crystals with such a band gap are known as omni-directional reflectors and can reflect photons of a certain range of frequencies incident at any angle and of any polarisation (assuming the source is far away and external). The photon source has to be far away since sources close to photonic crystals will emit exponentially decaying evanescent waves that will not be reflected.

Therefore a 1D photonic crystal can create an omni-directional reflector but this is not the same as a complete band gap. In a complete band gap photon transport is forbidden for certain frequencies even inside the photonic crystal. It is clear from Figure 7 that below the light cone there are modes that are able to travel at frequencies forbidden within the light cone, therefore this photonic crystal does not have a complete band gap. The reason a complete band gap does not exist in a 1D photonic crystal is that reflections and refractions only occur at parallel planes i.e. there are no interfaces in the x and y directions. The unbounded nature of the device in the x and y directions result in a continuum of allowed modes in these directions. A complete band gap would therefore normally require periodicity along all three axes.

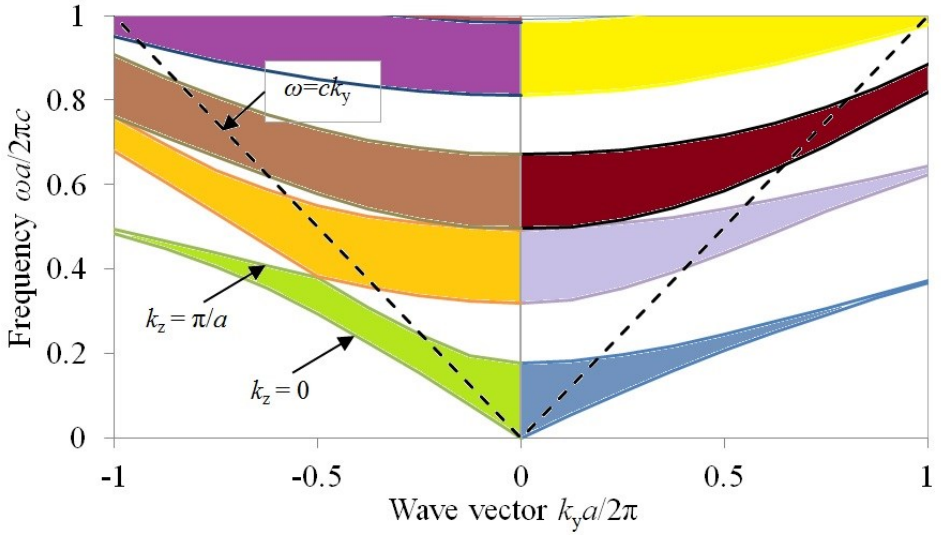

Figure 7 Dispersion relation in 1D photonic crystal obtained from the plane wave expansion method.

2.5.2. The transfer matrix method

In this section the dispersion relation of a 1D photonic crystal will be derived using the Transfer Matrix method. It will be shown that this method can also be used without much difficulty to obtain the dispersion relation of photonic crystals with only a finite number of layers. The following is adapted from Yeh (1988).

Consider a multilayer structure as shown in Figure 8, consisting of layers of dielectric constants, ε_n, magnetic permeability, μ_n and thicknesses, d_n, where the subscript n indicates the layer number. We once again assume that the periodicity of the photonic crystal is in the z direction and the plane of incidence is in the yz plane. Let the electric field at each point consist of a right travelling and a left travelling wave.

In the nth layer the amplitudes of the right and left travelling waves at the left interface will be denoted by a'_n and b'_n and at the right interface a_n and b_n.

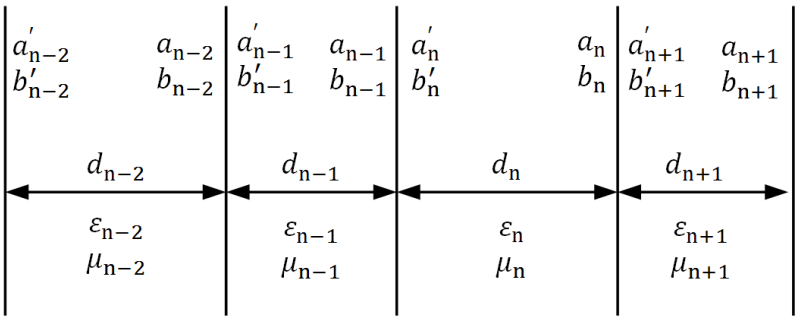

Figure 8 General multilayer structure.

At an interface between two media, from Maxwell's equations we know that if there are no charge sources the electric and magnetic fields are conserved i.e. the fields at the interface on both sides of the interface are equal.

Assuming an electromagnetic wave is incident from medium n to medium n + 1, then the continuity of the electric field at the interface for s polarisation (or transverse electric polarisation) i.e. electric field polarised in the x direction, can be written as:

$$a_{ns} + b_{ns} = a'_{(n+1)s} + b'_{(n+1)s} \tag{23}$$

The continuity of the magnetic field at the interface can be written as:

$$\sqrt{\frac{\varepsilon_n}{\mu_n}}(a_{\mathrm{ns}} + b_{\mathrm{ns}})\cos\nu_n = \sqrt{\frac{\varepsilon_{n+1}}{\mu_{n+1}}}\left(a'_{(\mathrm{n+1})\mathrm{s}} + b'_{(\mathrm{n+1})\mathrm{s}}\right)\cos\nu_{n+1} \tag{24}$$

where ν_{n} is the angle subtended by the electromagnetic wave with the interface in the n^{th} layer.

The above equations can be written in the form of a matrix:

$$D_{ns}\begin{pmatrix} a_{\mathrm{ns}} \\ b_{\mathrm{ns}} \end{pmatrix} = D_{(\mathrm{n+1})s}\begin{pmatrix} a'_{(\mathrm{n+1})\mathrm{s}} \\ b'_{(\mathrm{n+1})\mathrm{s}} \end{pmatrix} \tag{25}$$

where:

$$D_{ns} = \begin{pmatrix} 1 & 1 \\ \sqrt{\frac{\varepsilon_n}{\mu_n}}\cos\nu_n & \sqrt{\frac{\varepsilon_n}{\mu_n}}\cos\nu_n \end{pmatrix} \tag{26}$$

The corresponding expressions for *p* polarisation is given in Yeh (1988). Irrespective of polarisation we can write:

$$\begin{pmatrix} a_{\mathrm{n}} \\ b_{\mathrm{n}} \end{pmatrix} = D_n^{-1}D_{n+1}\begin{pmatrix} a'_{(\mathrm{n+1})} \\ b'_{(\mathrm{n+1})} \end{pmatrix} \tag{27}$$

The amplitudes of the electric field at the left interface in a layer is connected to the amplitudes at the right interface by a phase factor:

$$\begin{pmatrix} a'_{(\mathrm{n+1})} \\ b'_{(\mathrm{n+1})} \end{pmatrix} = P_{n+1}\begin{pmatrix} a_{\mathrm{n+1}} \\ b_{\mathrm{n+1}} \end{pmatrix} = \begin{pmatrix} e^{i\phi_{\mathrm{n+1}}} & 0 \\ 0 & e^{-i\phi_{\mathrm{n+1}}} \end{pmatrix}\begin{pmatrix} a_{\mathrm{n+1}} \\ b_{\mathrm{n+1}} \end{pmatrix} \tag{28}$$

where:

$$\phi_{\mathrm{n}} = k_{\mathrm{nz}} d_{\mathrm{n}} \tag{29}$$

where k_{nz} is the magnitude of the wave vector in the z direction at the n$^{\mathrm{th}}$ layer and d_{n} is the thickness of the n$^{\mathrm{th}}$ layer.

Similarly:

$$\begin{pmatrix} a_{\mathrm{n+1}} \\ b_{\mathrm{n+1}} \end{pmatrix} = D_{n+1}^{-1} D_{n+2} P_{n+2} \begin{pmatrix} a_{\mathrm{n+2}} \\ b_{\mathrm{n+2}} \end{pmatrix} \tag{30}$$

i.e.:

$$\begin{pmatrix} a_{\mathrm{n}} \\ b_{\mathrm{n}} \end{pmatrix} = D_{n}^{-1} D_{n+1} P_{n+1} D_{n+1}^{-1} D_{n+2} P_{n+2} \begin{pmatrix} a_{\mathrm{n+2}} \\ b_{\mathrm{n+2}} \end{pmatrix} \tag{31}$$

In this manner it is possible to connect the amplitude of the field in the first layer to the last layer:

$$\begin{pmatrix} a_0 \\ b_0 \end{pmatrix} = \mathrm{M} \begin{pmatrix} a_{\mathrm{S}} \\ b_{\mathrm{S}} \end{pmatrix} = \begin{pmatrix} \mathrm{M}_{11} & \mathrm{M}_{12} \\ \mathrm{M}_{21} & \mathrm{M}_{22} \end{pmatrix} \begin{pmatrix} a_{\mathrm{S}} \\ b_{\mathrm{S}} \end{pmatrix} \tag{32}$$

where for example a_0 and b_0 are the amplitudes in air and a_{S} and b_{S} are the amplitudes in the substrate, for example, glass and M is the product of the matrices that connect the electric field amplitudes between the layers.

Assuming the photons are incident onto the layered structure only from air then b_{S} is equal to zero and:

$$a_0 = \mathrm{M}_{11} a_{\mathrm{S}} \tag{33}$$

$$b_0 = \mathrm{M}_{21} a_{\mathrm{S}} \tag{34}$$

The reflectance, R_{top}, is then given by:

$$R_{\text{top}} = \left(\frac{b_0}{a_0}\right)^2 = \left(\frac{M_{21}}{M_{11}}\right)^2 \tag{35}$$

and transmittance, T,is given by:

$$T = \left(\frac{a_{\text{S}}}{a_0}\right)^2 = \left(\frac{1}{M_{11}}\right)^2 \tag{36}$$

One-dimensional photonic crystal (infinite stack)

If we consider a 1D photonic crystal consisting of an infinite stack of only two materials (denoted by subscripts 1 and 2) with refractive indices n_1 and n_2 and thickness b and a - b then:

$$\begin{pmatrix} a_{\text{n}} \\ b_{\text{n}} \end{pmatrix} = D_1^{-1} D_2 P_2 D_2^{-1} D_1 P_1 \begin{pmatrix} a_{\text{n+2}} \\ b_{\text{n+2}} \end{pmatrix} = \begin{pmatrix} \text{A} & \text{B} \\ \text{C} & \text{D} \end{pmatrix} \begin{pmatrix} a_{\text{n+2}} \\ b_{\text{n+2}} \end{pmatrix} \tag{37}$$

where A, B, C and D are the elements of the translational matrix that connects the field amplitudes between two unit cells. The specific expressions for the elements of the translational matrix depends on the polarisation and can be obtained from Yeh (1988).

From Bloch's theorem we know that:

$$\text{E}(\text{r}') = \text{e}^{\text{i}k_{\text{x}}x}\text{e}^{\text{i}k_{\text{y}}y}\text{e}^{\text{i}K_{\text{z}}z}u(z) \tag{38}$$

Also we know that:

$$u(z + a) = u(z) \tag{39}$$

Therefore:

$$\text{E}(\text{x}, \text{y}, \text{z} + \text{a}) = \text{e}^{\text{i}K_{\text{z}}a}\text{E}(\text{x}, \text{y}, \text{z}) \tag{40}$$

In terms of the amplitudes of the electric field we can write:

$$\begin{pmatrix} a_{\mathrm{n}} \\ b_{\mathrm{n}} \end{pmatrix} = \mathrm{e}^{\mathrm{i}K_{\mathrm{z}}a} \begin{pmatrix} a_{\mathrm{n}-2} \\ b_{\mathrm{n}-2} \end{pmatrix} \tag{41}$$

i.e.:

$$\mathrm{e}^{-\mathrm{i}K_{\mathrm{z}}a} \begin{pmatrix} a_{\mathrm{n}} \\ b_{\mathrm{n}} \end{pmatrix} = \begin{pmatrix} \mathrm{A} & \mathrm{B} \\ \mathrm{C} & \mathrm{D} \end{pmatrix} \begin{pmatrix} a_{\mathrm{n}} \\ b_{\mathrm{n}} \end{pmatrix} \tag{42}$$

$\mathrm{e}^{-\mathrm{i}K_{\mathrm{z}}a}$ is therefore the eigenvalue of the translational matrix and is given by:

$$\mathrm{e}^{\mathrm{i}K_{\mathrm{z}}a} = \frac{1}{2}(\mathrm{A}+\mathrm{D}) \pm \left[\frac{1}{4}(\mathrm{A}+\mathrm{D})^2 - 1\right]^{\frac{1}{2}} \tag{43}$$

Note that the above is true because the determinant of the translational matrix is equal to 1.

From the above for K_z to be real (i.e. to describe a propagating wave and not an evanescent wave):

$$\left|\frac{1}{2}(\mathrm{A}+\mathrm{D})\right| \leq 1 \tag{44}$$

This is because it can be shown that $A + D$ is real. The real part of the above expression should be less than or equal to 1 since the cosine of a real number cannot exceed 1.

Setting the refractive indices (dielectric constants) of the two materials (assumed to be transparent) as 1.4 and 3.6 and assuming the thicknesses are that of a quarter-wave stack (i.e. the same 1D photonic crystal modelled using the plane wave expansion method), the dispersion relation is obtained as shown in Figure 9. The right side of this figure represents *s* polarisation while the left hand side represent *p* polarisation.

The calculation used to determine the dispersion relation can be understood as follows. Both A and D depend on the wave vector in the z direction of both alternate layers, i.e. k_{1z} and k_{2z}. These in turn depend on the ω, k_y, n_1 and n_2, i.e.:

$$k_{1,2z} = \sqrt{\left(\frac{n_{1,2}}{c}\omega\right)^2 - k_y^2} \tag{45}$$

Therefore for a given ω and k_y corresponding values of A and D can be calculated (if n_1 and n_2 are known). The condition for propagating modes i.e. Equation (44) is then checked. Figure 9 shows modes that satisfy this condition. The results are seen to be the same as the dispersion relation obtained using the plane wave expansion method i.e. Figure 7. Note however, that in the plane wave expansion method, the Bloch condition is used directly in the wave equation (obtained first by a simplification of Maxwell's equation) i.e. Equation (15). In the case of the transfer matrix method, Maxwell's equations set the conditions that determine the relationships between the electric field amplitudes at the interface between adjacent layers. Bloch's theorem is then subsequently used to connect the electric field amplitudes in adjacent bi-layers i.e. Equation (41). Both methods are therefore simply different implementations of the same concept.

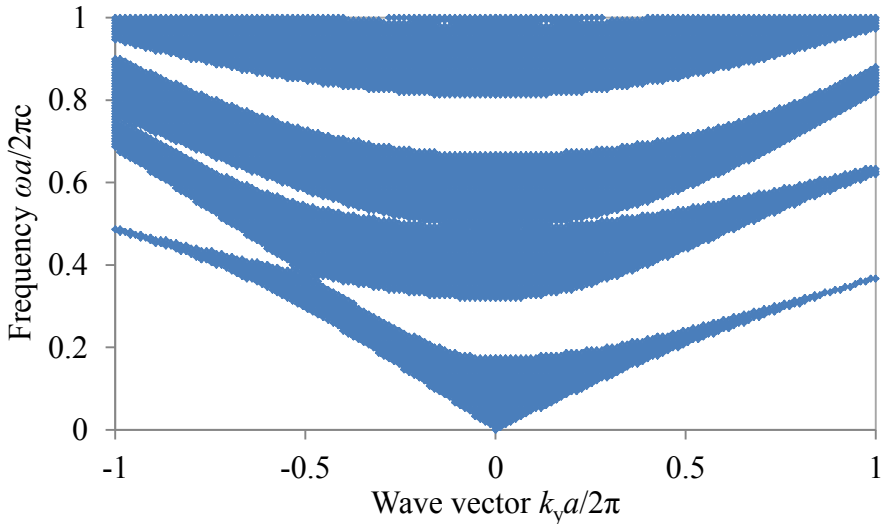

Figure 9 Dispersion relation in 1D photonic crystal obtained from the transfer matrix method.

One-dimensional photonic crystal (finite stack)

In this section the dispersion relation of the same1D photonic crystal but with N bilayers (i.e. a finite number of layers) is modelled and is based on Yeh (1988, pp. 319-

320). For a photonic crystal consisting of alternating bi-layers, the following expression connects the electric field amplitudes at the top and bottom layers:

$$\begin{pmatrix} a_0 \\ b_0 \end{pmatrix} = \mathrm{M} \begin{pmatrix} a_\mathrm{S} \\ b_\mathrm{S} \end{pmatrix} = \begin{pmatrix} \mathrm{A} & \mathrm{B} \\ \mathrm{C} & \mathrm{D} \end{pmatrix}^N \begin{pmatrix} a_\mathrm{S} \\ b_\mathrm{S} \end{pmatrix} \tag{46}$$

We are interested in modes that can propagate within i.e. are confined within the structure, therefore incidence at the top and bottom surfaces is set to 0, i.e.:

$$a_0 = b_\mathrm{s} = 0 \tag{47}$$

Therefore:

$$M_{11} = 0 \tag{48}$$

Modes satisfying the condition described in Equation (48) can propagate within the 1D photonic crystal. Figure 10, Figure 11 and Figure 12 shows the dispersion relation for *s* polarisation for the 1D photonic crystal with *N* equal to 1, 6 and 30. It is clear from these figures that as the number of layers increases, each discrete band splits into *N* bands. At *N* equal to 30 due to the finite thickness of the lines plotted, the dispersion relation starts to resemble the dispersion relation of an infinite stack i.e. Figure 9.

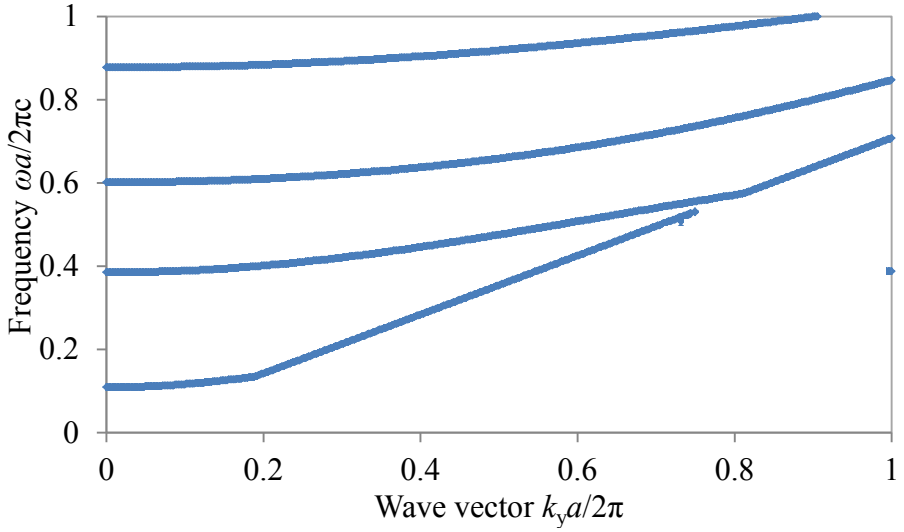

Figure 10 Dispersion relation in 1D photonic crystal for *N*=1.

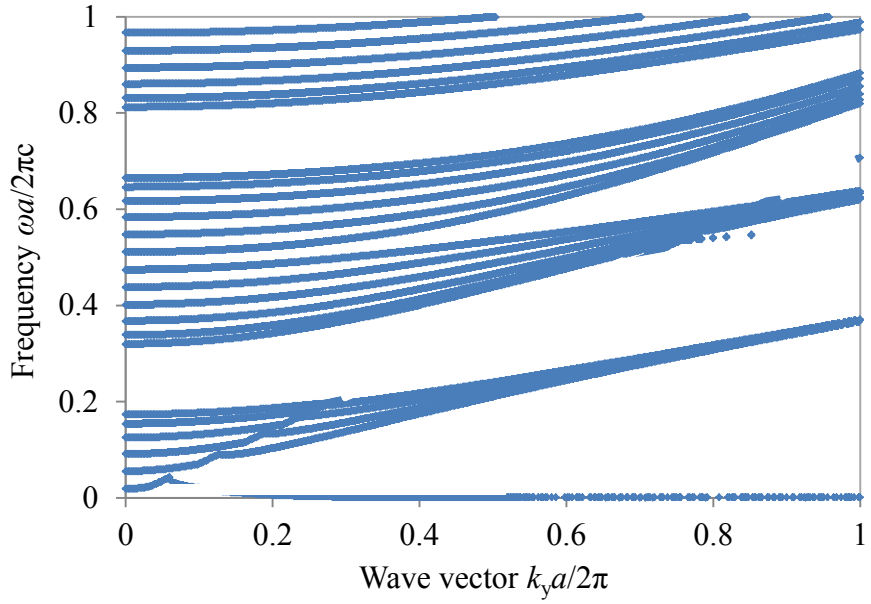

Figure 11 Dispersion relation in 1D photonic crystal for *N*=6.

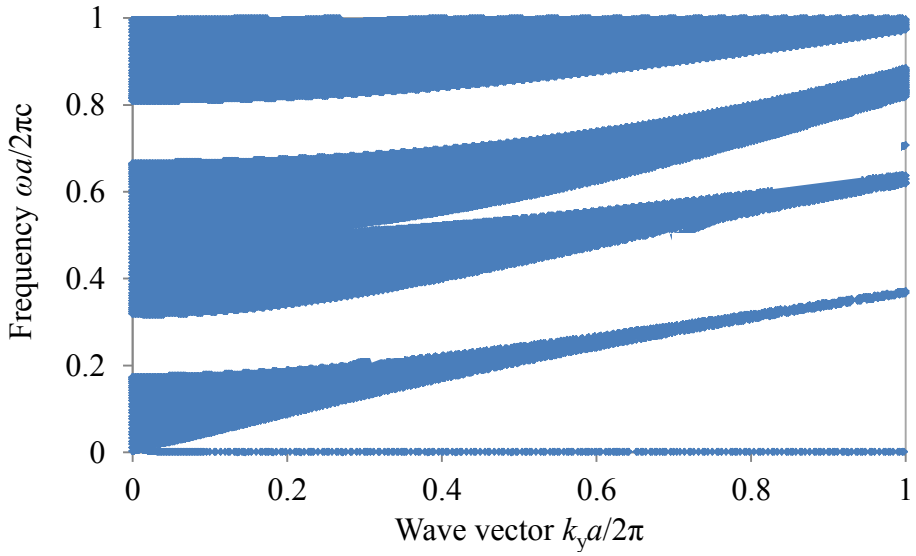

Figure 12 Dispersion relation in 1D photonic crystal for *N*=30.

2.6. Summary

The fundamental theories on the interaction between light and matter relevant to this project has been presented in this chapter. Building upon this the modelling of solar cells (Chapter 3) and fluorescent solar collectors (Chapter 5 and Chapter 6) will be developed in subsequent chapters.

References

Abelès, F., 1950. *Recherches sur la propagation des ondes electromagnetiques sinusoidales dans les milieux stratifies: application aux couches minces.* Annals of Physics. 12: 596-706.

Acuña, A. U., Amat-Guerri, F., Morcillo, P., Liras, M. and Rodríguez, B., 2009. *Structure and formation of the fluorescent compound of lignum nephriticum.* Organic Letters. 11: 3020-3023. DOI: 10.1021/ol901022g.

Atkins, P. and de Paula, J., 2010. *Physical Chemistry.* Oxford University Press: Oxford, UK.

Baierlein, R., 2000. *The elusive chemical potential*. American Journal of Physics. 69: 423-434. DOI: 10.1119/1.1336839.

Barth, M., Gruber, A. and Cichos, F., 2005. *Spectral and angular redistribution of photoluminescence near photonic stop band.* Physical Review B. 72: 085129. DOI: 10.1103/PhysRevB.72.085129.

Beer, A., 1852. *Bestimmung der absorption des rothen lichts in farbigen flüssigkeiten*. Annalen der Physik und Chemie. 162: 78-88. DOI: 10.1002/andp.18521620505.

Ben Abdelaziz, K., Zaghdoudi, J., Kanzari, M. and Rezig, B., 2005. *A broad omnidirectional reflection band obtained from deformed Fibonacci quasi-periodic one dimensional photonic crystals.* Journal of Optics A: Pure and Applied Optics. 7: 544-549. DOI: 10.1088/1464-4258/7/10/005.

Berberan-Santos, M.N., 2001. *Pioneering contributions of Jean and Francis Perrin to molecular luminescence.* In New trends in fluorescence spectroscopy. Springer: Germany. Chapter 2: 7-33.

Born, M. and Oppenheimer, R., 1927. *Zur quantentheorie der molekeln.* Annalen der Physik (Leipzig). 84: 457-484. DOI: 10.1002/andp.19273892002.

Bouguer, P., 1729. *Essai d'optique, sur la graduation de la lumiere*. Chez Claude Jomber: Paris, France.

Boyle, R., 1725. *The philosophical works of the honourable Robert Boyle.* Printed for W. and J. Innys, J. Obsorn and T. Longman: London, UK.

Busch, K. and John, S., 1998. *Photonic band gap formation in certain self-organising systems*. Physical Review E. 58: 3896-3908. DOI: 10.1103/PhysRevE.58.3896.

Bykov, V.P., 1975. *Spontaneous emission from a medium with a band spectrum.* Soviet Journal of Quantum Electronics. 4: 861-871. DOI: 10.1070/QE1975v004n07ABEH009654.

Gutmann, J., Zappe, H. and Goldscmidt, J.C., 2013. *Qualitative modeling of fluorescent emission in photonic crystals.* Physical Review B. 88: 205118 1-9. DOI: 10.1103/PhysRevB.88.205118.

Herrmann, F. and Würfel, P., 2005. *Light with nonzero chemical potential*. American Journal of Physics. 73: 717-721. DOI: 10.1119/1.1904623.

Ho, K.M., Chan, C.T. and Soukoulis, 1990. *Existence of a photonic band gap in periodic dielectric structures.* Physical Review Letters. 65: 3152-3155. DOI: 0.1103/PhysRevLett.65.3152.

John, S., 1987. *Strong localization of photons in certain disordered dielectric superlattices.* Physical Review Letters. 58: 2486-2489. DOI: 10.1103/PhysRevLett.58.2486.

Joannopoulos, J.D., Johnson, S.G., Winn, J.N. and Meade, R.D., 2008. *Photonic crystals: molding the flow of light*. Princeton University Press.

Kirchhoff, G., 1860. *Ueber das Verhältniss zwischen dem Emissionsvermögen und dem Absorptionsvermögen der Körper für Wärme and Licht.* Annalen der Physik und Chemie. 109: 275–301. Translated by Guthrie, F., 1860. *On the relation between the radiating and absorbing powers of different bodies for light and heat*. Philosophical Magazine. Series 4, 20: 1–21. DOI: 10.1080/14786446008642901.

Kolle, M., 2011. *Photonic structures inspired by nature.* Springer: Berlin, Germany. DOI: 10.1007/978-3-642-15169-9_2.

Lakowicz, J.R., 2010. *Principles of fluorescence spectroscopy.* Springer: New York, USA.

Lambert, J., 1760. *Photometria, sive de mensura et gradibus luminis, colorum et umbrae*. Eberhard Klett: Augsberg, Germany.

Landsberg, P.T. and Evans, D.A., 1968. *Thermodynamic limits for some light-producing devices*. Physical Review. 166: 242-246. DOI: 10.1103/PhysRev.166.242.

Ohtaka, K., 1979. *Energy band of photons and low-energy photon diffraction.* Physical Review B. 19: 5057-5067. DOI: 10.1103/PhysRevB.19.5057.

Perrin, J., 1920. *Atomes et lumière*. La Revue du Mois. 21: 113-166.

Perrin, F.H., 1948. *Whose absorption law?* Journal of the Optical Society of America. 38: 72-74. DOI: 10.1364/JOSA.38.000072.

Planck, M., 1914. *Theory of heat radiation*. P. Blakiston's Son & Co: Philadelphia, USA.

Rubinov, A.N. and Tomin, V.I., 1983. *Spectral properties of liquid polar solutions under conditions of dynamic inhomogenous orientational broadening*. Journal of Applied Spectroscopy. 38: 33-50. DOI: 10.1007/BF00659858.

Shumpert, J.D., 2001. *Modeling of periodic dielectric structures (electromagnetc crystals).* Ph.D. Thesis, University of Michigan.

Stokes, G.G., 1852. *On the change of refrangibility of light.* Philosophical Transactions of the Royal Society of London. 142: 463-562. DOI: 10.1098/rstl.1852.0022.

Strutt, J.W., 1887. *On the maintenance of vibrations by forces of double frequency, and on the propagation of waves through a medium endowed with a periodic strucuture.* Philosophical Magazine and Journal of Science. 24: 145-159.

Würfel, P., 1982. *The chemical potential of radiation*. Journal of Physics C: Solid State Physics. 15: 3967-3985. DOI: 10.1088/0022-3719/15/18/012.

Würfel, P., 2005. *Physics of solar cells: From principles to new concepts*. Wiley-VCH Verlag: Weinheim, Germany. DOI: 10.1002/9783527618545.

Yablonovitch, E., 1987. *Inhibited spontaneous emission in solid-state physics and electronics.* Physical Review Letters. 58: 2059-2062. DOI: 10.1103/PhysRevLett.58.2059.

Yablonovitch, E., Gmitter, T.J. and Leung, K.M., 1991. *Photonic band structure: the face-centered-cubic case employing nonspherical atoms.* Physical Review Letters. 67: 2295-2298. DOI: 10.1103/PhysRevLett.67.2295.

Yeh, P., 1977. *Electromagnetic propagation in periodic stratified media. I. General theory.* Journal of the Optical Society of America. 67: 423-438. DOI: 10.1364/JOSA.67.000423**.**

Yeh, P., 1988. *Optical waves in layered media.* John Wiley & Sons: New York, USA.

3. Basics of solar cell operation and modelling

3.1. Introduction

The photovoltaic effect was first observed as early as 1839 by Becquerel. It was noticed that current was generated when silver coated platinum deposited in an electrolyte was exposed to light (Nelson, 2003). In 1883 Fritts managed to build a solid state solar cell by coating selenium with gold (Nelson, 2003). These elements are now known to form what is called a Schottky junction which results in an electric field at the interface between the two elements. Modern solar cells are generally based on the so called *p-n* junction, an early report of which was given in the 1940s by Ohl at Bell Laboratories (Ohl, 1946). Ohl observed that a silicon rod with impurities of boron and aluminium on one side and phosphorous on the other side produced a large voltage when illuminated (see for example Riordan and Hoddeson, 1997 for a detailed account of this discovery). In the following decade Chapin, Fuller and Pearson reported the first practical silicon based solar cell with a *p-n* junction and an efficiency of 6% (Chapin *et al*., 1954).

This chapter describes the working of a modern solar cell based on such *p-n* junctions. The *p-n* junction is explained in terms of excited electrons in the conduction band and the vacant 'holes' in the valence band. This is followed by an explanation of the transport equations that describe the behaviour of electrons and holes in these solar cells. It is also shown how these equations can be used to determine the Internal and External Quantum Efficiencies (IQE and EQE) of these devices.

Following from the generalised Planck's law (Würfel, 1982) discussed in Chapter 2, the ideal solar cell efficiency i.e. the Shockley-Queisser limit (Shockley and Queisser, 1961) has also been derived and analysed.

3.2. The *p-n* junction, drift and diffusion

Solar cells, such as the crystalline silicon (cSi) based solar cells, can be formed by joining a *p*-type semiconductor to an *n*-type semiconductor, although in practice other methods such as diffusion of dopants into crystals are used to form *p-n* junctions. The *p-*

type semiconductor contains an excess of holes and the *n*-type semiconductor contains an excess of electrons due to the valance band characteristics of impurities. For example to make a silicon solar cell, boron doped silicon could be used to form the *p*-type and phosphorous doped silicon could form the *n*-type. On creation of a *p*-*n* junction, excess electrons from the *n*-type move to occupy holes in the *p*-type. This results in a net negative charge on the *p* side near the interface and a net positive charge on the *n* side of the interface. Therefore, there is an electric field pointing in the direction of the *p* side. The charged area near the interface between the *p* and *n* type is known as the depletion region since it is depleted of free carriers (holes and electrons).

In the depletion region, if the absorption of a photon results in the creation of an electron hole pair (due to the excitation of an electron from the valence to the conduction band), in a process known as drift, the electric field will move holes to the *p* side and electrons to the *n* side (Figure 13 shows the structure of a typical cSi solar cell, t is the solar cell thickness, z_p, z_d and z_n are the thicknesses of the *n*-type, depletion region and *p*-type respectively). Holes in the *n*-type and free electrons in the *p*-type are known as minority carriers. The minority carriers go through the depletion region while the majority carriers can be passed through a load and do work.

Farther away from the depletion region, the motion of minority carriers is determined by diffusion as described by Fick's law of diffusion (Fick, 1855). Solar cells can, therefore, be divided into two categories based on the dominant transport mechanism in these devices i.e. drift based solar cells and diffusion based solar cells. Certain solar cell are thin due to strong absorption as a result of a direct band gap, these solar cells are dominated by drift current since the minority carriers are generated close to the depletion region and their transport is dominated by the electric field present in this region. Examples of these devices include thin film solar cells such as amorphous silicon solar cells. Solar cells dominated by diffusion current are thicker due to weaker absorption as a result of the presence of an indirect band gap as in for example cSi based solar cells. A lot of the minority carriers are generated farther away from the depletion region in these devices, therefore their transport is dominated by diffusion.

See, for example, Wenham *et al.* (1994) for more on the structure and basic principles of solar cells.

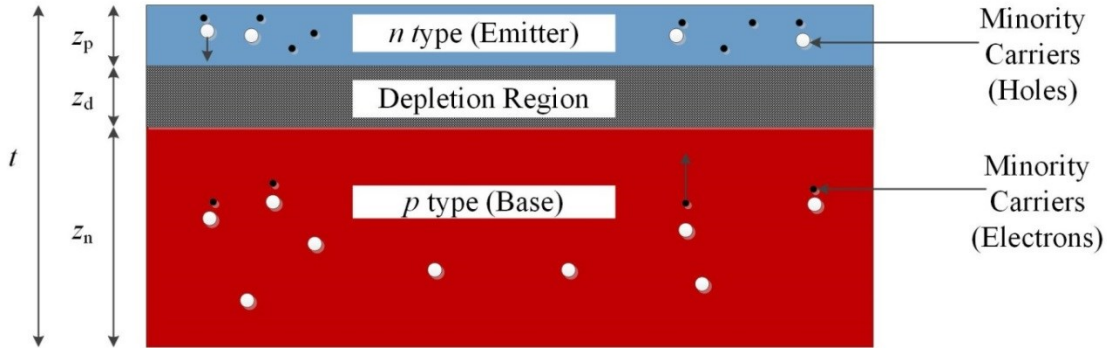

Figure 13 Structure of a cSi solar cell.

3.3. The transport equations

This section describes equations (known as semiconductor transport equations) that can be used to calculate the IQE and EQE of solar cells. The EQE is the fraction of photons incident on the solar cell at a particular wavelength that results in the output of current from the solar cell. The IQE is the same but defines incident photons as photons that are not reflected by the top surface of the solar cell.

We assume a diffusion dominated solar cell as seen in Figure 13 consisting of a uniformly doped *n*-type emitter, a uniformly doped *p*-type base and a depletion region in between. See (Gray, 2003) or (Sze and Ng, 2007) for a similar treatment.

The conservation of electrons and holes results in the so called continuity equations that relate the rate of change of minority carrier concentration with the motion of minority carriers as well as the generation and recombination rates of electron hole pairs. Recombination is a major loss mechanism in solar cells wherein electrons relax from the conduction band to the valence band.

The continuity equations for holes in *n*-type are given by:

$$\frac{\partial p}{\partial t'} = G - U + \frac{1}{q}\nabla . J_{\mathrm{p}} \tag{49}$$

where t' is time, p is the concentration of holes per unit volume, G and U are the generation and recombination rates of electrons and holes respectively and J_{p} is the hole current density in the *n*-type and q is the charge of an electron.

The electron and hole current densities in a solar cell are due to drift in the electric field and also carrier diffusion. The assumption of uniform doping implies that there is

no electric field outside the depletion region. Therefore, in a diffusion based solar cell we can ignore the drift current outside of the depletion region, therefore the hole current in the *n*-type is given by:

$$J_{\mathrm{p}} = qD_{\mathrm{p}}\nabla p \tag{50}$$

where D_{p} is the diffusion constant of holes in the emitter.

Under steady state conditions there should not be any change in carrier concentration. Assuming steady state and substituting Equation (50) into Equation (49), we obtain:

$$D_{\mathrm{p}}\frac{d^2(p-p_0)}{dz^2} = \frac{(p-p_0)}{\tau_{\mathrm{p}}} - G \tag{51}$$

where p_0 is a constant equal to the hole concentration per unit volume at thermal equilibrium in the *n*-type and τ_{p} is the recombination lifetime of holes in the *n*-type.

The recombination lifetime is given by:

$$\tau_{\mathrm{p}} = \frac{L_{\mathrm{p}}^2}{D_p} \tag{52}$$

where L_{p} is the diffusion length (i.e. average distance covered by minority carriers before recombination) of holes in the *n*-type.

3.3.1. Solving transport equations

The IQE and EQE of the solar cell can be calculated by directly solving the transport equations.

The electron-hole generation rate at a depth z is equal to the absorption rate at z as described by the Beer-Lambert law (Bouguer, 1729) (Perrin, 1948) (see Chapter 2). For incident photons of a particular wavelength it can be written as:

$$G(\lambda, z) = \alpha(\lambda)N_{\mathrm{inc}}(\lambda)\Big(1 - R_{\mathrm{top}}(\lambda)\Big)\exp(-\alpha(\lambda)z) \tag{53}$$

where λ is the wavelength, α is the absorption coefficient of the semiconductor, N_{inc} is the photon flux incident on the solar cell per unit area and R_{top} is the reflectance (i.e. fraction of incident light which is reflected) on the top surface of the solar cell.

Substituting Equation (53) into Equation (51) we obtain:

$$D_p \frac{d^2(p-p_0)}{dz^2} = \frac{D_p(p-p_0)}{L_\mathrm{p}^2} - \alpha(\lambda) N_\mathrm{inc}(\lambda)\left(1 - R_\mathrm{top}(\lambda)\right)\exp(-\alpha(\lambda)z) \tag{54}$$

The general solution to this is:

$$p - p_0 = A\cosh\left(\frac{z}{L_\mathrm{p}}\right) + B\sinh\left(\frac{z}{L_\mathrm{p}}\right) - \frac{\alpha(\lambda) N_\mathrm{inc}(\lambda)\left(1 - R_\mathrm{top}(\lambda)\right)\frac{L_\mathrm{p}^2}{D_p}\exp(-\alpha(\lambda)z)}{\alpha^2(\lambda)L_\mathrm{p}^2 - 1} \tag{55}$$

where A and B are constants.

The first boundary condition is obtained by introducing a constant known as the surface recombination velocity of holes in the *n*-type, S_p. At the surface (i.e. at $z = 0$) it is equal to the following ratio:

$$S_\mathrm{p} = \frac{p - p_0}{D_p \frac{d(p-p_0)}{dz}} \tag{56}$$

The second boundary condition is at the depletion region edge of the *n*-type, i.e at a depth equal to z_p. Due to the large electric field, the excess minority carrier concentration here is equal to 0:

$$p - p_0 = 0 \tag{57}$$

at:

$$z = z_\mathrm{p} \tag{58}$$

Solving the general solution using these boundary conditions the hole current at the depletion region edge of the *n*-type is obtained from:

$$J_{\mathrm{p}}(\lambda) = -qD_p\nabla p$$
$$= \frac{q\alpha(\lambda)N_{\mathrm{inc}}(\lambda)\left(1-R_{\mathrm{top}}(\lambda)\right)L_p}{\alpha^2(\lambda)L_{\mathrm{p}}^2-1}\left[\left\{\frac{S_{\mathrm{p}}L_{\mathrm{p}}}{D_p}+L_{\mathrm{p}}\alpha\right.\right.$$
$$-\exp\left(-\alpha(\lambda)z_{\mathrm{p}}\right)\left(\sinh\left(\frac{z_{\mathrm{p}}}{L_{\mathrm{p}}}\right)+\frac{S_{\mathrm{p}}L_{\mathrm{p}}}{D_p}\cosh\left(\frac{z_{\mathrm{p}}}{L_{\mathrm{p}}}\right)\right)\Bigg\} \tag{59}$$
$$/\left\{\cosh\left(\frac{z_{\mathrm{p}}}{L_{\mathrm{p}}}\right)+\frac{S_{\mathrm{p}}L_{\mathrm{p}}}{D_p}\sinh\left(\frac{z_{\mathrm{p}}}{L_{\mathrm{p}}}\right)\right\}$$
$$\left.-L_p\alpha(\lambda)\exp\left(-\alpha(\lambda)z_{\mathrm{p}}\right)\right]$$

Similarly the electron current density in the *p*-type, J_{n}, can be obtained. Due to the electric field in the depletion region, the collection efficiency in this region is assumed to be close to unity. The photo-current density in the depletion region, J_{d}, is therefore equal to the absorption within this region multiplied by the charge of an electron.

The total photocurrent, J_{tot} is given by the sum of the hole and electron current collected at the depletion region edges and the photocurrent generated in the depletion region:

$$J_{\mathrm{tot}}(\lambda) = J_{\mathrm{p}}(\lambda) + J_{\mathrm{n}}(\lambda) + J_{\mathrm{d}}(\lambda) \tag{60}$$

By taking into consideration the photon flux incident on the solar cell, the IQE and the EQE can be obtained:

$$\mathrm{IQE} = \frac{J_{\mathrm{tot}}(\lambda)}{qN_{\mathrm{inc}}(\lambda)\left(1-R_{\mathrm{top}}(\lambda)\right)} \tag{61}$$

and

$$\mathrm{EQE}(\lambda) = \frac{J_{\mathrm{tot}}(\lambda)}{qN_{\mathrm{inc}}(\lambda)} \tag{62}$$

If an antireflection coating is not applied the reflectance of light at each wavelength can be calculated from the real and imaginary parts of the refractive index, *n*, of the solar cell:

$$R_{\text{top}} = \frac{[1 - \text{Re}(n)]^2 + [\text{Im}(n)]^2}{[1 + \text{Re}(n)]^2 + [\text{Im}(n)]^2} \quad (63)$$

3.3.2. Results and discussion

To illustrate the utility of these expression, a typical cSi based solar cell has been modelled. Using the absorption coefficient of silicon as shown in Figure 14 and the values shown in Table 1 to define the solar cell, the IQE and EQE have been calculated (see Figure 15 and Figure 16).

Table 1 Assumed values of different variables in calculations. D_n is the diffusion constant of electrons in the *p*-type, L_n is the diffusion length of electrons in the *p*-type and S_n is the surface recombination velocity of electrons in the *p*-type.

Variable	Value
z_p	0.5 μm
z_d	0.5 μm
t	200 μm
L_p	10^{-4} cm
L_n	$300\text{x}10^{-4}$ cm
D_p	10.5 $cm^2 s^{-1}$
D_n	10.5 $cm^2 s^{-1}$
S_p	1000 cm s^{-1}
S_n	100 cm s^{-1}

From Figure 14 it is clear that the absorption by silicon is strong at short wavelengths. The absorption coefficient is low for wavelengths beyond 440 nm due the presence of an indirect band gap for low energies. This is also clear from the IQE and EQE of the cSi solar cell (Figure 15 and Figure 16)) that shows that the majority of current generated by short wavelength photons originates from the top of the solar cell i.e. at the emitter.

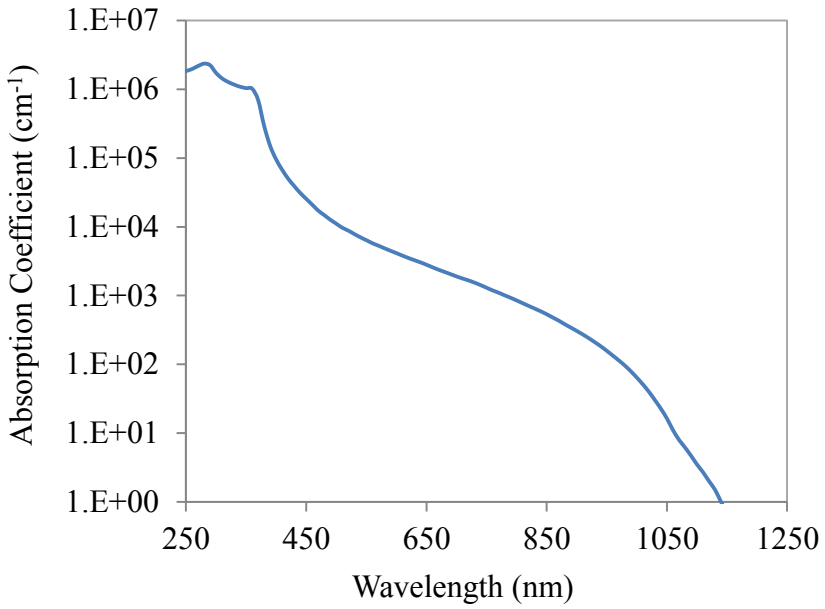

Figure 14 Absorption coefficient of silicon.

Longer wavelength photons are seen to be converted to current by the base, however for photons with wavelengths beyond 950 nm a sharp decline in the IQE and EQE is observed. This could be due to poor absorption and a long distance between depth of electron hole pair generation and the depletion region edge resulting in an increase in the probability of recombination.

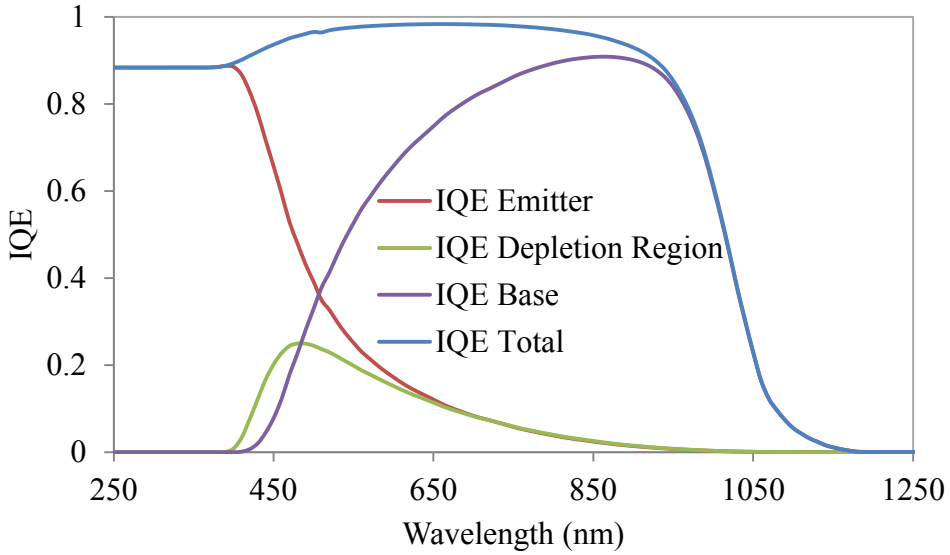

Figure 15 IQE of the solar cell calculated by solving the transport equations.

It is also clear from the results for the depletion region that even though it is assumed that all the electron hole pairs generated here are converted into current, its overall contribution to current generation is not very high most likely because it is a very thin layer.

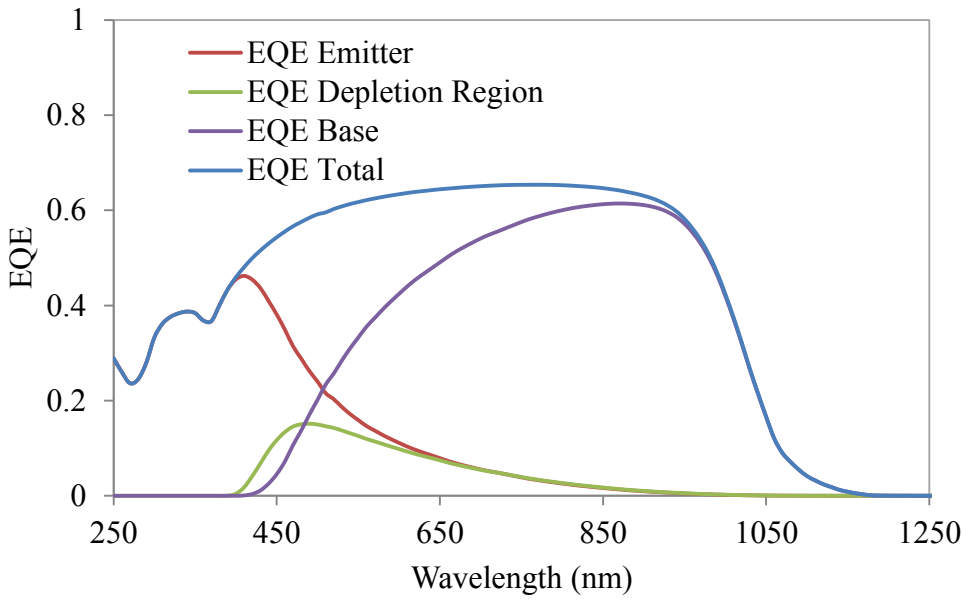

Figure 16 EQE of the solar cell calculated by solving the transport equations.

3.4. Ideal solar cell efficiencies and voltages

The Shockley-Queisser limit is the maximum power conversion efficiency of a solar cell with a single junction (Shockley and Queisser, 1961). Single junction solar cells can only absorb photons with energy greater than its band gap energy i.e. the energy difference between its valence and conduction band. The Shockley-Queisser limit assumes the solar cell to be a perfect absorber of light at energies higher than the band gap of the solar cell. It is a purely theoretical limit derived by assuming equality of the photon flux incident on a solar cell to what is emitted and extracted by it. Non-radiative recombination is neglected and only radiative recombination is taken into consideration.

The need to include radiative recombination is clear from the Einstein relation between absorption and emission rates. Einstein determined that the ratio of the rate of absorption and the rate of spontaneous emission is equal to a constant (Einstein, 1917)

i.e. emission accompanies absorption. This clearly indicates that radiative relaxation is an unavoidable process in solar cells.

The quasi-blackbody nature of this ideal solar cell removes the concept of a lifetime for emission since all the emitted light it assumed to be instantly re-absorbed. However, it is now possible to use the generalised Planck's law (see Chapter 2) to describe the emission of the solar cell in regions where it can absorb i.e. at greater than band gap energies.

The Shockley-Queisser limit builds upon work done by Trivich and Flinn (1955) who obtained the ultimate efficiency of solar cells. The ultimate efficiency considers two types of losses in a single junction solar cell, thermalisation loss and below band gap loss. The former is due to the absorption of photons with energies greater than the band gap energy of the solar cell. The excess energy is lost as the electrons in the excited state attain thermal equilibrium with its surroundings. Below band gap loss refers to photons with energies below the solar cell band gap energy that are not utilised since they cannot be absorbed by the solar cell.

Shockley and Queisser (1961) extended this treatment in order to include losses due to emission by the solar cell. The presence of these losses is indicated by the difference between open circuit voltage and band gap voltage as well as the effect of the fill factor. In a solar cell, maximum power is extracted at a voltage below the open circuit voltage and at a current less than the short circuit current, the fill factor connects the product of the open circuit voltage and short circuit current to this maximum power.

3.4.1. The ultimate efficiency: Trivich and Flinn

The ultimate efficiency assumes that each photon with energy greater than the band gap energy of the solar cell is absorbed by the solar cell and energy equal to the band gap energy can be extracted from these photons.

The ultimate efficiency, η_{u}, is therefore equal to:

$$\eta_{\mathrm{u}} = \frac{hcN_{\mathrm{inc},\lambda_{\mathrm{g}}}}{\lambda_{\mathrm{g}} P_{\mathrm{inc}}} \tag{64}$$

where h is Planck's constant, c is the speed of light, λ_g is the band gap wavelength of the solar cell, $N_{\mathrm{inc},\lambda_g}$ is the incident solar photon flux with energy greater than the band gap energy and P_{inc} is the total power of the incident photon flux.

Figure 17 shows the dependence of the ultimate efficiency on the band gap energy. The calculation of these results assumes that the solar photon flux can be approximated by emission from a blackbody at a temperature equal to 6000 K. A maximum efficiency of 44% is seen when the band gap energy is equal to 1.1 eV (i.e. close to the band gap of cSi). For solar cells with larger band gap energies, even though the energy of each excited electron is large, the total extracted power is lower since the number of excited electrons is smaller. The opposite is true when the band gap energy is low. The peak represents a balance between the quantity of excitons utilised and their energy.

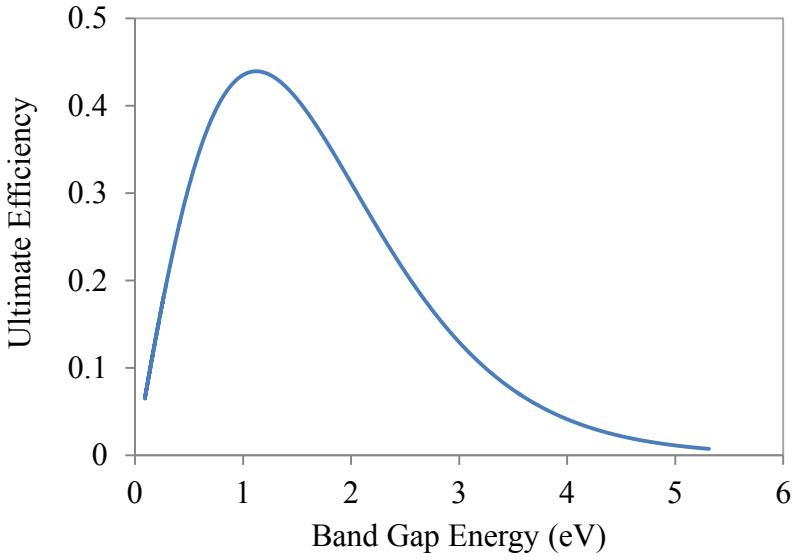

Figure 17 Variation in the ultimate efficiency with band gap energy.

3.4.2. The Shockley Queisser limit

The Shockely Queisser limit improves upon the ultimate efficiency by taking into consideration that some of the absorbed solar photon flux is emitted by the solar cell (see Würfel, 2005 for a similar treatment as described below).

In this case, the net photon flux utilised by the solar cell, N_{ex}, is equated to the difference between the absorbed and emitted photon flux:

$$N_{\mathrm{ex}} = N_{\mathrm{inc},\lambda_{\mathrm{g}}} - N_{\mathrm{cell},\lambda_{\mathrm{g}}} \tag{65}$$

where $N_{\mathrm{cell},\lambda_{\mathrm{g}}}$ is the photon flux emitted by the solar cell.

As mentioned an ideal solar cell is assumed to absorb all photons with energies greater than the band gap. It can, therefore, also only emit photons with energies above the band gap energy (Kirchhoff, 1860) (Würfel, 2005). This emission is given by the generalised Planck's law and depends on the temperature of the solar cell and a non-zero chemical potential, i.e.:

$$\begin{aligned} N_{\mathrm{ex}} = \xi_{\mathrm{inc}} \int_0^{\lambda_{\mathrm{g}}} \frac{2c}{\lambda^4} \frac{1}{\exp\left(\frac{\left(\frac{hc}{\lambda}\right)}{kT_{\mathrm{inc}}}\right) - 1} d\lambda \\ - \xi_{\mathrm{cell}} \int_0^{\lambda_{\mathrm{g}}} \frac{2c}{\lambda^4} \frac{1}{\exp\left(\frac{\left(\frac{hc}{\lambda}\right) - \mu_{\mathrm{cell}}}{kT_{\mathrm{cell}}}\right) - 1} d\lambda \end{aligned} \tag{66}$$

where k is Boltzmann's constant, μ_{cell} is the chemical potential of the electron hole gas of the solar cell, T_{cell} is the temperature of the solar cell, T_{inc} is the temperature of the Sun, ξ_{cell} is the étendue of the emission from the solar cell to its surroundings equal to πA_{cell} with A_{cell} being the surface area of the solar cell and ξ_{inc} is the étendue of the incident solar photon flux. For one Sun concentration:

$$\xi_{\mathrm{inc}} = \Omega_{\mathrm{inc}} A_{\mathrm{cell}} \tag{67}$$

where Ω_{inc} is the solid angle subtended by the Sun with respect to the solar cell. At maximum solar concentration:

$$\xi_{\mathrm{inc}} = \pi A_{\mathrm{cell}} \tag{68}$$

The photon flux from the Sun that reaches the solar cell is modelled as emission from a hemisphere onto a flat surface, while emission from the solar cell to its surroundings is modeled as emission from a flat surface to a hemisphere (not a sphere since we assume a perfect reflector on the back surface of the solar cell).

Due to the photon recycling that occurs due to repeated radiative recombination and re-absorption cycles by the solar cell, the photons emitted by the solar cell comes into thermal and chemical equilibrium with the electrons and holes of the semiconductor. Therefore the chemical potential of the emitted light is equal to the chemical potential of the solar cell i.e. the useful work that can be done. This is similar to how the chemical potential of emission by a fluorescent edge concentrator is similar to the chemical potential of the emitting fluorescent molecules (Meyer and Markvart, 2009), to be discussed in Chapter 5. Figure 18 shows the plot between the photon flux extracted by the solar cell and its chemical potential for one Sun concentration i.e. sunlight reaching the earth without concentration. The temperature of the Sun and solar cell are assumed to be equal to 6000 K and 298 K respectively, a band gap energy of 1.1 eV has also been assumed. This curve is effectively the current voltage curve of an ideal cSi solar cell differing only by a factor equal to the charge of an electron. It is clear that for the solar cell to extract a maximum number of photons, the chemical potential of the solar cell should be zero (i.e. short circuit current) and when the chemical potential is maximum no photons are extracted (i.e. open circuit voltage).

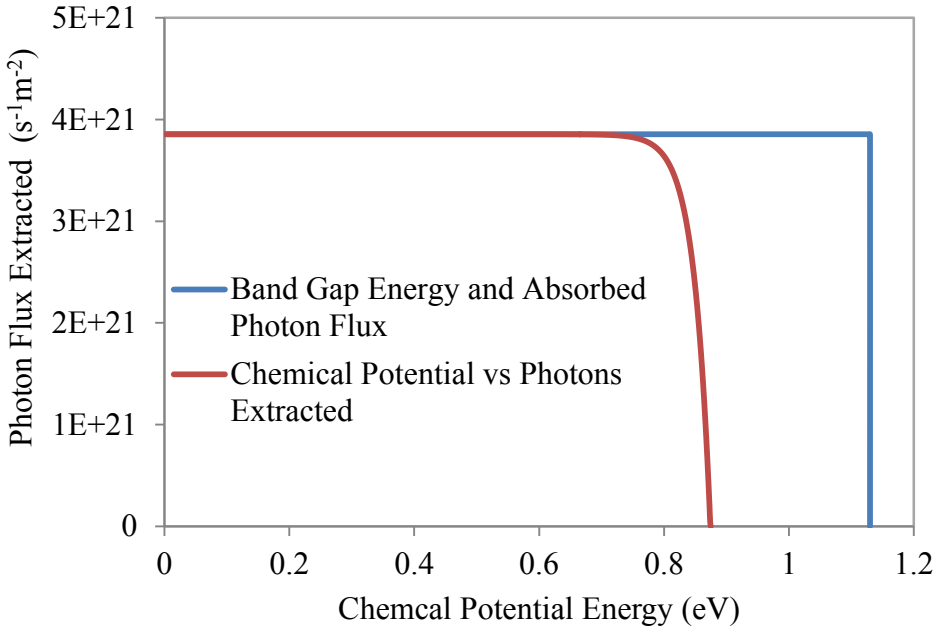

Figure 18 Relationship between the chemical potential of the emitted photon flux and the extracted photon flux for one Sun concentration.

Figure 19 shows the relationship between the extracted photon flux and the chemical potential for maximum solar concentration. Here it is clear that the maximum value of the chemical potential is close to the band gap energy unlike under one Sun concentration in which there is a substantial difference between the maximum chemical potential and the band gap energy. The additional loss under one Sun concentration can be understood to be a result of heat generation due to entropy production on the expansion of the solid angle of emitted light compared to incident light (Markvart, 2008).

Another loss seen for both one Sun concentration and maximum solar concentration is the decrease in the chemical potential as more photons are extracted. This can be interpreted as due to the production of entropy and therefore heat due to the extraction of a finite amount of current (Markvart, 2008).

The chemical potential of the solar cell is equal to the difference between the quasi Fermi levels of the electrons and holes in the semi-conductor and is connected to the voltage of the solar cell, V_{q}, as follows:

$$\mu_{\mathrm{cell}} = qV_{\mathrm{q}} \tag{69}$$

The solar cell current voltage relationship can be easily obtained from this treatment since the extracted photon flux only differs from the extracted current by a factor equal to the charge of an electron:

$$I = qN_{\mathrm{ex}} = qN_{\mathrm{inc},\lambda_{\mathrm{g}}} - qN_{\mathrm{cell},\lambda_{\mathrm{g}}} \tag{70}$$

where I is the current output of the solar cell.

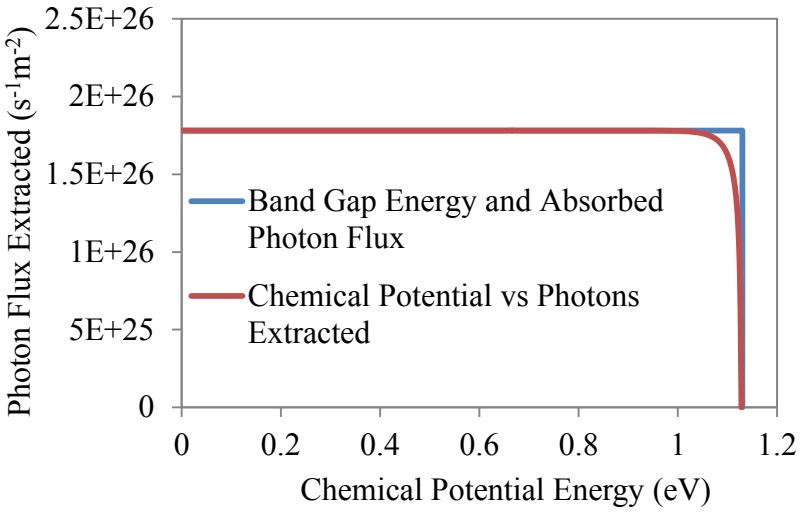

Figure 19 Relationship between the chemical potential of the emitted photon flux and the extracted photon flux for maximum solar concentration.

Work by Einstein (1917) indicates that the -1 in the denominator of the generalised Planck's law (i.e. Equation (10)) is due to stimulated emission i.e. the reverse of stimulated absorption wherein emission is stimulated by a photon. For low solar concentration, stimulated emission can be neglected since the population of electrons in the excited state is small and therefore the amount of stimulated emission will also be small. This approximation leads to the so called Boltzmann's approximation:

$$I \cong qN_{\text{inc},\lambda_g} - \exp\left(\frac{qV_q}{kT_{\text{cell}}}\right) qN_{\text{cell},\lambda_g,\mu_{\text{cell}}=0} \tag{71}$$

where $N_{\text{cell},\,\lambda_g,\mu_{\text{cell}}=0}$ is the emission by the solar cell at a chemical potential equal to 0.The short circuit current, I_{sc}, can be obtained by setting the voltage equal to zero:

$$I_{sc} = q\left(N_{\text{inc},\,\lambda_g} - N_{\text{cell},\,\lambda_g,\mu=0}\right) \tag{72}$$

Defining the reverse saturation current, I_0, as follows:

$$I_0 = qN_{\text{cell},\lambda_g,\mu=0} \tag{73}$$

We can now obtain the current voltage relationship for a solar cell as given by Shockley and Queisser (1961):

$$I = I_{sc} - I_0\left(\exp\left(\frac{qV_q}{kT_{\text{cell}}}\right) - 1\right) \tag{74}$$

The maximum power point, P_{mpp}, is the power corresponding to which the product of voltage and current is maximised. The ratio between this and the incoming energy flux gives the Shockley-Queisser limit, η_{SQ}:

$$\eta_{SQ} = \frac{P_{mpp}}{P_{inc}} \tag{75}$$

Figure 20 plots the Shockley Queisser limit as a function of the band gap energy for one Sun concentration and maximum solar concentration.

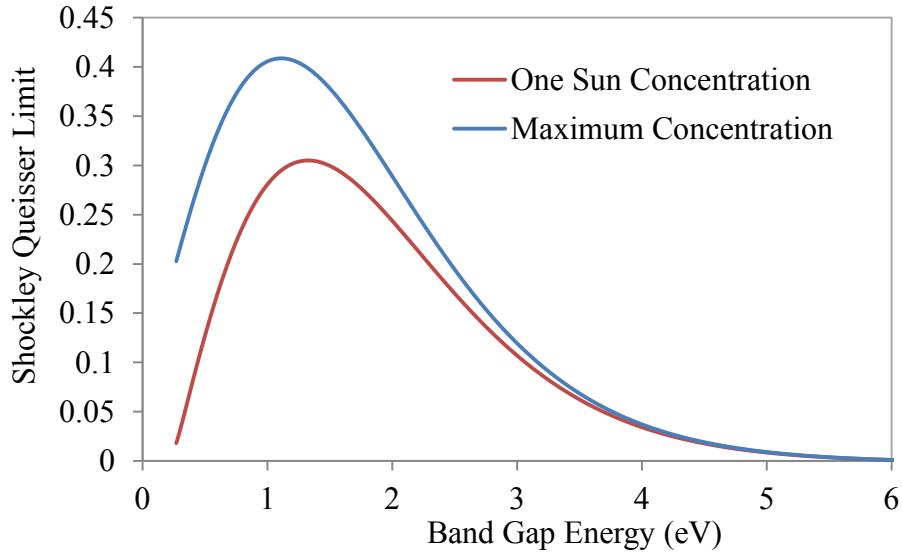

Figure 20 Shockley Queisser limit as a function of band gap energy.

3.5. Summary

This chapter has discussed the operation of solar cells, their modeling and potential in terms of power conversion efficiency. This chapter therefore serves as a general background to this thesis. Subsequent chapters will focus on specific devices i.e. fluorescent solar collectors that have the potential to deliver high efficiency, low cost solar electricity by concentrating sunlight onto solar cells.

References

Bouguer, P., 1729. *Essai d'optique, sur la graduation de la lumiere*. Chez Claude Jomber: Paris, France.

Chapin, D.M., Fuller, C.S. and Pearson, G.L., 1954. *A new silicon p-n junction photocell for converting solar radiation into electrical power*. Journal of Applied Physics. 25: 676-677. DOI: 10.1063/1.1721711.

Einstein, A., 1917. *Zur quantentheorie der strahlung*. Physikalische Zeitschrift. 18: 121-128. English translation: *On the quantum theory of radiation*. Sources of Quantum Mechanics (Van der Waerden, 1967). 63-77.

Fick, A., 1855. *On Liquid Diffusion*. Philosophical Magazine and Journal of Science. 10: 30-39.

Gray, J.L., 2003. *The physics of solar cells.* In Handbook of Photovoltaic Science and Engineering. Wiley: Chichester, UK. Chapter 3: 61-112. DOI: 10.1002/9780470974704.

Kirchhoff, G., 1860. *Ueber das Verhältniss zwischen dem Emissionsvermögen und dem Absorptionsvermögen der Körper für Wärme and Licht.* Annalen der Physik und Chemie. 109: 275–301. Translated by Guthrie, F., 1860. *On the relation between the radiating and absorbing powers of different bodies for light and heat*. Philosophical Magazine. Series 4, 20: 1–21. DOI: 10.1080/14786446008642901.

Markvart, T., 2008. *Solar cell as a heat engine: Energy-entropy analysis of photovoltaic conversion*. Physica Status Solidi. 205: 2752-2756. DOI: 10.1002/pssa.200880460.

Meyer, T.J.J. and Markvart, T., 2009. *The chemical potential of light in fluorescent solar collectors*. Journal of Applied Physics. 105: 063110 1-8. DOI: 10.1063/1.3097328.

Nelson, J., 2003. *The physics of solar cells*. Imperial College Press: London, UK. DOI: 10.1080/00107514.2012.727031.

Ohl, R.S., 1946. *Light-sensitive electric device*. U.S. Patent 2402662 A.

Perrin, F.H., 1948. *Whose absorption law?* Journal of the Optical Society of America. 38: 72-74. DOI: 10.1364/JOSA.38.000072.

Riordan, M. and Hoddeson, L., 1997. *The origins of the pn Junction*. IEEE Spectrum. 34: 46-51. DOI: 10.1109/6.591664.

Shockley, W. and Queisser H.J., 1961. *Detailed balance limit of efficiency of p-n junction solar cells*. Journal of Applied Physics. 32: 510-519. DOI: 10.1063/1.1736034.
Sze, S.M. and Ng, K.K., 2007. *Physics of semiconductor devices*. John Wiley & Sons: Hoboken, USA. DOI: 10.1002/0470068329.

Trivich, D. and Flinn, P.A., 1955. *Maximum efficiency of solar energy by quantum processes*. Solar Energy Research. Thames and Hudson: London, UK.

Wenham, S.R., Green, M.A. and Watt, M., 1994. *Applied photovoltaics*. University of New South Wales: Sydney, Australia.

Würfel, P., 1982. *The chemical potential of radiation*. Journal of Physics C: Solid State Physics. 15: 3967-3985. DOI: 10.1088/0022-3719/15/18/012.

Würfel, P., 2005. *Physics of solar cells: From principles to new concepts*. Wiley-VCH Verlag: Weinheim, Germany. DOI: 10.1002/9783527618545.

4. Review of fluorescent solar collectors

4.1. Introduction

This chapter presents a literature review of fluorescent solar collectors. The operation of different collectors such as the fluorescent edge concentrator, fluorescent down-shifting structures, concentrating fluorescent down-shifting structures and integrated photonic fluorescent solar collectors are outlined, as well as possible/popular fabrication methods and materials used. This forms the basis on which certain fabrication methods/materials were selected for this project as detailed in Chapter 7. Record efficiencies of fluorescent edge concentrators and costs have also been detailed. Major loss mechanisms in these photon management structures have also been described and the characterisation methods used to analyse these devices (such as the use of angular resolved measurements). The experimental and theoretical work that has been conducted in this project and outlined in Chapter 6 and Chapter 8 follows largely from this.

4.2. Conventional fluorescent solar collectors

4.2.1. Fluorescent edge concentrators

There are number of approaches to making cheaper solar cells. One is to reduce the cost of high efficiency solar cells and another is to concentrate light to reduce the amount of solar cell material required (Goetzberger and Wittwer, 1981). Concentration of light can be achieved using mirrors and lenses that require direct sunlight or through the use of fluorescent edge concentrators. An example of the latter is work reported by Garwin in 1960 for use in scintillators. It is a device in which light is collected from a large area and concentrated using fluorescence. Subsequent work on fluorescent edge concentrators was performed by Weber and Lambe as described in their landmark paper in 1976. They named these devices ‘luminescent greenhouse solar collectors’.

These devices operate by trapping light. Light is absorbed by the fluorescent material and is re-emitted isotropically (Garwin, 1960). Emitted photons incident on the top or bottom surface of the fluorescent edge concentrator at a zenith angle greater than the

critical angle, θ_c, will be trapped through total internal reflection and concentrated onto the edge. **Figure 21** (a) shows a typical fluorescent edge concentrator attached to a solar cell.

The use of fluorescent edge concentrators for solar electricity generation has a number of advantages. These devices reduce the amount of solar cells used and can concentrate both direct and diffuse light. There is therefore, no need to track the sun. Furthermore, in central and northern Europe around 50% of the light energy is diffuse (Mallinson and Landsberg, 1977) favouring fluorescent edge concentrators over geometric concentrators since the latter can only concentrate direct light. Fluorescent edge concentrators also have good heat dissipation due to a large surface area. This helps keep the solar cell cooler enhancing their performance as indicated by the Shockley-Queisser efficiency limit presented in Chapter 3 (Shockley and Queisser, 1961). Fluorescent emission can also be selected to match the optimum response of a solar cell.

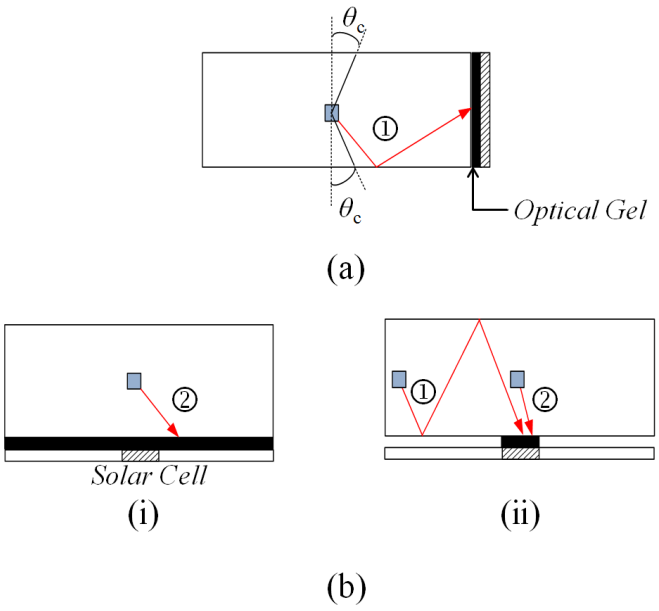

Figure 21 Comparison of different fluorescent solar collector geometries (the blue rectangle represents a fluorescent molecule): (a) an edge mounted fluorescent solar collector i.e. a fluorescent edge concentrator and (b) bottom mounted fluorescent solar collectors. The latter can be divided further into (i) a fluorescent down-shifting structure (no concentration, only wavelength shifting) and (ii) a concentrating fluorescent down-shifting structure. The different rays shown are 1) trapped fluorescence reaching the solar cell and 2) fluorescence directly reaching the solar cell/solar cell substrate.

Another advantage of fluorescent edge concentrators is that the efficiency of solar cells increases with concentration due to the corresponding increase in open circuit voltage (see Chapter 3 and Shockley and Queisser, 1961). A decrease in resistance due to the use of smaller solar cells will also improve the current voltage characteristics of the solar cell. Furthermore shadowing effects of top contacts can be removed by placing them outside the concentrator edge.

Fluorescent edge concentrators can also split incident light according to wavelength and concentrate it to different solar cells (Goetzberger and Greubel, 1977). These devices are known as multistage fluorescent edge concentrators and have the advantage of matching different wavelength regions of light to suitable band gap solar cells. The use of narrow incident wavelengths for a given solar cell allows the optimisation of the anti-reflection coating and the diffusion depth which are wavelength dependant.

Another advantage of stacking fluorescent edge concentrators in a multistage setup is that light that escapes from the top or bottom surfaces of the fluorescent edge concentrator can be recovered by an adjacent fluorescent edge concentrator (Goetzberger and Greubel, 1977).

It is difficult to compare the reported power conversion efficiencies since it depends to a large extent on the geometric gain of the system (i.e. the ratio between the fluorescent edge concentrator top surface area and the solar cell surface area). It also depends on the performance and number of solar cells attached, the use of backside reflectors etc., however it can still be useful as a rough estimate on the current state of this technology.

In the early 1980s Batchelder *et al*. (1981) claimed power conversion efficiencies between 2.5% and 3.2% for multi-dye thin films deposited on a substrate (coupled to 1 crystalline silicon (cSi) edge solar cell and 3 edge mirrors i.e. 1Cell setup). The geometric gain was equal to 11. Zastrow (1981) improved this to 4% though the use of four gallium arsenide (GaAs) edge solar cells (4Cell setup) and a stack of two single dye fluorescent edge concentrators (gain equal to 17).

These devices have seen renewed interest and some further efficiency gains within the past 6 years. Recent work by Currie *et al.* (2008) investigated the use of thin film multi-dye fluorescent edge concentrators with efficient Förster energy transfer between a dicyanomethylene and a rubrene dye. Based on the optical quantum efficiency (OQE) of these fluorescent edge concentrators the power conversion efficiencies when coupled to

gallium indium phosphide (GaInP) solar cells in the 4Cell setup were estimated to be 5.5% and 4.7% for a gain of 3 and 45 respectively.

The effect of placing this fluorescent edge concentrator in a stack with an edge concentrator containing the phosphorescent material platinum tetraphenyltetrabenzoporphyrin Pt(TPBP) was also investigated by Currie *et al.* (2008). With the second edge concentrator coupled to four GaAs edge solar cells, the power conversion efficiency for the entire system was estimated to equal 6.8% and 6.1% for a gain of 3 and 45 respectively. The OQE for both single and stacked (tandem) edge concentrators (as presented in Currie *et al.*, 2008) can be seen in Figure 22. For the stacked system it is observed that the OQE is consistently close to 60% between 400 nm and 600 nm.

Goldschmidt *et al.*, (2009a) measured a power conversion efficiency equal to 6.7% for a stack of two single dye fluorescent edge concentrators (based on BA241 dye and BA856 dye), surrounded by four GaInP solar cells. However, the gain for this device is only 0.8. Using only the BA241 fluorescent edge concentrator, the efficiency drops to 5.1% (gain equal to 1.7). Figure 23 shows the OQE of these fluorescent edge concentrators as well as others that were investigated in (Goldschmidt *et al.*, 2009a).

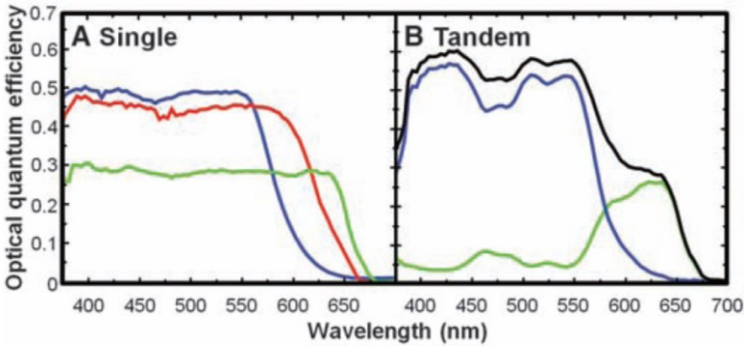

Figure 22 Optical quantum efficiency of (A) single dye fluorescent edge concentrators: dicyanomethylene fluorescent edge concentrator (blue), rubrene fluorescent edge concentrator (red) and Pt(TPBP) fluorescent edge concentrator (green) and (B) stacked systems: dicyanomethylene and rubrene fluorescent edge concentrator (blue), Pt(TPBP) fluorescent edge concentrator (green) and combined efficiency (black) (Currie *et al.*, 2008).

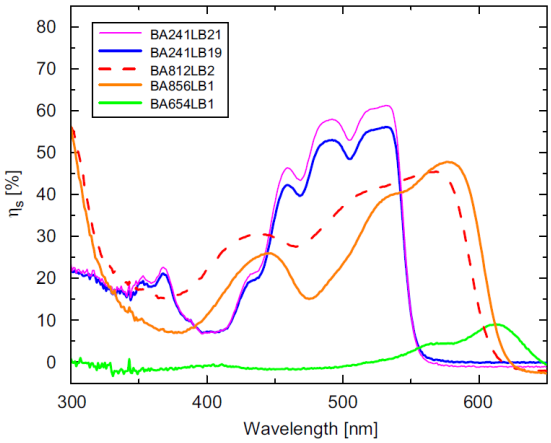

Figure 23 Optical quantum efficiencies (η_s in figure) of single dye fluorescent edge concentrators studied in Goldschmidt *et al.*, (2009a).

The perylene based dye by BASF, Lumogen F Red 305, has received considerable attention for use in fluorescent edge concentrators (Sloof *et al*., 2008) (Desmet *et al*., 2012). The fluorescent edge concentrator with the highest reported power conversion efficiency consists of a mixture of Lumogen F Red 305 and CRS040 (a coumarin dye by Radiant Color). The power conversion efficiency (gain of 2.5) when surrounded by four GaAs solar cells and a diffuse backside reflector was measured to be 7.1%. However, this includes the impact of bottom reflection of light not absorbed by the fluorescent edge concentrator, removing the backside reflector the efficiency was reported to decrease to 5.3%.

Depending on the gain used, a fair comparison would put the record power conversion efficiency (not including back reflectors etc.) of a single fluorescent edge concentrator somewhere between 4.5% and 5.5% and for a stack between 6% and 6.8%. The inclusion of back reflectors might further increase these values by a few percentages.

4.2.2. Fluorescent down-shifting structures

A number of solar cells display a poor spectral response to short wavelength light. One reason for a poor short wavelength external quantum efficiency (EQE) is that a large fraction of short wavelength light is absorbed in the top micron of the solar cell, an area that has generally a high recombination (Klampaftis et al., 2009). In certain solar cells such as those based on cadmium telluride (CdTe), the buffer/window layer consists

of cadmium sulphide (CdS) that absorbs short wavelength light. This results in a poor response to these wavelength regions.

There are two methods of improving the short wavelength response of a solar cell, the first is to improve the electronic properties of the solar cell, for example, through the use of a thinner window/buffer layer. Some improvements to the electronic properties are however expensive to implement and some of them have detrimental effects on the performance of the solar cell (Hovel et al., 1979). The second method, an early example of which is reported in (Hovel et al., 1979), is through the use of fluorescent down-shifting structures that shift incident short wavelength light to longer wavelengths where the response of the solar cell is superior. **Figure 21** (b-i) shows a typical fluorescent down-shifting structure applied on top of a solar cell.

Fluorescent down-shifting structures have been applied to a number of different solar cells including cSi (Sarti *et al*., 1981)(McIntosh *et al*, 2009), amorphous silicon (Hovel *et al*, 1979), CdS/copper sulphide (Hovel *et al*, 1979), CdS/CdTe (Maruyama and Kitamura, 2001)(Hong and Kawano, 2003) (Hong and Kawano, 2004) and copper indium gallium diselenide (CIGS) (Glaeser and Rau, 2007)(Klampaftis *et al.,*2012), an extensive list including efficiency improvements can be found in (Klampaftis *et al.,*2009).

Direct comparisons on the effect of different fluorescent down-shifting structure in different studies are, however, difficult since the enhancements observed strongly depend on the EQE of the solar cell that is used.

The advantages of fluorescent down-shifting structures is that optimisation can take place independent of the solar cell. The blue-shifting of diffuse light (Mallinson and Landsberg, 1977) also makes down-shifting even more effective.

Another advantage of fluorescent down-shifting structures is that these devices can also be incorporated into existing structures like the polymer encapsulation layer used in cSi modules (McIntosh et al., 2009).

In CdTe and CIGS based solar cells in particular, there are however some detrimental effects in using fluorescent down-shifting structures. The absorption by the CdS buffer layer in these solar cells affects its current voltage relationship (Köntges *et al.*, 2002). A lack of ultraviolet (UV) light is known to increase the energy of the conduction band in the buffer layer and therefore act as a barrier to electron transport (Pudov *et al*., 2005).

Furthermore, laboratory based solar cells now show much better response to short wavelength light, if this high performance can be transferred into large scale production the possibility of improvements using fluorescent down-shifting structures will become less.

4.2.3. Concentrating fluorescent down-shifting structures

Though fluorescent edge concentrators, as shown in **Figure 21** (a) are normally edge mounted, bottom mounted configurations similar to fluorescent down-shifting structures have also been proposed (Boling, 1980) and have been investigated for increasing the performance of cSi solar cells (Oska *et al.*, 1986) (Sakuta *et al.*, 1994) (Mansour, 2003) (Corrado *et al.*, 2013). In (Rau *et al.*, 2005) a bottom mounted fluorescent edge concentrator was considered when calculating the efficiency limit of fluorescent edge concentrators for different band gap solar cells. The advantage of such a configuration is that it ensures that concentration onto the solar cell acts to augment the performance of directly excited solar cells. It has also been suggested that these devices could be suitable for building integrated systems and recent calculations indicate a reduction in the cost/watt of such systems coupled to cSi to be around 28% (Corrado *et al.*, 2013).

The concept of fluorescent down-shifting structure and bottom mounted fluorescent edge concentrators can be taken one step further with concentrating fluorescent down-shifting structure that simultaneously improves the short wavelength response of, for example, CdTe/CdS solar cells and also concentrate light. A schematic is shown in **Figure 21** (b-ii).

A concentrating fluorescent down-shifting structure has a number of key advantages. These structures can be used to collect light from regions where, for example, shading due to front contacts or gaps between modules prevents capture of solar energy. Additionally, the poor short wavelength response found in many solar cells is simultaneously improved. This offers the possibility of achieving higher efficiencies on existing solar cell devices.

Furthermore, in central and northern Europe around 50% of the solar energy reaching the ground is diffuse (Mallinson and Landsberg, 1977). A concentrating fluorescent down-shifting structure can concentrate diffuse light unlike geometric concentrators and the high content of blue light in diffuse radiation enhances the effect of wavelength shifting. Concentrating fluorescent down-shifting structures therefore benefit from

advantages of both fluorescent edge concentrators and fluorescent down-shifting structures.

An early investigation into concentrating fluorescent down-shifting structures for application to cSi solar cell is presented in (Sarti *et al.*, 1981). The concept of combining spectral matching with solar concentration for cSi solar cells was further developed in (Lifante *et al.*, 1983). In (Lifante *et al.*, 1983) a theoretical model was developed to describe concentration of light (using back scattering) onto a bottom mounted solar cell and the results were compared to experiments. The addition of fluorescent molecules to the device to incorporate spectral matching was investigated experimentally but the model was not extended to include this additional complexity.

More recently in (Semichaevsky *et al.*, 2011) the technique of combining spectral matching and light concentration was used to concentrate as well as shift photons to the low reflectivity region of a silicon microcell array. Simultaneous use of light concentration and spectral matching has also been shown to increase the current output of a photo-electro-chemical cell attached to one edge of a liquid concentrating fluorescent down-shifting structure (Muller and Manassen, 1983). However, to our knowledge the application of a fluorescent down-shifting structure to CdTe/CdS has not been investigated previously.

A number of studies have, however, investigated fluorescent down-shifting structures incorporated into module encapsulation layers slightly larger than the solar cell active area. This has been undertaken for different solar cells such as cSi (McInosh *et al.*, 2009) and CIGS (Glaeser and Rau, 2007) (Klampaftis *et al.*, 2012). Also, in (Maruyama and Kitamura., 2001) for example, a fluorescent down-shifting structure applied on a slightly smaller CdS/CdTe solar cell was investigated. However, even though there might be some concentration of light due to the differences in sizes between the solar cell and the fluorescent down-shifting structure in these devices, these studies were focused on the wavelength shifting property of fluorescent solar collectors.

4.2.4. Losses in conventional fluorescent solar collectors

There are a number of sources of loss in conventional fluorescent solar collectors. A major loss mechanism in these devices is escape of fluorescence from surfaces not coupled to mirrors or solar cells. This escape cone loss consists of fluorescence incident at an interface below the critical angle. The escape solid angle consists of a cone with its

apex angle equal to twice the critical angle. Re-absorption (or self absorption) of fluorescence increases the top and bottom escape cone losses in fluorescent edge concentrators since each re-absorption event results in more photons being emitted out of the device as indicated by the theory developed in (Weber and Lambe, 1976) and (Batchelder *et al*., 1979) (to be discussed in detail in Chapter 5).

Other loss mechanisms include additional reflection on the solar cell surface. The isotropic emission by fluorescent molecules results in an increase in the average angle of incidence of light hitting the solar cell, large angles of incidence have been seen to result in a larger reflectance (Parretta et al., 1999). There can also be losses due to scattering of light and parasitic losses due to absorption by the host material (Klampaftis et al., 2009). The increase in gain due to the application of a collector needs to, therefore compensate for all these losses.

Angular measurements of the photon flux/fluorescence escaping the edge of fluorescent solar collectors have previously been measured in (Goldschmidt *et al.,* 2008)(Bendig *et al.,* 2008)(Goldschmidt, 2009b)(Sträter *et al.,* 2011) to determine angles of emission corresponding to the greatest loss of photons. A cylindrical lens coupled to the collector edge in (Goldschmidt *et al.,* 2008) (Bendig *et al.,* 2008) and (Goldschmidt, 2009b) was used to 'see' inside these structures. Monte Carlo simulations of the photon flux exiting the fluorescent solar collector edge were also presented in these publications. In (Sträter *et al.,* 2011) the collector edge was not coupled to a lens and a simple numerical model that qualitatively explains fringe-like patterns detected for spot illumination was presented. However, to our knowledge, angular resolved measurements and modelling of fluorescent solar collectors with edges coupled to solar cells/mirrors has not been previously reported. Studying photon flux streams of fluorescent solar collectors with edges coupled to solar cells/mirrors is critical since this is how collectors for photovoltaic applications are used in operation.

4.3. Integrated photonic fluorescent solar collectors

The incorporation of photonics structures to fluorescent solar collectors in order to decrease the escape cone loss was recently proposed (see for example, Richards *et al.*, 2004) and the potential of these devices was quantified in (Rau *et al.*, 2005) and (Markvart, 2006). The devices considered in these studies consisted of a photonic band stop filter placed on top of a fluorescent solar collector. The filter is tuned so as to

reflect at the emission wavelengths of the collector and transmit at its absorptions wavelengths. Indeed, the detailed balance efficiency limit of fluorescent solar collectors with photonic filters on top has been calculated to be 26.8% when coupled to silicon solar cells (Markvart, 2006, to be described in detail and expanded upon in Chapter 6) i.e. 90% of the Shockley-Queisser efficiency limit for silicon solar cells (Shockley and Queisser, 1961, see Chapter 3). Experimental work has also demonstrated efficiency enhancements in practical devices (Glaeser and Rau, 2006)(Goldshmidt *et al.*, 2008).

A related but more advanced concept which will be referred to as an integrated photonic fluorescent solar collector (Goldschmidt *et al.*, 2010) is also being considered as a method of improving the efficiency of collectors even further. These devices combine the concepts of photonic crystals and photon management structures into an integrated device i.e. a photonic crystal doped with fluorescent molecules. The modification of the density of states in these devices and concentration of the electric field at certain positions is expected to result in the suppression of emission in certain directions and frequencies and enhancement at other directions and frequencies. This property could be utilised to increase the efficiency of fluorescent solar collectors by not only decreasing the escape cone loss but by also increasing the quantum yield (i.e. probability that photon absorption will result in emission), absorption and emission properties of the fluorescent molecules. Directional emission would also decrease the parasitic absorption losses and quantum yield losses (due a decrease in re-absorption).

Designs suggested in Goldschmidt *et al.* (2010) include doping photonic fibers with fluorescent molecules (Figure 24 (b)) and also embedding fluorescent molecules in three dimensional photonic crystals i.e. opaline films that form three dimensional photonic crystals (Figure 24 (c)).

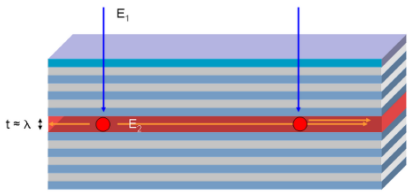

(a)

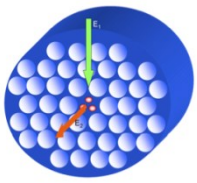

(b)

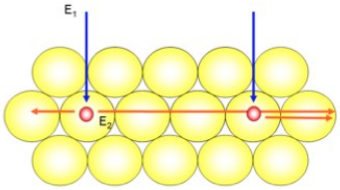

(c)

Figure 24 (a) 1D, (b) 2D and (c) 3D integrated photonic fluorescent solar collectors (Goldschmidt *et al.*, 2010).

There has been some interest in 2D integrated photonic fluorescent solar collectors (Rousseau and Wood, 2013) and 3D integrated photonic collectors have already been fabricated and characterized in (Gutmann *et al.*, 2012).

A 1D integrated photonic fluorescent solar collector (Figure 24 (a)) is, however, more suitable for solar concentration application since suppression of emission in all directions is not desirable as photons need to be collected by an edge mounted solar cell. However, to our knowledge there have been no publications on the fabrication and characterisation of these devices.

4.4. Materials for fluorescent solar collectors

Fluorescent solar collectors consist of fluorescent molecules dissolved within a host material. There are a number of different host materials that can be used to make these devices as well as a range of different types of fluorescent molecules. This section compares different host materials and fluorescent molecules used in collectors and the classification of these photon management structures.

4.4.1. Host

The requirements for a good host material for fluorescent solar collectors include low scattering of light, high transparency, suitability for dissolving luminescent species and good photo-stability over manufacturing and the lifetime of the solar cell (Klampaftis et al., 2009).

Widely used host materials include poly(methyl methacrylate) (PMMA) (Maruyama *et al.*, 2000), polyvinyl acetate (Marchionna *et al*., 2006) and inorganic crystalline materials such as aluminium oxide (Hovel *et al*., 1979) or calcium fluoride (Kawano *et al.*, 1997a). Various glass types (see for example Kawano *et al*. 1997b), organic molecule silicates (Li *et al*., 2000) and organic paint thinners (Maruyama *et al.*, 1998) have also been previously doped with fluorescent molecules.

Advantages of polymeric materials include suitability as a host for organic dye molecules (Hovel *et al*., 1979) and the use of UV stabilisers and absorbers can increase stability over extended periods (Czanderna and Pern, 1996). Crystalline materials have good photo-stability and also show high transparency. However they are expensive and difficult to process (Klampaftis et al., 2009).

4.4.2. Luminescent species

Requirements for suitable fluorescent molecules for fluorescent solar collectors includes high luminescent quantum yields, wide absorption bands, large absorption coefficients, small overlap between absorption and emission (to reduce re-absorption), low cost and good photo-stability. The three main types of luminescent materials that can be used are quantum dots, organic dyes and rare-earth ion complexes (Klampaftis et al., 2009).

Quantum dots are nano-sized semiconductors. Their absorption and emission wavelengths can be tuned according to their size (Kongkanand *et al.*, 2008). They generally display wide absorption bands and good photo-stability. Drawbacks include poor fluorescence quantum yields and high costs.

The second type of luminescent material is organic dyes. These dyes have been associated with a number of issues such as poor photo-stability (Goetzberger and Wittwer, 1981), narrow absorption bands and high re-absorption (Rowan et al., 2008). The use of multiple dyes with energy transfer can however improve the absorption bandwidth and Stokes shift (see for example, Swartz *et al.*, 1977) and recent progress has also resulted in organic dyes that have good photo-stability (Rowan et al., 2008). Organic dyes also are easy to process in a polymeric matrix and have high quantum yields (Seybold and Wagenblast, 1988). Also, there is a large selection of organic dyes available to choose from (Goetzberger and Wittwer, 1981).

Rare earth luminescent species can have high fluorescence quantum yields but low absorption coefficients (Rowan *et al*., 2008). The absorption coefficient can however be improved by using higher concentrations or through the use of antenna structures with high absorption and good energy transfer to the rare earth ion. Furthermore they do not show stability problems (Goetzberger and Wittwer, 1981).

4.4.3. Classification of fluorescent solar collectors

Fluorescent solar collectors can either be made from organic or inorganic fluorescent materials doped in either a liquid or solid state host (Goetzberger and Wittwer, 1981).

Solid inorganic collectors consist of rare earth or uranium doped in glass. In solid organic fluorescent collectors, host materials like PMMA can be used with organic dyes.

Organic-inorganic collectors consist of glass with a thin layer of highly concentrated organic fluorescent dyes (Rapp and Boling, 1978). Doped thin film layers deposited on glass in which fluorescence is trapped in the glass substrate has the advantage over bulk doped plates of lower re-absorption and scattering due to impurities (Reisfeld *et al.*,1994).

Liquid fluorescent solar collectors consist of organic fluorescent dyes dissolved in liquid, placed in between transparent plates. This allows the fluorescent dyes to be drained and replaced if performance deteriorates. Fluorescent molecules are however less stable in liquid than solid medium due to easier chemical reactions and these

collectors are also thick due to the container resulting in lower edge concentration (Goetzberger and Wittwer, 1981).

4.5. Fabrication

4.5.1. Conventional fluorescent solar collectors

Fabrication methods of fluorescent solar collectors include spin coating (Rapp and Boling, 1978), casting (Bakr *et al.*, 1999) and thermal evaporation (Currie *et al.*, 2008). In (Rapp and Boling, 1978) and (Currie *et al.*, 2008) spin coating and thermal evaporation were used for depositing organic fluorescent layers on inorganic substrates (i.e. glass) while moulding is often used to dope organic fluorescent molecules in an organic host material like poly(methyl methacrylate). Spin coating consists of depositing a fluorescent solution onto a substrate and rotating at a fixed speed. The rotational speed determines the thickness of the fluorescent layer deposited on top of the substrate. Casting is achieved by solidifying the fluorescent solution within a mould. Solidification is triggered for example by the application of heat or UV radiation and the addition of suitable catalysts. The highest efficiency edge concentrators fabricated were made using thermal evaporation (Currie *et al.*, 2008) and moulding (Sloof *et al*., 2008) (Goldschmidt *et al.*, 2009a). Both of these fabrication methods should therefore result in high quality collectors. Spin coated edge concentrators have, however, been seen to suffer from losses due to scattering (Soleimani *et al.*, 2012). One advantage of thermal evaporation is that it is more suitable for enabling energy transfer between different fluorescent species since the thin film layers are highly concentrated and therefore the fluorescent molecules are very close to each other. Moulded collectors, however, can avoid negative effects of high concentration such as formation of dye aggregates but can still maintain a large absorbance due to their larger thickness.

4.5.2. Integrated photonic fluorescent solar collector

Fabrication of a 3D integrated photonic fluorescent solar collector from PMMA colloids was reported in (Gutmann *et al.*, 2012). Rhodamine B was incorporated within the polymerisation process in order to dope the photonic crystal. On characterisation of

the device, anisotropic emission was detected, however, the results indicated that the performance of the device suffered possibly due to cracks and defects in the photonic crystal

Techniques such as Langmuir Blodgett (LB) deposition (Danos *et al.*, 2008) have also been successfully used to deposit thin film organic fluorescent dyes on a substrate and might be suitable for making integrated photonic based photon management structures. Indeed, 3D photonic crystals have been fabricated using the LB technique (Reculusa and Ravaine, 2003).

Rugate filters consist of structures with a continuous variation in the refractive index leading to high reflectance at certain wavelength ranges. Carr *et al.* (1991) reported the fabrication of a Rugate filter using LB films using organic molecules. The patent filed by the authors (Carr *et al.,* 1991) states that peak reflection can be increased to close to 100% by increasing the thickness of the filter to over 10 μm, though this is also expected to result in increases in scattering.

The major challenge in the fabrication of photonic crystals using the LB techniques lies in the synthesis of the appropriate organic molecules. The LB technique can only be used to deposit so called amphiphilic molecules. These molecules consist of a hydrophobic tail and a hydrophilic head. The deposition of a LB film requires the amphiphilic molecule to be dissolved in a solvent and then mixed with water. On evaporation of the solvent if the hydrophobic and hydrophilic forces balance each other, a monolayer will form on the surface of the water. Dipping a substrate in this water will attach this monolayer to the substrate. This process can be repeated to build thicker layers.

One possible method of fabricating 1D integrated photonic fluorescent solar collectors would be by spin coating sol gel solutions of silicon dioxide (SiO_2) and titanium dioxide (TiO_2). Reports in the literature (Biswas et al., 1987) (Almeida and Wang, 2002) indicate that SiO_2 deposited by spin coating SiO_2 sol gel solution has successfully been used in multilayer structures with TiO_2. Furthermore, recently published results indicate that it is possible to dope BASF Red 305 fluorescent dye (a commonly used dye for fluorescent solar collector applications) into SiO_2 sol gel solution (Reisfeld *et al.*, 2012).

In Löffler *et al.* (2012) it was also suggested that it would be possible to fabricate a 1D integrated photonic collector by depositing alternating layers of TiO_2 (sol gel) and fluorescent dye doped PMMA (dissolved in toluene) by spin coating. Another suggested

method was to sandwich a fluorescent layer in between Bragg stacks containing SiO_2 and silicon nitride. The Bragg stacks could be fabricated, for example, by plasma enhanced chemical vapour deposition.

Evaporation can also be applied to make both organic and inorganic thin films. Thermal evaporation, as mentioned, has been used rather successfully by Currie *et al.* (2008) to create high efficiency fluorescent edge concentrators, this technique has also been proven to be effective in the fabrication of Bragg reflectors using relatively simple compounds (Zenou *et al.*, 2006). If the high temperature processing of inorganic layers is seen to destroy the fluorescent properties of organic dyes, inorganic fluorescent materials such as rare earth ions could be considered.

4.6. Summary

This chapter has given an overview of progress on fluorescent solar collector research. Based on this, in Chapter 6, Chapter 7 and Chapter 8, certain important areas of research of collectors that has not been addressed have been pursued. This includes investigation (modelling and experimental) of the 4Cell (fluorescent edge concentrator) setup for which the highest power conversion efficiencies have been reported. The application of concentrating fluorescent down-shifting structure to CdTe will also be investigated since these solar cells greatly benefit from wavelength shifting. The introduction of light concentration is also expected to augment the solar cell current output further.

To our knowledge the nature of emission in 1D integrated photonic fluorescent solar collectors has also not been demonstrated experimentally, therefore this will also be investigated in Chapter 7 and Chapter 8.

References

Almeida, R.M. and Wang, Z., 2002. *Sol-gel preparation of one-dimensional photonic bandgap structures.* Proceedings of SPIE Photonic Bandgap Materials and Devices. 4655: 24-33. DOI: 10.1117/12.463898.

Bakr, N.A., Mansour, A.F. and Hammam, M., 1999. *Optical and thermal spectroscopic studies of luminescent dye dope poly(methyl methacrylate) as solar concentrator.*

Journal of Applied Polymer Science. 74: 3316-3323. DOI: 10.1002/(SICI)1097-4628(19991227)74:14<3316::AID-APP4>3.0.CO;2-U.

Batchelder, J. S., Zewail, A. H. and Cole, T., 1979. *Luminescent solar concentrators. 1: Theory of operation and techniques for performance evaluation*. Applied Optics. 18: 3090-3110. DOI: 10.1364/AO.18.003090.

Batchelder, J. S., Zewail, A. H. and Cole, T., 1981. *Luminescent solar concentrators 2: Experimental and theoretical analysis of their possible efficiencies*. Applied Optics. 20: 3733-3754. DOI: 10.1364/AO.20.003733.

Bendig, M., Hanika, J., Dammertz, H., Goldschmidt, J.C., Peters, M. and Weber, M., 2008. *Simulation of fluorescent concentrators*. IEEE Symposium on Interactive Ray Tracing. August 9-10, Los Angeles, USA. DOI: 10.1109/RT.2008.4634628.

Biswas, P.K., Kundu, D. and Ganguli, D., 1987. *Preparation of wavelength-selective reflectors by sol-gel processing*. Journal of Materials Science Letters. 6: 1481-1482. DOI: 10.1007/BF01689330.

Boling, N.L., 1980. *Luminescent solar collector structure*. United States Patent 4190465 A.

Carr, N., Goodwin, M., Harrison, K.J. and Lewis, K.L, 1991. *Optical filters*. European Patent 0445268 A1.

Czanderna, A.W. and Pern, F.J., 1996. *Encapsulation of PV modules using ethylene vinyl acetate copolymer as a pottant: A critical review.* Solar Energy Materials and Solar Cells. 43: 101-181. DOI: 10.1016/0927-0248(95)00150-6.

Corrado, C., Leow, S.W., Osborn, M., Chan, E., Balaban, B. and Carter, S.A., 2013. *Optimization of gain and energy conversion efficiency using front-facing photovoltaic cell luminescent solar concentrator design*. Solar Energy Materials and Solar Cells. 111: 74-81. DOI: 10.1016/j.solmat.2012.12.030.

Currie, M.J., Mapel, J.K., Heidel, T.D., Goffri, S. and Baldo M.A., 2008. *High efficiency organic solar concentrators for photovoltaics*. Science. 321: 226-228. DOI: 10.1126/science.1158342.

Danos, L., Greef, R. and Markvart, T., 2008. *Efficient fluorescence quenching near crystalline silicon from Langmuir-Blodgett dye films*. Thin Solid Films. 516: 7251-7255. DOI: 10.1016/j.tsf.2007.12.103.

Desmet, L., Ras, A.J.M., de Boer, D.K.G. and Debije, M.G., 2012. *Monocrystalline silicon luminescent solar concentrator with 4.2% power conversion efficiency.* Optics Letters. 37: 3087-3089. DOI: 10.1364/OL.37.003087.

Garwin, R.L., 1960. *The collection of light from scintillation counters*. Review of Scientific Instruments. 31: 1010-1011. DOI: 10.1063/1.1717105.

Glaeser, G.C. and Rau, U., 2006. *Collection properties of photovoltaic fluorescent systems - simulations and experiments*. IEEE 4th World Conference on Photovoltaic Energy Conversion. 1: 205-208. May 7-12, Waikoloa, Hawaii, USA. DOI: 10.1109/WCPEC.2006.279418.

Glaeser, G.C. and Rau, U., 2007. *Improvement of photon collection in Cu(In,Ga)Se_2 solar cells and modules by fluorescent frequency conversion*. Thin Solid Films. 515: 5964-5967. DOI: 10.1016/j.tsf.2006.12.142.

Goetzberger, A. and Greubel, W., 1977. *Solar energy conversion with fluorescent collectors*. Applied Physics. 14: 123-139. DOI: 10.1007/BF00883080.

Goetzberger, A. and Wittwer, V., 1981. *Fluorescent planar collector-concentrators: A review*. Solar Cells. 4: 3-23. DOI: 10.1016/0379-6787(81)90033-8.

Goldschmidt, J.C., Peters, M., Prönneke, L., Steidl, L., Zentel, R., Bläsi, B., Gombert, A., Glunz, S., Willeke, G. and Raa, U., 2008. *Theoretical and experimental analysis of*

photonic structures for fluorescent concentrators with increased efficiencies. Physica Status Solidi A. 205: 2811-2821. DOI: 10.1002/pssa.200880456.

Goldschmidt, J. C., Peters, M., Bösch, A., Helmers, H., Dimroth, F., Glunz, S. W. and Willeke, G., 2009a. *Increasing the efficiency of fluorescent concentrator systems*. Solar Energy Materials and Solar Cells. 93: 176–182. DOI: 10.1016/j.solmat.2008.09.048.

Goldschmidt, J.C., 2009b. *Novel Solar Cell Concepts*. Verlag Dr. Hut, München.

Goldschmidt, J.C., Peters, M., Gutmann, J., Steidl, L., Zentel, R., Bläsi, B. and Hermle, M., 2010. *Increasing fluorescent concentrator light collection efficiency by restricting the angular emission characteristic of the incorporated luminescent material: the 'nano-fluko' concept.* Proceedings of SPIE Photonics for Solar Energy Systems III. April 13-15, Brussels, Belgium. 7725: 0S1-0S11. DOI: 10.1117/12.854278.

Gutmann, J., Posdziech, J., Peters, M., Steidl, L., Zentel, R., Zappe, H. and Goldschmidt, J.C., 2012. *Emission of rhodamine B in PMMA opals for luminescent solar concentrators.* Proceedings of SPIE. 8438: 843810 1-7. DOI: 10.1117/12.922681.

Hong, B. and Kawano, K., 2003. *PL and PLE studies of $KMgF_3$:Sm crystal and the effect of its wavelength conversion on CdS/CdTe solar cell*. Solar Energy Materials and Solar Cells. 80: 417-432. DOI: 10.1016/j.solmat.2003.06.013.

Hong, B. and Kawano, K., 2004. *Organic dye-doped thin films for wavelength conversion and their effects on the photovoltaic characteristics of CdS/CdTe solar cell*. Japanese Journal of Applied Physics. 43: 1421-1426. DOI: 10.1143/JJAP.43.1421.

Hovel, H.J., Hodgson, R.T. and Woodall, J.M., 1979. *The effect of fluorescent wavelength shifting on solar cell spectral response*. Solar Energy Materials. 2: 19-29. DOI: 10.1016/0165-1633(79)90027-3.

Kawano, K., Hashimoto, N. and Nakata, R., 1997a. *Effects on solar cell efficiency of fluorescence of rare-earth ions.* Materials Science Forum. 239-241: 311-314. DOI: 10.4028/www.scientific.net/MSF.239-241.311.

Kawano, K., Arai, K., Yamada, H., Hashimoto, N. and Nakata, R., 1997b. *Application of rare_earth complexes for photovoltaic precursors.* Solar Energy Materials and Solar Cells. 48: 35-41. DOI: 10.1016/S0927-0248(97)00066-4.

Klampaftis, E., Ross, D., McIntosh, K.R. and Richards, B.S., 2009. *Enhancing the performance of solar cells via luminescent down-shifting of the incident spectrum: A review*. Solar Energy Materials and Solar Cells. 93: 1182-1194. DOI: 10.1016/j.solmat.2009.02.020.

Klampaftis, E., Ross, D., Seyrling, D., Tiwari, A.N. and Richards, B.S., 2012. *Increase in short-wavelength response of encapsulated CIGS devices by doping the encapsulation layer with luminescent material.* Solar Energy Materials and Solar Cells. 101: 62-67. DOI: 10.1016/j.solmat.2012.02.011.

Kongkanand, A., Tvrdy, K., Takechi, K., Kuno, M. and Kamat, P.V., 2008. *Quantum dot solar cells. Tuning photorepsonse through size and shape control of CdSe-TiO architecture.* Journal of the American Chemical Society. 130: 4007-4015. DOI: 10.1021/ja0782706.

Köntges, M., Reineke-Koch, R., Nollet, P., Beier, J., Schäffler, R. and Parisi, J., 2002. *Light induced changes in the electrical behaviour of CdTe and Cu(In,Ga)Se_2 solar cells*. Proceeding of Symposium of Thin Film Materials for Photovoltaics. 403-404: 280-286. DOI: 10.1016/S0040-6090(01)01507-3.

Li, H., Inoue, S., Ueda, D., Machida, K. and Adachi, G., 2000. *ORMOSIL composite phosphors incorporated with lanthanide complexes.* Bulletin of the Chemical Society of Japan. 73: 251-258. DOI: 10.1246/bcsj.73.251.

Lifante, G., Cusso, F., Meseguer, F. and Jaque, F., 1983. *Solar concentrators using total internal reflection*. Applied Optics. 22: 3966-3970. DOI: 10.1364/AO.22.003966.

Löffler, J., Gutmann, J. and Goldschmidt, J.C., 2012. *Fabrication of one-dimensional photonic crystals for luminescent solar concentrators.* Optics for Solar Energy. November 11-14, Eindhoven, Netherlands. DOI: 10.1364/OSE.2012.ST2A.5.

Mallinson, J.R. and Landsberg, P.T., 1977. *Meteorological effects on solar cells*. Proceedings of the Royal Society London A. 355: 115-130. DOI: 10.1098/rspa.1977.0089.

Mansour, A.F., 2003. *On enhancing the efficiency of solar cells and extending their performance life*. Polymer Testing. 22: 491-495. DOI: 10.1016/S0142-9418(02)00055-7.

Marchionna, S., Meinardi, F., Acciarri, M., Binetti, S., Papagni, A., Pizzini, S., Malatesta, V. and Tubino, R., 2006. *Photovoltaic quantum efficiency enhancement by light harvesting of organo-lanthanide complexes.* Journal of Luminescence. 118: 325-329. DOI: 10.1016/j.jlumin.2005.09.010.

Markvart, T., 2006. *Detailed balance method for ideal single-stage fluorescent collectors.* Journal of Applied Physics. 99: 026101 1-3. DOI: 10.1063/1.2160710.

Maruyama, T., Shinyashiki, Y. and Osaka, S., 1998. *Energy conversion efficiency of solar cells coated with fluorescent coloring agent.* Solar Energy Materials and Solar Cells. 56: 1-6. DOI: 10.1016/S0927-0248(98)00105-6.

Maruyama, T., Enomoto, A. and Shirasawa, K., 2000. *Solar cell module colored with fluorescent plate*. Solar Energy Materials and Solar Cells. 64: 269-278. DOI: 10.1016/S0927-0248(00)00227-0.

Maruyama, T. and Kitamura, R., 2001. *Transformation of the wavelength of the light incident upon CdS/CdTe solar cells*. Solar Energy Materials and Solar Cells. 69: 61-68. DOI: 10.1016/S0927-0248(00)00373-1.

McIntosh, K.R., Lau, G., Cotsell, J.N., Hanton, K., Bätzner, D.L., Bettiol, F. and Richards, B.S., 2009. *Increase in external quantum efficiency of encapsulated silicon solar cells from a luminescent down-shifting layer*. Progress in Photovoltaics: Research and Applications. 17: 191-197. DOI: 10.1002/pip.867.

Muller, N. and Manassen, J., 1983. *Fluorescent window as wavelength shifter for a polysulfide containing photoelectrochemical cell*. Solar Energy Materials. 9: 207-216. DOI: 10.1016/0165-1633(83)90044-8.

Oska, T., Hamalainen, M., Saarinen, P. and Harkonen, J., 1986. *A modified luminescent solar concentrator.* Proceedings of SPIE Optical Materials Technology for Energy Efficiency and Solar Energy Conversion V. Innsbruck, Austria. 0653: 114-118. DOI: 10.1117/12.938317.

Parretta, A., Sarno, A., Tortora P., Yakuba, H., Maddalena, P., Zhao, J. and Wang, A., 1999. *Angle-dependant reflectance measurements on photovoltaic materials and solar cells*. Optics Communications. 172: 139-151. DOI: 10.1016/S0030-4018(99)00561-1.

Pudov, A.O., Sites, J.R., Contreras, M.A., Nakada, T. and Schock, H.W., 2005. CIGS J-V *distortion in the absence of blue photons*. Thin Solid Films. 480-481: 273-278. DOI: 10.1016/j.tsf.2004.11.099.

Rau, U.， Einsele, F. and Glaeser, G.C. 2005. *Efficiency limits of photovoltaic fluorescent collectors*. Applied Physics Letters. 87: 171101 1-3. DOI: 10.1063/1.2112196.

Rapp, C.F. and Boling, N.L., 1978. *Luminescent solar concentrators*. Proceedings of the 13th Photovoltaic Specialists Conference. June 5-8, Washington, USA. 690-693.

Reculusa. S. and Ravaine, S., 2003. *Synthesis of colloidal crystals of controllable thickness through the Langmuir-Blodgett technique.* Chemistry of Materials. 15: 598-605. DOI: 10.1021/cm021242w.

Reisfeld, R., Shamrakov, D. and Jorgensen, C., 1994. *Photostable solar concentrators based on fluorescent glass films*. Solar Energy Materials and Solar Cells. 33: 417-427. DOI: 10.1016/0927-0248(94)90002-7.

Reisfeld, R., Levchenko, V., Saraidarov, Ts., Rysiakiewicz-Pasek, E., Barnowski, M., Podhorodecki, A., Misiewicz, J. and Antropova, T., 2012. *Steady state and femtosecond spectroscopy of perylimide red dye in porous and sol-gel glasses.* Chemical Physical Letters. 546: 171-175. DOI: 10.1016/j.cplett.2012.07.073.

Richards, B.S., Shalav, A. and Corkish, R.P., 2004. *A low escape-cone-loss luminescent solar concentrator.* Proceedings of the 19th European Photovoltaics Solar Energy Conference. June 7 -11, Paris, France. 113-116.

Rowan, B.C., Wilson, L.R. and Richards, B.S., 2008. *Advanced material concepts for luminescent solar concentrators.* IEEE Journal of Selected Topics in Quantum Electronics. 14: 1312-1322. DOI: 10.1109/JSTQE.2008.920282.

Sakuta, K., Sawata, S. and Tanimoto, M., 1994. *Luminescent concentrator module of a practical size*. First World Conference on Photovoltaic Energy Conversion. December 5-9, Hawaii, USA. 1: 1115-1118. DOI: 10.1109/WCPEC.1994.520157.

Sarti, D., Le Poull, F. and Gravisse, Ph., 1981. *Transformation du rayonnement solaire par fluorescence: Application a l'encapsulation des cellules*. Solar Cells. 4: 25-35. DOI: 10.1016/0379-6787(81)90034-X.

Semichaevsky, A.V., Johnson, H.T., Yoon, J., Nuzzo, R.G., Li, L. and Rogers, J., 2011. *Theory for optimal design of waveguiding light concentrators in photovoltaic microcell arrays*. Applied Optics. 50: 2799-2808. DOI: 10.1364/AO.50.002799.

Seybold, G. and Wagenblast, G., 1989. *New perylene and violanthrone dyestuffs for fluorescent collectors.* Dyes and Pigments. 4: 303-317. DOI: 10.1016/0143-7208(89)85048-X.

Shockley, W. and Queisser H.J., 1961. *Detailed balance limit of efficiency of p-n junction solar cells*. Journal of Applied Physics. 32: 510-519. DOI: 10.1063/1.1736034.

Sloof, L.H., Bende, E.E., Burgers, A.R., Budel, T., Pravettoni, M., Kenny, R.P., Dunlop, E.D. and Büchtemann, A., 2008. *A luminescent solar concentrator with 7.1% efficiency*. Physica Status Solidi - Rapid Research Letters. 2: 257-259. DOI: 10.1002/pssr.200802186.

Soleimani, N., Knabe, S., Bauer, G.H., Markvart, T. and Muskens, O.L., 2012. *Role of light scattering in the performance of fluorescent solar collectors.* Journal of Photonics for Energy. 2: 021801 1-10. DOI: 10.1117/1.JPE.2.021801.

Sträter, H., Knabe, S., Meyer, T.J.J. and Bauer, G.H., 2011. *Spectrally and angle-resolved emission of thin film fluorescence collectors.* Progress in Photovoltaics: Research and Applications. 21: 554-560. DOI: 10.1002/pip.1228.

Swartz, B.A., Cole, T. and Zewail, A.H., 1977. *Photon trapping and energy transfer in multiple-dye plastic matrices. An efficient solar-energy concentrator.* Optical Letters. 1: 73-75. DOI: 10.1364/OL.1.000073.

Weber, W. H. and Lambe, J., 1976. *Luminescent greenhouse collector for solar radiation*. Applied Optics. 15: 2299-2300. DOI: 10.1364/AO.15.002299.

Zastrow, A., 1981. *Physikalische analyse der energieverlustmechanismen im fluoreszenzkollektor*. PhD Theisis. Albert-Ludwigs-Universität: Frieburg, Germany.

Zenou, M., Goldin, S.Y., Klebanov, M., Lyubin, V., Bruner, A., and Sfez, B., 2006. *Design, fabrication and characterisation of thermally evaporated photonic crystal mirrors*. IEEE 24th Convention of Electrical and Electronics Engineers in Israel. November 15-17, Eilat, Israel. 423-425. DOI: 10.1109/EEEI.2006.321124.

5. Modelling fluorescent solar collectors

5.1. Introduction

This chapter reviews work on the modelling/simulation of fluorescent solar collectors from the literature. Following on from the generalised Planck's law (Würfel, 1982) described in Chapter 2, it will be shown how the emission from collectors has been modelled.

An alternative method for characterising these devices involves the calculation of the re-absorption probability of different photon flux streams in these photon management structures in order to obtain their efficiencies. This method will also be outlined.

The latest developments on the modelling of emission within photonic crystals will also be described as well as how to calculate the effect of photonic crystals on the properties of the embedded fluorescent molecules such as its quantum yield. Simulations of 1D integrated photonic fluorescent solar collectors from the literature will also be briefly discussed as well the implication of these results on the potential of this technology.

5.2. Conventional fluorescent solar collectors

Two approaches to modelling conventional fluorescent solar collectors are detailed in the following sections. The models that will be presented were all originally intended to describe fluorescent edge concentrators but should also be applicable to fluorescent down-shifting structures and concentrating fluorescent down-shifting structures with some modifications (see Chapter 6). The first method of modelling collectors involves the use of statistical thermodynamics to predict emission. This assumes thermal equilibrium of the fluorescent molecules with its surrounding allowing the use of the generalised Planck's law (see Chapter 2). The second method focuses on modelling the re-absorption probability (Weber and Lambe, 1976) in order to track the effect of multiple absorption and emission events (Batchelder *et al.*, 1979).

5.2.1. Modelling emission in fluorescent edge concentrators

This section looks at models that predict the photon flux emitted by fluorescent edge concentrators. Following from the generalised Planck's law**,** Meyer and Markvart (2009)

showed how the edge fluorescence in fluorescent edge concentrators can be calculated from the chemical potential of the fluorescent molecules and its Kennard-Stepanov temperature (Kenard, 1918).

A more complex model proposed by Chatten *et al.* (2003) adapts Chandrasekhar's transfer equations (Chandrasekhar, 1950) to fluorescent edge concentrators. These equations consider the balance between absorption and emission to calculate the resultant photon fluxes found within fluorescent edge concentrators and those emitted from its surfaces.

5.2.1.1. Meyer & Markvart model

Meyer and Markvart (2009) showed experimentally that in fluorescent edge concentrators, the chemical potential of the light emitted from the edge is very close to the chemical potential of the fluorescent molecules.

The chemical potential of the fluorescent molecules was obtained as follows. Consider an illuminated fluorescent edge concentrator consisting of fluorescent molecules in a mixture of excited (with concentration N^*) and ground states (with concentration N_*), that transition from one state to the other. The chemical potential, at thermal equilibrium, of the ground and excited state fluorescent molecules (μ_{N_*} and μ_{N^*} respectively) can be written as (Kittel and Koremer, 1980):

$$\mu_{N_*} = \mu_{\mathrm{N}_{*0}} + kT_{\mathrm{g}} \ln(N_*) \tag{76}$$

and

$$\mu_{\mathrm{N}^*} = \mu_{\mathrm{N}_0^*} + kT_{\mathrm{g}} \ln(N^*) \tag{77}$$

where $\mu_{\mathrm{N}_{*0}}$ and $\mu_{\mathrm{N}_0^*}$ are the lowest energies of the ground and excited states of the fluorescent molecules respectively, k is Boltzmann's constant and T_{g} is the temperature of the fluorescent material. The second term on the right hand side of Equation (76) and Equation (77) are related to the entropy generated due to the transition between the two states. The free energy per particle, μ_{f}, i.e. the chemical potential of the fluorescent molecules, is given by the difference in the chemical potential of excited and ground state fluorescent molecules:

$$\mu_{\mathrm{f}} = \mu_{\mathrm{N}^*} - \mu_{N_*} = \mu_{\mathrm{N}_0^*} - \mu_{\mathrm{N}_{*0}} + kT_{\mathrm{g}} \ln\left(\frac{N^*}{N_*}\right) = h\nu_0 + kT_{\mathrm{g}} \ln\left(\frac{N^*}{N_*}\right) \tag{78}$$

where ν_0 corresponds to a frequency with energy equal to the transition energy from the ground to the excited state and h is Planck's constant.

In steady state, the number of electrons that relax from the excited to the ground state per unit time, is equal to the photon flux absorbed. The absorbed photon flux includes absorption directly from the solar photon flux and re-absorption of fluorescence. Neglecting the re-absorption of the photon flux emitted within the escape cones in a fluorescent edge concentrator, the absorbed photon flux is given by:

$$\frac{N^*}{\tau_{\mathrm{tot}}} = N_{\mathrm{inc}} Q_{\mathrm{a}} + \frac{N^*}{\tau_{\mathrm{rad}}}(1 - P)R \tag{79}$$

where τ_{tot} and τ_{rad} are the total and radiative lifetimes of the fluorescent molecules respectively, N_{inc} is the excitation photon flux incident on the fluorescent edge concentrator, Q_{a} is the absorption efficiency i.e. the fraction of the incident solar photon flux absorbed by the fluorescent edge concentrator, R is the average re-absorption probability of the fluorescence trapped in the fluorescent edge concentrator and P is the fraction of emitted fluorescence emitted within the escape cones. For an fluorescent edge concentrator P is equal to the fraction of photons emitted into the top and bottom escape cones and can be obtained by calculating the fraction of emission trapped within the fluorescent edge concentrator or from the refractive index, n, of the fluorescent edge concentrator:

$$P = \frac{\Omega_{\mathrm{t}}}{4\pi} = 1 - \left(1 - \frac{1}{n^2}\right)^{1/2} \tag{80}$$

where Ω_{t} is the solid angle of trapped emission.

The solar photon flux incident on the fluorescent edge concentrator is given by:

$$N_{\mathrm{inc}} = \xi_{\mathrm{inc}} \int_0^{\infty} \frac{2c}{\lambda^4} \frac{1}{\exp\left(\frac{hc}{\lambda k T_{\mathrm{inc}}}\right) - 1} d\lambda \tag{81}$$

where h is Planck's constant, c is the speed of light, k is Boltzmann's constant, λ is the wavelength, T_{inc} is the temperature of the Sun and ξ_{inc} is the étendue of the incident solar

photon flux equal to $A_{\mathrm{FSC}}\Omega_{\mathrm{inc}}$. A_{FSC} is the area of the fluorescent edge concentrator top surface and Ω_{inc} the solid angle subtended by the Sun with respect to the solar cell.

Rearranging Equation (79) we obtain:

$$N^{*} = \frac{N_{\mathrm{inc}} Q_{\mathrm{a}} \tau_{\mathrm{tot}}}{1 - \phi_{\mathrm{f}}(1-P)R} \tag{82}$$

where ϕ_{f} is the quantum yield of the fluorescent molecule.

Substituting Equation (82) into Equation (78) results in:

$$\mu_{\mathrm{f}} = h\nu_0 + kT_{\mathrm{g}} \ln\left(\frac{\frac{N_{\mathrm{inc}} Q_{\mathrm{a}} \tau_{\mathrm{tot}}}{1 - \phi_{\mathrm{f}}(1-P)R}}{N_{*}}\right) \tag{83}$$

This chemical potential can be used to calculate the edge emission in fluorescent edge concentrators in regions where there is an overlap between absorption and emission. In these wavelength regions, assuming unity quantum yield, due to repeated absorption and emission events (i.e. photon recycling), the fluorescent molecules are brought into thermal equilibrium and can be described by the Kenard-Stepanov temperature (Kenard, 1918). Using the calculated chemical potential and the Kenard-Stepanov temperature in the generalised Planck's law (see Chapter 2) the emission from the fluorescent edge concentrator edge can be obtained.

5.2.1.2. Chatten model: trapped, top and bottom photon flux

The Chatten model (Chatten *et al.*, 2003) derives expressions for the photon flux within fluorescent edge concentrators and emitted from fluorescent edge concentrators by considering the balance between absorption and emission.

In this model the approximation used in the method of Schwarzschild and Milne (for more information see Milne, 1921) is applied in which the angular dependence of the intensity of emission within the fluorescent edge concentrator is ignored, the intensity of emission in the forward (+) and backward (-) directions i.e. directions normal to the top and bottom surfaces of the fluorescent edge concentrator is assumed as shown in Figure 25 (t is the thickness of the edge concentrator and θ_{c} is the critical angle). However, two different 'streams' are distinguished, namely the photon flux emitted at angles greater

than the critical angle and hence trapped in the fluorescent edge concentrator and the photon flux emitted below the critical angle that can escape through the escape cones. Expressions for the trapped and escape cone emissions as well as description of how the chemical potential of light is treated in the Chatten model will be described.

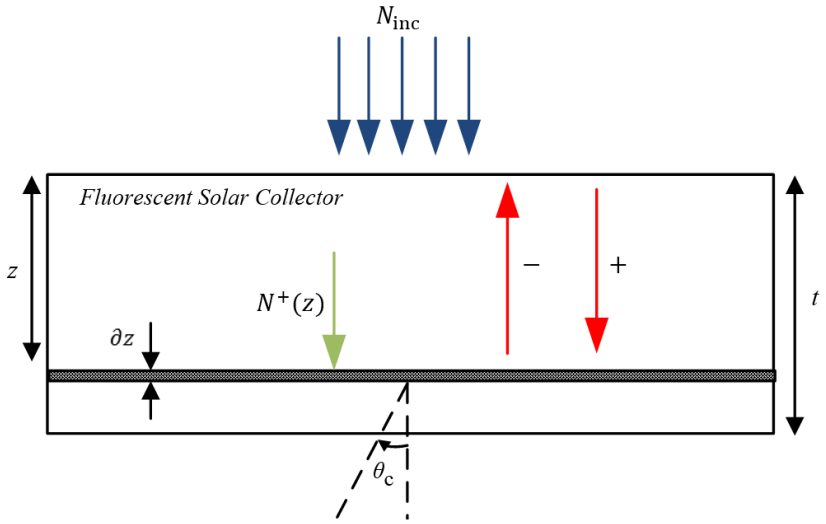

Figure 25 The model proposed by Chatten *et al.* (2003) divides the photon flux inside the fluorescent edge concentrator into forward (+) and backward (-) fluxes. Two different streams are also considered, i.e. trapped emission at angles below the critical angle and the escape emission.

The change in the photon flux per unit area of trapped light, dN_t, within a thickness dz can be written in the form of a radiative transfer equation:

$$dN_t(\lambda, z) = -\alpha(\lambda)N_t(\lambda, z)dz + \alpha(\lambda)\Omega_t \frac{2c}{\lambda^4} \frac{1}{\exp\left(\frac{\left(\frac{hc}{\lambda} - \mu_\gamma\right)}{kT_g}\right) - 1} dz \tag{84}$$

where α is the absorption coefficient of the fluorescent edge concentrator and μ_γ is the chemical potential of the photon flux. The first term on the right hand side of the above equation is the decrease in photon flux due to absorption in element dz (see Figure 25) while the second term (based on the generalised Planck's law) is the increase in photon flux due to emission.

In the Chatten model, as mentioned, the trapped photon flux is then further divided into forward and backward directions. The photon fluxes in the forward, N_t^+, and backward, N_t^-, directions are equal at the top and bottom surfaces. Assuming that the

chemical potential of the trapped photon flux does not vary with depth, applying these boundary conditions and solving gives the following expression for the trapped photon flux:

$$N_{\mathrm{t}}(\lambda) = N_{\mathrm{t}}^{+}(\lambda) + N_{\mathrm{t}}^{-}(\lambda) = \Omega_{\mathrm{t}} \frac{2c}{\lambda^4} \frac{1}{\exp\left(\frac{\left(\frac{hc}{\lambda} - \mu_{\gamma}\right)}{kT_{\mathrm{g}}}\right) - 1} \tag{85}$$

The photon flux per unit area inside the fluorescent edge concentrator within the escape cone, N_{es}, can also been divided into fluxes in the forward and backward directions. Figure 26 shows the photon flux incident on the top and bottom surfaces of the fluorescent edge concentrator. In this figure N_{top} is the photon flux emitted from the top surface of the fluorescent edge concentrator per unit area and N_{bottom}, is the photon flux emitted from the bottom surface of the fluorescent edge concentrator per unit area. From Figure 26 the boundary conditions, for example, at the top surface of the fluorescent edge concentrator is given by:

$$N_{\mathrm{es}}^{+}(\lambda) = \left(1 - R_{\mathrm{top}}\right) N_{\mathrm{inc}}(\lambda) + R_{\mathrm{top}} N_{\mathrm{es}}^{-}(\lambda) \tag{86}$$

and:

$$N_{\mathrm{top}}(\lambda) = R_{\mathrm{top}} N_{\mathrm{inc}}(\lambda) + \left(1 - R_{\mathrm{top}}\right) N_{\mathrm{es}}^{-}(\lambda) \tag{87}$$

where R_{top} is the reflectance from the top surface of the edge concentrator.

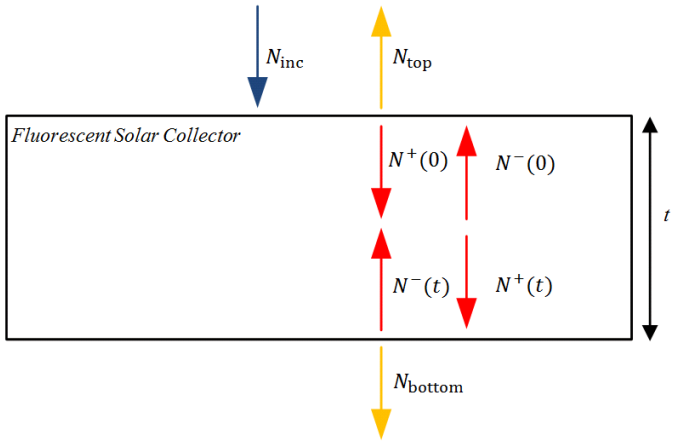

Figure 26 The photon flux incident at the top and bottom surfaces of the fluorescent edge concentrator.

Applying these boundary conditions (as well as similar ones for the bottom surface) and solving the radiative transfer equation for the escape cone photon flux gives expressions for the photon flux emitted from the bottom, top and within the escape cone (see Chatten *et al.*, 2003).

The chemical potential of light within the fluorescent edge concentrator, assuming it to be a constant over the depth of the structure, is calculated by ensuring that the following expression is satisfied:

$$\int \alpha(\lambda) N_{\mathrm{es}}(\lambda) d\lambda + \int \alpha(\lambda) N_{\mathrm{t}}(\lambda) d\lambda = \frac{4\pi}{\phi_{\mathrm{f}}} \int \alpha(\lambda) \frac{2c}{\lambda^4} \frac{1}{\exp\left(\frac{\left(\frac{hc}{\lambda} - \mu_\gamma\right)}{kT_{\mathrm{g}}}\right) - 1} d\lambda \tag{88}$$

i.e. within the fluorescent edge concentrator the trapped and escape cone emission is equal to the total emission in all directions (i.e. 4π solid angle) scaled according to the quantum yield of the fluorescent species.

Chatten *et al.* (2003) noted that the approximation of a constant chemical potential across the thickness of the fluorescent edge concentrator is only valid in devices below a certain thickness. For thicker fluorescent edge concentrators, the chemical potential would have to be calculated at different depths and the emission from the fluorescent edge concentrator will need to be solved numerically.

5.2.2. Re-absorption, collection efficiency and optical quantum efficiency

Another method of modelling the performance of fluorescent edge concentrators is by calculating the re-absorption probability of fluorescence. The re-absorption probability of trapped fluorescence was first calculated by Weber and Lambe (1976) and was used by Batchelder *et al.* (1979) to develop an expression for the collection efficiency i.e. the ratio between excitation photons absorbed by the concentrator and fluorescence reaching a solar cell. From the collection efficiency, the optical quantum efficiency (OQE), i.e. the ratio between excitation photons incident on the concentrator and fluorescence reaching a solar cell, can be calculated. This efficiency can be measured experimentally and can also be connected to the power conversion efficiency of the entire system (see Chapter 6 and Chapter 8)

5.2.2.1. Re-absorption probability of trapped photons: Weber & Lambe model

Weber and Lambe (1976) were the first to derive an expression for the probability of re-absorption of the trapped fluorescence in a fluorescent edge concentrator attached to 1 edge solar cell (1Cell setup). They defined the fluorescent edge concentrator to be infinitely long in the x direction with a perfectly reflecting mirror at $y = 0$ and a solar cell at $y = L$ (shown in Figure 27). Due to symmetry, this geometry is equivalent to a fluorescent edge concentrator with 1 edge mounted solar cell and 3 edge mounted mirrors assuming unity reflection from the 2 mirrors adjacent to the edge solar cell. For simplicity, the following derivation will assume unity reflection for all 3 edge mirrors.

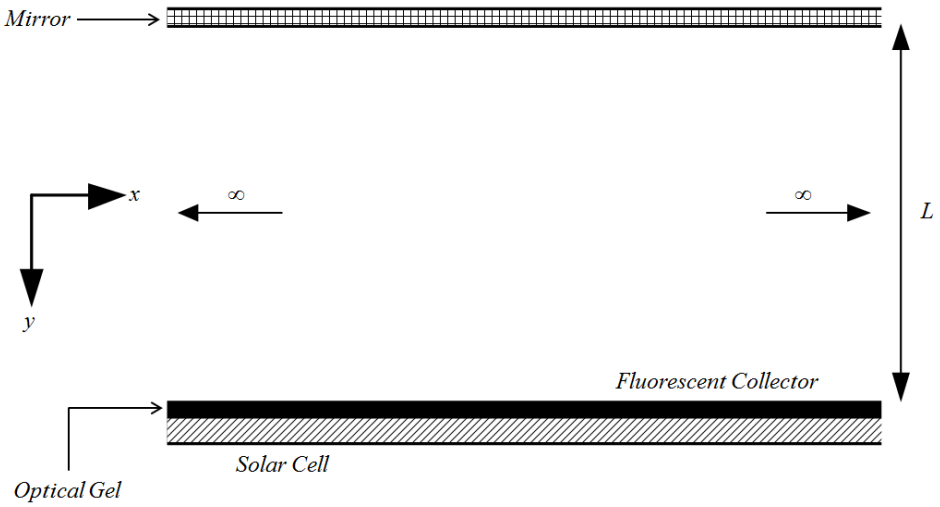

Figure 27 The fluorescent edge concentrator considered in the Weber and Lambe re-absorption model is infinitely long in the *x* direction, has a mirror at *y = 0* and a solar cell at *y = L*.

The probability, $p_a dV$, that a photon absorbed by the fluorescent edge concentrator is absorbed in a volume element dV is given by:

$$p_a dV = \frac{dxdydz}{V} \tag{89}$$

where V is the volume of the fluorescent edge concentrator.

Assuming unity quantum yield, the probability, $p_r d\Omega$, that an absorbed excitation photon is re-emitted within a solid angle element $d\Omega$ and is not re-absorbed is given by:

$$p_{\mathrm{r}} d\Omega = \frac{\exp\left(-\alpha_{\mathrm{em}} l(y)\right) d\Omega}{4\pi} \tag{90}$$

where α_{em} is the absorption coefficient at the emission wavelength, l is the path length of the light from point of emission till the solar cell. This equation is based on the Beer-Lambert law (see Chapter 2).

If a photon is emitted towards the solar cell the path length becomes:

$$l(y) = \frac{L - y}{\sin\theta \sin\phi} \tag{91}$$

where θ and ϕ are the polar angles.

If it is emitted towards the mirror, l is given by:

$$l(y) = \frac{L + y}{\sin\theta \sin\phi} \tag{92}$$

The collection probability, Q_{c1}, defined as the probability that a photon absorbed by the fluorescent edge concentrator results in a fluorescent photon reaching a solar cell without being re-absorbed, is given by:

$$Q_{\mathrm{c}_1} = \int_{V,\Omega_{\mathrm{t}}} p_{\mathrm{r}} p_{\mathrm{c}} dV d\Omega \tag{93}$$

The integration is over the entire volume of the fluorescent edge concentrator and over the solid angle of trapped emission.

From this the collection probability can be re-written as:

$$Q_{\mathrm{c1}} = \frac{\int_0^L \int_0^{\pi} \int_{\theta_c}^{\pi-\theta_c} \left(e^{\frac{-\alpha_{\mathrm{em}}(L-y)}{\sin\theta \sin\phi}} + e^{\frac{-\alpha_{\mathrm{em}}(L+y)}{\sin\theta \sin\phi}} \right) \sin\theta \, d\theta d\phi dy}{4\pi L} \tag{94}$$

where:

$$d\Omega = \sin\theta \, d\theta d\phi \tag{95}$$

The collection probability is in fact the product of the probability that an emitted photon is trapped in the concentrator and the probability that the trapped photon is not re-absorbed, i.e.:

$$Q_{c1} = (1 - P)(1 - r) \tag{96}$$

where r is the probability that a trapped photon is re-absorbed.

Re-arranging we obtain:

$$1 - r = \frac{Q_{c1}}{1 - P} \tag{97}$$

Figure 28 shows the dependence of the re-absorption probability of trapped photons on the product of the absorption coefficient and the length of the fluorescent edge concentrator calculated using the Weber and Lambe re-absorption model. As expected, for fluorescent edge concentrators with strong absorption the re-absorption probability is predicted to be very high.

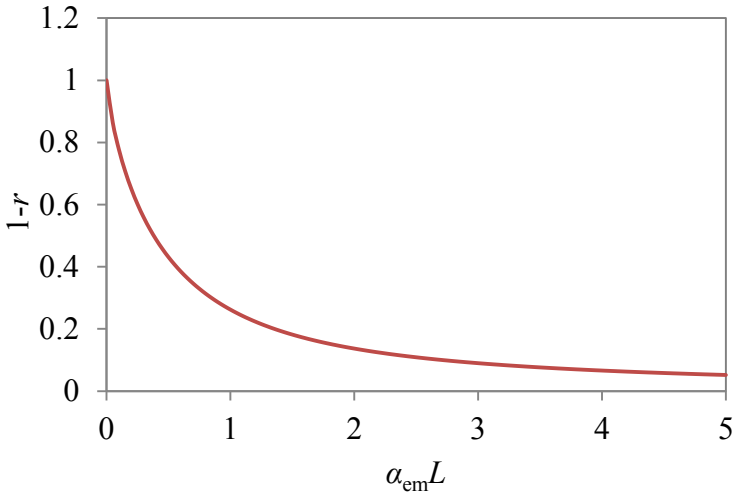

Figure 28 The relationship between the re-absorption probability and the absorption coefficient at the emission wavelength calculated from the Weber and Lambe re-absorption model.

5.2.2.2. Collection efficiency: Batchelder model

Expanding upon the Weber and Lambe re-absorption model, Batchelder *et al.* (1979) derived an expression for the collection efficiency, Q_c, of a single dye fluorescent edge concentrator based on the re-absorption probability and quantum yield of its fluorescent molecules.

Emission by fluorescent molecules will result in a certain fraction being collected by the solar cell, a certain fraction being re-absorbed and a certain fraction escaping from

the top or bottom escape cones. The re-absorbed light will again be emitted with a probability equal to the quantum yield of the dye. This once more leads to a certain fraction of the re-emitted fluorescence being collected by the solar cell, a certain fraction being re-absorbed and some escaping and so on. The end result is an infinite series of re-absorption and re-emission events. i.e.:

$$Q_c = (1-P)(1-R)\phi_f + (1-P)(1-R)[PR_{t\&b} + (1-P)R]\phi_f^2 + (1-P)(1-R)[PR_{t\&b} + (1-P)R]^2\phi_f^3 \ldots \quad (98)$$

where $R_{t\&b}$ is the average re-absorption probability of photons emitted within the top and bottom escape cones.

This can also be written as:

$$Q_c = Q_{c1} + Q_{c2} + Q_{c3} + Q_{c4} \ldots \ldots Q_{cn} \quad (99)$$

where Q_{cn} indicates the probability of an absorbed excitation photon resulting in a fluorescent photon reaching a solar cell after the nth absorption event.

Setting:

$$x = [PR_{t\&b} + (1-P)R]\phi_f \quad (100)$$

Equation (98) then becomes:

$$Q_c = (1-P)(1-R)\phi_f[1 + x + x^2 + x^3 \ldots] = (1-P)(1-R)\phi_f \frac{1}{1-x} \quad (101)$$

i.e.:

$$Q_c = \frac{(1-P)(1-R)\phi_f}{1 - \phi_f[(1-P)R + PR_{t\&b}]} \quad (102)$$

5.2.2.3. Collection efficiency: Kittidachachan model

Kittidachachan *et al*. (2007) also derived the same expression for the collection efficiency as Batchelder *et. al.* (1979) but used the photon balance within the fluorescent edge concentrator to arrive at the same result.

Let's assume that:

$$N_{\mathrm{a}} = N_{\mathrm{es}} + N_{\mathrm{t}} + N_{\mathrm{nr}} \tag{103}$$

where N_{a} is the photon flux absorbed by the edge concentrator and N_{nr} is the flux of non-radiative relaxation.

The photons that escape the fluorescent edge concentrator are photons emitted within the top and bottom escape cones that are not re-absorbed:

$$N_{\mathrm{es}} = \frac{N^*}{\tau_{\mathrm{rad}}}\big(P(1 - R_{\mathrm{t\&b}})\big) \tag{104}$$

The photon flux reaching the edge comprise of trapped photons that are not re-absorbed:

$$N_{\mathrm{t}} = \frac{N^*}{\tau_{\mathrm{rad}}}(1 - P)(1 - R) \tag{105}$$

Since the collection efficiency is defined as the ratio between absorbed excitation photons and fluorescent photons reaching a solar cell i.e. photons reaching the concentrator edge:

$$Q_{\mathrm{c}} = \frac{N_{\mathrm{t}}}{N_{\mathrm{a}}} = \frac{\frac{N^*}{\tau_{\mathrm{rad}}}(1 - P)(1 - R)}{\frac{N^*}{\tau_{\mathrm{rad}}}\big((1 - P)(1 - R)\big) + \frac{N^*}{\tau_{\mathrm{rad}}}\big(P(1 - R_{\mathrm{t\&b}})\big) + \frac{N^*}{\tau_{\mathrm{nr}}}} \tag{106}$$

where τ_{nr} is the non-radiative lifetime of the fluorescent molecules. Re-arranging we obtain the same expression derived in the Batchelder model, i.e. Equation (102):

$$Q_{\mathrm{c}} = \frac{(1 - P)(1 - R)\phi_{\mathrm{f}}}{1 - \phi_{\mathrm{f}}\big((1 - P)R + PR_{\mathrm{t\&b}}\big)} \tag{107}$$

The average re-absorption probabilities, R and $R_{\mathrm{t\&b}}$, are calculated by weighing the wavelength dependant re-absorption probabilities with the first generation fluorescence probability density, f_{l} (i.e. the probability distribution of re-absorption free fluorescence).

$$R = \int_0^\infty r(\lambda) f_1(\lambda) d\lambda \tag{108}$$

$$R_{\mathrm{t\&b}} = \int_0^\infty r_{\mathrm{t\&b}}(\lambda) f_1(\lambda) d\lambda \tag{109}$$

where $r_{\mathrm{t\&b}}$ is the re-absorption probability of photons emitted into the top and bottom escape cones.

The re-absorption probabilities of emission at a particular wavelength for trapped photons can be obtained from the Weber and Lambe re-absorption model from the absorption coefficient at that wavelength. The first generation fluorescence distribution is obtained by normalising the first generation fluorescence so as to satisfy the following condition:

$$\int_0^\infty f_1(\lambda)\, d\lambda = 1 \tag{110}$$

5.2.2.4. Optical quantum efficiency

The OQE is directly proportional to the product of the collection efficiency and the absorption efficiency:

$$OQE(\lambda) = \left(1 - R_{\mathrm{top}}\right) Q_{\mathrm{a}}(\lambda) Q_{\mathrm{c}} \tag{111}$$

The absorption efficiency can be easily obtained from the absorbance, *A*, (see Chapter 7 regarding measurements of absorbance) of the fluorescent edge concentrator:

$$Q_{\mathrm{a}}(\lambda) = 1 - 10^{-A(\lambda)} \tag{112}$$

The reflectance of the fluorescent edge concentrator can be calculated in a similar manner to the reflectance of a solar cell without an antireflection coating as described in Chapter 3.

5.3. Integrated photonic fluorescent solar collectors

This section reviews key works that investigated the modelling and simulation of integrated photonic fluorescent solar collectors. Integrated photonic collectors are

photonic crystals doped with fluorescent molecules. These devices have the potential to decrease some of the fundamental loss mechanisms seen in conventional fluorescent solar collectors such as the escape cone loss (Goldschmidt *et al.*, 2010). Key studies that have investigated the effect of photonic crystals on the properties of fluorescent molecules such as the fluorescence emission distribution, quantum yield etc. as well the expected benefits of integrated photonic collectors for solar concentration application obtained both through modelling and simulations will be reviewed.

5.3.1. Fluorescence in photonic crystals

Firstly, the effect of fluorescence on photonic crystals is discussed. The emission of fluorescence has been shown to depend on the density of states of the photonic crystal. The total density of states, N_{D}, at a frequency ω is obtained by adding up all the allowed modes with this frequency (Busch and John, 1998):

$$N_{\mathrm{D}}(\omega, r') = \sum_{n} \int_{1.\mathrm{BZ}} d^3 k_r \delta(\omega - \omega_n) \tag{113}$$

where r' is the position in the *xyz* plane and k_{r} is the wave number. 1.BZ indicates that integration is over the first Brillouin zone. If an excited fluorescent molecule is assumed to be at a location within the photonic crystal, for radiative emission to occur, from Chapter 2 it is clear that a photon needs to be emitted into an allowed propagating mode of the photonic crystal. The radiative lifetime of this excited atom is determined by the local interaction between this atom and the allowed propagating modes of the photonic crystal. Coupling is greater if the amplitude of an eigenmode is greater since the excited molecule can 'feel' the field intensity of the mode. To take into account the effect of the field intensity on the emission, the local density of states, N_{L}, is introduced: i.e. (Busch and John, 1998):

$$N_{\mathrm{L}}(\omega, r') = \sum_{n} \int_{1.\mathrm{BZ}} d^3 k_{\mathrm{r}} |E_{\mathrm{n}}(k_{\mathrm{r}})|^2 \delta(\omega - \omega_n) \tag{114}$$

where E_{n} is the electric field.

In a recently published study (Gutmann *et al.* 2013a) this local density of states was used to model the emission of Rhodamine B inside opal photonic crystals. The experimental measurements presented in this work showed good agreement with the fractional local density of states (i.e. local density of states within the measured solid angle) similar to results presented in (Barth *et al.*, 2005).

5.3.2. Quantum yield and lifetime in photonic crystals

Modelling of the effects of photonic crystals on the quantum yield and lifetime of fluorescent molecules was also investigated in (Gutmann *et al.*, 2013a) and will be briefly described below.

The rate of spontaneous emission in a fluorescent substance is assumed to be equal to the product of the number of excited state molecules and the probability of radiative relaxation to the ground state. In a homogenous medium, the latter is given by integrating the Einstein coefficient, A_{rad}, over the shape function of emission g (g is normalised so as to represent a probability distribution). Within a photonic crystal, the local density of states modifies emission, therefore the probability of radiative relaxation to the ground state, $P_{\mathrm{rad,pc}}$, becomes:

$$P_{\mathrm{rad,pc}}(r') = \int A_{\mathrm{rad}} g(\omega)\, \gamma_{\mathrm{L}}(r', \omega) d\omega \tag{115}$$

where γ_{L} is the ratio of the local density of states in the photonic crystal to the local density of states in a homogenous medium. From $P_{\mathrm{rad,pc}}$, the quantum yield of fluorescent molecules within a photonic crystal, i.e. ϕ_{pc}, can be obtained (see Gutmann *et al.*, 2013a for details):

$$\phi_{\mathrm{pc}}(r') = \frac{\phi_{\mathrm{h}} \kappa(r')}{1 + \phi_{\mathrm{h}}(\kappa(r') - 1)} \tag{116}$$

where ϕ_{h} is the quantum yield of the fluorescent molecule in a homogenous medium and κ is the emission probability enhancement factor (enhancement relative to homogenous medium).

The average quantum yield for when fluorescent molecules are distributed over different positions requires weighting with an absorption probability enhancement

factor. (Gutmann *et al.*, 2013a) also showed how the excited state lifetime of the fluorescent molecule within a photonic crystal can be written in terms of this average quantum yield.

5.3.3. One-dimensional integrated photonic fluorescent solar collectors

This section will present a brief review of the application of modelling and simulations to 1D integrated photonic fluorescent solar collectors specifically for solar concentration application.

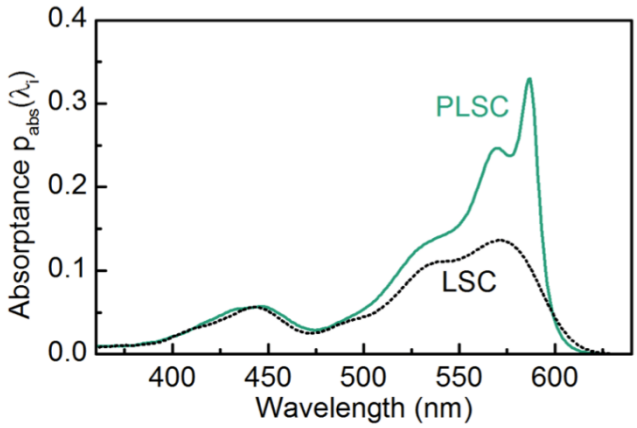

Figure 29 Theoretical calculations of the absorptance of a 1D integrated photonic fluorescent solar collector (denoted by PLSC) and a fluorescent edge concentrator (denoted by LSC). The thickness and dye concentration of the fluorescent layers in both devices are assumed to be the same. The scattering matrix method was used to calculate absorption (Gutmann *et al.*, 2013b).

Since this is a new area of research, only a few studies have so far been published. One such study is (Gutmann *et al.*, 2013b) in which theoretical calculations of the trapped fraction (i.e. $1 - P$) and the quantum yield of the fluorescent molecule were presented for a 1D integrated photonic collector (quarter-wave stack). These parameters were calculated based on the theory detailed in (Gutmann *et al.*, 2013a) and based on work found in (Busch and John, 1998) (Barth *et al.*, 2005) detailed in the previous sections. A theoretical framework similar to Batchelder *et al.* (1979) for obtaining the OQE of such 1D integrated photonic photon management structures was also outlined in Gutmann *et al.* (2013b). The results of this work indicates that absorption can be

enhanced significantly due to the concentration of electromagnetic fields in the fluorescent layer. Figure 29 is a figure published in this work that shows the expected enhancement in absorption calculated using the scattering matrix method. The scattering matrix method connects the outgoing waves from the layered structure to the incoming waves and is related to the transfer matrix method. A detailed description of this method is beyond the aim of this thesis but can be found in (Whittaker and Culshaw, 1999).

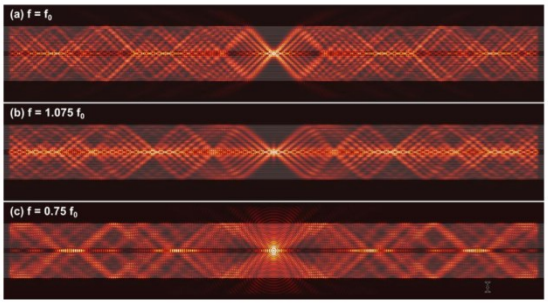

(a)

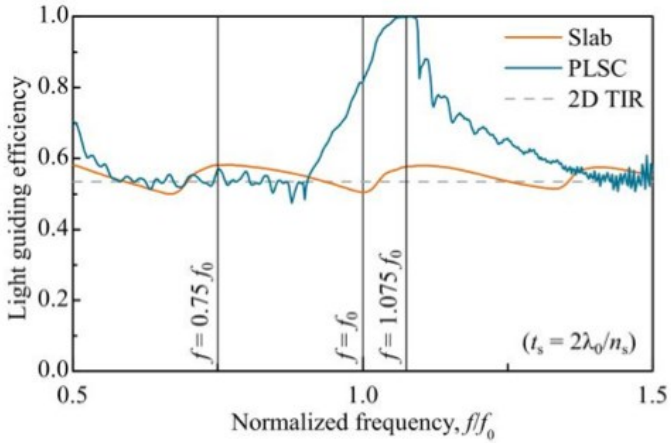

(b)

Figure 30 (a) Suppression of emission in certain directions at certain frequencies and (b) a corresponding increase in the collection probability (light guiding efficiency): PLSC refers to the 1D integrated photonic fluorescent solar collector and 'Slab' refers to a fluorescent edge concentrator. These figures are both from (Gutmann *et al.*, 2012).

In Gutmann *et al.* (2011) and Gutmann *et al.* (2012) results of two dimensional simulations of 1D integrated photonic fluorescent solar collectors, using the finite difference time domain method implemented by the software MEEP, were presented. The device was assumed to consist of layers with refractive indices of 1.5 and 2 with

thickness of a quarter-wave stack. The fluorescent layer thickness was set to $\lambda/2n_1$ where λ was the target wavelength of peak reflectance and n_1 was the refractive index of the fluorescent layer. The results of the simulations indicated that in such structures, emission is expected to be suppressed in certain directions at certain frequencies due to the formation of a band gap as shown in Figure 30 (a) (published in Gutmann *et al.*, 2012). This was seen to result in an increase in the fraction of photons trapped in the 1D integrated photonic collector i.e. an increase in the light guiding efficiency is observed as shown by Figure 30 (b) (also published in Gutmann *et al.*, 2012). Note that in both of these figures f_0 indicates the frequency of the maximum normal reflectance. It is suggested that the peak trapped fraction occurs at a slightly higher frequency than f_0 due to the fact that reflectance of the structure at angles close to the critical angle peaks at a higher frequency compared to that for normal propagation. The simulations also indicated that only minimal increases in collection probability could be obtained after thickness greater than 20 bi-layers.

5.4. Summary

This chapter has outlined key work on the modelling of fluorescent solar collectors. Two different methods for modelling conventional collectors have been presented. The first directly calculates the emission exiting fluorescent solar collectors based on the generalised Planck's law. The second method looks directly at the re-absorption probability of the trapped photon flux in the 1Cell setup and incorporates this in expressions to calculate the efficiency of these photon management structures. The first approach will be used in Chapter 6 to calculate the ultimate efficiency of photonic fluorescent solar collectors while re-absorption models will be extended in Chapter 6 so as to calculate the performance of fluorescent edge concentrators in the 4Cell (i.e. edge concentrator coupled to 4 edge solar cells) setup and also for analysing the re-absorption probability of other photon flux streams in collectors. Key work on the modelling and simulation of integrated photonic fluorescent solar collectors has also been presented. The effect of photonic crystals on the emission of fluorescent molecules in terms of frequency distribution, direction and quantum yield has been discussed. Results from modelling and simulations from the literature showing the potential of 1D integrated photonic collectors to enhance the performance of frequency management structures beyond conventional limits has also been presented.

References

Barth, M., Gruber, A. and Cichos, F., 2005. *Spectral and angular redistribution of photoluminescence near photonic stop band.* Physical Review B. 72: 085129. DOI: 10.1103/PhysRevB.72.085129.

Batchelder, J. S., Zewail, A. H. and Cole, T., 1979. *Luminescent solar concentrators. 1: Theory of operation and techniques for performance evaluation*. Applied Optics. 18: 3090-3110. DOI: 10.1364/AO.18.003090.

Busch, K. and John, S., 1998. *Photonic band gap formation in certain self-organising systems*. Physical Review E. 58: 3896-3908. DOI: 10.1103/PhysRevE.58.3896.

Chatten, A.J, Barham, K.W.J., Buxton, B.F., Ekins-Daukes, N.J. and Malik, M.A., 2003. *A new approach to modelling quantum dot concentrators.* Solar Energy Materials and Solar Cells. 75: 363-371. DOI: 10.1016/S0927-0248(02)00182-4.

Chandrasekhar, S., 1950. *Radiative transfer*. Oxford University Press: Oxford, UK.

Goldschmidt, J.C., Peters, M., Gutmann, J., Steidl, L., Zentel, R., Bläsi, B. and Hermle, M., 2010. *Increasing fluorescent concentrator light collection efficiency by restricting the angular emission characteristic of the incorporated luminescent material: the 'nano-fluko' concept.* Proceedings of SPIE Photonics for Solar Energy Systems III. April 13-15, Brussels, Belgium. 7725: 0S1-0S11. DOI: 10.1117/12.854278.

Gutmann, J., Peters, M., Bläsi, B., Hermle, M., Zappe, H. and Goldschmidt, J.C., 2011. *Towards photonic luminescent solar concentrators.* Proceedings of SPIE Next Generation (Nano) Photonic and Cell Technologies for Solar Energy Conversion II. 8111: 0K 1-9. DOI: 10.1117/12.893104.

Gutmann, J., Peters, M., Bläsi, B., Hermle, M., Gombert, A., Zappe, H. and Goldschmidt, J.C., 2012. *Electromagnetic simulations of photonic luminescent solar concentrator*. Optics Express. 20: A157:A167. DOI: 10.1364/OE.20.00A157.

Gutmann, J., Zappe, H. and Goldscmidt, J.C., 2013a. *Qualitative modeling of fluorescent emission in photonic crystals.* Physical Review B. 88: 205118 1-9. DOI: 10.1103/PhysRevB.88.205118.

Gutmann, J., Zappe, H. and Goldschmidt, J., 2013b. *Predicting the performance of photonic luminescent solar concentrators.* IEEE Photovoltaics Specialists Conference. June 16-21, Tampa, Florida, USA. 1864-1868. DOI: 10.1109/PVSC.2013.6744506.

Kenard, E.H., 1918. *On the thermodynamics of fluorescence.* Physical Review Letters. 11: 29-38. DOI: 10.1103/PhysRev.11.29.

Kittel, C. and Kroemer, H., 1980. *Thermal Physics*. W.H. Freeman: New York, USA.

Kittidachachan, P., Danos, L., Meyer, T.J.J., Alderman, N. and Markvart, T., 2007. *Photon collection efficiency of fluorescent solar collectors*. Chimia International Journal for Chemistry. 61: 780-786. DOI: 10.2533/chimia.2007.780.

Meyer, T.J.J. and Markvart, T., 2009. *The chemical potential of light in fluorescent solar collectors*. Journal of Applied Physics. 105: 063110 1-8. DOI: 10.1063/1.3097328.

Milne, E.A., 1921. *Radiative equilibrium in the outer layers of stars.* Monthly Notices of the Royal Astronomical Society. 81: 361-388.

Weber, W. H. and Lambe, J., 1976. *Luminescent greenhouse collector for solar radiation*. Applied Optics. 15: 2299-2300. DOI: 10.1364/AO.15.002299.

Whittaker, D.M. and Culshaw, I.S., 1999. *Scattering-matrix treatment of patterned multilayer photonic structures.* Physical Review B. 60: 2610-2618.

Würfel, P., 1982. *The chemical potential of radiation*. Journal of Physics C: Solid State Physics. 15: 3967-3985. DOI: 10.1088/0022-3719/15/18/012.

PART II: RESULTS AND DISCUSSIONS

6 Theory

6.1 Introduction

This chapter presents different models that have been developed to describe fluorescent solar collectors. On comparing the models described in Chapter 5, it was decided that treatments similar to the Weber and Lambe re-absorption model and the Batchelder model will be used to model practical fluorescent collectors due to their simplicity and ability to focus on different streams of photons within fluorescent collectors. A general model of the current output of collectors has also been detailed. This will be shown in Chapter 8 to be useful in analysing the current output of fluorescent down-shifting structures and concentrating fluorescent down-shifting structures.

The Weber and Lambe re-absorption model (Weber and Lambe, 1976) has also been adapted to look at the re-absorption probability of different photon flux streams including the emission escaping the fluorescent solar collector edge, top and bottom.

Expressions describing the re-absorption in the 4Cell setup, i.e. edge concentrator coupled to four edge solar cells, will also be presented. This setup does not suffer from some non-ideal losses present in the 1Cell setup (i.e. edge concentrator coupled to one edge solar cell and three edge mirrors) such as losses due to reflection from mirrors or large re-absorption for emission in certain directions. The highest reported power conversion efficiencies in the literature for fluorescent edge concentrators all use the 4Cell setup (Sloof *et al*., 2008)(Goldschmidt *et al.*, 2009a), so modelling this setup is important and will be useful for the understanding of fluorescent edge concentrators and their optimisation.

Re-absorption has also further been modelled for the 1Cell and 4Cell setups as a function of the angle of emission to 'see' how photons are lost at steeper angles. In Chapter 8 this will be compared to experimental measurement of fluorescent edge concentrators attached to solar cells and/or mirrors. Previous work on angular resolved measurements (Goldschmidt *et al.,* 2008)(Bendig *et al.,* 2008)(Goldschmidt,

2009b)(Sträter *et al.,* 2011) has focused on studying the emission escaping fluorescent solar collectors with uncoupled edges, however in operation these devices have mirrors/solar cells attached to their edges. These effects, therefore, also need to be studied in order to properly understand the operation of fluorescent edge concentrators.

The potential of photonic photon management structures has also been illustrated by looking into detail on the ultimate efficiency of photonic fluorescent solar collectors. This follows on from work found in Markvart (2006). Crucially the work presented here will move beyond the previous results to show the ultimate limits of quantities used to characterise collectors such as absorption, collection and optical quantum efficiencies. The chemical potential of light inside such ultimate photonic fluorescent solar collectors will also be quantified for the first time and compared with the chemical potential of carriers in the solar cell similar to the analysis of the Shockley-Queisser limit in Chapter 3. In addition the modelling of the electric field intensity outside integrated photonic fluorescent solar collectors will be presented.

6.2 General framework for modelling fluorescent solar collectors

In this section a general expression for modelling different types of fluorescent solar collectors will be presented. We assume the excitation photon flux to consist of uniform, parallel rays to be incident normal to the top surface of a collector. A solar cell(s) is also assumed to be attached to the fluorescent solar collector at an inclination angle, γ, with respect to its top surface i.e. for fluorescent edge concentrators this angle is equal to 90° while for bottom mounted fluorescent edge concentrators, fluorescent down-shifting structures and concentrating fluorescent down-shifting structures this angle is equal to 0°. The short circuit current output, I_{sc}, of the solar cell due to solar photons of a particular excitation wavelength, λ, is given by:

$$\begin{aligned} I_{sc}(\lambda) &= I_f(\lambda) + I_d(\lambda) \\ &= q\{1 - R_{top}(\lambda)\}Q_c(\lambda)Q_a(\lambda)EQE_f(\lambda)N_{inc}(\lambda) \\ &+ \frac{q\{1 - R_{top}(\lambda)\}A_{cell}\cos\gamma}{A_{FSC}}\{1 - Q_a(\lambda)\}EQE(\lambda)N_{inc}(\lambda) \end{aligned} \quad (117)$$

where I_f is the current produced in the solar cell due to fluorescence, I_d is the current produced by the solar cell due to the direct incidence of excitation light, q is the charge

of an electron, R_{top} is the reflectance from the top surface of the collector, Q_c is the collection efficiency, Q_a is the absorption efficiency, EQE_f is the average external quantum efficiency (EQE) of the solar cell to the fluorescence incident on it, EQE is the EQE of the solar cell, N_{inc} is the photon flux incident on the top surface of the fluorescent solar collector, A_{cell} is the top surface area of the solar cell and A_{FSC} is the top surface area of the collector. Equation (117) is a more general expression than what is given in (Danos *et al.*, 2012) and describes the current output of solar cells coupled to fluorescent edge concentrators, fluorescent down-shifting structures or concentrating fluorescent down-shifting structures.

The variation of Q_c and EQE_f with the excitation wavelength can be explained as follows. Re-absoprtion occurs when the emitted fluorescence is absorbed due to overlap between the absorbance and emisison of the fluorescent species. Though fluorescence emitted by a molecule is independent of the excitation wavelength, the fluorescence reaching a solar cell travels a finite distance leading to a certain amount of re-absorption, which distorts the fluorescence spectrum. The probability of re-absorption depends upon the path length travelled which in turn depends upon the depth at which the excitation photon is absorbed. The probability of the latter is related to the absorbption coefficient of the fluorescent solar collector and varies with the excitation wavelength. Therefore the spectral distribution of the fluorescence that reaches the solar cell can vary with the excitation wavelength. This explains why EQE_f might also change for different excitation wavelengths.

It has been shown in Chapter 5 that Q_c depends upon the re-absorption probabiltiy (Batchelder *et al.*, 1979)(Kittidachachan *et al.*, 2007). The variation in the re-absorption probability with the excitation wavelength also makes Q_c dependent on the excitation wavelength. Furthermore, the fluorescence collected from a fluorescent solar collector containing a number of different fluorescent species will be determined by additional factors such as the energy transfer efficiency between the different fluorescent molecules present and the absorption coefficient corresponding to each fluorescent species at a given excitation wavelength.

Q_c and EQE_f are, therefore, only independent of the excitation wavelength in specific systems where, for example, the absorbance does not vary significantly with the excitation wavelength and there is, either, only one type of fluorescent molecule or there

exists perfect energy transfer to the acceptor molecules in the case there are different fluorescent species.

In such a system if R_{top} is also assumed to be independent of the excitation wavelength, the current output of a solar cell attached to the collector reduces to:

$$I_{sc}(\lambda) = CQ_a(\lambda)N_{inc}(\lambda) + D\{1 - Q_a(\lambda)\}EQE(\lambda)N_{inc}(\lambda) \quad (118)$$

where C and D are constants. From Equation (118), it is possible to obtain the contribution of wavelength shifting and light concentration on the current output of the solar cell and also to estimate the current output at excitation wavelengths not measured.

The constant C can be obtained by fitting the experimentally measured current output in wavelength regions where the solar cell has a low EQE. The constant D can similarly be obtained by fitting the measured current output in regions where the absorbance of these photon management structures is close to zero.

From the constant D, R_{top} can be obtained and from C, Q_c can also be obtained if EQE_f can be estimated. These parameters can be used to quantify losses. By comparing Q_c for different fabrication methods or configurations i.e. for example, with and without edge mirrros, losses can be identified and the design of the fluorescent solar collector adapted accordingly.

6.3 Escape cone re-absorption in conventional fluorescent solar collectors

This section looks at modelling re-absorption in fluorescent solar collectors and goes beyond the Weber and Lambe re-absorption model (Weber and Lambe, 1976). A more general expression is used to derive the re-absorption probabilities of different streams of photons found within a collector.

One such stream is that which can be detected coming out of the fluorescent solar collector edge. Inside the collector, only photons emitted within the edge escape cone exits the edge, these photons have a shorter path length than the average photon which reaches the collector edge, and their re-absorption probabilities are therefore also different.

A related stream is the photon flux that is emitted from the top and bottom surfaces of these photon management structures, these consist of photons emitted within the top and

bottom escape cones. The difference between this stream and the edge escape cone stream, other than shorter path lengths, is that emission is in the same direction as the direction of the incident light. The depth at which absorption of incident light takes places, therefore starts to become important due to its effect on the path length travelled i.e. an assumption of uniform absorption across the fluorescent solar collector thickness is not valid as assumed in the Weber and Lambe re-absorption model (Weber and Lambe, 1976).

The re-absorption models described will all follow from the following general expression:

$$1 - r_{\Omega}(\lambda) = \int \frac{dV}{V} \int_{\Omega} \exp(-\alpha_{\mathrm{em}}(\lambda) l) \frac{d\Omega}{\Omega} \tag{119}$$

which describes the re-absorption probability, r_{Ω}, of the photon flux of wavelength λ emitted into a solid angle Ω in an ideal fluorescent solar collector. V is the volume of the collector, dV is a small volume element, $d\Omega$ is a small solid angle element, l is a measure of the path length from point of emission to a solar cell and α_{em} is the absorption coefficient at the emission wavelength.

6.3.1 Edge escape cone re-absorption

In the Weber and Lambe re-absorption model the solar cell is assumed to be optically coupled to the edge of the fluorescent edge concentrator. However, during spectroscopic measurements there exists an air gap between the detector and the fluorescent edge concentrator edge resulting in only light within the edge escape cone reaching the detector (Figure 31). The re-absorption probability of these photons is therefore not the same as what is obtained from the Weber and Lambe re-absorption model.

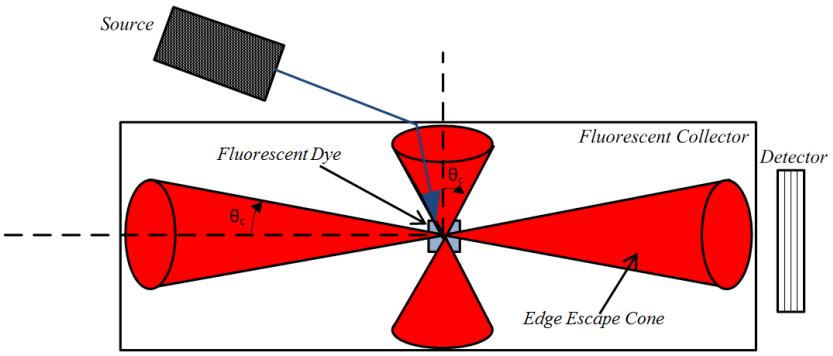

Figure 31 In spectroscopic measurements only the edge escape cone is measured by the detector.

We assume the fluorescent solar collector geometry considered by Weber and Lambe but without a solar cell coupled to one edge, i.e. a collector of length L with a perfect reflector at one edge and an uncoupled edge on the opposite edge. The width of the fluorescent solar collector is assumed to be infinitely long. This is equivalent to a fluorescent edge concentrator coupled to three edge mirrors (assuming lossless reflectance) and the remaining edge uncoupled to a solar cell/mirror.

Approximating the edge escape cone solid angle to be equal to a pyramid, the edge escape cone re-absorption probability, r_{edge}, is simply obtained by appropriate selection of the limits of integration of the azimuthal and zenith angles that defines the relevant solid angle in Equation (119). The path length terms are the same as what is given in the Weber and Lambe re-absorption model presented in Chapter 5, and the assumption of uniform absorption with depth z similarly requires in an integration only along the y axis:

$$1 - r_{\text{edge}} = \int \frac{dy}{L} \int_{\Omega_{\text{edge}}} \exp(-\alpha_{\text{em}}(\lambda) l) \frac{d\Omega}{\Omega_{\text{edge}}}$$

$$= \int_0^L \int_{\frac{\pi}{2}-\theta_c}^{\frac{\pi}{2}+\theta_c} \int_{\frac{\pi}{2}-\theta_c}^{\frac{\pi}{2}+\theta_c} \frac{dy}{L} \left(e^{\frac{-\alpha_{\text{em}}(L-y)}{\sin\theta \sin\phi}} + e^{\frac{-\alpha_{\text{em}}(L+y)}{\sin\theta \sin\phi}} \right) \frac{\sin\theta \, d\theta d\phi}{\Omega_{\text{edge}}} \quad (120)$$

where θ and ϕ are the polar angles, θ_c is the critical angle below which photons can escape from the fluorescent solar collector surface and Ω_{edge} is the solid angle of emission within the edge escape cone. This pyramid shaped solid angle is only an

approximation since the escaping solid angle is actually in the shape of a cone. In order to shape the pyramid to a cone the following condition must also be met:

$$\sin\theta \sin\phi > \cos\theta_c \tag{121}$$

Figure 32 shows a comparison between the Weber and Lambe re-absorption model and the edge escape cone model. The noticeable difference between the two is that the re-absorption probability is lower on average for the edge escape cone photon flux than the average for photon concentrated onto the collector edge. This is because the re-absorption probability increases with increasing path length and the average path length of light from emission to the collector edge is less for light emitted within the edge escape cone.

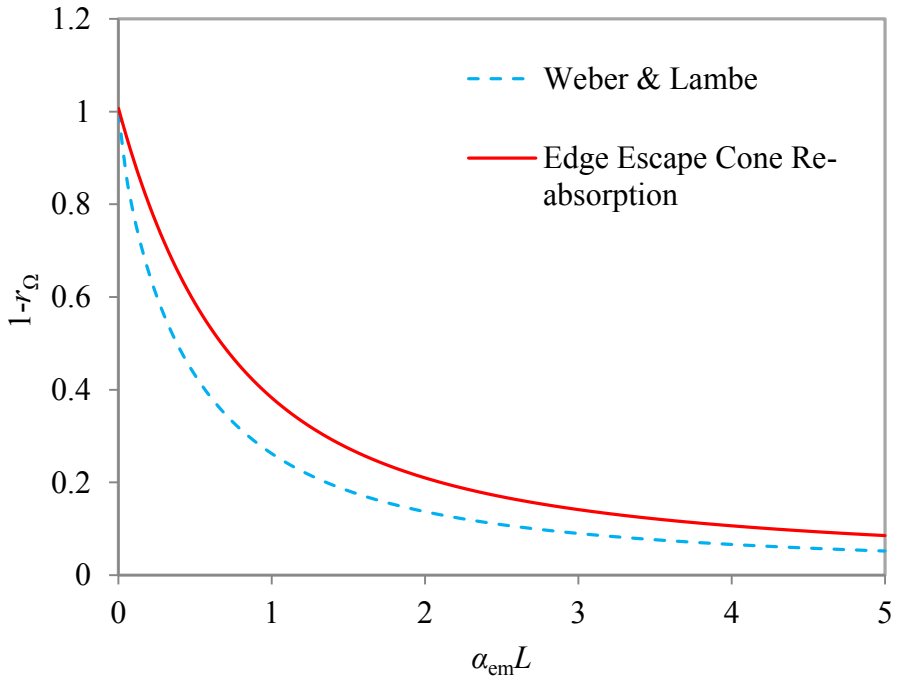

Figure 32 Comparison of the edge escape cone re-absorption model with the Weber and Lambe re-absorption model.

6.3.2 Top and bottom escape cone re-absorption

Another escape cone emission in fluorescent solar collectors that can also be measured easily is the top and bottom escape cones. These escape cones represent a fundamental loss mechanism in collectors and are a major barrier to high efficiency devices. The modelling of the top and bottom escape cones however requires additional considerations to what has been presented so far.

We consider a fluorescent solar collector of thickness t (**Figure 33**), this photon management structure is assumed to be infinitely long and infinitely wide. The re-absorption probability for the top and bottom escape cones in this collector can be obtained using a similar approach to the edge escape cone model, however, in this case the main difference is that photons are emitted parallel to the incident photon flux. The assumption of uniform absorption across the thickness of the fluorescent solar collector might therefore not be an accurate approximation. For example, if the absorption coefficient at the excitation wavelength is large, a large part of the incident light will be absorbed close to the top surface of the fluorescent solar collector. The top escape cone stream will therefore have a low re-absorption probability due to a short path length while the bottom escape cone stream will have a larger re-absorption probability, i.e. the re-absorption probabilities depends on the depth at which absorption takes place.

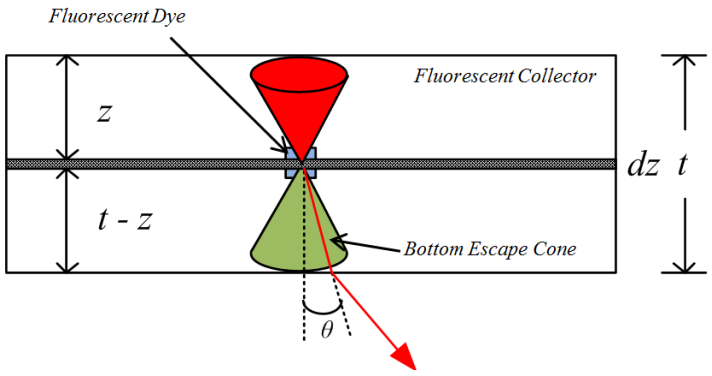

Figure 33 The top and bottom escape cones.

Assuming, absorption occurs at a depth z, the path length from point of emission to the top surface of the collector is given by:

$$l(z) = \frac{z}{\cos\theta} \tag{122}$$

and the path length from the point of emission to the bottom surface of the fluorescent solar collector will be:

$$l(z) = \frac{t - z}{\cos\theta} \tag{123}$$

Assuming a Beer-Lamert absorption distribution with depth and by also incorporating Equation (122) and Equation (123) into Equation (119), the average top and bottom escape cone reabsorption probability, $r_{t\&b}$, can be obtained from:

$$\begin{aligned} 1 - r_{t\&b} &= \int \frac{\alpha_{ex}\exp(-\alpha_{ex}z)dz}{1-\exp(-\alpha_{ex}t)} \int_{\Omega_{t\&b}} \exp(-\alpha_{em}(\lambda)l)\frac{d\Omega}{\Omega_{t\&b}} \\ &= \int_0^t \int_0^{\theta_c} \frac{\alpha_{ex}\exp(-\alpha_{ex}z)dz}{1-\exp(-\alpha_{ex}t)} \left[\exp\left(-\alpha_{em}\left(\frac{z}{\cos\theta}\right)\right)\right. \\ &\quad \left. + \exp\left(-\alpha_{em}\left(\frac{t-z}{\cos\theta}\right)\right)\right] \frac{2\pi\sin\theta\, d\theta}{\Omega_{t\&b}} \end{aligned} \tag{124}$$

where α_{ex} is the absorption coefficient at the excitation wavelength, $\Omega_{t\&b}$ is the solid angle of emission within the top and bottom escape cone. The ratio containing exponentials in Equation (124) indicates the fraction of absorbed photons absorbed within a depth between z and $z + dz$.

Figure 34 plots the dependence of $r_{t\&b}$ on α_{ex} and α_{em}. It is clear that $r_{t\&b}$ becomes larger with increasing α_{ex}. This indicates an increase in the average path length needed for light to exit the collector in the case of stronger absorption.

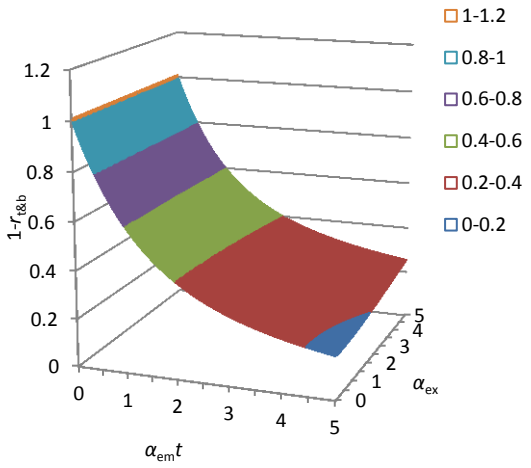

Figure 34 Top and bottom escape cone re-absorption probability

6.4 Trapped photon flux re-absorption and the angular collection efficiency

A general expression for the re-absorption probability of light trapped in a fluorescent solar collector will be presented in this section. In order to pinpoint losses within collectors it is useful to look at the angular distribution of the photon flux stream reaching the collector edge. For this purpose the angular collection efficiency will also be introduced and connected to Q_c. The specific case of the re-absorption probability of the trapped photon flux in the 4Cell setup has also been presented.

The trapped photon flux within a fluorescent solar collector travels orthogonal to the direction of excitation and therefore the assumption of uniform absorption across the thickness of the fluorescent solar collector can be used similar to the Weber and Lambe and the edge escape cone re-absorption models. Applying this assumption and expanding $d\Omega$ in Equation (119), the trapped re-absorption probability, r, can be written as:

$$1 - r(\lambda) = \int \frac{dA_{\mathrm{FSC}}}{A_{\mathrm{FSC}}} \int_{\Omega_{\mathrm{t}}} \exp(-\alpha_{\mathrm{em}}(\lambda) l) \frac{d\Omega}{\Omega_{\mathrm{t}}}$$

$$= \int \frac{dA}{A_{\mathrm{FSC}}} \int_{0}^{2\pi} \int_{\theta_c}^{\pi-\theta_c} \exp(-\alpha_{\mathrm{em}}(\lambda) l) \frac{\sin\theta \, d\theta d\phi}{\Omega_{\mathrm{t}}} \tag{125}$$

$$= \int_{0}^{2\pi} \frac{d\phi}{2\pi} \int \frac{dA}{A_{\mathrm{FSC}}} \int_{\theta_c}^{\pi-\theta_c} \exp(-\alpha_{\mathrm{em}}(\lambda) l) \frac{\sin\theta \, d\theta}{2(1-P)}$$

where dA_{FSC} is a small area element, Ω_{t} is the solid angle of emission of the trapped photon flux and P is the fraction of photons emitted within the top and bottom escape cones. The above expression is a general expression that can describe r for different setups i.e. both the 1Cell and 4Cell setups.

The re-absorption probability for different azimuthal angles of emission, Γ, follows from Equation (125):

$$1 - \Gamma(\phi, \lambda) = \int \frac{dA}{A_{\mathrm{FSC}}} \int_{\theta_c}^{\pi-\theta_c} \exp(-\alpha_{\mathrm{em}}(\lambda) l) \frac{\sin\theta \, d\theta}{2(1-P)} \tag{126}$$

The average angular re-absorption probability, Γ' is calculated using an expression similar to the connection between R and r detailed in (Kittidachachan *et al.*, 2007) and explained in Chapter 5, i.e.:

$$\Gamma'(\phi) = \int_{0}^{\infty} \Gamma(\phi, \lambda) f_1(\lambda) d\lambda \tag{127}$$

where f_1 is the first generation fluorescence. Assuming that the wavelength distribution of fluorescence emitted is independent of the excitation wavelength, building upon expressions presented in (Kittidachachan *et al.*, 2007), Γ' can be connected to the average angular collection efficiency, ρ i.e. the probability that an absorbed excitation photon results in a photon reaching a solar cell at an angle ϕ:

$$\rho(\phi) = \frac{\phi_{\mathrm{f}}\{1 - \Gamma'(\phi)\} \frac{(1-P)}{2\pi}}{1 - \phi_{\mathrm{f}}[(1-P)R + PR_{\mathrm{t\&b}}]} \tag{128}$$

where ϕ_f is the fluorescent quantum yield of the fluorescent species, R is the average re-absorption probability of the trapped photon flux and $R_{t\&b}$ is the average re-absorption probability of the escape cone photon flux. The denominator in Equation (128) corresponds to the effect of photon recycling due to re-absorption. From Equation (128) it is clear that $\rho(\phi)$ is directly proportional to 1 - $\Gamma'(\phi)$ in an ideal fluorescent solar collector i.e. a collector without additional losses such as due to scattering, reflection, parasitic absorption etc.

The photon flux emitted at an angle ϕ that reaches the edge, N_{edge}, can be written as (assuming only the trapped photon flux reaches the fluorescent solar collector edge):

$$N_{edge}(\phi) = \rho(\phi) \int Q_a(\lambda) N_{inc}(\lambda) d\lambda \tag{129}$$

In Equation (129) the term in the integral is a constant independent of ϕ, therefore:

$$N_{edge}(\phi) \propto \rho(\phi) \propto 1 - \Gamma'(\phi) \tag{130}$$

The above shows that in an ideal fluorescent solar collector, we expect the angular distribution of the photon flux exiting the collector edge to be proportional to 1 - $\Gamma'(\phi)$.

In (Kittidachachan *et al.*, 2007), Q_c for a fluorescent solar collector is decomposed into an integration over the spectral collection efficiency. We can similarly decompose Q_c into an integration over ρ:

$$Q_c = \int \rho(\phi) d\phi \tag{131}$$

Integrating (131) expressions for Q_c from (Kittidachachan *et al.*, 2007) and (Batchelder *et al.*, 1979) are reproduced:

$$Q_c = \frac{\phi_f(1-P)}{1-\phi_f[(1-P)R + PR_{t\&b}]} \int_0^{2\pi} \frac{\{1-\Gamma'(\phi)\}}{2\pi} = \frac{\phi_f(1-P)(1-R)}{1-\phi_f[(1-P)R + PR_{t\&b}]} \tag{132}$$

For the 1Cell setup, by using the Weber and Lambe re-absorption model as the foundation the different re-absorption probabilities i.e. angular, spectral etc. can be obtained. However, in the case of the 4Cell setup, a new model must be introduced. In order to calculate r in the 4Cell setup, it is necessary to model the system in two

dimensions as can be seen in Figure 35. ϕ_1 and ϕ_2 in this figure represent the extent of the azimuthal angle of emission from a fluorescent molecule towards the solar cell placed at the edge shown at the top of this figure. The path length (and therefore the re-absorption probability) therefore depends on the solar cell an emitted ray is emitted towards. In a square collector of length L surrounded by four solar cells (Figure 35), the distance l for a ray emitted towards the top solar cell i.e. as shown in Figure 35 is given by:

$$l(x,y) = \frac{L-y}{\sin\theta \sin\phi(x,y)}, \phi_1 \leq \phi(x,y) < \phi_2 \tag{133}$$

Simple trigonometric arguments that follow from Figure 35 allows ϕ_1 and ϕ_2 to be determined for emission from a given point in the xy plane as well as the two additional azimuthal angles required for a complete description.

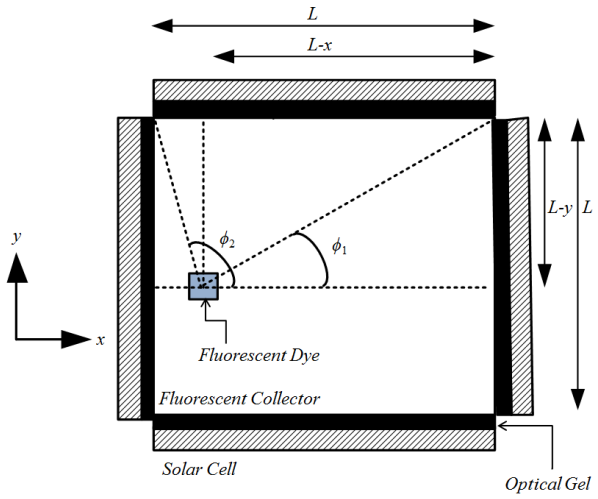

Figure 35 Top view of a 4Cell setup fluorescent edge concentrator.

Γ and Γ' (and therefore R) are obtained from Equations (126) and (127), in addition to Equation (133) for the 4Cell setup and expressions from (Weber and Lambe, 1976) detailed in Chapter 5 for the 1Cell setup.

$R_{t\&b}$ is obtained from $r_{t\&b}$ i.e. Equation (124), averaged over f_1. This is an approximation since this is only strictly valid if $r_{t\&b}$ is a constant for different fluorescence generations. The absorption distribution (i.e. the Beer Lambert distribution) described in Equation (124) describes the absorption distribution resulting from the

normal incidence of excitation photons. This is the absorption distribution that emits the the first generation fluorescence. However, the absorption distribution from which subsequent generations of fluorescence emerge is different since it is no longer due to the absorption of normally incident excitation photons. Combining the calculated R and $R_{t\&b}$, Q_c can be obtained from Equation (131).

6.5 Optical and power conversion efficiency

Expressions for calculating the OQE and power conversion efficiency in systems using fluorescent solar collectors have been outlined in this section. In a fluorescent solar collector where the wavelength distribution of fluorescence emitted can be assumed to be independent of the excitation wavelength, the OQE can be written as the product of two terms, a wavelength dependent term related to the absorbance i.e. Q_a of the collector and a wavelength independent term i.e. Q_c:

$$OQE(\lambda) = Q_a(\lambda)Q_c \tag{134}$$

Q_c obtained from Equation (131) for the 1Cell and 4Cell setups do not, for example, include non-ideal losses such as due to scattering or reflection from mirrors. These non-ideal losses should be wavelength independent and only primarily affect Q_c. Comparing the difference between ideal models and experimentally measured results would allow the estimation of these non-ideal transport losses in collectors.

The calculated OQE can be connected to the power conversion efficiency, η_p, using:

$$\eta_p = \frac{V_{oc}FFq \int N_{inc}(\lambda)OQE(\lambda)EQE_f(\lambda)d\lambda}{\int P_{inc}(\lambda)d\lambda} \tag{135}$$

where FF is the fill factor of the attached solar cells, V_{oc} is the open circuit voltage of the solar cell and P_{inc} is the power of the incident light.

6.6 Theoretical potential of photonic fluorescent solar collectors

The maximum theoretical efficiency of a photonic fluorescent solar collector has been calculated by Markvart (2006). The photon flux entering and exiting the photonic collector is assumed to be restricted by the effect of a photonic band stop filter that only transmits light below its critical wavelength, λ_{abs}, and reflects light of longer wavelengths. Similar to the Shockley Queisser limit, this efficiency limit is calculated by only taking into account the photon flux streams emitted by ideal absorbers that constitute the system i.e. the photon management structure is assumed to be a perfect absorber below a certain wavelength, λ_g. The fluorescent quantum yield is also assumed to be equal to unity.

The light is assumed to enter the photonic collector through an area A_{FSC}, there is an exit of area A_{cell} at which a solar cell is placed. The absorbed light is emitted with some of the light going back through the entrance while the remaining reaches the solar cell placed at the exit.

In the ideal photonic collector that is considered, fluorescence will be re-absorbed and re-emitted until the dye molecules reach thermal equilibrium with its surrounding (similar to the solar cell considered in the Shockley Queisser limit). This allows the use of the generalised Planck's law with a non-zero chemical potential to describe the emission.

Equating the absorbed photon flux to the photon flux emitted out of the photonic fluorescent solar collector and trapped inside, we obtain:

$$N_{\mathrm{inc},\lambda_{\mathrm{abs}}} = N_{\mathrm{top},\lambda_{\mathrm{abs}}} + N_{\mathrm{t},\lambda_{\mathrm{abs}},\lambda_{\mathrm{g}}} \tag{136}$$

where $N_{\mathrm{inc},\lambda_{\mathrm{abs}}}$ is the total incident photon flux below the critical wavelength of the photonic band stop filter. $N_{\mathrm{top},\lambda_{\mathrm{abs}}}$ and $N_{\mathrm{t},\lambda_{\mathrm{abs}},\lambda_{\mathrm{g}}}$ are the photon fluxes emitted by the photonic fluorescent solar collector that escapes from the entrance and which is trapped inside respectively. Similar to the emission from a solar cell, the emission from the photonic collector to the surroundings is modelled as emission from a flat surface to a hemisphere.

Following from Markvart (2006), we know that the balance between absorption, emission and trapped photon flux can be expanded to the following:

$$\xi_{\text{inc}} \int_0^{\lambda_{\text{abs}}} \frac{2c}{\lambda^4} \frac{1}{\exp\left(\frac{hc}{\lambda k T_{\text{inc}}}\right) - 1} d\lambda$$

$$= \xi_{\text{top}} \int_0^{\lambda_{\text{abs}}} \frac{2c}{\lambda^4} \frac{1}{\exp\left(\frac{\left(\frac{hc}{\lambda} - \mu_\gamma\right)}{k T_{\text{FSC}}}\right) - 1} d\lambda \tag{137}$$

$$+ \xi_{\text{t}} \int_{\lambda_{\text{abs}}}^{\lambda_{\text{g}}} \frac{2c}{\lambda^4} \frac{1}{\exp\left(\frac{\left(\frac{hc}{\lambda} - \mu_\gamma\right)}{k T_{\text{FSC}}}\right) - 1} d\lambda$$

where c is the speed of light, h is Planck's constant, k is Boltzmann's constant, T_{inc} is the temperature of the Sun, T_{FSC} is the temperature of the collector, μ_γ is the chemical potential of the fluorescence inside the collector, ξ_{inc}, ξ_{top} and ξ_{t} are the étendue of the incident, escaping and trapped photon fluxes respectively and are given by:

$$\xi_{\text{top}} = \pi A_{\text{top}} \tag{138}$$

$$\xi_{\text{t}} = \pi n A_{\text{FSC}} \tag{139}$$

$$\xi_{\text{inc}} = \Omega_{\text{inc}} A_{\text{FSC}} \tag{140}$$

where Ω_{inc} is the solid angle subtended by the Sun with respect to the collector and n is the refractive index of the collector.

Markvart (2006) can be extended to quantify the chemical potential of the light inside the photonic fluorescent solar collector and also of the carriers of the coupled solar cell. This can be obtained by calculating the number of photons extracted, N_{ex}, by the solar cell attached to the photonic collector, i.e.:

$$N_{\mathrm{ex}} = \xi_{\mathrm{t}} \int_{\lambda_{\mathrm{abs}}}^{\lambda_{\mathrm{g}}} \frac{2c}{\lambda^4} \frac{1}{\exp\left(\frac{\left(\frac{hc}{\lambda} - \mu_{\gamma}\right)}{kT_{\mathrm{FSC}}}\right) - 1} d\lambda - \xi_{\mathrm{t}} \int_{\lambda_{\mathrm{abs}}}^{\lambda_{\mathrm{g}}} \frac{2c}{\lambda^4} \frac{1}{\exp\left(\frac{\left(\frac{hc}{\lambda} - \mu_{\mathrm{cell}}\right)}{kT_{\mathrm{cell}}}\right) - 1} d\lambda \quad (141)$$

where μ_{cell} is the chemical potential of the solar cell and T_{cell} is the temperature of the solar cell.

In this manner μ_{γ} and μ_{cell} (at the maximum power point of the solar cell) has been obtained numerically and can be seen in Figure 36. Values of variables used in the calculation are as follows: the temperature of the Sun is assumed to be 6000 K while the solar cell and photonic collector are both assumed to be at 298 K, the band gap of a crystalline silicon solar cell has been assumed (i.e. 1.1 eV), the refractive index of the photonic fluorescent solar collector is set equal to 1.7 and the ratio between the A_{top} and A_{cell} has been set to 289.

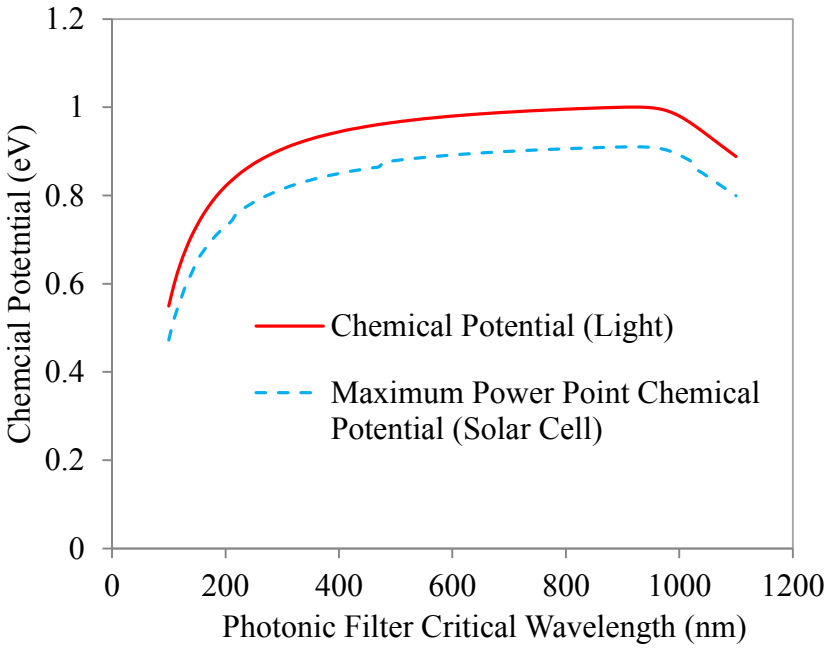

Figure 36 The chemical potential of trapped photons inside the photonic fluorescent solar collector and also of the solar cell carriers (for operation at the maximum power point).

Figure 36 shows the chemical potential of the solar cell corresponding to the maximum power point as a function of the photonic filter critical wavelength. It is interesting to note that μ_{cell} at the maximum power point is always lower than μ_γ of the trapped photon flux. This indicates that the conversion to electrical energy is accompanied by some irreversible losses similar to the discussions on the Shockley Quiesser limit in Chapter 3.

Extending the concepts presented in (Markvart, 2006), the properties of the ultimate photonic fluorescent solar collector in terms of quantities used to characterise collectors such as Q_{a}, Q_{c} and OQE can also be calculated from:

$$Q_{\text{a}} = \frac{N_{\text{inc},\lambda_{\text{abs}}}}{N_{\text{inc}}} \tag{142}$$

$$Q_{\text{c}} = \frac{N_{\text{t},\lambda_{\text{abs}},\lambda_{\text{g}}}}{N_{\text{inc},\lambda_{\text{abs}}}} \tag{143}$$

$$OQE = \frac{N_{\text{t},\lambda_{\text{abs}},\lambda_{\text{g}}}}{N_{\text{inc}}} \tag{144}$$

where N_{inc} is given by:

$$N_{\text{inc}} = \xi_{\text{inc}} \int_0^\infty \frac{2c}{\lambda^4} \frac{1}{\exp\left(\frac{hc}{\lambda k T_{\text{inc}}}\right) - 1} d\lambda \tag{145}$$

These quantities have been plotted in Figure 37. It is clear from this that to maximise OQE a balance between the need to absorb light and the need to collect the fluorescence emitted is required. If the critical wavelength of the photonic band stop filter is at a short wavelength, less light will be absorbed but a large fraction of emission will be trapped and collected. Selecting a photonic band stop filter with its critical wavelength at longer wavelengths, the photonic fluorescent solar collector will absorb a lot of light but a lot of it will also escape resulting in a low Q_{c}.

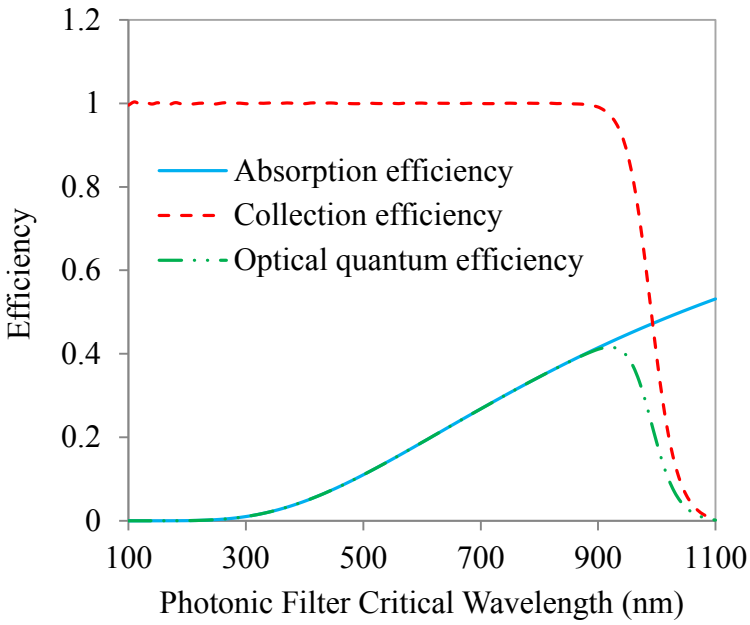

Figure 37 Ultimate limits on Q_a, Q_c and *OQE*.

The power conversion efficiency of the photonic fluorescent solar collector is given by:

$$\eta_p = \frac{P_{mpp}}{P_{inc}} \tag{146}$$

where P_{mpp} is the solar cell power output at the maximum power point and given by:

$$P_{mpp} = \mu_{mpp} N_{mpp} \tag{147}$$

where μ_{mpp} is the chemical potential of the solar cell at the maximum power point and N_{mpp} is the extracted photon flux at the maximum power point.

η_p has been calculated using Equation (146) and a key result presented in (Markvart, 2006) has been reproduced as shown in Figure 38. It is seen from the results that a peak efficiency of 26.9% is obtained when using a photonic band stop filter with its critical wavelength at 920 nm.

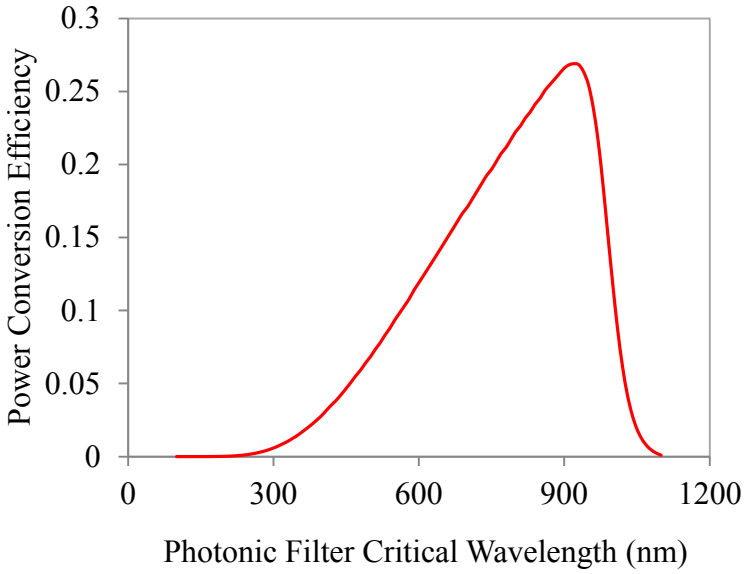

Figure 38 The ultimate efficiency of photonic fluorescent solar collector based systems.

6.7 Electric field outside 1D integrated photonic collectors

A method for calculating the electric field amplitude due to emission within an integrated photonic collector is presented in this section. We consider an emitting layer (labeled as 2 in Figure 39) with interfaces on the left and righthand side to media labeled as 1 and 3 in Figure 39. We assume emission towards the right. A left travelling and right travelling wave is assumed in the emitting layer. d is the thickness of the emitting layer and z_f is the distance between the emitting line and the left interface.

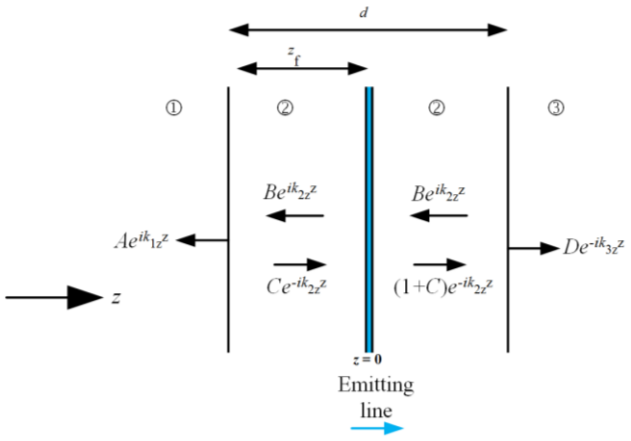

Figure 39 An emitting layer with interfaces on either side.

The boundary conditions are:

$$Ae^{ik_{1z}(-z_f)} = t_{21}Be^{ik_{2z}(-z_f)} \tag{148}$$

$$Ce^{-ik_{2z}(-z_f)} = r_{21}Be^{ik_{2z}(-z_f)} \tag{149}$$

$$r_{23}(1+C)e^{-ik_{2z}(d-z_f)} = Be^{ik_{2z}(d-z_f)} \tag{150}$$

$$t_{23}(1+C)e^{-ik_{2z}(d-z_f)} = De^{-ik_{3z}(d-z_f)} \tag{151}$$

where k_{1z}, k_{2z}, k_{3z} are the z components of the wave vector in medium 1, 2 and 3 respectively, A, B, C and D are the electric field amplitudes in different medium/directions as shown in Figure 39, r and t are the Fresnel reflection and transmission coefficients with subscripts denoting the applicable interface (i.e. t_{21} indicates the Fresnel transmission coefficient for a wave travelling from medium 2 to medium 1).

For emitting layers within photonic structures, the Fresnel transmission coefficients can, for example, be obtained by taking the ratio between the field amplitude outside the structure i.e. either in air or the substrate and the electric field amplitude at the boundary between the emitting layer and the multi-layers (reflection coefficients are similarly obtained). From the boundary conditions, the field amplitudes inside the emitting layer can be obtained, i.e.:

$$C = \frac{r_{21}r_{23}e^{-ik_{2z}d}}{e^{ik_{2z}d} - r_{21}r_{23}e^{-ik_{2z}d}} \tag{152}$$

and:

$$B = \frac{r_{23}e^{-ik_{2z}(d-z_f)}}{e^{ik_{2z}(-z_f)}(e^{ik_{2z}d} - r_{21}r_{23}e^{-ik_{2z}d})} \tag{153}$$

From this A and D can be obtained. For emission in the left direction, the boundary conditions are:

$$Ae^{ik_{1z}(-z_f)} = t_{21}(1+B)e^{ik_{1z}(-z_f)} \tag{154}$$

$$Ce^{-ik_{2z}(-z_f)} = r_{21}(1+B)e^{ik_{2z}(-z_f)} \tag{155}$$

$$r_{23}Ce^{-ik_{2z}(d-z_f)} = Be^{ik_{2z}(d-z_f)} \tag{156}$$

$$t_{23}Ce^{-ik_{2z}(d-z_f)} = De^{-ik_{3z}(d-z_f)} \tag{157}$$

Solving, the electric field amplitude inside the emitting layer is obtained, i.e.:

$$C = \frac{r_{21}e^{-ik_{2z}d}e^{ik_{2z}(d-z_f)}}{e^{-ik_{2z}(d-z_f)}(e^{ik_{2z}d} - r_{21}r_{23}e^{-ik_{2z}d})} \tag{158}$$

and:

$$B = \frac{r_{21}r_{23}e^{-ik_{2z}d}}{e^{ik_{2z}d} - r_{21}r_{23}e^{-ik_{2z}d}} \tag{159}$$

Again *A* and *D* can be obtained from *C* and *D*. From *A* and *D*, the intensity of the electric field exiting the top and bottom surfaces of photonic fluorescent solar collectors can be calculated.

6.8 Summary

This chapter has presented models describing the performance of fluorescent solar collectors. A general expression describing the current output of collectors coupled to solar cells has been described and should be useful in analysing the current output of these devices. Some of these models will be compared to experimental measurements in Chapter 8.

Re-absorption models for different photon flux streams in fluorescent solar collectors as well as for fluorescent edge concentrators in the 4Cell setup have also been presented.

In order to look at photon transport in collectors in detail the angular collection efficiency has be proposed and has been linked to the re-absorption probability and Q_c.

The ultimate photonic fluorescent solar collector has also been characterised in depth by extending existing treatments to determine the ultimate limits of quantities such as *OQE,* Q_a and Q_c that are frequently used to characterise such photon management structures. It is also shown how the chemical potential of the photon flux trapped in such photonic fluorescent solar collectors is greater than the chemical potential of the carriers in the attached solar cell. This relationship bears a resemblance to a similar discussion of the Shockley-Queisser limit as detailed in Chapter 3. The amplitude of the electric field for 1D integrated photonic fluorescent solar collectors has also been modelled, this will also be used in Chapter 8 to analyse experimental measurements.

References

Batchelder, J. S., Zewail, A. H. and Cole, T., 1979. *Luminescent solar concentrators. 1: Theory of operation and techniques for performance evaluation*. Applied Optics. 18: 3090-3110. DOI: 10.1364/AO.18.003090.

Bendig, M., Hanika, J., Dammertz, H., Goldschmidt, J.C., Peters, M. and Weber, M., 2008. *Simulation of fluorescent concentrators*. IEEE Symposium on Interactive Ray Tracing. August 9-10, Los Angeles, USA. DOI: 10.1109/RT.2008.4634628.

Danos, L., Parel, T., Markvart, T., Barrioz, V., Brooks, W.S.M. and Irvine, S.J.C., 2012. *Increased efficiencies on CdTe solar cells via luminescence down-shifting with excitation energy transfer between dyes*. Solar Energy Materials and Solar Cells. 98: 486-490. DOI: 10.1016/j.solmat.2011.11.009.

Goldschmidt, J.C., Peters, M., Prönneke, L., Steidl, L., Zentel, R., Bläsi, B., Gombert, A., Glunz, S., Willeke, G. and Raa, U., 2008. *Theoretical and experimental analysis of photonic structures for fluorescent concentrators with increased efficiencies*. Physica Status Solidi A. 205: 2811-2821. DOI: 10.1002/pssa.200880456.

Goldschmidt, J. C., Peters, M., Bösch, A., Helmers, H., Dimroth, F., Glunz, S. W. and Willeke, G., 2009a. *Increasing the efficiency of fluorescent concentrator systems*. Solar Energy Materials and Solar Cells. 93: 176–182. DOI: 10.1016/j.solmat.2008.09.048.

Goldschmidt, J.C., 2009b. *Novel Solar Cell Concepts*. Verlag Dr. Hut, München.

Kittidachachan, P., Danos, L., Meyer, T.J.J., Alderman, N. and Markvart, T., 2007. *Photon collection efficiency of fluorescent solar collectors*. Chimia International Journal for Chemistry. 61: 780-786. DOI: 10.2533/chimia.2007.780.

Markvart, T., 2006. *Detailed balance method for ideal single-stage fluorescent collectors*. Journal of Applied Physics. 99: 026101 1-3. DOI: 10.1063/1.2160710.

Sloof, L.H., Bende, E.E., Burgers, A.R., Budel, T., Pravettoni, M., Kenny, R.P., Dunlop, E.D. and Büchtemann, A., 2008. *A luminescent solar concentrator with 7.1% efficiency*. Physica Status Solidi - Rapid Research Letters. 2: 257-259. DOI: 10.1002/pssr.200802186.

Sträter, H., Knabe, S., Meyer, T.J.J. and Bauer, G.H., 2011. *Spectrally and angle-resolved emission of thin film fluorescence collectors*. Progress in Photovoltaics: Research and Applications. 21: 554-560. DOI: 10.1002/pip.1228.

Weber, W. H. and Lambe, J., 1976. *Luminescent greenhouse collector for solar radiation*. Applied Optics. 15: 2299-2300. DOI: 10.1364/AO.15.002299.

7. Experimental details

7.1. Introduction

Following from the theory developed in Chapter 6 and from the literature (Chapter 2 and Chapter 5), experimental measurements were conducted in order to study fluorescent solar collectors and also analyse the validity of the modelling developed. This chapter goes through all the experimental details, including the settings used for ray tracing simulations. Fabrication of collectors by spin coating (Spin-fluorescent solar collector) as well as descriptions of measurements used to characterise these devices including absorbance, transmittance, emission, ellipsometry and electrical measurements of solar cells will be presented.

7.2. Fabrication of fluorescent solar collectors

7.2.1. Conventional fluorescent solar collectors

The conventional collectors used in this study consists of 20 x 20 x 1 mm moulded collectors (Mold-fluorescent solar collectors) supplied by Teknova AS and Spin-fluorescent solar collectors consisting of a poly(methyl methacrylate) (PMMA) host material (refractive index equal to 1.49 at 587.6 nm) doped with fluorescent molecules. BASF Lumogen F series Violet570 (V), Yellow083 (Y), Orange240 (O) and Red305 (R) are the fluorescent species used.

The Spin-fluorescent solar collectors consists of a thin film layer deposited onto optical glass (BK7 windows, polished edges) by spin coating (Laurell) a solution of PMMA (Microchem 950 C 10) doped with fluorescent dye. Figure 40 shows the spin coater used in this project (Laurell WS-650SZ-6NPP/LITE). It consists of a stage in the middle where the glass substrate is placed. A hole in the middle of the spin coater stage applies vacuum to the substrate in order to hold it in place. The stage rotates at a selected speed, depositing a thin film onto the glass substrate.

Figure 40 Spin coater used in this project (Laurell WS-650SZ-6NPP/LITE).

The dye-PMMA mixtures were put in a sonicator for 30 minutes and left overnight prior to deposition in order to ensure complete dissolution. The PMMA and glass substrates have a refractive index of 1.52 and reflection loss of 8.1% for 2 surfaces (at 587.6 nm). A glass thickness of 1 mm was selected.

The following naming convention has been adopted for different samples: the dye concentration in the PMMA solution, i.e. before deposition or moulding, is written in units of g/l after the letter representing each dye. The peak absorbance of the sample is also written in square brackets. For example a sample consisting of 4 g/l Y dye and 2 g/l O dye with a peak absorbance of 1.8 will be denoted by Y4,O2 [1.8].

7.2.2. Integrated photonic fluorescent solar collectors

A 13 layer 1D integrated photonic collector was also deposited on a 20 x 20 x 1 mm glass substrate (BK7 windows, 8.1% reflection for 2 surfaces at 587.6 nm, polished edges) by spin coating (Laurell) sol gel solutions.

Alternating layers of titanium dioxide (TiO_2) and R dye doped silicon dioxide (SiO_2) formed the 1D integrated photonic fluorescent solar collector (see Figure 41). The synthesis of the TiO_2 sol gel stock solution is related to the procedure outlined in (Barbé et al., 2011). 6 ml titanium butoxide (Sigma Aldrich) was mixed with 4.2 ml acetyl

acetone (Sigma Aldrich) and stirred in a beaker for 15 minutes at 300 rpm, 22.9 ml 2-propanol and 0.6 ml acetic acid (drop wise) were added and the resulting mixture was stirred for 1 hour at 300 rpm. This stock solution was diluted with ethanol at a ratio of 2:1 and spin coated at 10,000 rpm with an acceleration of 2,000 rpm/s for 60 seconds.

The SiO_2 sol gel stock solution was obtained following the procedure outlined in (Reisfeld, 2012). 6 ml of tetraethylorthosilicate (Sigma Aldrich) was mixed with 27 ml ethanol, 10.2 ml de-ionised water, 1.8 ml 10% nitric acid and 0.75 ml triton (Sigma Aldrich). This mixture was stirred for 20 hours at 300 rpm. The doped SiO_2 layers were deposited by spin coating a solution consisting of 2.5 ml of the SiO_2 stock solution added to a mixture of 2.5 ml of ethanol and 0.266 ml of R dye in dimethyl formamide. The solution obtained had a total dye concentration of 100 mg/l. Deposition was with a spin speed of 3,000 rpm, an acceleration of 375 rpm/s and a duration of 60 seconds. After deposition each layer was heated at 250°C on a hot plate for 5 minutes to evaporate any solvents and solidify the layers. Before depositing a new layer, the top layer was cleaned by spraying with ethanol and dried under nitrogen. This method was seen to give samples without any visible signs of cracking.

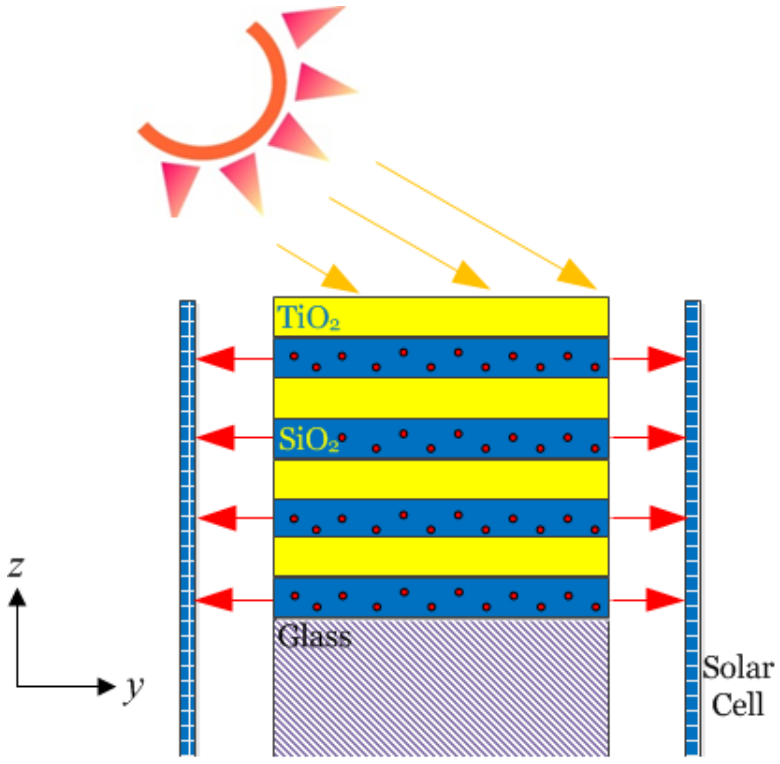

Figure 41 Schematic of the 1D integrated photonic fluorescent solar collector fabricated.

7.3. Absorbance/transmittance measurements

The fluorescent solar collectors were characterised by their absorbance and transmittance. The absorbance, A, of a sample will be defined as the logarithm of the ratio between the un-reflected incident photon flux and the transmitted photon flux:

$$A(\lambda) = \log_{10}\left(\frac{N_{\mathrm{inc}}(\lambda) - N_{\mathrm{R}}(\lambda)}{N_{\mathrm{T}}(\lambda)}\right) \tag{160}$$

where N_{inc} is the incident photon flux, N_{R} is the photon flux reflected from the collector top surface and N_{T} is the transmitted photon flux (see **Figure 42** for the setup used for measuring the absorbance).

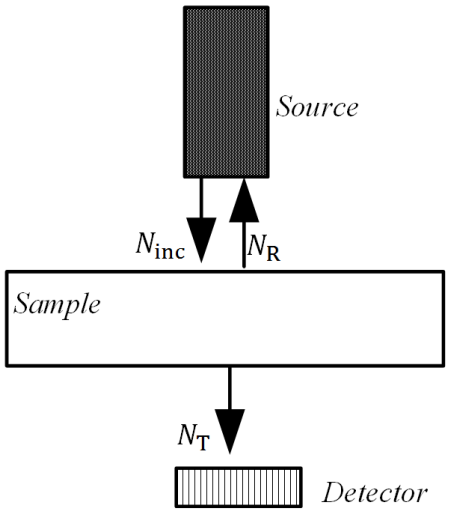

Figure 42 Setup for absorbance measurements.

In absorbance measurements N_{inc} - N_{R} is obtained using a reference i.e. in the case of collectors, an un-doped fluorescent solar collector (assumed to be weakly absorbing) is used as a reference. For photonic collectors assumed to be weakly absorbing, the reflectance, R_{top}, is obtained from:

$$R_{\mathrm{top}}(\lambda) = 1 - \frac{N_{\mathrm{T}}(\lambda)}{N_{\mathrm{inc}}(\lambda)} \tag{161}$$

with air used as reference to obtain N_{inc}. The transmittance, T, is given by:

$$T(\lambda) = 1 - R_{\text{top}}(\lambda) \tag{162}$$

The absorbance of the conventional fluorescent solar collector was measured using a Bentham spectrometer (glass/undoped PMMA reference). For the 1D integrated photonic collector an Avantes spectrometer (AvaSpec-2048, grating UA (200 - 1100 nm), slit 25 μm) was used (air reference) to obtain the transmittance. All samples were excited with a IL1 100 W halogen light source.

7.4. Thin film thickness measurement

The accurate control of film thickness in the fabrication of 1D integrated photonic fluorescent solar collectors is vital. A number of different techniques have been used to estimate the thickness of thin films in this project including ellipsometry and reflectometry. An ellipsometer consists of a light source that emits photons onto a sample through a polariser. The reflected light is also detected after passing through a polariser (Woollam, 2014). The ellipsometer measures the complex reflectance ratio, χ_e, which is a ratio between the Fresnel *s* and *p* reflection coefficients (Yeh, 1988):

$$\chi_e = \frac{r_s}{r_p} = \frac{|r_s|}{|r_p|} e^{i(\Delta_s - \Delta_p)} = \tan\psi\, e^{i\Delta} \tag{163}$$

where Δ_s and Δ_p are the phase angle of the *s* and *p* reflection coefficients (i.e. r_s and r_p), the difference of which is given by Δ. $\tan\psi$ gives the ratio of amplitudes of the reflection coefficients. As a ratio is measured, an ellipsometer does not require a reference sample.

To determine unknown optical constants or thicknesses of the layers on which light is incident, unknown parameters are varied in order to calculate the reflection coefficients from the Fresnel equations. The best fit to experimentally measured data gives the unknown parameters.

Figure 43 A Woollam ellipsometer.

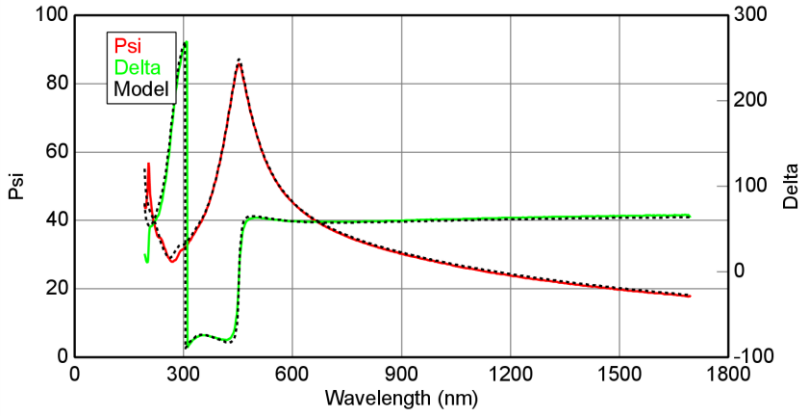

(a)

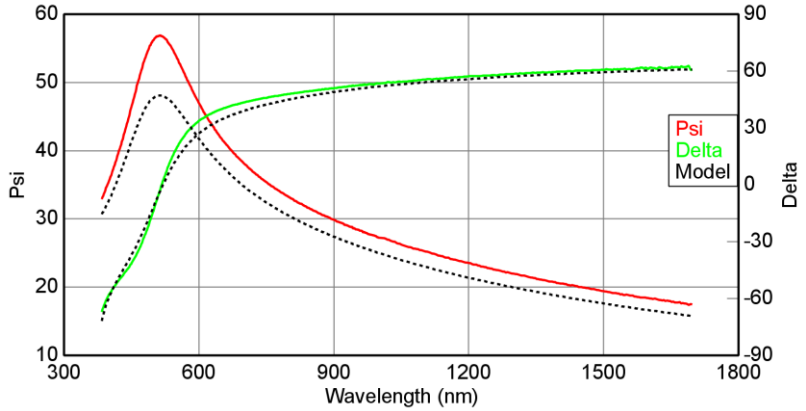

(b)

Figure 44 Ellipsometry measurements and fits obtained from CompleteEase for (a) SiO_2 and (b) TiO_2 layers. *y* axes show Psi (ψ) and Delta (Δ).

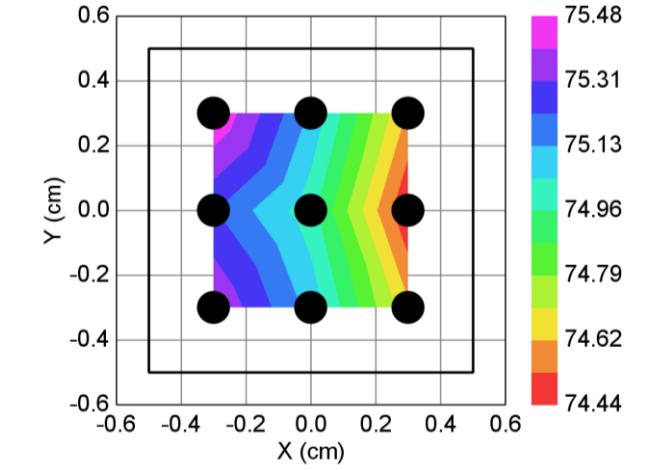

(a)

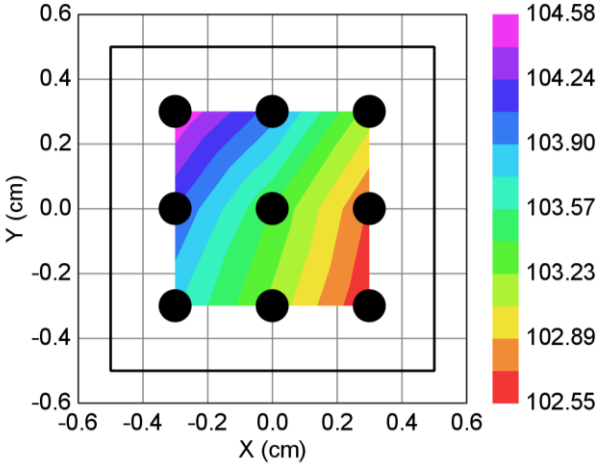

(b)

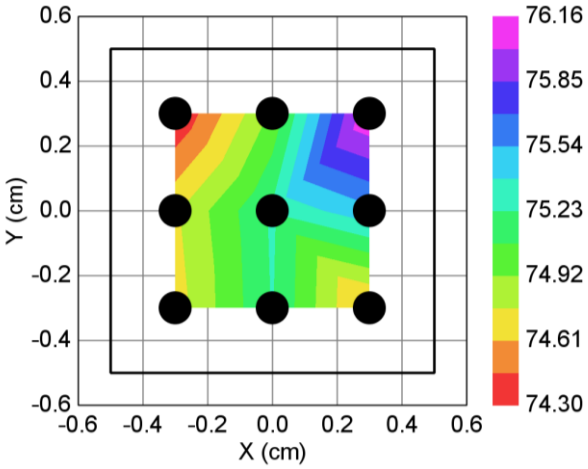

(c)

Figure 45 Uniformity of (a) first layer (TiO_2), (b) second layer (SiO_2) layer and (c) third layer (TiO_2) layer.

A Woollam MD2000D Ellipsometer (Figure 43 shows a Woollam ellipsometer) was used to measure the complex reflectance of TiO_2 and SiO_2 thin film layers deposited on a silicon substrate. The software package CompleteEase was used to obtain the thickness of the thin film layers from the complex reflectance i.e. the optical constants of the thin film was defined and the thickness was fitted so as to fit the measured data. The software comes with a selection of optical constants corresponding to different materials including TiO_2 and SiO_2. It was observed that the optical constants in the CompleteEase database for SiO_2 gave a good fit with the experimental data (Figure 44 (a) shows the fit for a SiO_2 layer) however it was not possible to get a very close fit with any of the available TiO_2 optical constants as shown in Figure 44 (b), therefore it is expected that the actually thicknesses and refractive index for the TiO_2 varies slightly from what was calculated. The transfer matrix method (Yeh, 1988) as described in Chapter 2 was, therefore, used to model the transmittance of the 1D integrated photonic fluorescent solar collector fabricated (the absorption by the fluorescent layers was neglected). This was used to check the thicknesses obtained from ellipsometry. In this manner it was determined that the 1D integrated photonic collector fabricated consisted of alternating layers of thicknesses 83 nm and 103.5 nm and refractive indices of 1.83 and 1.46 at 600 nm.

The CompleteEase software was also used to measure the uniformity of the deposited layers (deposited on a silicon substrate). Layer by layer measurements of 9 points for up to 3 layers on a 100 mm^2 area at the centre of the sample indicated a thickness variation of less than 2 nm as shown in Figure 45.

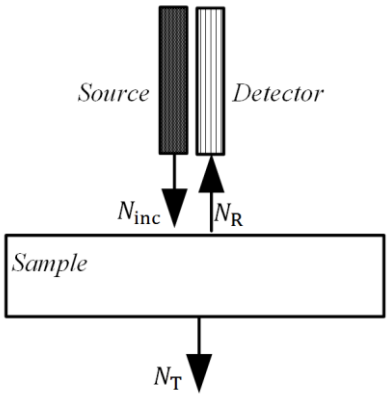

Figure 46 Setup for reflectometry measurements.

In order to study the effect of spin coater rotation speed on the thickness of deposited PMMA layers (conventional Spin-fluorescent solar collectors), PMMA was deposited onto a silicon substrate at different rotational speeds. Using bare silicon as a reference and the refractive index of PMMA, the thickness was measured using reflectometry. An Avantes spectrometer (AvaSpec-2048) and a reflection probe that excites the sample normally and also detects the reflected light normally were used in reflectometry measurements (Figure 46). The light source was a IL1 100 W halogen lamp. Figure 47 shows the dependence of the PMMA layer thicknesses on spin coating speed as obtained from these measurements.

Thick fluorescent layers are required so as to maintain a high absorbance while minimising fluorescence quenching effects associated with high dye concentrations (Valeur, 2001). For this reason a relatively low spin coating speed of 500 rpm was selected for fabricating the majority of the conventional Spin-fluorescent solar collectors. The resulting film thickness is around 8 μm.

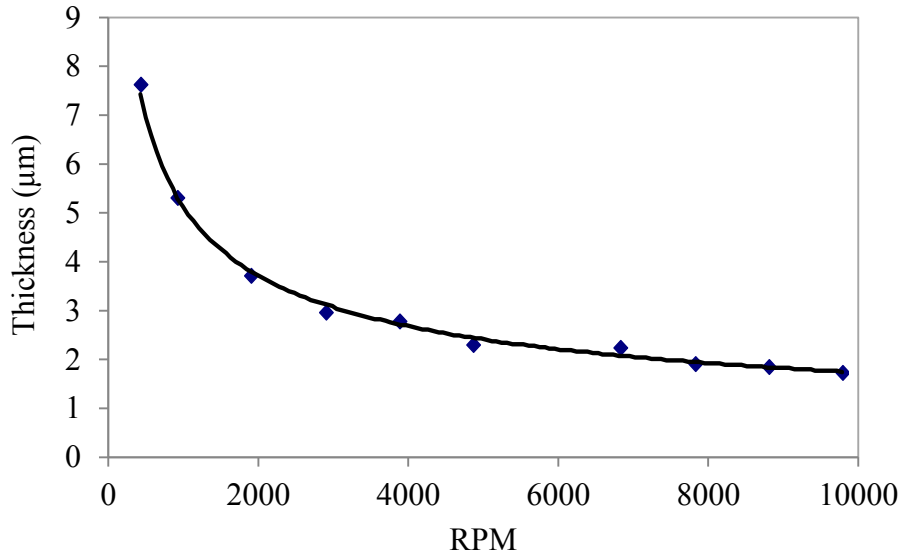

Figure 47 Dependence of PMMA layer thickness on spin coating speed i.e. revolutions per minute (rpm).

7.5. Emission measurements

The emission of fluorescent solar collectors was measured in order to analyse their performance as well as to compare with predictions of theory. The emission gives useful information about these photon management structures i.e. for example the degree of re-

absorption present in a fluorescent solar collector can be determined. This can then be used to verify the modelling presented in Chapter 6. The change in emission intensity or spectral distribution with angle of emission can also give information about the losses in collectors. For 1D integrated photonic fluorescent solar collectors the emission can give insights into the propagation of light within such structures and can be used to ascertain the effectiveness of such structures in decreasing fundamental loss mechanisms found in conventional fluorescent solar collectors, such as escape cone losses.

The experimental setup for measuring the top, bottom and edge emission as well as the that for angular resolved measurements are presented in this section. Fluorescence measurements vary according to the setup so the emission results are generally normalised as follows:

$$\int_0^\infty f(\lambda)\, d\lambda = 1 \tag{164}$$

where f is the fluorescence normalised so as to represent a probability density and λ is the wavelength.

7.5.1. Conventional fluorescent solar collector

This section details the experimental setup for measuring emission from conventional fluorescent solar collectors. Measurements of top, bottom and edge fluorescence, as well as angular resolved measurements are detailed.

7.5.1.1. Top, bottom and edge emission

The top and bottom fluorescence emitted from conventional fluorescent solar collectors was detected using an Avantes (AvaSpec-2048) spectrometer and an 89 North PhotoFluor II 200 W Metal Halide lamp. To measure the edge fluorescence, the collector was illuminated by a 300 W Xenon lamp. The setup for the edge and top fluorescence is shown in Figure 48 (a) and (b) respectively (θ_c is the critical angle).

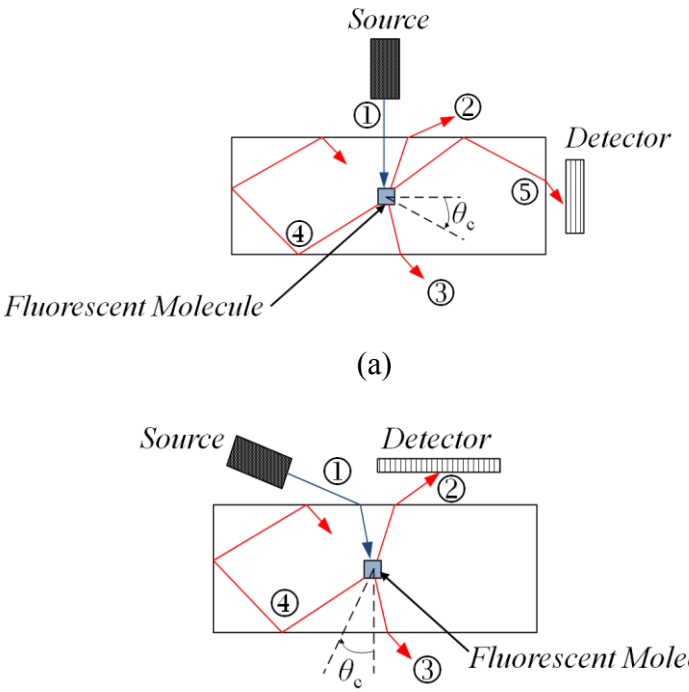

Figure 48 Setup for (a) edge fluorescence and (b) top fluorescence measurements. The different rays shown are 1) excitation light, 2) top escape cone fluorescence, 3) bottom escape cone fluorescence, 4) trapped fluorescence and 5) edge escape cone fluorescence.

7.5.1.2. Angular resolved emission measurements

The emission exiting fluorescent edge concentrator edges when coupled to 1 edge solar cell and 3 edge mirrors (1Cell setup) and 4 edge solar cells (4Cell setup) was analysed as a function of angle by attaching a square silicon photo diode (Thorlabs, 1 mm x 1 mm) to a motorised system. The detector was setup to move in a semi-circle at a distance of 8 cm about the central point of concentrator edge within a plane parallel to its top surface (Figure 49 and Figure 50 shows the setup and the plane of rotation. ϕ is the azimuthal angle of emission and β is the angle of incidence on the solar cell). The emission spectrum of the edge emission was also analysed as a function of the emission angle (Avantes AvaSpec-2048 spectrometer) and an iris diaphragm was attached at the detector to limit the angular range detected. A flexible silicon solar cell (Sol Expert Group) was used to measure the photon flux reaching a 1 mm thick semi-circle 8 cm from the concentrator edge centre and used to normalise the area under the measured

angular distribution. The fluorescent edge concentrator was illuminated uniformly at the top surface by a LED Luxeon light source.

A cylindrical 15 mm focal length lens was attached to the edge of the concentrator in order to 'see' inside the device and directly lead light towards the detector without refraction or reflection affecting its path. Optical gel (Thorlabs) was also used to couple the concentrator edge to the lens. Finally, a thin black surface was used as a blind in order to block any light coming from directions other than the concentrator edge from reaching the detector.

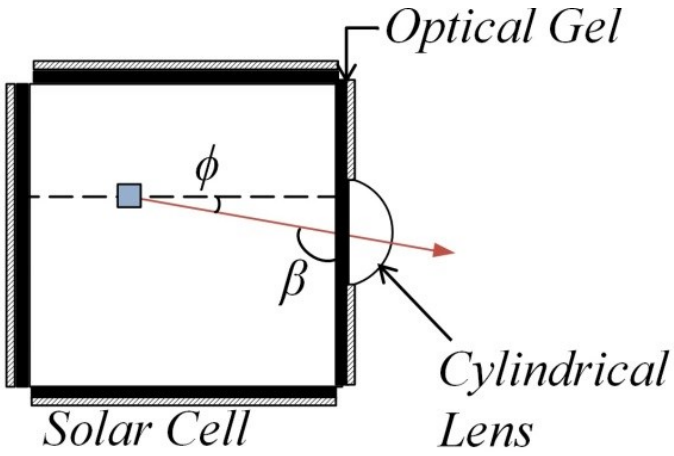

Figure 49 Angles ϕ and β in the 4Cell setups.

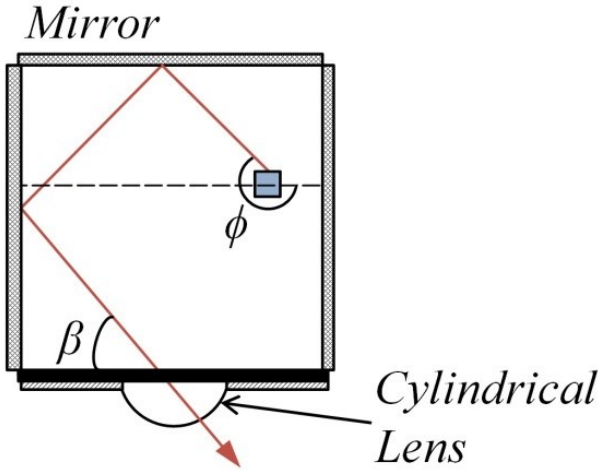

Figure 50 Angles ϕ and β in the 1Cell setup.

7.5.2. Integrated photonic fluorescent solar collector

The fluorescence of the 1D integrated photonic fluorescent solar collector fabricated was measured using a Varian Cary Eclipse spectrometer. To measure the edge

fluorescence, the 1D integrated photonic collector was excited from the top at 530 nm (2 nm bandwidth). A beam size of 5 x 2 mm was incident at the centre of the 1D integrated photonic fluorescent solar collector top surface. A blind was used to ensure that only photons escaping from the edge entered the detector placed 70 mm from the integrated photonic collector edge (Figure 51 (a), 1D IP-FSC indicates 1D integrated photonic fluorescent solar collector).

For measuring the top fluorescence, the 1D integrated photonic fluorescent solar collector was excited at 530 nm (2 nm bandwidth) from the edge. A blind with a 10 mm diameter hole at a distance of 4 mm from the top face of the 1D integrated photonic fluorescent solar collector (between the detector and the 1D integrated photonic collector) with the centre of its hole aligned to the centre of the collector top surface ensured that only photons emitted close to the normal direction (with respect to of the top surface of the photonic fluorescent solar collector) would reach the detector. The distance from the top of the 1D integrated photonic fluorescent solar collector to the detector was 80 mm (Figure 51 (b)).

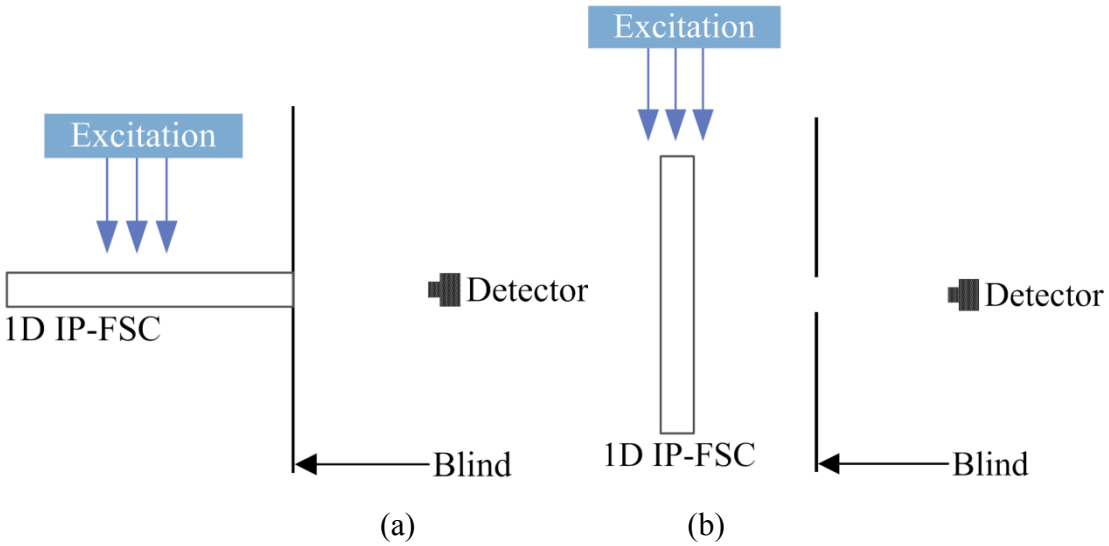

Figure 51 Measurements of (a) edge and (b) top fluorescence

7.6. Re-absorption measurements

Re-absorption is a fundamental loss mechanism in these photon management structures and can be studied experimentally from the absorbance and emission of fluorescent solar collectors. The re-absorption obtained from experimental

measurements can be used to verify the validity of models like the edge escape cone and the top and bottom escape cone models presented in Chapter 6.

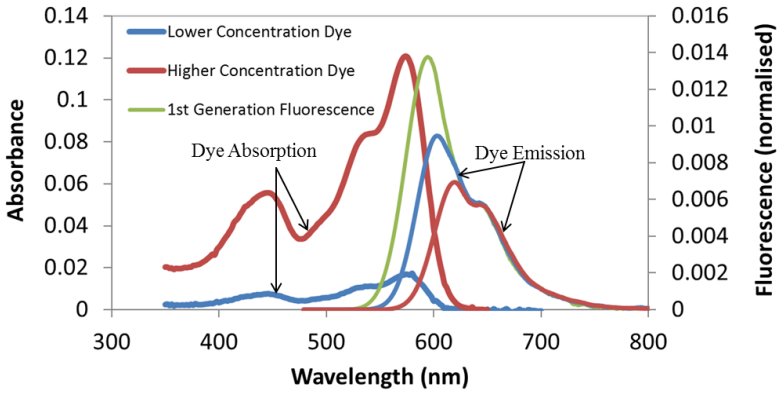

(a)

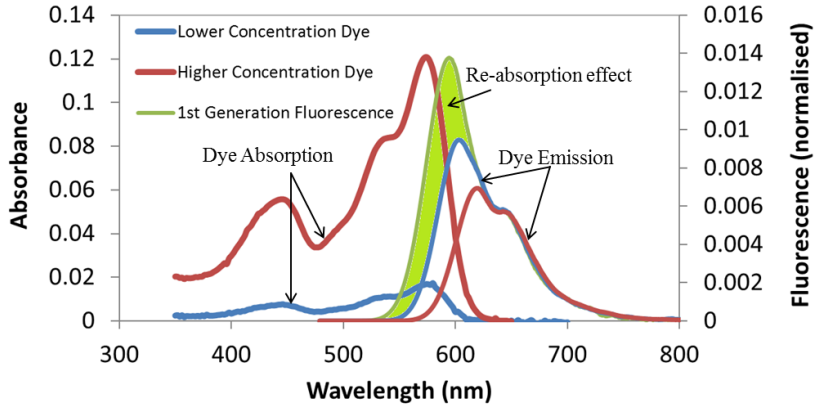

(b)

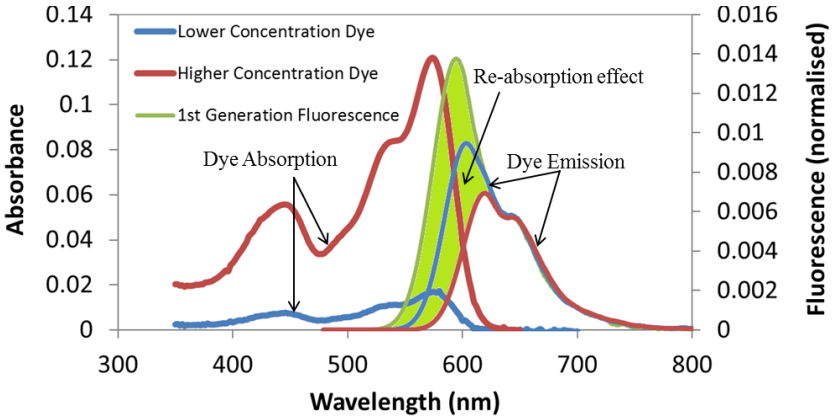

(c)

Figure 52 (a) Fluorescence emitted by low dye concentration and high dye concentration fluorescent solar collectors scaled to match the normalised first generation fluorescence at long wavelength regions. The shaded area indicates re-absorption of (b) a low dye concentration fluorescent solar collector and (c) a high dye concentration fluorescent solar collector.

Since the first generation fluorescence is free of re-absorption, the amount of re-absorption in a sample can be calculated by comparing the shape of its fluorescence with the first generation fluorescence. In long wavelength regions where there is little overlap between absorption and fluorescence, re-absorption is assumed to be small, therefore the fluorescence in this region can be scaled so as to fit the normalised first generation fluorescence. As explained in (Kittidachachan *et al.*, 2007) the relative decrease (after scaling to fit at long wavelengths) between a fluorescence spectrum and the first generation fluorescence is equal to the re-absorption probability (see Figure 52).

Re-absorption is small when the absorbance is small, a fluorescent solar collector with a small absorbance can be obtained by using low dye concentrations or by reducing the thickness of the active layer. This is clear from the Beer-Lambert law (Bouguer, 1729) (Perrin, 1948) described in Chapter 2 which tells us that the ratio of incident and transmitted light is small when either or both the absorption coefficient or the thickness is small. The absorption coefficient is small, for example, for low dye concentrations (Beer, 1852) (Perrin, 1948).

Since the first generation fluorescence is the re-absorption free fluorescence, it was obtained for the Mold-fluorescent solar collectors by grinding down the thickness and measuring the top fluorescence till no further changes in spectra was observed. For the Spin-fluorescent solar collectors, the top fluorescence of a low dye concentration samples was used to obtain the first generation fluorescence. The re-absorption probability can then be plotted against the absorption coefficient at emission wavelengths, α_{em}, obtained from A using the following equation:

$$\alpha_{\mathrm{em}} = \frac{A \ln 10}{t_{\mathrm{a}}} \tag{165}$$

where t_{a} is the thickness of the absorbing layer. Spin-fluorescent solar collectors in which the thin absorbing layer is deposited on a transparent substrate of a similar refractive index can be considered to be a homogenous plate with an effective absorption coefficient, α_{eff}. This takes into account propagation within the non-absorbing substrate (Kittidachachan *et al.*, 2007). The substrate thickness is closely connected to the re-absorption probability of trapped light within Spin-fluorescent solar collectors. Thicker substrates will result in fewer passes through the absorbing layer and

therefore a lower probabilities of re-absorption of trapped photons. The effective absorption coefficient is given by:

$$\alpha_{\text{eff}} = \alpha_{\text{em}} \frac{t_{\text{a}}}{t} \tag{166}$$

where t is the total thickness of the collector (including substrate). Figure 53 gives an example of experimentally measured results that shows the relationship between the re-absorption probability of the edge emission in the 1Cell setup, $r_{1\text{Cell}}$, and α_{em}. L is the length of the edge concentrator.

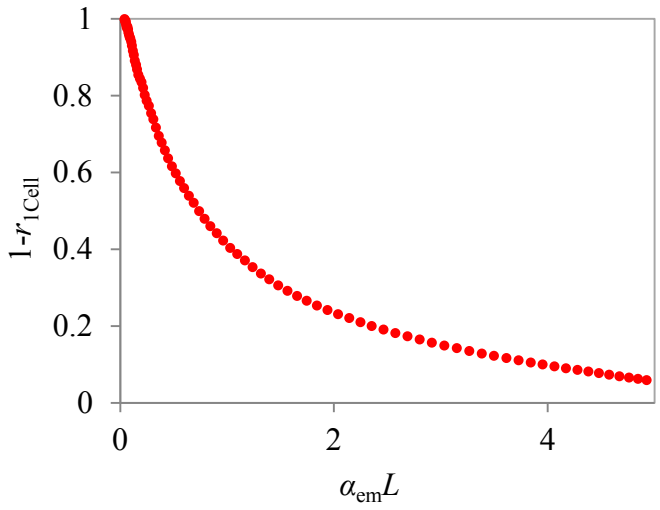

Figure 53 An example of an experimentally determined plot between the re-absorption probability and α_{em}.

7.7. Re-absorption: ray tracing simulations

The ray tracing software TracePro by Lamda Research has also been used to calculate the re-absorption probability of the different photon flux streams found within collectors. Ray tracing is useful for isolating photon flux streams that are difficult or impossible to measure like the trapped photon flux stream in the 4Cell setup. This can then be used to validate the models developed in Chapter 6. It can also be used to pin point losses or performance bottlenecks in more complicated structures such as for example in a system consisting of a fluorescent down-shifting structure coupled to a solar cell with a thick glass substrate and no edge mirrors.

The ray tracing models developed all calculate the re-absorption probability of different photon flux streams by first calculating the first generation collection efficiency, Q_{c1}, or first generation escape efficiency, Q_{e1} which are obtained by taking the ratio of the power reaching the solar cell/escaping the collector and the power emitted at that wavelength within the collector. The re-absorption probability is then obtained from the relevant solid angle of the photon flux stream considered:

$$1 - r_{\Omega} = \frac{Q_{e1,c1}}{\Omega/4\pi} \tag{167}$$

where r_{Ω} is the re-absorption probability of the photon flux emitted into solid angle, Ω. The denominator gives the fraction of emitted photons emitted into the relevant solid angle. In the two ray tracing models constructed, one assumes a uniform absorption distribution with depth while the other defines a Beer-Lambert distribution.

7.7.1. Uniform absorption profile

Ray tracing simulations were used to verify the model developed in Chapter 6 describing the re-absorption probability of the trapped photon flux of edge concentrators in the 4Cell setup. This model assumed uniform absorption across the concentrator thickness i.e. the depth of absorption of excitation photons is assumed not to affect the re-absorption probability.

The ray tracing model constructed therefore consists of a rectangular source (of the same size as the fluorescent solar collector top surface), placed at a certain depth within the collector. This rectangular source was defined to emit 10^6 monochromatic uniformly spaced rays with isotropic emission. The simulation only took into account one re-absorption event since this is how the re-absorption probability is calculated in the analytical model derived in Chapter 6. The total power of the emitted light was set to 1 W and the collector edges were modelled as perfect absorbers to simulate solar cells.

7.7.2. Non-uniform absorption profile

Ray tracing simulations of photon fluxes escaping the top and bottom escape cones in fluorescent solar collectors were run in order to verify the escape cone re-absorption

model developed in Chapter 6. The ray tracing model constructed can also explain losses in for example fluorescent down-shifting structures or concentrating fluorescent down-shifting structures, so these devices were also analysed using ray tracing. From the escape cone model developed in Chapter 6 we know that photon flux streams such as the top or bottom escape cone photon flux or the photon flux reaching a fluorescent down-shifting structure or a concentrating fluorescent down-shifting structure depends on the absorption distribution with depth i.e. it is necessary to define a non-zero absorption coefficient at excitation wavelengths.

A ray tracing model consisting of a collector that absorbs photons according to this absorption coefficient and emits fluorescence was therefore defined. A uniform source emitting parallel streams of 10^6 rays normal to the top surface of the fluorescent solar collector was also assumed

At each emission wavelength the fluorescent solar collector was also defined to have a corresponding absorption coefficient. The simulation only took into account one re-absorption event since this is how the re-absorption probability is calculated in the analytical model derived in Chapter 6.

7.8. Electrical measurements

Electrical measurements of the current output of solar cells in a solar simulator can be used to characterise the solar cells and fluorescent solar collectors used. Quantities such as the optical quantum efficiency (OQE) and short circuit current output of these systems can be used to validate the theory developed in Chapter 6 and quantify losses.

A solar simulator (T.S. Space Systems) equipped with a 300 W Xenon lamp approximating the AM1.5 spectrum and a filter selection wheel (350−1100 nm, step 50 nm) was used to measure the current output of the solar cell(s) coupled to the collectors. The Xenon lamp was calibrated using a silicon standard solar cell calibrated at the National Renewable Energy Laboratory for standard test conditions (AM1.5, 1000 W/m^2 at 25°C).

Optical gel (Thorlabs) was used for index matching (refractive index of 1.46 at 589.3 nm) between the solar cell and the collector. Index matching gel applied at the interface between the fluorescent solar collector and the solar cell ensures that light from a full hemisphere reaches the solar cell.

7.8.1. External quantum efficiency

The external quantum efficiency (EQE) of a solar cell was calculated using:

$$EQE(\lambda) = EQE_{\text{ref}}(\lambda)\frac{J_{\text{cell}}(\lambda)}{J_{\text{ref}}(\lambda)} \tag{168}$$

where J_{cell} is the short circuit current density output of the solar (i.e. the current output per unit area of the solar cell active area), J_{ref} is the short circuit current density output of the reference solar cell and EQE_{ref} is the EQE of the reference solar cell.

7.8.2. Optical quantum efficiency: fluorescent edge concentrators

The fluorescent edge concentrators tested were optically coupled to solar cells (crystalline silicon, National Renewable Energy Centre Photovoltaic Technology Centre) and/or mirrors depending on the setup. The jig that has been fabricated to make the current measurements can be seen in Figure 54 (in 4Cell setup). In the 1Cell setup three edges solar cells are replaced with mirrors.

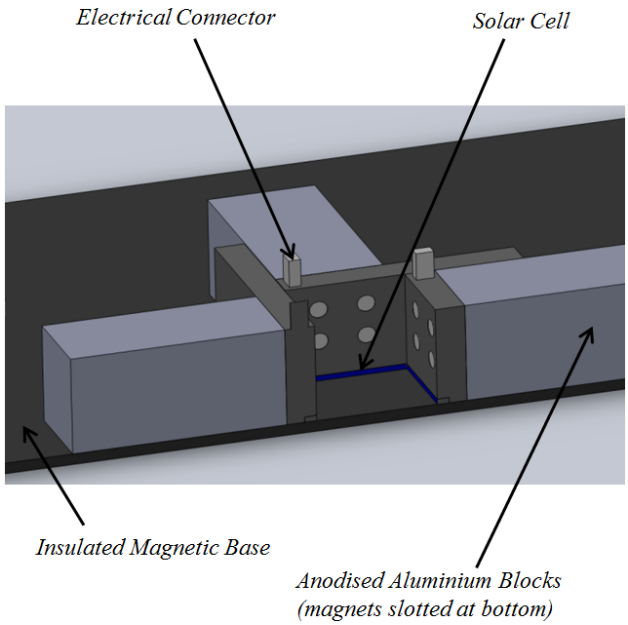

Figure 54 Jig fabricated to measure the current output of solar cells in the 4Cell setup.

The photon flux reaching the edges of the fluorescent edge concentrator, N_{edge}, in the ideal case (where the incident photon flux is perfectly parallel to the edge solar cells) is given by:

$$N_{\mathrm{edge}}(\lambda) = \frac{I_{\mathrm{sc}}(\lambda)}{qEQE_{\mathrm{f}}} \tag{169}$$

where I_{sc} is the short circuit current measured by solar cells coupled to the concentrator edges and q is the charge of an electron. EQE_{f} can be approximated by weighing the edge fluorescence with the EQE of the solar cell. This is an approximation since the measured edge fluorescence is only the edge escape cone fluorescence and does not have the true distribution of the fluorescence reaching the collector edge. Another source of error in the calculated EQE_{f} is the small number of wavelengths at which the EQE of the solar cell has been measured.

The photon flux incident on the top surface of the fluorescent edge concentrator, N_{inc}, is obtained by measuring the solar cell current output when illuminated directly by the excitation light (i.e. the solar cell surface is placed normal to the excitation light) and is given by:

$$N_{\mathrm{inc}}(\lambda) = \frac{I_{\mathrm{sc}}(\lambda)A_{\mathrm{FSC}}}{qEQE(\lambda)A_{\mathrm{cell}}} \tag{170}$$

where A_{FSC} is the area of the edge concentrator top surface and A_{cell} is the solar cell surface area. The OQE is given by:

$$OQE(\lambda) = \frac{N_{\mathrm{edge}}(\lambda)}{N_{\mathrm{inc}}(\lambda)} \tag{171}$$

Due to experimental error and also since the light source used emits to a finite solid angle, some light might reach the solar cell without first being absorbed. To improve the accuracy of the experimental results this also needs to be taken into consideration.

Excitation light incident on a solar cell coupled to an edge concentrator can be divided into two categories. The first category consists of light that hits the solar cell without

going through the fluorescent edge concentrator and the second category consists of light that passes through the fluorescent edge concentrator and is not absorbed and subsequently reaches the solar cell.

The fraction of excitation photons that directly reach the solar cell without being absorbed by the fluorescent edge concentrator can be calculated by averaging the OQE measure at long wavelength regions where the fluorescent edge concentrator does not absorb.

The fraction of excitation photons that directly reaches the solar cell without passing through the fluorescent edge concentrator can also be calculated in the same way but with the current measurements made with the top surface of the fluorescent edge concentrator covered in black tape. Taking these effects into account a more accurate value for OQE is determined.

7.8.3. Current output: fluorescent down-shifting structures

The current output of solar cells with fluorescent down-shifting structures and concentrating fluorescent down-shifting structures applied on top were also measured in a solar simulator. These fluorescent solar collectors were applied on top of cadmium sulphide (CdS)/cadmium telluride (CdTe) solar cells fabricated at the Centre for Solar Energy Research, Glyndŵr University (see, for example Irvine *et al.*, 2008 for the methodology used to manufacture them). These solar cells have been fabricated specifically for wavelength down-shifting applications and contain a relatively thick CdS buffer layer (380 nm). The solar cell performance is shown in Figure 55 (V_{oc} is the open circuit voltage, V_q is the voltage, FF is the fill factor, J_{cell} is the short circuit current density, J is the current density, P_{mpp} is the maximum power point and η_p is the power conversion efficiency). In operation, a fixed surface area (5 x 5 mm) of the solar cell was continuously exposed to incoming light.

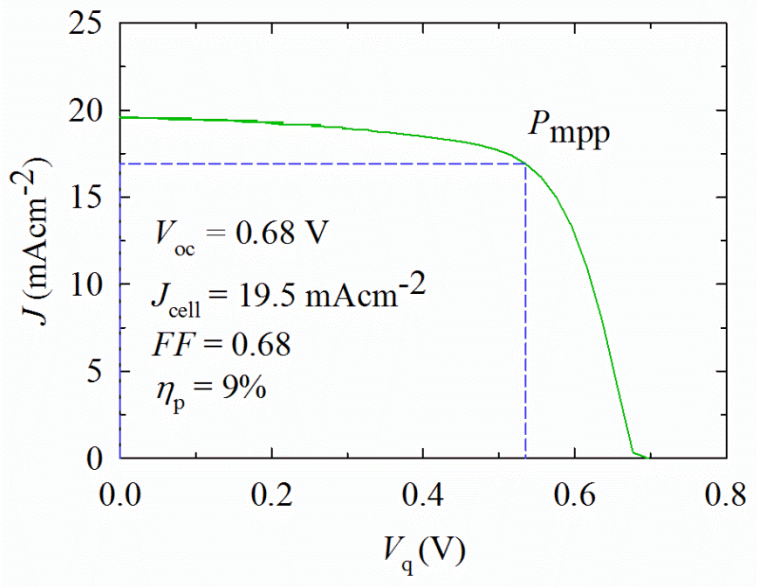

Figure 55 CdS/CdTe solar cell performance.

In the concentrating fluorescent down-shifting configuration, the collector must be much larger than the solar cell and selective index matching to areas only on top of the solar cell (as shown in Figure 56 (b)) should allow a significant amount of light to be concentrated onto the solar cell while also improving the short wavelength spectral response of the solar cell. A uniform application of index matching gel extending to the solar cell substrate (as shown in Figure 56 (a), on the other hand, should not produce any concentration effect and is, therefore, expected to give a lower current output. To highlight the benefits of a concentrating fluorescent down-shifting structure, the results of current outputs measured for both the concentrating fluorescent down-shifting and fluorescent down-shifting configurations were investigated.

The solar cell current output was also measured for an un-doped fluorescent solar collector applied on the CdS/CdTe solar cell. This was used to compare the effect of wavelength down-shifting and light concentration while ensuring that effects associated with the substrate and PMMA are not taken into consideration.

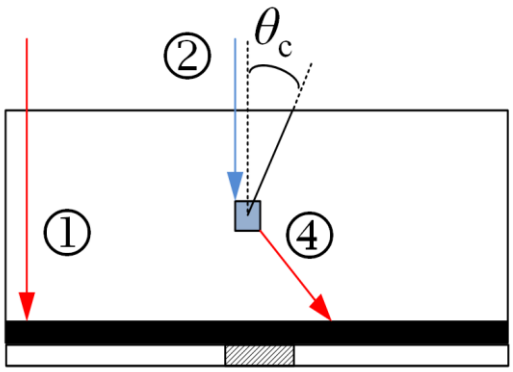

(a)

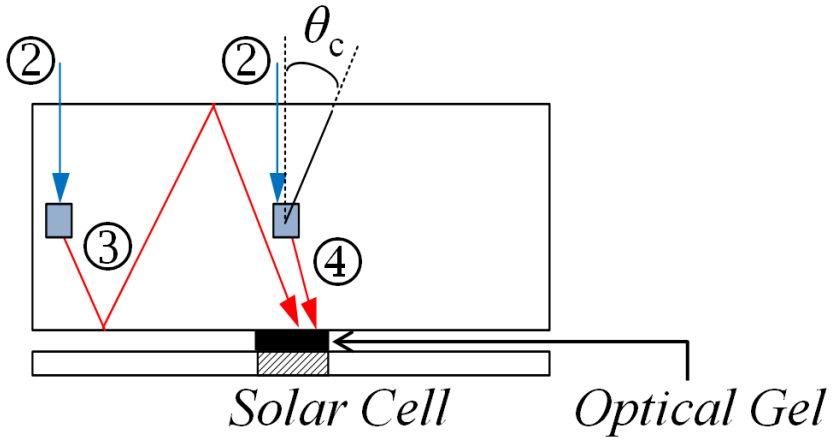

(b)

Figure 56 Comparison of: (a) a fluorescent down-shifting structure and (b) a concentrating fluorescent down-shifting structure. The different rays shown are 1) long wavelength incident ray not absorbed by fluorescent solar collector, 2) short wavelength incident ray absorbed by fluorescent solar collector, 3) trapped fluorescence reaching the solar cell and 4) fluorescence directly reaching solar cell/solar cell substrate. The blue rectangle represents a fluorescent molecule.

7.9. Summary

This chapter has outlined the fabrication and characterisation of fluorescent solar collectors conducted in this project. Methods discussed include fabrication by spin coating as well as characterisation using ellipsomtry, reflectometry, spectrometers and solar simulators. Settings used in ray tracing simulations have also been outlined. The results of this experimental work will be presented in the next chapter along with

comparisons with the theory developed in Chapter 6 and from the literature i.e. Chapter 2 and Chapter 5.

References

Barbé, J., Thomson, A.F., Wang, E, McIntosh, K. and Catchpole, K., 2011. *Nanoimprinted TiO_2 sol-gel passivating diffraction gratings for solar cell applications.* Progress in Photovoltaics: Research and Applications. 20: 143-148. DOI: 10.1002/pip.1131.

Beer, A., 1852. *Bestimmung der absorption des rothen lichts in farbigen flüssigkeiten*. Annalen der Physik und Chemie. 162: 78-88. DOI: 10.1002/andp.18521620505.

Bouguer, P., 1729. *Essai d'optique, sur la graduation de la lumiere*. Chez Claude Jomber: Paris, France.

Irvine, S.J.C., Barrioz, V., Lamb, D., Jones, E.W. and Rowlands-Jones, R.L., 2008. *MOCVD of thin film photovoltaic solar cells-Next-generation production technology?* Journal of Crystal Growth. 310: 5198-5203. DOI: 10.1016/j.jcrysgro.2008.07.121.

Kittidachachan, P., Danos, L., Meyer, T.J.J., Alderman, N. and Markvart, T., 2007. *Photon collection efficiency of fluorescent solar collectors*. Chimia International Journal for Chemistry. 61: 780-786. DOI: 10.2533/chimia.2007.780.

Perrin, F.H., 1948. *Whose absorption law?* Journal of the Optical Society of America. 38: 72-74. DOI: 10.1364/JOSA.38.000072.

Reisfeld, R., Levchenko, V., Saraidarov, Ts., Rysiakiewicz-Pasek, E., Barnowski, M., Podhorodecki, A., Misiewicz, J. and Antropova, T., 2012. *Steady state and femtosecond spectroscopy of perylimide red dye in porous and sol-gel glasses.* Chemical Physical Letters. 546: 171-175. DOI: 10.1016/j.cplett.2012.07.073.

Valeur, B., 2001. *Molecular fluorescence: Principles and applications.* Wiley-VCH Verlag: Weinheim, Germany. DOI: 10.1002/3527600248

Woollam, J.A., 2014, *Ellipsometry tutorial*. www.jawoollam.com. [Accessed 15 March 2014].

Yeh, P., 1988. *Optical waves in layered media.* John Wiley & Sons: New York, USA.

8. Results and discussion

8.1. Introduction

This chapter details the key results following on from the theory developed in Chapter 6 and the experimental details from Chapter 7. Experimental and computer simulations have been used to verify the models presented in Chapter 6. Analyses of the losses and efficiencies found in the fabricated conventional fluorescent solar collectors as well as optimisation of fluorescent edge concentrators have also been presented. The theory of photonic crystals has also been used to explain the emission measurements detected. The results presented in this chapter can be divided into four sections, i.e.:

- Re-absorption in conventional collectors: re-absorption models developed in chapter 6 for different photon flux streams will be validated by comparisons with experimental measurements where possible or ray tracing simulation results.
- Fluorescent edge concentrators:
    - Angular resolved measurements for different fluorescent edge concentrator configurations, i.e. concentrators coupled to 1 edge solar cell and 3 edge mirrors (1Cell setup) or coupled to 4 edge solar cells (4Cell setup), will be presented. The 4Cell setup will be seen to perform close to that of an ideal device.
    - The optical quantum efficiency (OQE) of ideal models will be compared to practical devices and losses will be quantified.
    - The power conversion efficiency of ideal systems will be optimised using the models developed.
- Concentrating fluorescent down-shifting structures:
    - The theory of operation of these devices will be used to explain the current output of concentrating fluorescent down-shifting structures. The contribution of fluorescence and direct excitation light to the current output will be estimated from theory.
    - The losses found in these devices will be explored through experimental work and ray tracing simulations.
- 1D integrated photonic fluorescent solar collector:

- The measured transmittance of the integrated photonic fluorescent solar collector fabricated will be compared to calculations based on the transfer matrix method.
- The characteristic emission distribution detected from the integrated photonic collector will be used to show the potential of these devices and will be seen to be well described by the band structure of the integrated photonic collector.
- The photon transport for an integrated photonic fluorescent solar collector consisting of an infinite stack will be analysed using the band structure of the device. This will be used to approximate the trapped photon flux in order to illustrate the potential of these devices.

8.2. Re-absorption in conventional fluorescent solar collectors

This section compares the re-absorption probabilities obtained from experimental measurements and ray tracing simulations to predictions of modelling developed in Chapter 6. The effect of re-absorption has a large impact on to the performance of fluorescent solar collectors, therefore accurate modelling of this is important in the understanding and design of high efficiency collector based systems. The re-absorption probabilities of the edge escape cone, top and bottom escape cones and of the trapped photon flux (4Cell setup) have been studied. The performance of the 4Cell setup is especially important since, as detailed in Chapter 4, the highest efficiency fluorescent edge concentrators reported in the literature all use this setup, a greater understanding of this setup is therefore important. As stated in Chapter 6, the re-absorption models were all derived using the following general expression:

$$1 - r_{\Omega}(\lambda) = \int \frac{dV}{V} \int_{\Omega} \exp(-\alpha_{\mathrm{em}}(\lambda) l) \frac{d\Omega}{\Omega} \tag{119}$$

which describes the re-absorption probability, r_{Ω}, of the photon flux of wavelength λ emitted into a solid angle Ω in a fluorescent solar collector. V is the volume of the fluorescent solar collector, dV is a small volume element, $d\Omega$ is a small solid angle element, l is a measure of the path length from point of emission to a solar cell and α_{em} is the absorption coefficient at the emission wavelength.

8.2.1. Edge escape cone re-absorption

A comparison between the results of the theoretical model of the edge escape cone re-absorption probability with the experimental measurements of spin coated collectors (Spin-fluorescent solar collectors) R0.4 [0.09] and R0.6 [0.12] can be seen in Figure 57 (recall the collector naming convention adopted in Chapter 7 i.e. a collector is classified by the letters designating different dyes followed by the dye concentration in g/l and the peak absorbance of the collector. R0.4 [0.09], therefore, indicates a collector consisting of BASF Lumogen F series Red 305 dye doped at 0.4 g/l and with a peak absorbance of 0.09). In this figure, r_{edge} is the re-absorption probability of the edge escape cone photon flux and L is the length of the edge concentrator. It is clear from the results that the spectroscopic measurements of the emission exiting the collector edge agree well with the edge escape cone model.

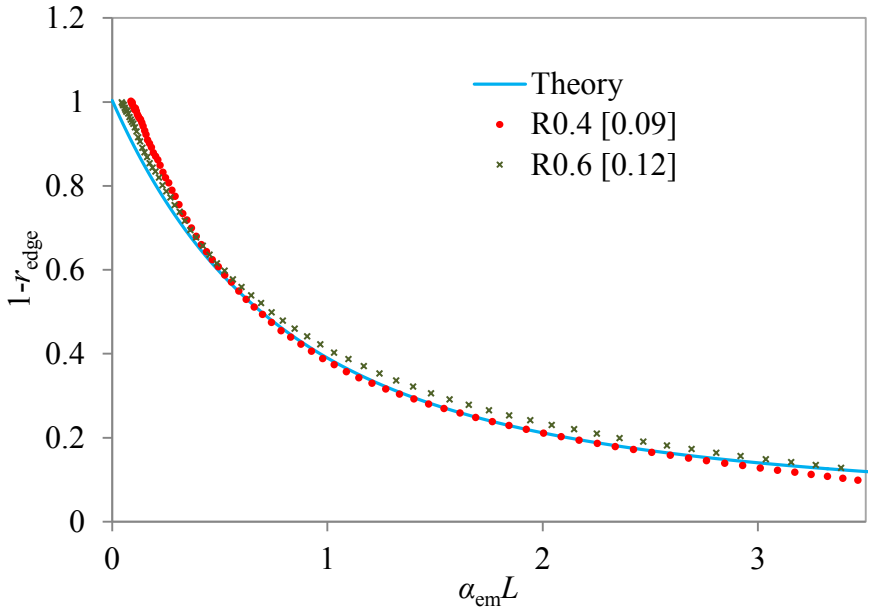

Figure 57 Comparison of the edge escape cone re-absorption model with experimental measurements.

8.2.2. Escape cone re-absorption

A comparison between the analytical model and ray tracing simulations for the top and bottom escape cone re-absorption probability can be seen in Figure 58 (in this figure $r_{t\&b}$ is the re-absorption probability of the top and bottom escape cone photon

flux and t is the thickness of the collector). The following have been assumed: the absorption coefficient at the excitation wavelength is equal to 0.23 mm^{-1}, the fluorescent solar collector has a refractive index of 1.5 and dimensions equal to 20 x 20 x 1 mm. The results of the ray tracing appear to agree well with the re-absorption model.

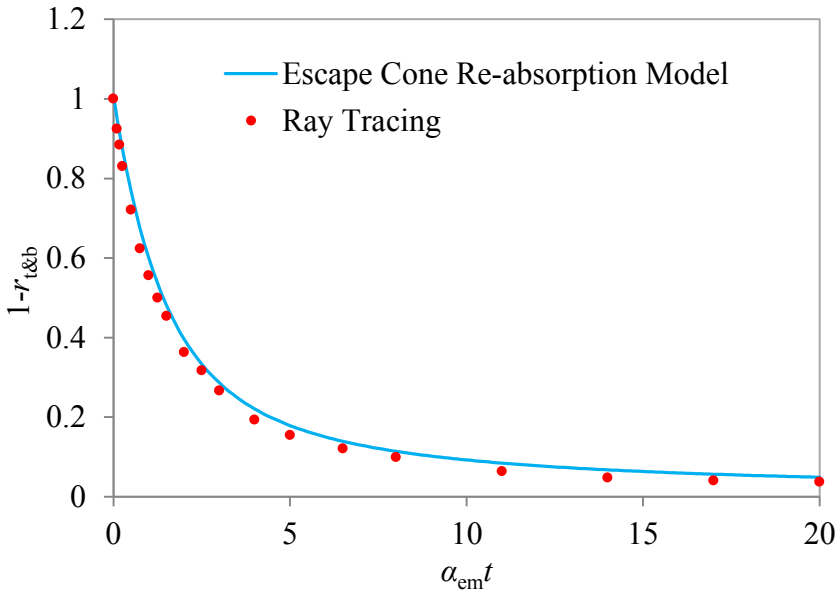

Figure 58 Top and bottom escape cone re-absorption model compared to ray tracing results. Absorption coefficient at the excitation wavelength assumed to be 0.23 mm^{-1}.

Similar to the re-absorption of the edge emission that can be studied spectroscopically, the top and bottom escape cone re-absorption can also be studied in a similar manner. Even though the light exiting the fluorescent solar collector through these escape cones is not the same as that which is 'seen' by the solar cell, the measured light can be used to validate modelling of these devices and add to the understanding of the top and bottom escape cone loss.

The analytical model of the bottom fluorescence has, therefore, been compared with experimental measurements of Spin-fluorescent solar collectors named O0.4 [0.9] and O0.8 [0.16] (O indicated BASF Lumogen F series Orange 240 dye). These collectors were deposited at a speed of 10,000 rpm and the results are shown in Figure 59 (r_b in this figure is the re-absorption probability of the bottom escape cone). These results indicate agreement between the model and experimental results.

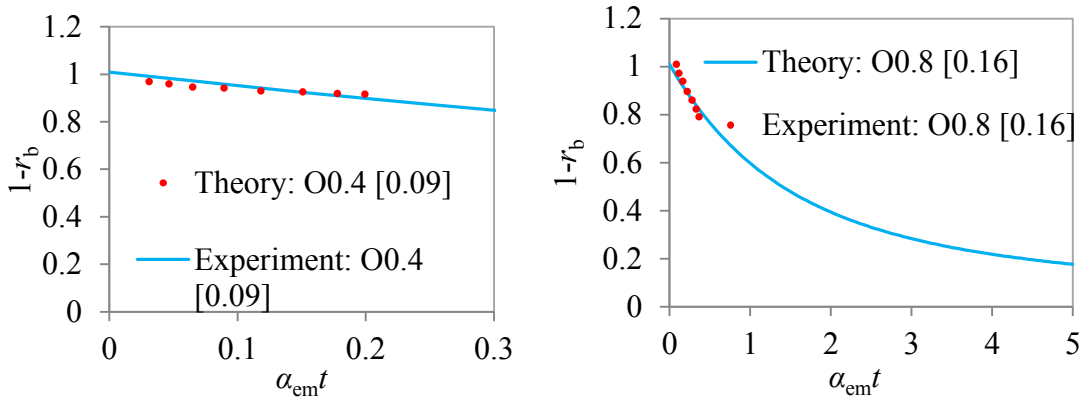

(a) (b)

Figure 59 Bottom escape cone re-absorption: comparison between theory and experiment for (a) O0.4 [0.9] and (b) O0.8 [0.16] fluorescent solar collectors.

8.2.3. Four solar cell configuration: trapped photon re-absorption

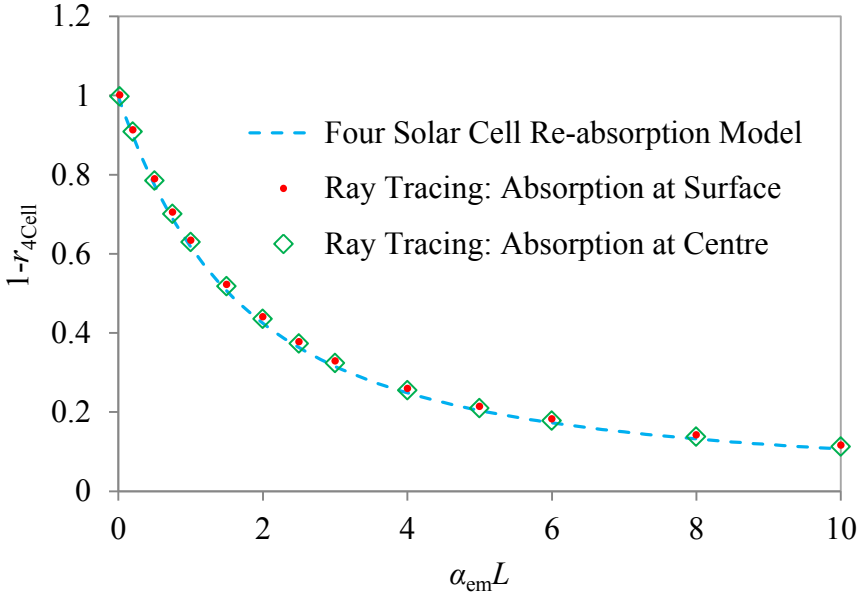

Figure 60 Comparison between the 4Cell re-absorption model and ray tracing results.

Ray tracing has again been used to verify the re-absorption model for the trapped photon flux in a 4Cell setup. The results are plotted in Figure 60 (the fluorescent edge concentrator dimensions have been defined as 20 x 20 x 1 mm and the refractive index is equal to 1.5). r_{4Cell} in this figure is the re-absorption probability of the trapped photon flux in the 4Cell setup. It is seen that the re-absorption probability predicted by the

model is similar to the results of the ray tracing. The ray tracing simulations have been conducted for emission occurring at two different depths i.e. emission occurring only at the top surface and emission occurring only at the center of the fluorescent edge concentrator thickness. For both depths of emission the results are the same, this validates the assumption that the depth of emission does not affect the re-absorption probability of the trapped photon flux.

8.3. Fluorescent edge concentrators

8.3.1. Angular resolved measurements of edge fluorescence

A study of the angular characteristics of the fluorescence emitted from a R0.3 [0.85] moulded collector (Mold-fluorescent solar collector) has been conducted for different azimuthal angles of emission. This has been conducted so as to pinpoint loss of photons within the device. This study should therefore give insights into the design of high efficiency fluorescent solar collector based systems.

As described in Chapter 6 the re-absorption probability for different azimuthal angles, ϕ, of emission, Γ, is given by:

$$1 - \Gamma(\phi, \lambda) = \int \frac{dA_{\mathrm{FSC}}}{A_{\mathrm{FSC}}} \int_{\theta_c}^{\pi-\theta_c} \exp(-\alpha_{\mathrm{em}}(\lambda) l) \frac{\sin\theta \, d\theta}{2(1-P)} \tag{126}$$

where A_{FSC} is the fluorescent edge concentrator top surface area, dA_{FSC} is a small area element, P is the fraction of photons emitted into the escape cones, θ is the zenith angle of emission and θ_c is the critical angle. The specific re-absorption probabilities for the different setups depend on the calculation of the path lengths as detailed in Chapter 6.

We also recall that the average angular re-absorption probability, Γ' is calculated using an expression similar to the connection between the average re-absorption probability of trapped photons, R, and the re-absorption probability of trapped photons, r, as detailed in (Kittidachachan *et al.*, 2007), i.e.:

$$\Gamma'(\phi) = \int_0^{\infty} \Gamma(\phi, \lambda) f_1(\lambda) d\lambda \tag{127}$$

where f_1 is the first generation fluorescence.

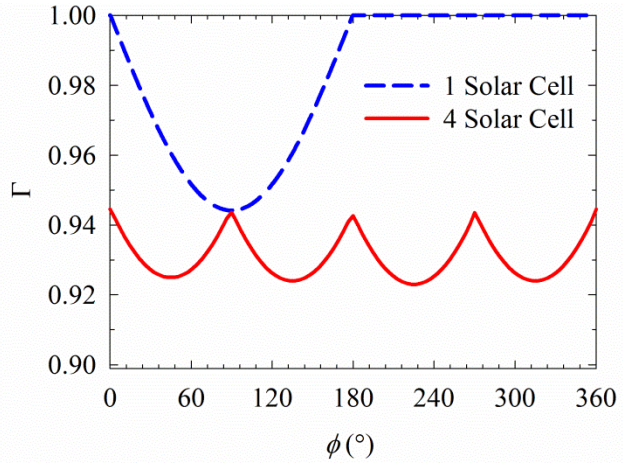

Figure 61 The angular dependence of the re-absorption probability in the 4Cell and 1Cell setups for fixed edge concentrator dimensions (analytical).

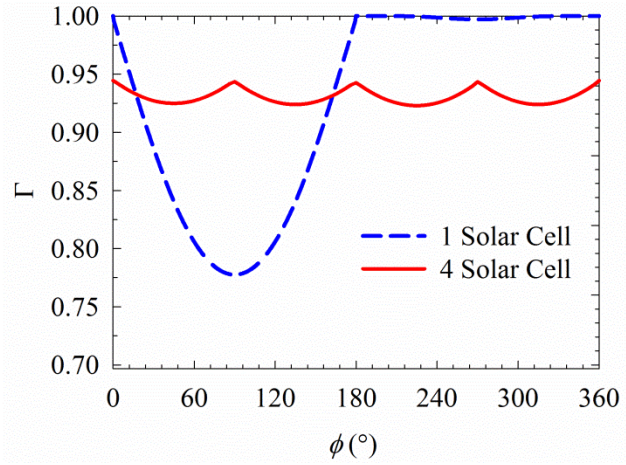

Figure 62 The angular dependence of the re-absorption probability in the 4Cell and 1Cell setups for fixed edge concentrator gain (analytical).

The expressions described have been used to study the photon transport for the 1Cell and 4Cell setups. For simplicity, photon transport at only the peak emission wavelength, i.e. 600 nm (α_{em} equal to 0.8 mm^{-1}) will be described. Γ calculated for the two setups using the models described is shown in Figure 61 for fixed dimensions of the fluorescent edge concentrator while in Figure 62 the gain is fixed (the gain is defined as the ratio between the fluorescent edge concentrator top surface area and edge solar cell area).

The results indicate that the variation of Γ with ϕ for the 4Cell setup is fairly constant. For the 1Cell setup, Γ is seen to go to unity for azimuthal angles of emission close to parallel to the edge mounted solar cell due to long path lengths.

Furthermore, there is a significant difference in Γ for fluorescence emitted towards and away from the solar cell. For the 4Cell setup it is noticed that photons emitted directly towards a solar cell surface (i.e. close to 90°) have higher re-absorption. This is most likely because, these rays, no matter their point of origin can only reach one particular solar cell and therefore travel longer path lengths on average. It is noticed that when the dimensions of the fluorescent edge concentrator are kept constant the fluorescence within the 4Cell setup experiences significantly lower re-absorption while when the gain is fixed the total re-absorption (as represented by the area under the curves) is similar for both setups. This indicates that in ideal fluorescent edge concentrators, the performance should be similar for both configurations if the gain is kept constant.

Figure 63 shows the measured variation in the photon flux of emission reaching the edge(s) in a 4Cell and 1Cell setup (fixed fluorescent edge concentrator dimensions) with the azimuthal angle of incidence on the solar cell (β). The plotted curves have been normalised such that the integration over all angles gives the photon flux measured by a flexible solar (note that the total photon flux for the 4Cell setup is four times the photon flux measured by the flexible solar cell at one edge).

For both setups it is clear that the photon flux decreases for angles close to parallel to a given edge mounted solar cell. Furthermore, as expected (due to lower re-absorption) more photons reach the edge(s) in the 4Cell setup than in the 1Cell setup. Spectroscopic measurements strongly indicate that the reduction in photon flux at certain angles for the two different setups is for very different reasons. For the 4Cell setup it is in fact seen that fluorescence reaching the fluorescent edge concentrator edge at azimuthal angles close to parallel to the edge is blue-shifted compared to fluorescence incident perpendicular to the edge (Figure 64 shows spectra with angle β). This indicates that re-absorption is lower at angles close to parallel to the solar cell. This could be because for emission at steep angles to reach a given solar cell, the point of emission must be very close to the fluorescent edge concentrator edge otherwise this emission will reach another solar cell. This also explains why the distribution of the photon flux with angle β is only large for a smaller range of angles for the 4Cell setup. The situation is seen to be reversed for the 1Cell setup where the spectra indicates that the re-absorption probability increases from emission perpendicular to parallel to the edge mounted solar cell as seen by the corresponding red-shift (Figure 65).

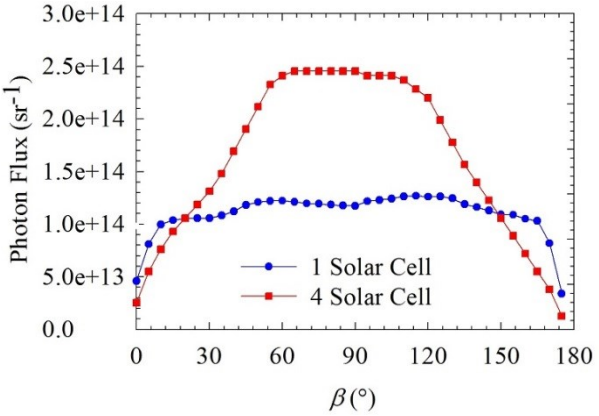

Figure 63 The photon flux reaching solar cells in a Mold-fluorescent edge concentrator in the 1Cell and 4Cell setups as a function of angle β.

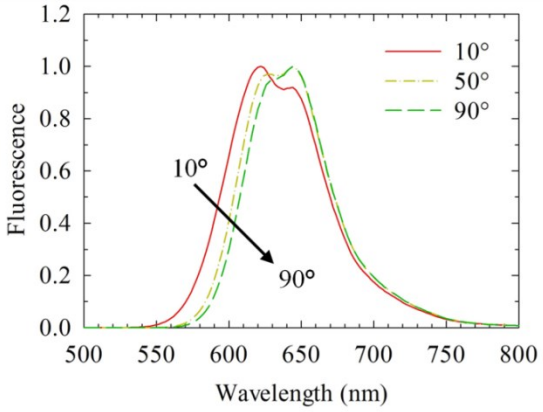

Figure 64 Spectra of emission reaching the solar cell between 10° and 90° (angle β) for a Mold-fluorescent edge concentrator in the 4Cell setup.

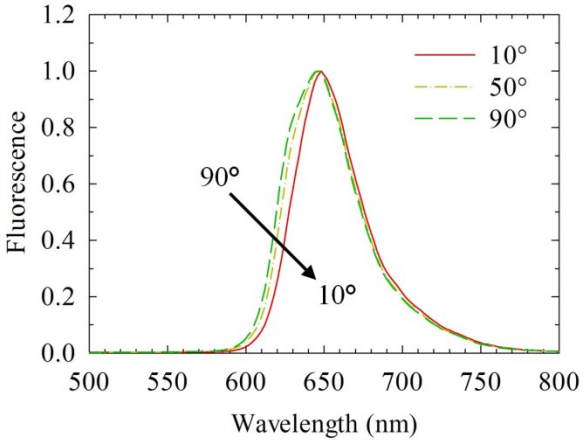

Figure 65 Spectra of emission reaching the solar cell between 10° and 90° (angle β) for a Mold-fluorescent edge concentrator in the 1Cell setup.

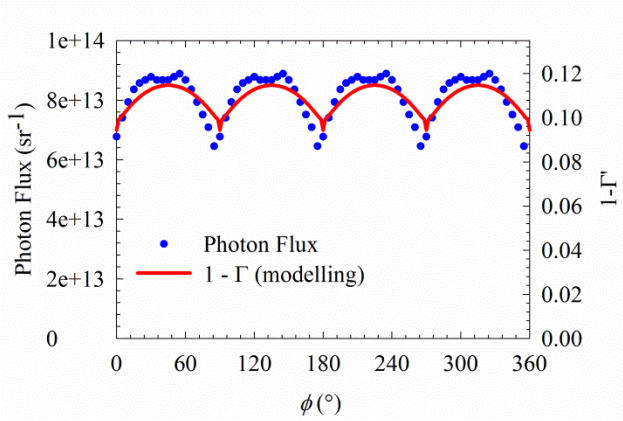

Figure 66 The photon flux reaching the solar cells coupled to a Mold-fluorescent edge concentrator in the 4Cell setup, as a function of angle ϕ, compared to 1 - Γ'.

Assuming that in the 4Cell setup each solar cell sees the same distribution of the photon flux with angle β, then a summation of these photon fluxes will give the photon flux distribution as a function of the emission angle ϕ reaching a solar cell. To compare this with the modelling, Γ' was calculated using Equation (127)) for the R0.3 [0.85] Mold-fluorescent solar collector. The results have been plotted in Figure 66. It is seen from the results that the angular distribution of the photon flux shows the same pattern as the corresponding 1 - Γ'.

From Chapter 6 we know that the photon flux emitted at an angle ϕ reaching the edge, N_{edge}, can be written as (assuming only the trapped photon flux reaches the fluorescent solar collector edge):

$$N_{\text{edge}}(\phi) = \rho(\phi) \int Q_a(\lambda) N_{\text{inc}}(\lambda) d\lambda \tag{129}$$

where ρ is the angular collection efficiency, Q_a is the absorption efficiency and N_{inc} is the incident photon flux. In Equation (129)) the term in the integral is a constant independent of ϕ, therefore:

$$N_{\text{edge}}(\phi) \propto \rho(\phi) \tag{130}$$

In Chapter 6 it was also shown how in an ideal edge concentrator ρ is directly proportional to 1 - Γ' (ϕ), so in such devices N_{edge} should also be directly proportional

to 1 - Γ' (ϕ). The angular results plotted in Figure 66, is consistent with the performance of the 4Cell Mold-fluorescent solar collector being well described by ideal models.

8.3.2. Optical quantum efficiency

The theoretical OQE for the 4Cell setup has been compared to the experimentally measured OQE. This should give an indication of the accuracy of the models developed as well as estimates of non-ideal losses in the devices studied. We recall from Chapter 6 how the OQE can be obtained from the collection efficiency, Q_{c}, which in turn is obtained from the re-absorption probabilities detailed in the previous section:

$$OQE(\lambda) = Q_{\mathrm{a}}(\lambda)Q_{\mathrm{c}} \tag{130}$$

Figure 68 and Figure 70 shows the comparison between experiment and theory for the OQE of R0.3 [0.85] and R0.8 [6.5] Mold-fluorescent edge concentrators respectively. The theory is seen to fit with experiment rather well. Figure 67 and Figure 69 shows the absorbance, first generation fluorescence and edge fluorescence for the R0.3 [0.85] and R0.8 [6.5] fluorescent edge concentrators respectively. The absorbance of the R0.8 [6.5] sample is seen to saturate so the R0.3 [0.85] absorbance has been scaled to match it in regions where there is no saturation so as to give a better approximation of its true absorbance.

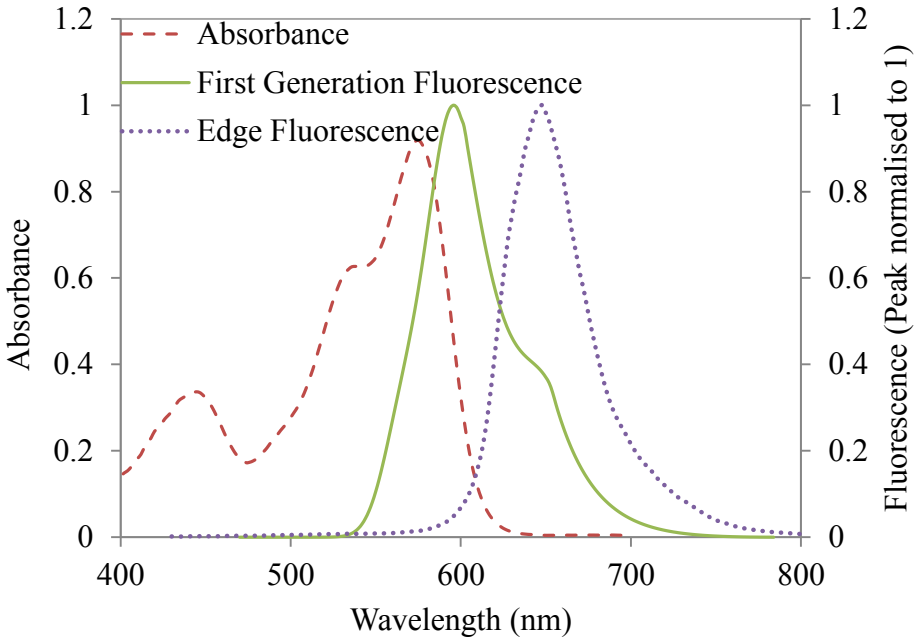

Figure 67 Absorbance, first generation fluorescence and edge fluorescence of R0.3 [0.85].

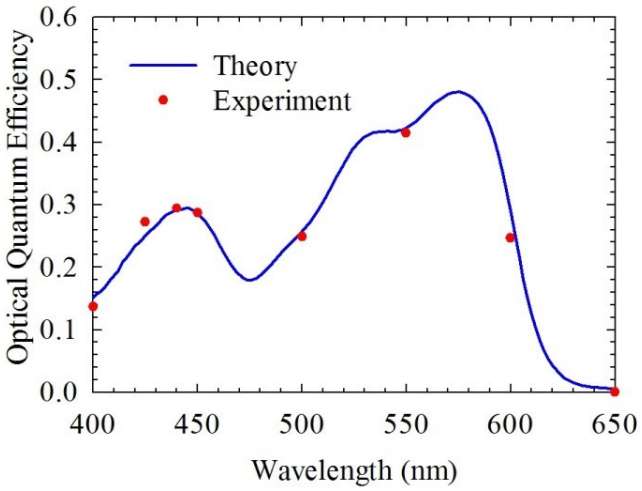

Figure 68 Comparison between theory and experimental results for a R0.3 [0.85] Mold-fluorescent edge concentrator in the 4Cell setup.

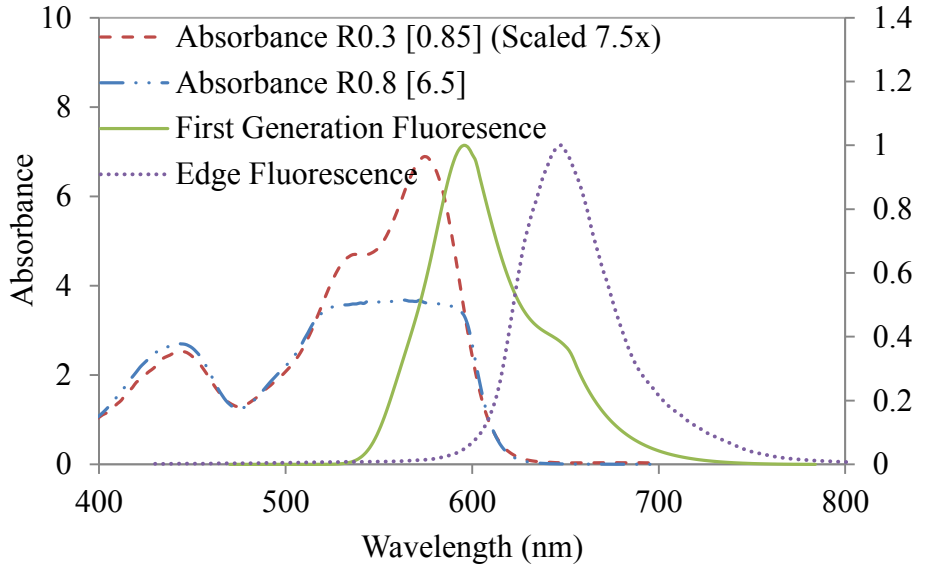

Figure 69 Absorbance, first generation fluorescence and edge fluorescence of R0.8 [6.5].

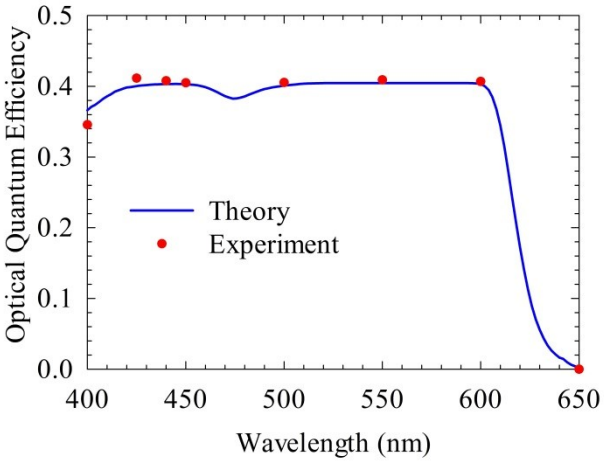

Figure 70 Comparison between theory and experimental results for a R0.8 [6.5] Mold-fluorescent edge concentrator in the 4Cell setup.

It is clear that the R0.3 [0.85] sample has a relatively low absorbance, the OQE follows the shape of the absorbance (or more accurately, the shape of Q_a). The OQE of the R0.8 [6.5] sample is seen to be rather flat since its absorbance is consistently higher than 1 for incident photons of wavelengths between 400 nm and 600 nm. This near constant OQE indicates that the variation in Q_c with wavelength is relatively small.

On comparing the calculated OQE with experimental results of a Mold-fluorescent solar collector and Spin-fluorescent solar collector (doped at 300 mg/l) in the 1Cell

setup (Figure 71 and Figure 72, FSC is fluorescent solar collector) it is apparent that for these there are non-ideal losses. This loss has been highlighted in green in Figure 71 and Figure 72. For the Mold-fluorescent solar collector in the 1Cell setup we notice a 22% drop in the OQE across all absorbing wavelengths. This wavelength independent difference indicates that this is due to non-ideal transport losses most likely due to reflection at edges coupled to mirrors. For the Spin-fluorescent solar collector this loss increases to 75% most likely due to scattering in the thin film layers. The ability to quantify these non-ideal losses would be useful in the optimisation and design of non-ideal fluorescent solar collectors.

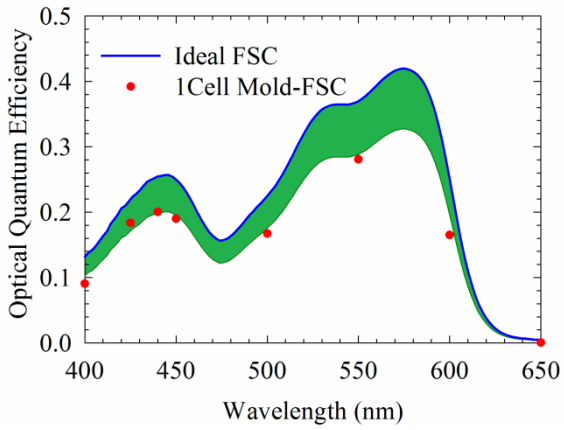

Figure 71 Comparison between theory and experimental results for a R0.3 [0.85] Mold-fluorescent edge concentrator in the 1Cell setup.

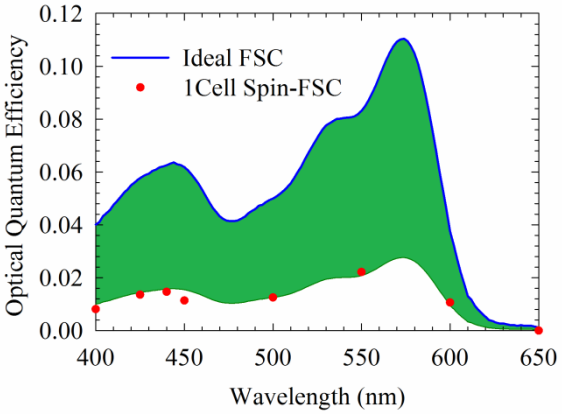

Figure 72 Comparison between theory and experimental results for a R0.3 [0.09] Spin-fluorescent edge concentrator in the 1Cell setup.

8.3.3. Optimisation of fluorescent edge concentrator

This section demonstrates a useful application of the models developed i.e. a tool for the optimisation of Mold-fluorescent edge concentrators in the 4Cell setup (shown in the previous section to be well described by the models developed).

The absorbance, i.e. Q_a in Equation (130)), of fluorescent edge concentrators doped with R dye has been optimized. The absorbance of the Mold-fluorescent edge concentrator R0.3 [0.85] has been scaled and the OQE has been calculated for different scaling factors as shown in **Figure 73**. It is seen that as the absorbance increases, the OQE becomes flatter across absorbing wavelengths. A peak OQE close to 50% for excitation at 570 nm is seen on doubling the absorbance of the R0.3 [0.85] Mold-fluorescent edge concentrator.

On increasing the absorbance further a decrease in the peak OQE is seen due to the competing requirements for high Q_a and Q_c. After a certain absorbance the benefit of greater absorption does not compensate for the higher re-absorption resulting in a decrease in the Q_c (as indicated by Equation (130))).

We recall from Chapter 6 that the OQE can be connected to the power conversion efficiency, $\eta_{p,}$ i.e.:

$$\eta_p = \frac{V_{oc} FF q \int N_{inc}(\lambda) OQE(\lambda) EQE_f(\lambda) d\lambda}{\int P_{inc}(\lambda) d\lambda} \tag{135}$$

where V_{oc} is the open circuit voltage, FF is the fill factor, q is the charge of an electron, EQE_f is the average external quantum efficiency (EQE) of the solar cell to the incident fluorescence and P_{inc} is the power of the incident photon flux.

Figure 74 shows the power conversion efficiency calculated from Equation (135)) when coupled to four gallium arsenide solar cells. The solar cells are assumed to have V_{oc} equal to 1.11 and a fill factor of 0.87 (Green *et al.*, 2011) (it is assumed that the increase in V_{oc} with concentration is negligible). The fluorescence incident on the solar cell is also assumed to be converted with an EQE of 0.95.

The results indicate that a peak power conversion efficiency of close to 4.5% is expected if the absorbance of the R0.3 [0.85] Mold-fluorescent edge concentrator is

scaled by a factor of 4. After this peak, a slight decrease is observed due to the effect of re-absorption.

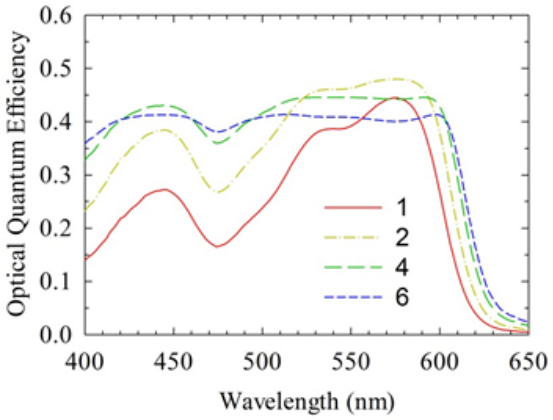

Figure 73 Optical quantum efficiency with scaled absorbance.

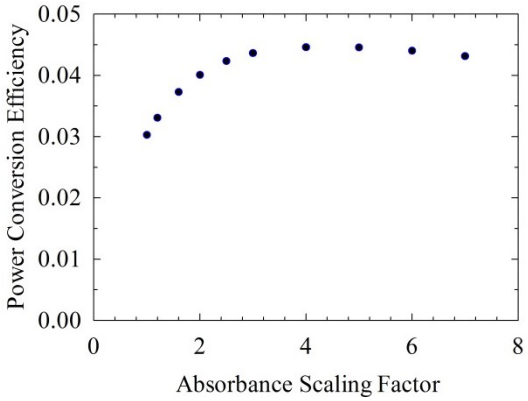

Figure 74 Power conversion efficiency with scaled absorbance.

8.4. Concentrating fluorescent down-shifting structures

This section details experimental results of the current output of cadmium sulphide (CdS)/ cadmium telluride (CdTe) solar cells coupled to fluorescent down-shifting structures and concentrating fluorescent down-shifting structures. An attempt has also been made to estimate the current contribution of down-shifted light based on the Q_a of the collector, the incident photon flux and the EQE of the solar cell.

A number of losses in these systems have also been studied including losses due to the fluorescent solar collector and solar cell substrate thicknesses and edge escape cones. Figure 75 shows the absorbance and emission (i.e. first generation fluorescence) spectra

of the Y (Y indicates BASF Lumogen F series Yellow 083 dye) and O dye, the EQE of the CdS/CdTe solar cell used and the photon flux distribution of a typical Xenon lamp. It is readily apparent that absorbance by the O and Y dyes takes place in regions where the EQE of this solar cell is poor. The fluorescence of the O dye occurs however at wavelengths converted with a much higher EQE.

The large overlap between the emission of the Y dye and the absorbance of the O dye indicates the possibility of energy transfer that should result in a red shift of the emission in samples containing a mixture of both dyes. The benefit of this is that emission of fluorescence at longer wavelengths results in better electrical conversion by the solar cell.

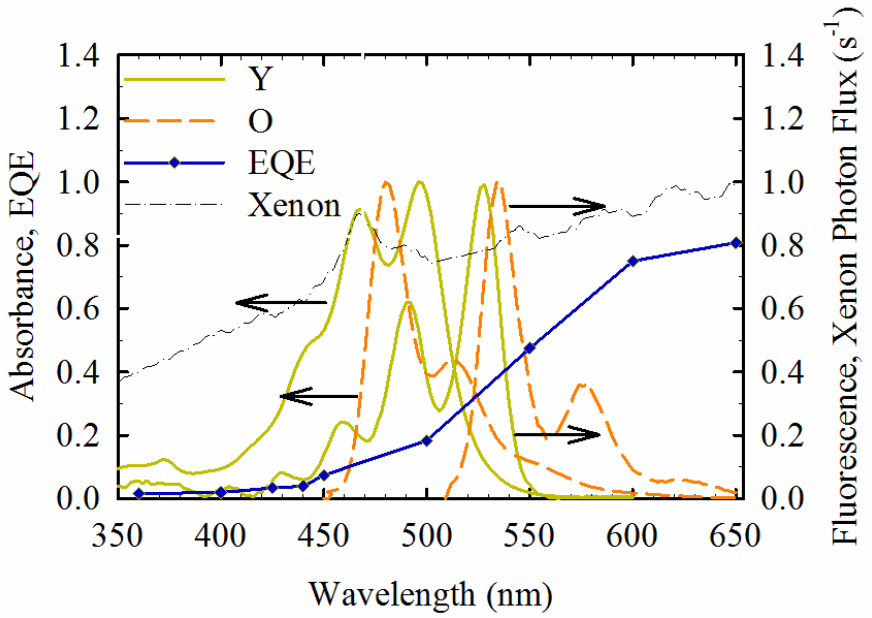

Figure 75 Absorbance and first generation fluorescence spectrum of Y and O dyes. The EQE of the CdS/CdTe solar cell used is also plotted. The peaks have been normalized to unity. The absolute value of the Xenon lamp photon flux at 650 nm is 2.7x1018 $s^{-1}m^{-2}nm^{-1}$.

8.4.1. Current output of solar cell coupled to fluorescent down-shifting structures

Measurements under white light (Xenon lamp) of CdS/CdTe solar cells coupled to concentrating fluorescent down-shifting structures with different Y dye concentrations were conducted so as to get a range of suitable dye concentrations for large solar cell current output. The results indicate that a Y dye concentration of 5 g/l gave the greatest increase in solar cell current output as shown in Figure 76 (I_{sc} in this figure is the short

circuit current, C-FDS is concentrating fluorescent down-shifting structure and poly(methyl methacrylate) (PMMA) (in caption) is poly(methyl methacrylate)). Beyond this dye concentration a reduction is observed possibly due to diminishing returns in Q_a and increases in re-absorption losses (similar to the optimisation results of the R dye based fluorescent edge concentrators).

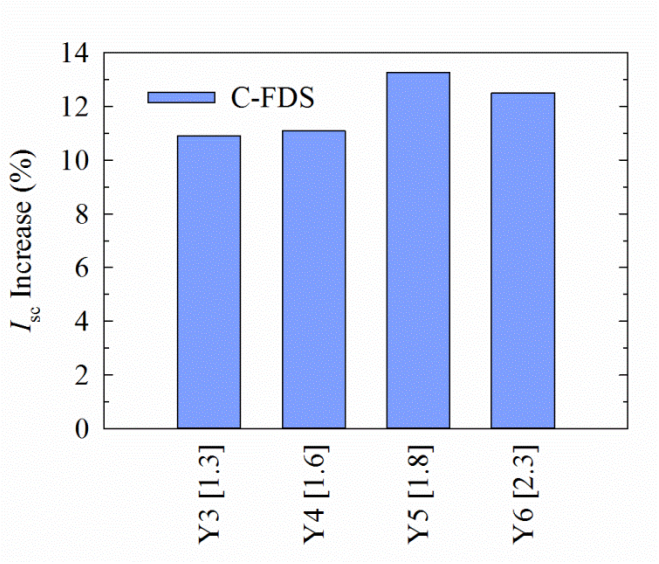

Figure 76 Measured increase in I_{sc} of solar cell coupled to Y dye concentrating fluorescent down-shifting structures relative to un-doped PMMA structures.

Subsequently, fluorescent solar collectors of different mixtures of V (V indicates BASF Lumogen F series Violet 570 dye), Y and O dye were fabricated and tested as fluorescent down-shifting structures and concentrating fluorescent down-shifting structures. Figure 77 (FDS is fluorescent down-shifting structure) shows the relative increase in I_{sc} of CdS/CdTe solar cells coupled to different collectors (measurements were again conducted under calibrated Xenon white light). The results indicate that Y and O dyes are superior for light concentration most likely because there are more excitation photons at the absorbing wavelengths of these dyes. V dye is seen to be useful primarily for enhancing the wavelength shifting effect since the EQE of the solar cell is very poor at the absorbing wavelengths of this dye. A total dye concentration beyond 6 g/l was not observed to increase the current output of concentrating fluorescent down-shifting structures possibly due to greater re-absorption. Indeed, in some samples higher dye concentrations are seen to lead to a smaller enhancement in current output. From the results it appears that, among the samples studied, application

of the Y4,O2 [1.8] collector with a total dye concentration of 6 g/l results in the largest increases in current output.

It is seen that on application of the Y4 [1.6] fluorescent down-shifting structure, a close to 5% increase in current output was measured while for the same collector as a concentrating fluorescent down-shifting structure a resulting current increase near 10% is observed due to concentration of photons. This is further improved to over 20% on addition of the O.

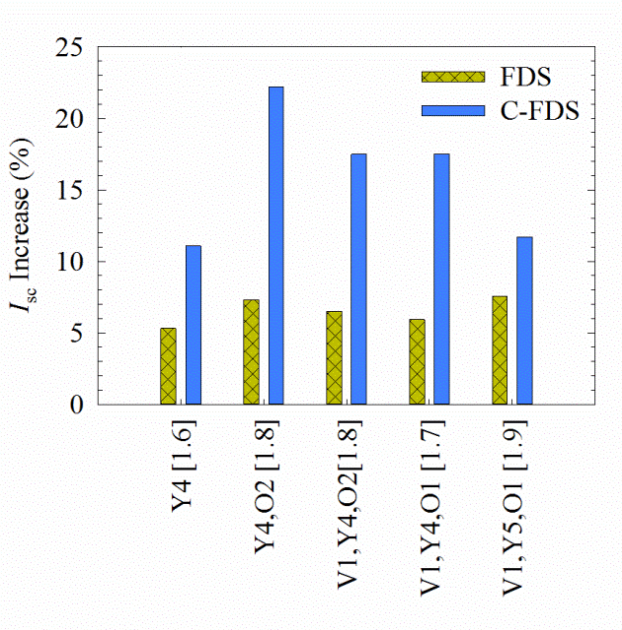

Figure 77 Measured increases in I_{sc} relative to an un-doped PMMA collector for fluorescent down-shifting structures and concentrating fluorescent down-shifting structures.

8.4.2. Fitting current output of solar cell with down-shifting structures applied

The current output resulting from excitation at different wavelengths has also been measured. We recall from Chapter 6 that in systems where Q_c, EQE_f and the collector top surface reflectance, R_{top}, can be assumed to be wavelength independent, the following general expression gives the short circuit current output, I_{sc}, of fluorescent solar collectors:

$$I_{sc}(\lambda) = CQ_a(\lambda)N_{inc}(\lambda) + D\{1 - Q_a(\lambda)\}EQE(\lambda)N_{inc}(\lambda) \quad (118)$$

where C and D are constants and EQE is the EQE of the solar cell. This equation can be used to separate the contribution of fluorescence and excitation light on the solar cell current output. The current output for excitation wavelengths not measured can also be approximated from this expression.

In order to achieve this, Equation (118)) has been used to calculate a theoretical fit for different collectors. The constants C and D were obtained i.e. the constant C is the scaling factor where the EQE of the solar is poor (i.e. at short wavelengths) while the constant D is the scaling factor at wavelengths corresponding to weak absorption by the collector. For the theoretical fit, the photon flux for a typical Xenon lamp (shown in Figure 75) has been used as the incident photon flux. The fit is observed (Figure 78) to match the current measurements rather well in spite of the large variation in the absorbance of these photon management structures. This indicates that the assumption of constant Q_c and EQE_f with the excitation wavelength is a good approximation in the devices fabricated.

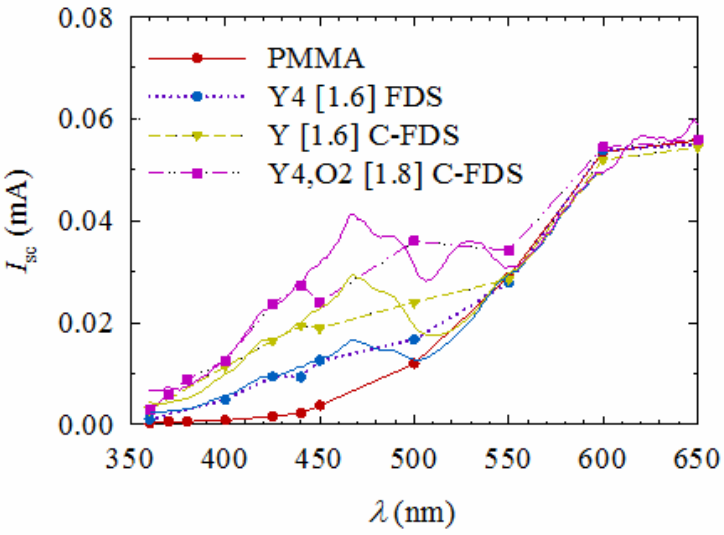

Figure 78 Current output of solar cells coupled to a fluorescent down-shifting structure and concentrating fluorescent down-shifting structures. Fit based on Equation (118)) also shown as solid lines.

By integrating the theoretical fits, a calculated increase in I_{sc} has been obtained and is compared to the experimentally measured values as shown in Figure 79. A reasonably good correlation is observed. Figure 79 also shows the increase in I_{sc} predicted under

AM1.5G that has been calculated by using the AM1.5G spectrum for the incident photon flux term in Equation (118)).

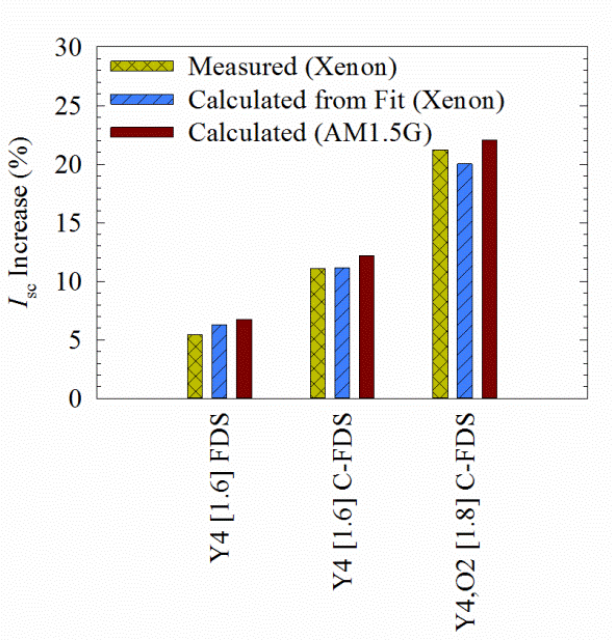

Figure 79 Measured and calculated (from fit based on Equation (118))) increases in I_{sc} of solar cell coupled to down-shifting structures relative to an un-doped PMMA collector.

Figure 80 shows the absorbance and fluorescence escaping the bottom surface (excitation at 440 nm) for the Y4 [1.6] and Y4,O2 [1.8] fluorescent solar collectors (note that the detected fluorescence was subject to multiple re-absorption and re-emission events). It is clear that for incident excitation photons at wavelengths below 450 nm the absorbance is not significantly different for the two different collectors since the concentration of Y dye is the same for both. The bottom fluorescence (excitation at 440 nm) is, however, seen to be red-shifted for the Y4,O2 [1.8] fluorescent solar collector as compared to the Y4 [1.6] collector. This indicates energy transfer from the Y to the O dye with emission taking place mostly in the O dye. The larger EQE of the solar cell to the red-shifted bottom fluorescence of the Y4,O2 [1.8] collector compared to the Y4 [1.6] collector explains the larger current output seen in Figure 78 on coupling to a solar cell even at wavelengths corresponding to identical absorbance for both samples.

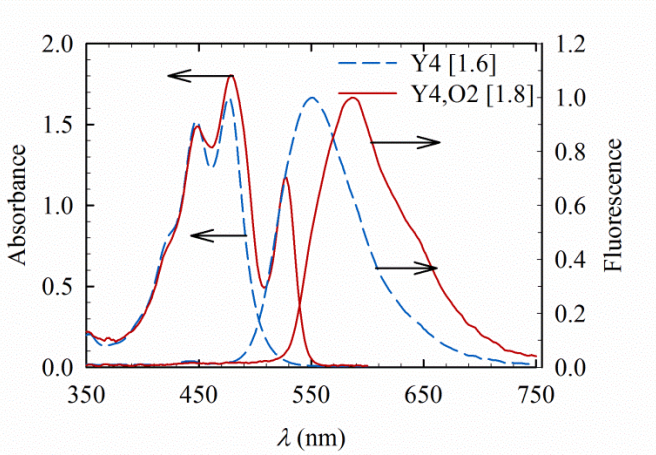

Figure 80 Absorbance and bottom fluorescence of the Y4 [1.6] and Y4,O2 [1.8] fluorescent solar collectors.

The contribution of fluorescence, I_f, and direct excitation light, I_d, on the current output have also been determined from Equation (118)), i.e. the first term on the right hand side of Equation (118)) corresponds to I_f while the second term corresponds to I_d (as described in detail in Chapter 6). The results are plotted in Figure 81 for the Y4,O2 [1.8] concentrating fluorescent down-shifting structure. As shown clearly in this figure Equation (118)) allows an estimation of the effect of the collector even at wavelengths where current is due to a mixture of direct and fluorescent photons. It is clear from Figure 81 that the current output due to short wavelength excitation photons is primarily due to the effect of the collector, however as the EQE of the solar cell increases and the absorbance of the collector decreases, the current output is due to a mixture of fluorescent and direct excitation photons. Finally, at long wavelengths where the collector does not absorb light, the current output is entirely due to the direct electrical conversion of excitation photons. The constants C and D obtained from Equation (118)) can also be used to estimate the reflectance and transport losses in fluorescent solar collectors. This will be useful for optimising the design of such systems.

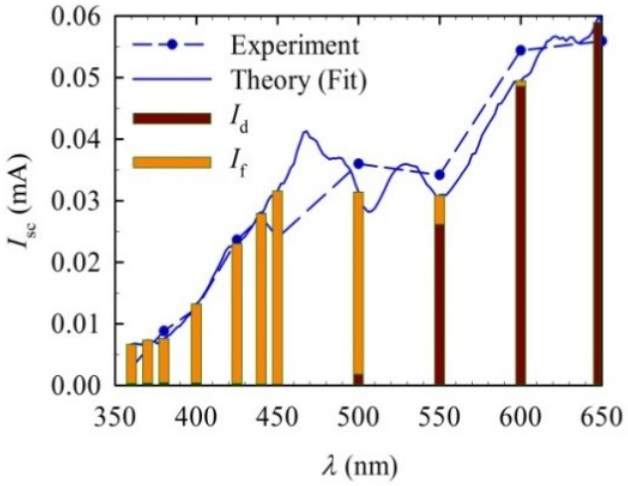

Figure 81 Contribution of Y4,O2 [1.8] and excitation light on the current output of the solar cell: obtained from a fit based on Equation (118)).

8.4.3. Losses in down-shifting structures

This section looks at the results of investigations into certain losses present in fluorescent down-shifting structures and concentrating fluorescent down-shifting structures. The effects of the collector/solar cell substrate thicknesses and edge mirrors have been investigated. Analysis of the sources of loss in these devices will allow the design of higher efficiency fluorescent down-shifting structures and concentrating fluorescent down-shifting structures.

To compare the effect of the collector substrate thickness on fluorescence emission, a collector using 100 μm thick glass substrates was compared with those using 1 mm glass substrates (Y0.2 [0.1], Y0.8 [0.9] and Y3 [1.6] fluorescent solar collectors). An increase in bottom and top fluorescence when thinner glass substrates are used is shown in Figure 82. One possible reason for the increase seen is due to a greater number of passes through the active dye layer. This will lead to an increase in the re-absorption probability of trapped light and therefore re-emission of this light into the top or bottom escape cones. If the trapped light is not re-absorbed, it would be lost through the collector edge. Therefore, fluorescent edge concentrators with thicker substrates are expected to reduce escape of light through the top and bottom surfaces and therefore maximise collection of light at the edges while fluorescent down-shifting structures and concentrating fluorescent down-shifting structures benefit from thinner glass substrates.

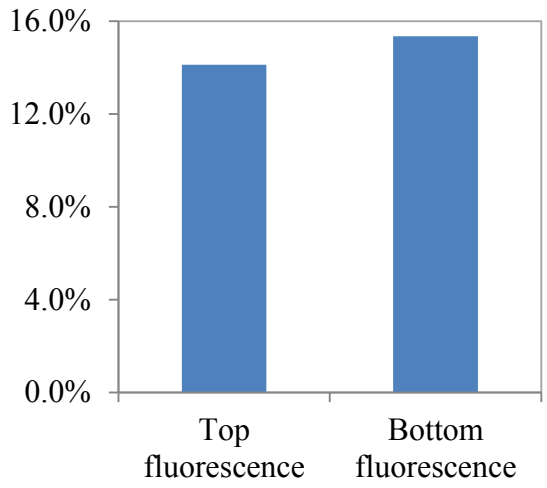

Figure 82 Fluorescence increases with the use of a thin glass substrates (Y0.2 [0.1], Y0.8 [0.9] and Y3 [1.6] results averaged).

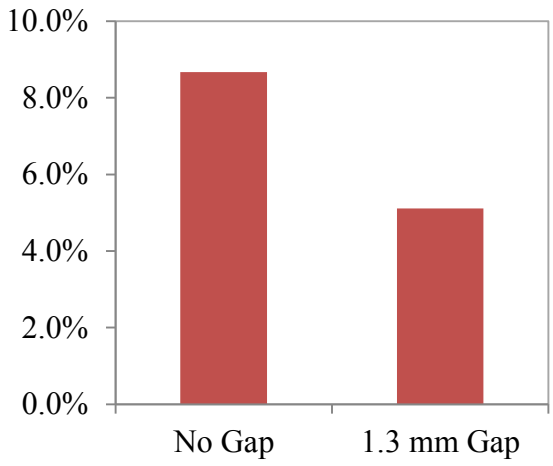

Figure 83 Increases in bottom fluorescence on application of edge mirrors with a 1.3 mm air gap and no air gap (Y0.2 [0.1], Y0.8 [0.9] and Y3 [1.6] results averaged).

The impact of placing mirrors near the fluorescent solar collector edges on the bottom fluorescence has also been investigated in a Y dye based collector (mirror dimensions equal to 11 x 11 mm). Figure 83 shows the increase in bottom fluorescence when mirrors are used to limit these edge losses. It is apparent from these results that using a 1.3 mm air gap between the edge and mirror is less effective than when a mirror is placed in contact with the edge. This is possibly due to more light being reflected back onto the edge when there is no air gap. It is important to note however, that there is likely to be an optimum air gap distance, since if the mirror is touching the edge, internally reflected rays might also be reflected by the mirror at a lower efficiency than when there is an air gap.

The effect of the solar cell glass substrate thickness on the performance of fluorescent down-shifting structures has been studied using ray tracing. Figure 84 shows ray tracing results for the collection probability (i.e. Q_{c1} is the collection probability for the first generation fluorescence) for different thicknesses of the solar cell glass substrate (the model consists of an 11 x 11 x 1 mm PMMA based fluorescent down-shifting structures placed on top of a solar cell consisting of an 11 x 11 mm active layer and 15 x 15 mm glass substrate, refractive indices of PMMA and glass are set equal to 1.5). As α_{em} goes to zero Q_{c1} equals the fraction of emission emitted towards the solar cell. The results

indicate that the use of thicker solar cell glass substrates increases the potential for loss through the edges. In the ideal case where the solar cell glass substrate is removed and perfectly reflecting mirrors are placed on the fluorescent solar collector edges, approximately 88% of photons are emitted towards the solar cell, this value is cut in half when the mirrors are removed and a 3 mm thick glass substrate is used.

This appears to be similar to what is expected. For a rectangular fluorescent down-shifting structure without any mirrors or solar cells attached, assuming a refractive index of 1.5, emission within the escape cone associated with any one of the collector's six surfaces will comprise of approximately 12.5% of the total fluorescence emitted.

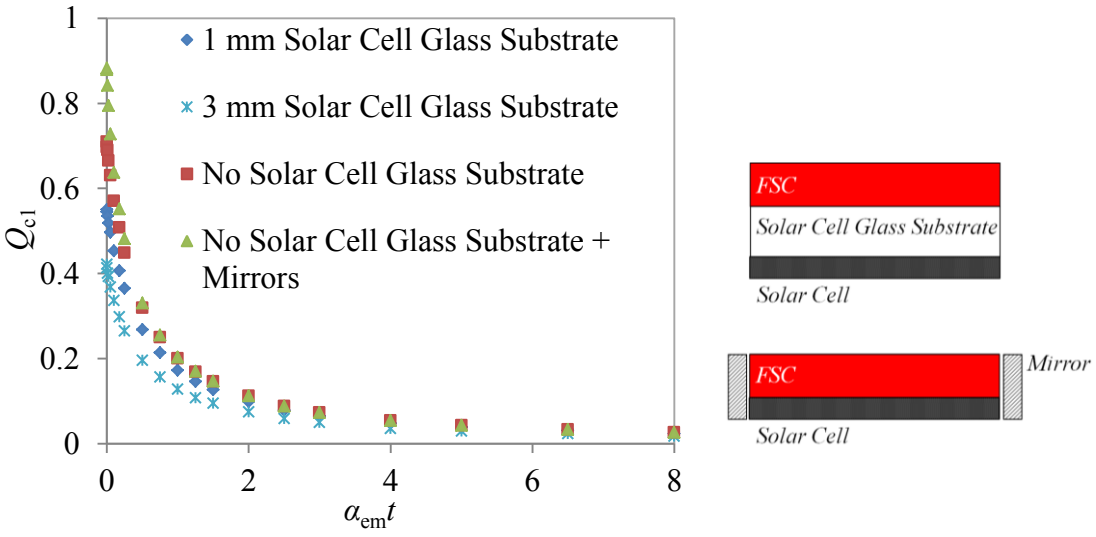

(a) (b)

Figure 84 (a) Q_{c1} when the fluorescent down-shifting structure and the solar cell are the same size. The absorption coefficient at the excitation wavelength is equal to 0.23 mm^{-1} and (b) schematic of systems: different solar cell glass substrate thicknesses as well as with and without the application of edge mirrors modelled.

So in the case of a fluorescent down-shifting structure coupled to perfectly reflecting edge mirrors and placed on top of a solar cell without a glass substrate, as α_{em} approaches zero, the only loss will be from the top escape cone i.e. 12.5% of fluorescence emitted. Therefore from this basic calculation the collection probability should be close to 87.5%. The value obtained from ray tracing which includes processes such as Fresnel reflection from the top surface come to 88%.

For other configurations it becomes more complicated to obtain rough estimates, for example if we remove the mirrors from the fluorescent down-shifting structure edges not all the emission within the edge escape cones will escape, it will depend on the position of the emitting dye molecule and the direction of emission. What is clear however is that as the glass thickness of the solar cell increases more of the photons emitted within the edge escape cone is expected to escape. This is consistent with the changes observed on Q_{c1} as the solar cell glass thickness increases from 0 mm to 3 mm.

8.5. Integrated photonic fluorescent solar collector

This section presents measurements of the fabricated 1D integrated photonic fluorescent solar collector. In order to design these structures for high efficiency solar concentrating applications, it is important to know the effect of these devices on photon transport. Two types of measurements i.e. transmittance and emission from these devices have been used to characterise photon transport in 1D integrated photonic collectors. The transmittance of this device will be compared with calculations using the transfer matrix method. It will also be shown that the emission from the 1D integrated photonic collector is consistent with calculations of its band structure. The effectiveness of theoretical tools to predict photon transport will be useful in the design of 1D integrated photonic fluorescent solar collectors for high efficiency solar concentration. The potential of these devices will also be investigated by looking at the band structure of an equivalent device with an infinite number of layers. This will be used to approximate the increases in light trapping possible with these devices.

8.5.1. Transmittance

The transmittance of the fabricated 1D integrated photonic fluorescent solar collector has been measured. The transfer matrix method has been used to compare the measurements with theory (see Chapter 7 for details about the structure) with prediction from theory (see Figure 85). We recall from Chapter 2 that the transmittance, T, is obtained from the element M_{11} of the matrix M connecting the electric field amplitudes at the top and bottom of the multi-layer device, i.e.:

$$T = \left(\frac{a_S}{a_0}\right)^2 = \left(\frac{1}{M_{11}}\right)^2 \tag{36}$$

where a_S is the electric field amplitude in the glass substrate and a_0 is the electric field amplitude in air. The results comparing the experimental measurements to the transfer matrix method shown in Figure 85 shows a reasonably good correlation.

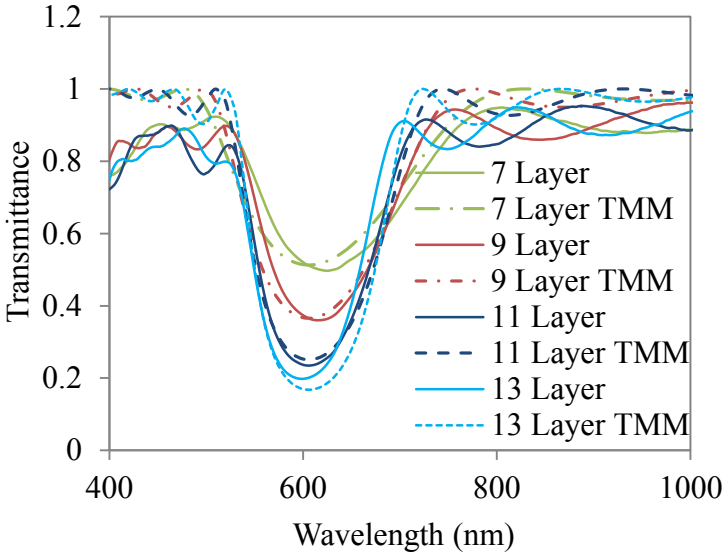

Figure 85 Comparison between calculated and measured transmittance of 1D integrated photonic fluorescent solar collector. TMM is transfer matrix method.

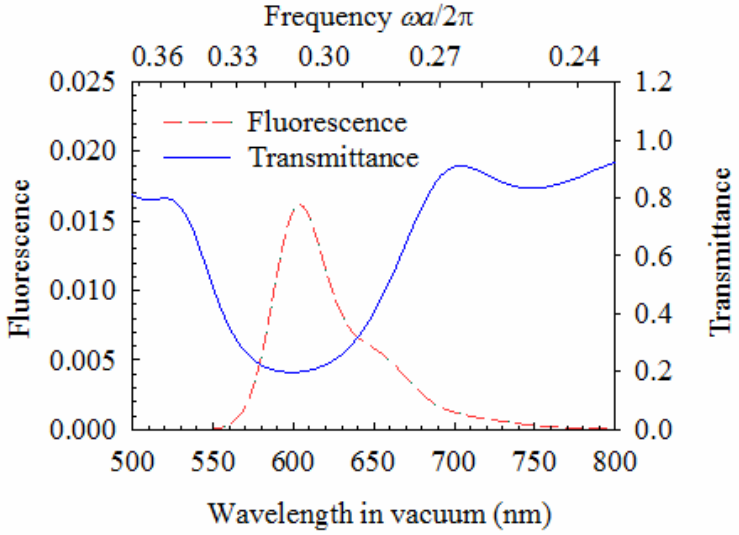

Figure 86 Transmittance of 13 layer 1D integrated photonic fluorescent solar collector compared with first generaton fluorescence of R dye in SiO_2.

The measured transmittance of the 1D integrated photonic fluorescent solar collector (for 13 layers) is shown in Figure 86 along with the first generation fluorescence of a

conventional collector consisting of a silicon dioxide (SiO_2) layer doped with R dye. As shown in this figure, the 1D integrated photonic collector has been tuned to have a peak reflectance in the normal direction at around 600 nm since this corresponds to the peak emission of the fluorescence of the R dye in SiO_2.

8.5.2. Emission from an integrated photonic fluorescent solar collector

The emission from the 1D integrated photonic collector is likely to reveal information about its structure and suitability for solar concentrating application. In this section the emission of the fabricated photonic collector will be presented and analysed. Figure 87 shows the top and edge emission for different number of layers. Note that the area under the emission curves have been normalised to unity so as to represent a probability distribution.

It is clear from these results that the top emission is suppressed at wavelengths corresponding to the greatest normal reflectance. The edge emission is however more complex and seems to vary considerably for different number of layers.

Since the layers fabricated are very thin and only lightly doped with fluorescent molecules, distortion of the emission due to re-absorption is not expected and therefore this cannot explain the distribution of the edge emission detected. Measurements of the top and edge emission of a conventional Spin-fluorescent solar collector with the same active dye layer thickness i.e. 6 SiO_2 layers thick (103.5 x 6 nm), is shown in Figure 88 (IP-FSC indicates integrated photonic fluorescent solar collector). These measurements verify that re-absorption effects if any have a minimal impact. From this it is clear that any distortion in the spectra must be due to the effect of the photonic crystal.

To explain the edge emission it is necessary to investigate the nature of the band structure of the fabricated 1D integrated photonic collector. From Chapter 2, we know that to calculate the band structure of a 1D photonic crystal requires that the element M_{11} of the matrix M connecting the electric field amplitudes within air and the glass substrate satisfies the following condition:

$$M_{11} = 0 \tag{48}$$

Figure 89 (a) and Figure 90 (a) show the modes that satisfy this condition for the 1D integrated photonic fluorescent solar collector (13 layer stack) for angles of emission (i.e. zenith angle, θ, within SiO_2) close to 0° and 90° respectively (only *s* polarisation

has been considered). The *x* axis shows the wavelength of emission (in air). For a finite stack the band structure is seen to consist of discrete bands. The wavelengths corresponding to propagating modes as well as the centre between adjacent propagating modes have been labelled A-F for both emission at 0° and 90°. These angles correspond to the detected top (0°) and edge emission (90°) respectively.

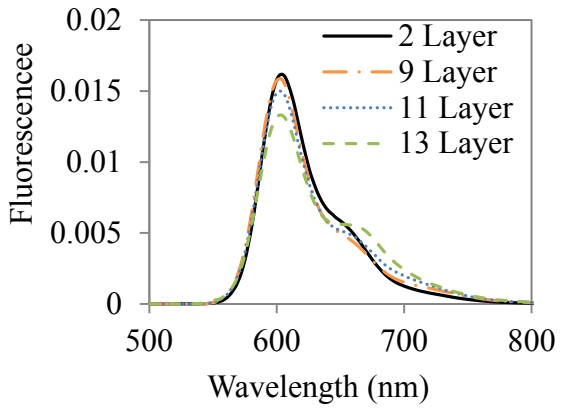

(a)

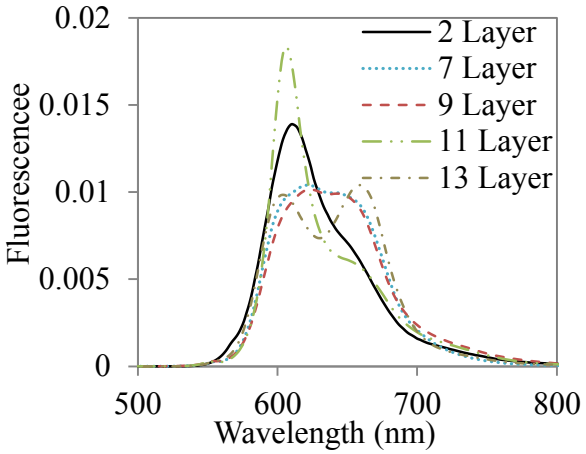

(b)

Figure 87 (a) Top and (b) edge emission of fabricated 1D integrated photonic collector.

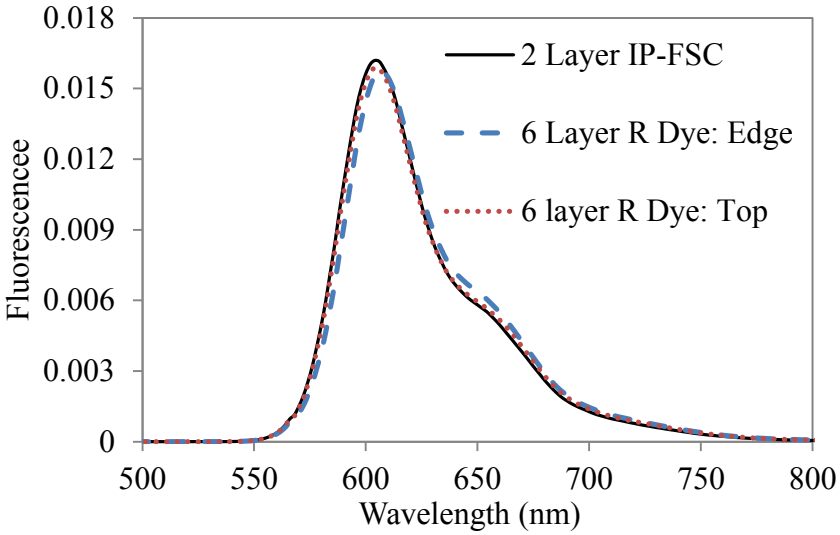

Figure 88 Edge and top emission of a 6 layer R dye doped SiO_2 Spin-fluorescent solar collector compared to the top emission (equivalent to the first generation fluorescence) of a 2 layer 1D integrated photonic fluorescent solar collector.

To compare the calculated band structure to the emission measured, the normalised top and edge fluorescence of the 1D integrated photonic collector has been plotted next to the relevant band structures in Figure 89 (b) and Figure 90 (b). The top and edge emissions have been normalised by dividing by the first generation emission from a conventional Spin-fluorescent solar collector (SiO_2 host and glass substrae). This allowes the effect of the photonic crystal on the emission to be seen.

The emission distributions show features corresponding to suppression and enhancement of emission. Enhancements of emission have been labelled A, C, D and F while suppressions have been labelled B and E. From Figure 89 and Figure 90 it is clear that the width of the suppression as well as its frequency ranges are seen to correspond with the calculated band structure.

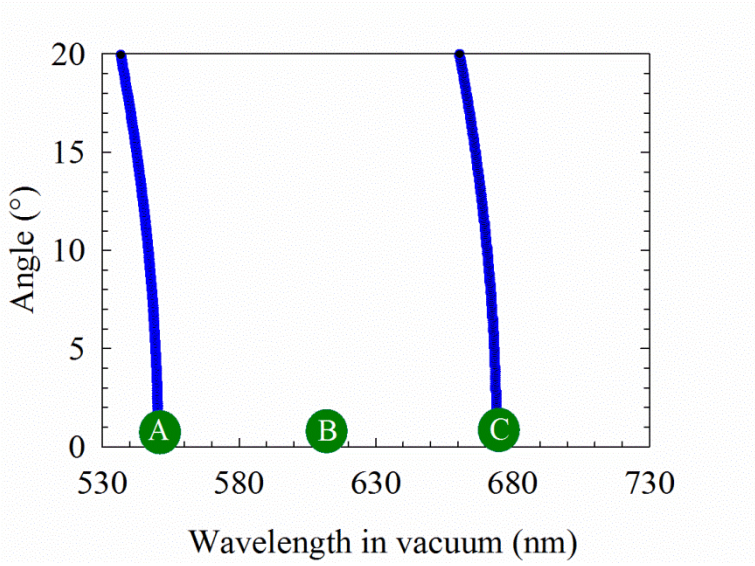

(a)

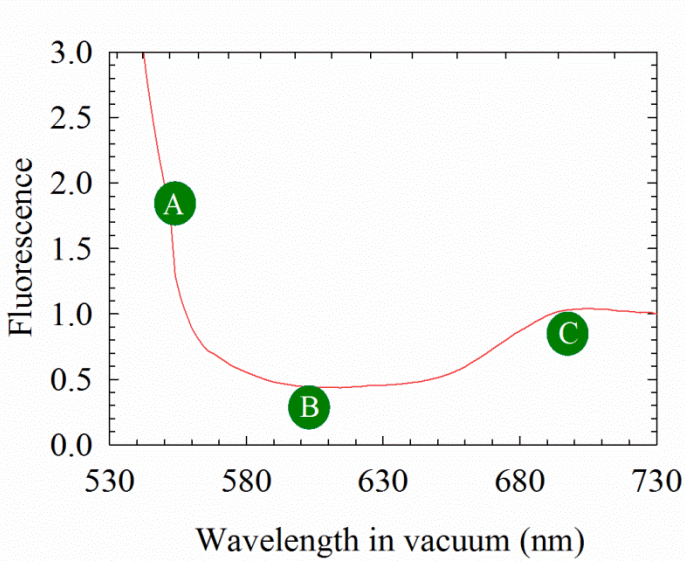

(b)

Figure 89 (a) Band structure of a 13 layer 1D integrated photonic fluorescent solar collector for emission in SiO_2 close to 0° and (b) experimentally measured normalised top emission. Enhancement of emission at the band edges and suppression in the gap is clearly visible.

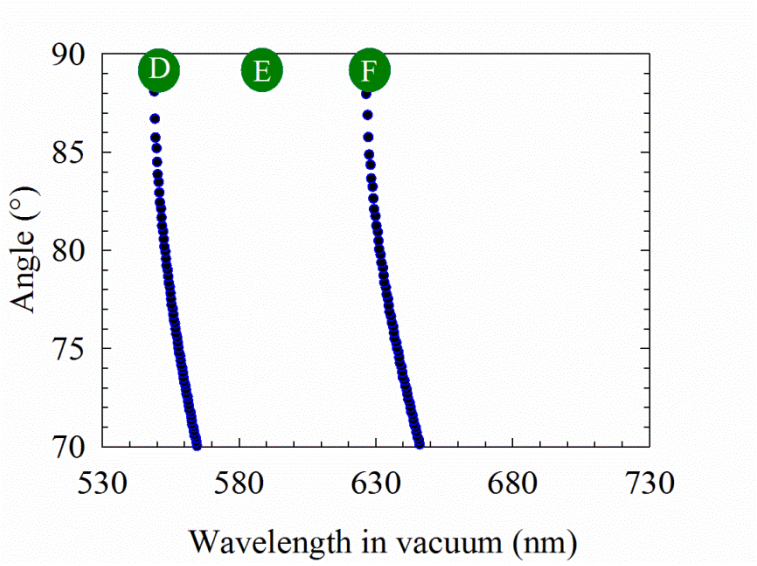

(a)

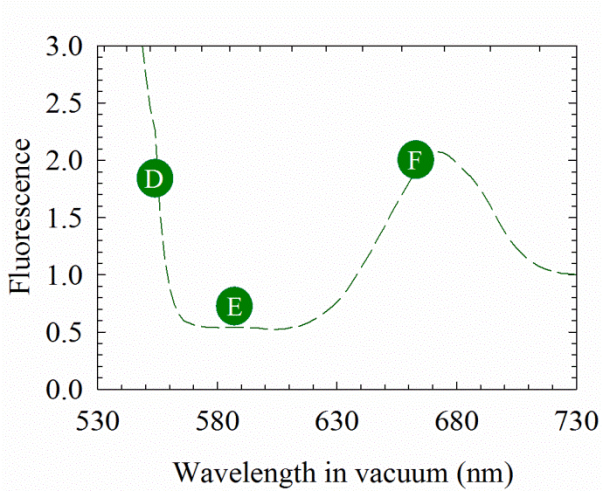

(b)

Figure 90 (a) Band structure of a 13 layer 1D integrated photonic fluorescent solar collector for emission in SiO_2 close to 90° and (b) experimentally measured normalised edge emission. Again a clear enhancement at the band edges and suppression in the gap is observed.

As the number of layers increases, the number of allowed modes will increase forming continuous bands separated by photonic band gaps. The evolution of the band structure is clearly apparent for example when comparing the band structure of the 13 layer 1D integrated photonic fluorescent solar collector to that for 100 layers as shown in Figure 91.

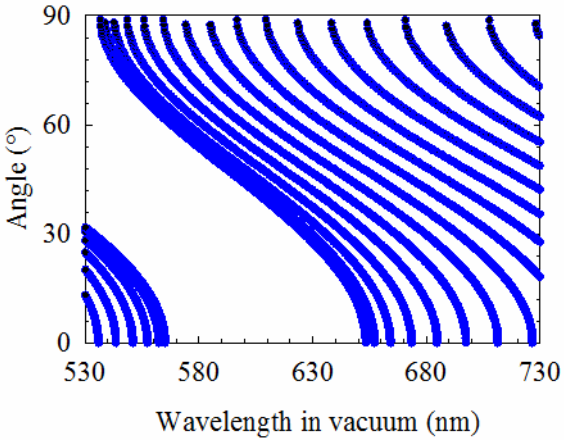

Figure 91 Band structure of a 100 layer 1D integrated photonic fluorescent solar collector.

The normalised edge emission of the 1D integrated photonic collector for different number of layers is plotted in Figure 92 and Figure 93. It is clear from these results that as the number of layers is increased the wavelength of peak emission enhancement is red-shifted. In Figure 92 the moving peak is labelled ① while the shifting peaks are labelled ② in Figure 93.

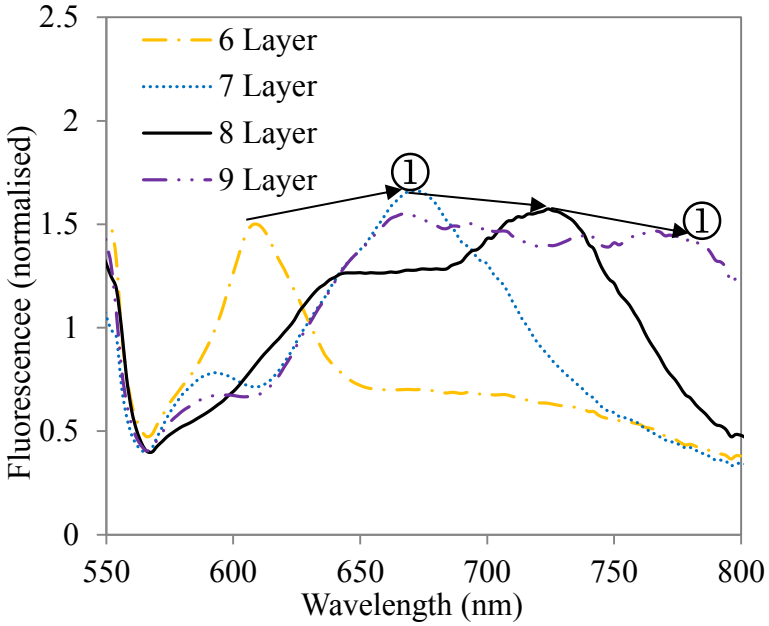

Figure 92 Normalised edge emission for a 6 to 9 layered 1D integrated photonic fluorescent solar collector.

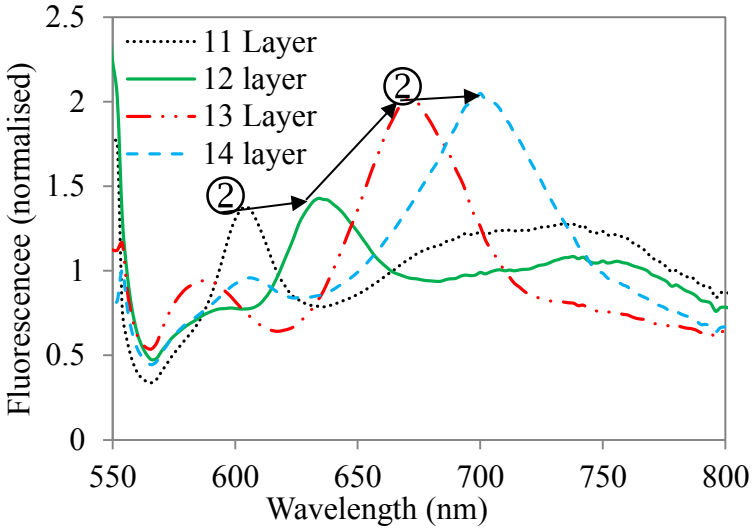

Figure 93 Normalised edge emission for an 11 to 14 layered 1D integrated photonic fluorescent solar collector.

The dispersion relation indicates angles and wavelengths of photon propagation. The reflectance of the 1D integrated photonic fluorescent solar collector is another measure of modes that can propagate through the crystal. Assuming that the incident rays originate from a semi-infinite SiO_2 medium (above the top layer of the photonic collector) the transmittance of light incident on the top surface of the 1D integrated photonic fluorescent solar collector for different number of layers has been calculated (only *s* polarisation has been considered). The transfer matrix method (Equation (36))) has been used and the results are plotted in Figure 94 as a function of the angle (i.e. zenith angle θ) of propagation within SiO_2 and the wavelength (in air). The evolution (red-shift) of the sub-bands with increasing number of layers and their effect especially at angles close to 90° is clear in these results. It is also clear that the peaks seen in the normalised edge emissions as shown in Figure 92 and Figure 93 correspond to larger transmittance as shown in Figure 94 for angles close to 90°. The red-shift of the sub-band labelled ① with increasing number of layers as seen in Figure 94 corresponds to the shift in the emission enhancement peak labelled ① in Figure 92. The red-shift of the sub-band labelled ② with increasing number of layers as seen in Figure 94 corresponds to the shift in the enhancement peak labelled ② in Figure 93. From these results it is clear that the changes in the distribution of the edge emission with number of layers can be explained by the evolution of the band structure in the 1D integrated photonic fluorescent solar collector.

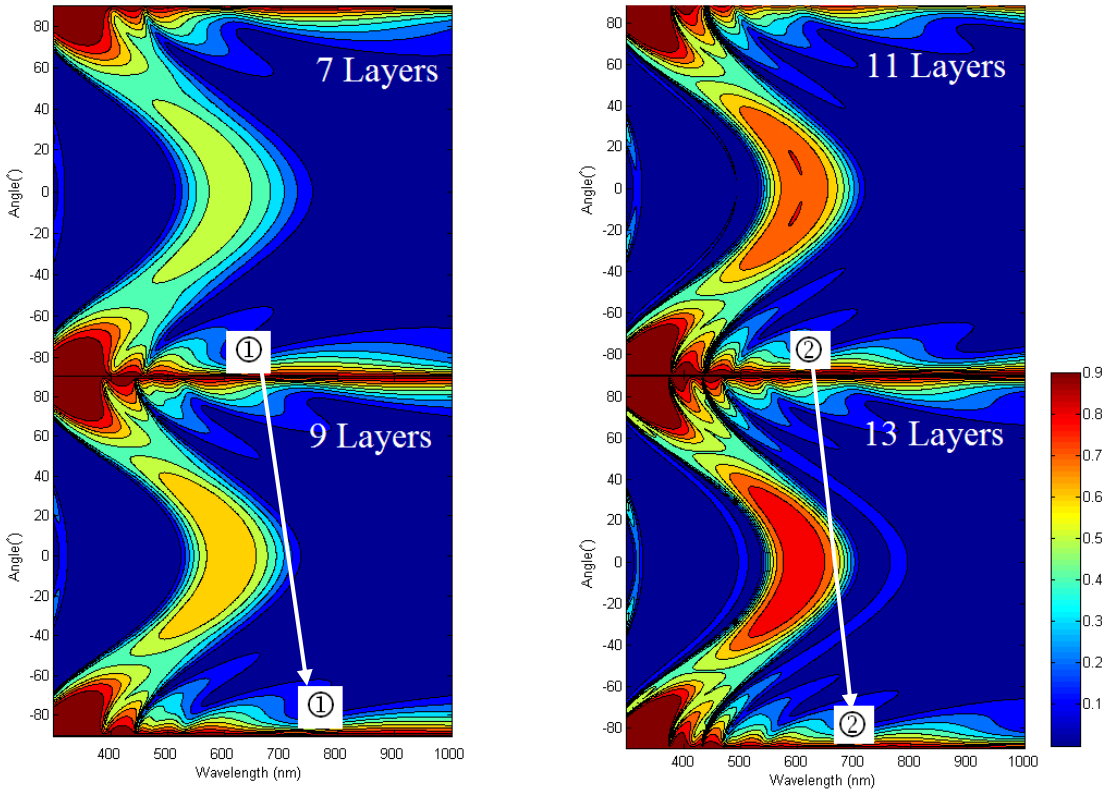

Figure 94 The evolution of the reflectance of the 1D integrated photonic fluorescent solar collector with increasing number of layers.

The measured emission results demonstrate that not only can a fundamental and major loss mechanism, i.e. the top and bottom escape cone loss, in fluorescent solar collectors be reduced using 1D integrated photonic collectors but that the distribution of fluorescence can also be tuned for trapped fluorescence. This could allow the design of 1D integrated photonic collectors with a lower overlap between absorption and trapped emission spectra and therefore lower re-absorption. Another possibility would be to tune emission according to the response of the coupled solar cell.

In Chapter 6, it was shown that the electric field amplitudes of the left travelling, *B*, and right travelling, *C*, waves within the emitting layer inside a 1D photonic crystal can be obtained from:

$$C = \frac{r_{21}e^{-ik_{2z}d}e^{ik_{2z}(d-z_f)}}{e^{-ik_{2z}(d-z_f)}(e^{ik_{2z}d} - r_{21}r_{23}e^{-ik_{2z}d})} \quad (158)$$

and:

$$B = \frac{r_{21} r_{23} e^{-ik_{2z}d}}{e^{ik_{2z}d} - r_{21} r_{23} e^{-ik_{2z}d}} \tag{159}$$

where r_{21} and r_{23} are Fresnel reflection coefficients, k_{2z} is the wave number in the z direction within the emitting layer, d is the thickness of the emitting layer and z_f is the distance between the emitting molecule and the left interface of the emitting layer. From these electric field amplitudes the electric field amplitudes outside the 1D integrated photonic fluorescent solar collector can be obtained.

In this manner the electric field intensity (s polarisation) outside the top and bottom surfaces of the 13 layer 1D integrated photonic fluorescent solar collector (effect of glass has been ignored and the intensity has been averaged over different points of emission within all the dye layers of the structure) has been obtained. The results are shown in Figure 95 as a function of angle (i.e. zenith angle, θ, in air) and the wavelength (in air). The results clearly show suppression of the field within the band gap and some enhancements at the band edges consistent with the experimental results seen in Figure 89 and Figure 90.

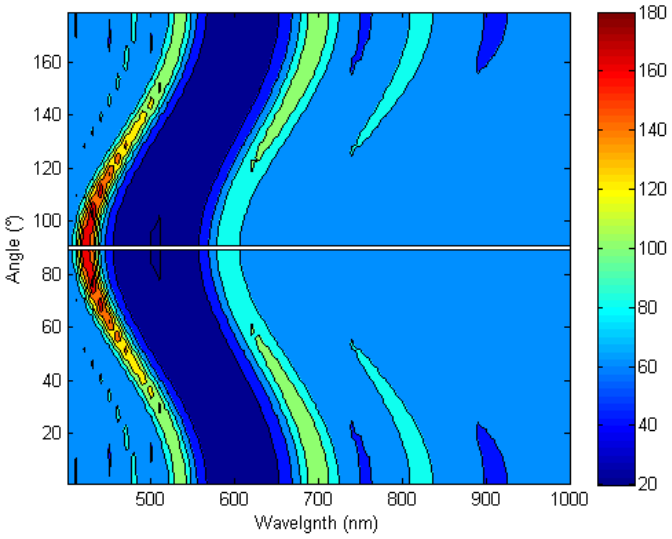

Figure 95 The electric field intensity exiting the top and bottom surfaces of the 13 layer 1D integrated photonic fluorescent solar collector.

8.5.3. Propagation within the photonic crystal (infinite stack)

The propagation of photons within the photonic collector similar to the one fabricated but with an infinite number of layers has been analysed. Its dispersion relation has been used to analyse the potential of the fabricated 1D integrated photonic collector.

The dispersion relation is calculated using the plane wave expansion method. From Chapter 2 we know that the wave equation describes propagation of electromagnetic waves in a 1D photonic crystal, i.e. for *s* polarisation assuming the plane of incidence to be in the *yz* plane:

$$-\frac{\partial^2 \mathrm{E}_x(\mathrm{y},\mathrm{z})}{\partial z^2} - k_\mathrm{y}^2 \mathrm{E}_x(\mathrm{y},\mathrm{z}) = \left(\frac{\omega}{c}\right)^2 \varepsilon(r')\mathrm{E}_x(\mathrm{y},\mathrm{z}) \tag{15}$$

where E_x is the electric field in the *x* direction, k_y is the wave number in the *y* direction, ω is the angular frequency, c is the speed of light, ε is the dielectric constant and r' is the position.

Incorporating into the wave equation Bloch's theorem which consists of the Bloch wave number, K_z, and a periodic function *u*:

$$\mathrm{E}_x(\mathrm{y},\mathrm{z}) = \mathrm{e}^{\mathrm{i}k_y y}\mathrm{e}^{\mathrm{i}K_\mathrm{z} z}u(z) \tag{13}$$

and Fourier expanding quantities that vary periodically in the *z* direction:

$$u(z) = \sum_{n=-\infty}^{\infty} c_\mathrm{n} e^{-in\bar{a}z} \tag{16}$$

$$\varepsilon(z) = \sum_{m=-\infty}^{\infty} d_\mathrm{m} e^{-im\bar{a}z} \tag{17}$$

where c_n and d_m are Fourier expansion coefficients and $\bar{a}$ is the reciprocal lattice constant, an eigenvalue equation is obtained:

$$\Lambda \bar{C} = \left(\frac{\omega}{c}\right)^2 \bar{C} \tag{20}$$

where the operator, Λ, is a matrix that depends on k_y and K_z and eigenmode $\bar{C}$. The eigenvalues of this operator gives allowed values of ω for a given k_y and K_z i.e. the dispersion relation. A similar treatment can be used to obtain the dispersion relation for *p* polarisation (see Chapter 2).

Using the plane wave expansion method, the dispersion relation has been plotted for the fabricated photonic collector assuming it consists of an infinite stack. The results are shown in Figure 96, Figure 97 and Figure 98 (the right side of these figures shows the dispersion relation for *s* polarisation while the left side shows for *p* polarization, *a* is the length of the unit cell in the 1D photonic crystal, n_1 and n_2 are the low and high refractive indices and $\bar{n}$ is the average i.e. weighted by thickness). From Figure 96 it is clear that the dispersion relation is a mix of discrete and continuous bands. Looking at the continuous bands in detail (i.e. Figure 97) it appears that the refractive index contrast of the materials used is not sufficient to make an omni-directional filter i.e. it is not possible to obtain unity reflection of light incident from air at all angles and for both polarisations at a particular wavelength. This follows from the fact that there is no wavelength (or frequency) for which there exists forbidden modes within the light cone (see Chapter 2 for light cone) for both *s* and *p* polarisations.

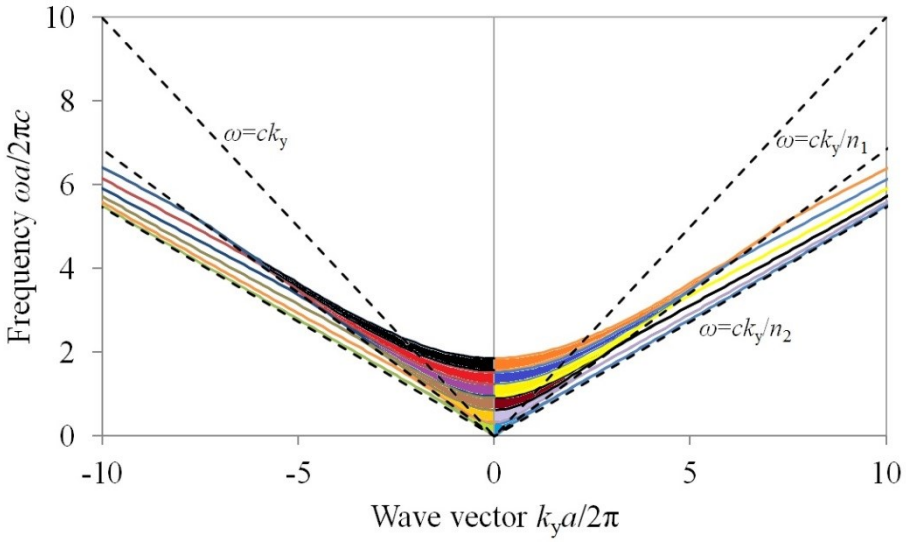

Figure 96 Dispersion relation in 1D integrated photonic fluorescent solar collector showing discrete and continuous bands.

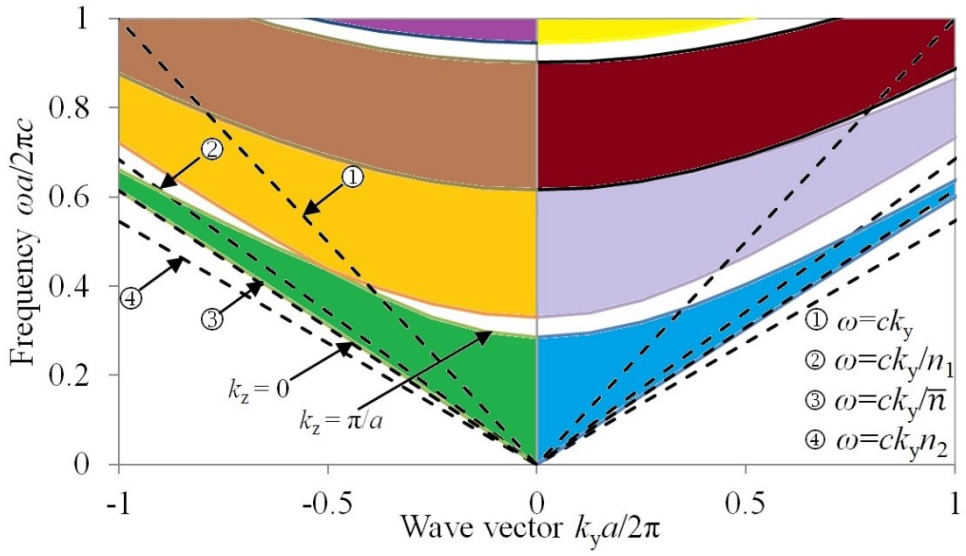

Figure 97 Dispersion relation 1D integrated photonic fluorescent solar collector showing continuous bands.

Figure 98 looks at the discrete bands in detail. It is clear that the discrete band and continuous bands are separated by the light line between the large refractive index and small refractive index material, i.e. below this line all modse are trapped within the high refractive index material while above it photons are free to propagate within the whole infinite stack. The finite thickness of the high refractive index material results in discrete allowed modes while the infinite thickness of the 1D integrated photonic collector leads to continuous bands. Indeed since the refractive index of glass is similar to that of the small refractive index material of the fabricated collector (i.e. SiO_2 layer), it is expected that there will be substantial propagation of light within the glass substrate.

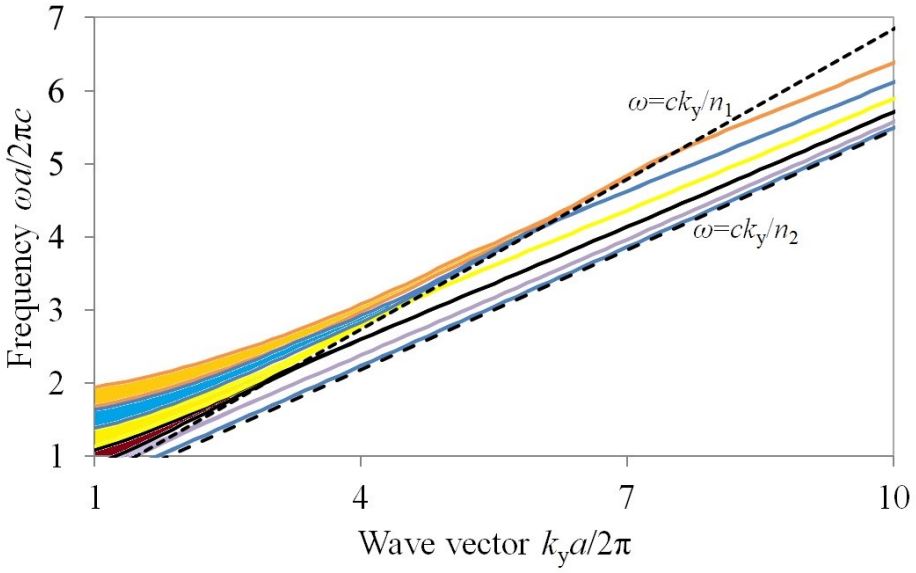

Figure 98 Dispersion relation of 1D integrated photonic fluorescent solar collector showing boundary between discrete and continuous bands.

Below the light line with respect to air there will be total internal reflections of rays travelling within the entire structure similar to the motion in conventional fluorescent solar collectors.

At a given frequency if there exists forbidden modes for a range of values of k_y between k_{1y} and k_{2y}, assuming emission is within the low refractive index material and negligible absorption, the angular extent of the forbidden modes with the low refractive index material i.e. θ_1 and θ_2 will be given by:

$$\theta_{1,2}(\omega) = \operatorname{asin}\left(\frac{k_{1,2y}}{\frac{\omega n_1}{c}}\right) \tag{172}$$

where n_1 is the low refractive index. The angles θ_1 and θ_2 (i.e. zenith angles within the low refractive index material) have been calculated from the dispersion relation of the infinite structure for *s* polarisation and is shown in Figure 99. It is clear from the results that the photonic crystal can strongly limit propagation of escape cone and trapped photons at certain frequencies. Indeed, bottom mounting solar cells to such photonic structures will also increase the efficiency of the solar cell. This is due to a reduction in the entropy generated due to smaller emission solid angles (Markvart, 2008).

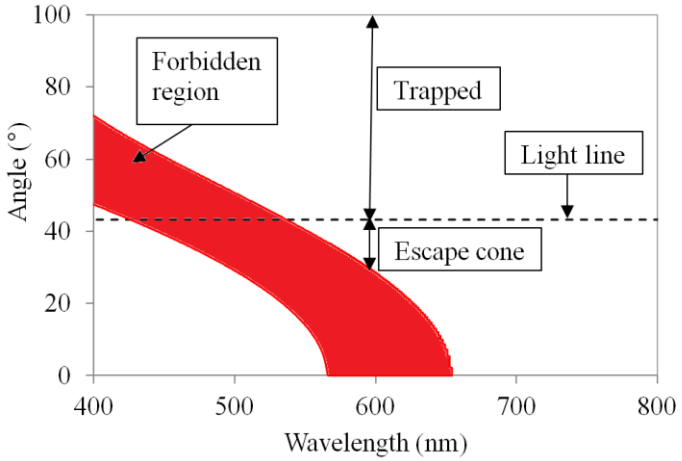

Figure 99 Forbidden region for *s* polarisation shown in red. Trapped and escape cone angular ranges at 600 nm also shown. Axes show angle of propagation in SiO_2 and wavelength (in air).

The trapped fraction assuming isotropic emission into allowed modes (i.e. neglecting the effect of the electric field intensity on emission) can be approximated from the ratio of the solid angle corresponding to propagating modes and the solid angle of a sphere (i.e. 4π). This has been plotted in Figure 100 (the *x* axis shows the wavelength in air). These results indicate strong enhancement of the trapped fraction peaking at close to 95%. This compares to a trapped fraction of 75% in a conventional Spin-fluorescent edge concentrator consisting of a fluorescent layer (SiO_2 host) deposited on a glass substrate.

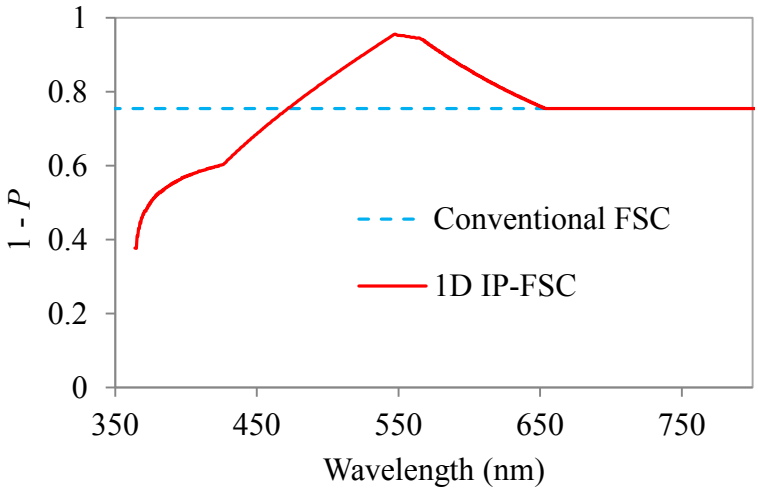

Figure 100 The trapped fraction for an infinite stack 1D photonic fluorescent solar collector.

8.6. Summary

The key results of this thesis has been presented:

- Re-absorption models developed in Chapter 6 have been verified using experimental measurements and/or results from ray tracing simulations.
- Angular resolved measurements are shown to indicate that the 4Cell setup (Mold-fluorescent edge concentrator) behaves like an ideal fluorescent edge concentrator.
- The OQE of fluorescent edge concentrators in 1Cell and 4Cell setups and fabricated by spin coating and moulding have been compared to theoretical predictions. Mold-edge concentrators in the 4Cell setup are again seen to behave close to an ideal fluorescent edge concentrator. It is also shown that losses in non-ideal devices can be quantified by comparing the OQE obtained from measurements with ideal models.
- Ideal fluorescent edge concentrators in the 4Cell setup has been optimised using the models developed.
- A general expression describing the current output of fluorescent solar collectors (presented in Chapter 6) has been used to highlight key features in the current output of fluorescent down-shifting structures and concentrating fluorescent down-shifting structures. This expression is also shown to allow separation of the contributions of fluorescent and excitation photons on the current output of the coupled solar cell.
- The effect of collector/solar cell glass substrate and edge mirrors on fluorescent down-shifting structures and concentrating fluorescent down-shifting structures has been analysed experimentally and using ray tracing simulations.
- The transmittance and emission from the first 1D integrated photonic fluorescent solar collector fabricated have been presented and is seen to be described well by the band structure of the device. It is clear that these 1D photonic collectors have the potential to reduce a number of fundamental loss mechanisms in conventional collectors such as the escape cone loss and re-absorption. Results from the edge emission also indicate the potential to tune emission frequency. This technique has the potential to minimise re-absorption or match emission according to the response of the coupled solar cell.

- The potential of the integrated photonic collector has been illustrated by looking at the photon transport within it assuming an infinite structure. The potential for the device to trap photon flux has been approximated and is seen to be substantially enhanced at certain wavelengths of emission when compared to conventional collectors.

References

Green, M.A., Emery, K., Hishikawa, Y., Warta, W. and Dunlop, E.D., 2011. *Solar cell efficiencies Tables (version 39).* Progress in Photovoltaics: Research and Applications. 20: 12-20. DOI: 10.1002/pip.2163.

Kittidachachan, P., Danos, L., Meyer, T.J.J., Alderman, N. and Markvart, T., 2007. *Photon collection efficiency of fluorescent solar collectors*. Chimia International Journal for Chemistry. 61: 780-786. DOI: 10.2533/chimia.2007.780.

Markvart, T., 2008. *Solar cell as a heat engine: Energy-entropy analysis of photovoltaic conversion*. Physica Status Solidi. 205: 2752-2756. DOI: 10.1002/pssa.200880460.

9. Conclusions and future work

This project has looked into the operation of fluorescent solar collectors and its application to solar cells. The major results of this work can be divided into three sections:

- An in-depth semi-analytical model describing conventional fluorescent solar collectors has been developed and verified experimentally.
- Losses in edge concentrators have been characterised in detail using a novel approach to resolve the angular distribution of rays in the collector. This has also been analysed using the theoretical model developed.
- A new type of photonic fluorescent collector, in the form of an integrated 1D photonic collector, has been designed, fabricated and characterised.

Thermodynamic treatments have been used to derive the maximum theoretical efficiencies of solar cells and collectors based upon previous work (Würfel, 2005)(Markvart, 2006) (see Chapter 2 and Chapter 6). This has lead to new insights into the operation of these devices such as the effect of light concentration on the current voltage relationship of a solar cell and the limits of efficiencies used to characterise fluorescent edge concentrators.

Theoretical models describing the re-absorption probabilities of different streams of photons within conventional fluorescent solar collectors have been developed in Chapter 6 extending the Weber and Lambe re-absorption model (Weber and Lambe, 1976). It is seen that a general expression can be used to unify the modelling of the different types of fluorescent solar collectors investigated. The 4Cell setup (i.e. edge concentrator coupled to four edge solar cells) has been studied in-depth since these devices do not suffer from certain loss mechanisms found in the 1Cell setup (i.e. edge concentrators coupled to 1 edge solar cell and 3 edge mirrors). Losses have been quantified by comparison with ideal models. The re-absorption models developed have also been verified experimentally and through the use of computer simulations.

The re-absorption probabilities calculated from these models allow the calculation of the optical quantum efficiencies of single dye fluorescent edge concentrators based on

established methods (Batchelder *et. al*, 1979)(Kittidachachan *et al*.,2007). These have been compared with experimental measurements and show good agreement. Single dye fluorescent edge concentrators tested in the laboratory are seen to have an estimated power conversion efficiency close to 4%.

Indeed, by refining the definitions of certain terms it is seen that the expressions describing fluorescent edge concentrators is also valid for fluorescent downshifting structures, even those that concentrate light..

It has also been shown experimentally how concentrating fluorescent down-shifting structure can be used to both concentrate light and improve the performance of cadmium telluride (CdTe) solar cells in wavelength regions showing a poor spectral response. The loss mechanisms in these devices have been explored and it is seen that losses from the collector edges and due to thicker glass substrates are substantial. The use of multi-dye collectors with energy transfer has also been shown to be effective in enhancing the wavelength shifting effect of fluorescent collectors. This is seen to be especially effective in improving the performance of CdTe solar cells.

A novel type of fluorescent solar collector, a 1D integrated photonic fluorescent solar collector has been fabricated using spin coating and characterised in detail (Chapter 6-8). Theoretical methods used to model this device include the transfer matrix method and the plane wave expansion method for 1D photonic crystals. The results indicate that 1D integrated photonic collectors have the potential to reduce a fundamental loss mechanism found in conventional collectors such as the escape cone loss. Additionally, it is predicted than the enhancement of emission in certain directions and wavelengths can be used to further reduce re-absorption and match emission to solar cell performance.

Future work should focus on the design and fabrication of collectors that have strong absorption across a wider range of wavelengths. This is important for both conventional and photonic based fluorescent solar collectors. The modelling and optimisation of such systems needs to be investigated in order to design and optimise high efficiency fluorescent solar collectors. In addition, for 1D integrated photonic collectors, alternative fabrication methods more suitable for making high quality, precise and a large number of layers should be determined.

References

Batchelder, J. S., Zewail, A. H. and Cole, T., 1979. *Luminescent solar concentrators. 1: Theory of operation and techniques for performance evaluation*. Applied Optics. 18: 3090-3110. DOI: 10.1364/AO.18.003090.

Kittidachachan, P., Danos, L., Meyer, T.J.J., Alderman, N. and Markvart, T., 2007. *Photon collection efficiency of fluorescent solar collectors*. Chimia International Journal for Chemistry. 61: 780-786. DOI: 10.2533/chimia.2007.780.

Markvart, T., 2006. *Detailed balance method for ideal single-stage fluorescent collectors.* Journal of Applied Physics. 99: 026101 1-3. DOI: 10.1063/1.2160710.

Weber, W. H. and Lambe, J., 1976. *Luminescent greenhouse collector for solar radiation*. Applied Optics. 15: 2299-2300. DOI: 10.1364/AO.15.002299.

Würfel, P., 2005. *Physics of solar cells: From principles to new concepts*. Wiley-VCH Verlag: Weinheim, Germany. DOI: 10.1002/9783527618545.